Experimental and numerical investigation of incipient plasticity in FCC polycrystals by X-ray synchrotron topotomography and CPFEM

Nicolas Guéninchault

THÈSE DE DOCTORAT

de l'Université de recherche Paris Sciences et Lettres
PSL Research University

Préparée à MINES ParisTech

Experimental and numerical investigation of incipient plasticity in FCC polycrystals by X-ray synchrotron topotomography and CPFEM

Étude expérimentale et numérique des premiers stades de la plasticité dans un polycrystal CFC par topotomographie aux rayons X et CPFEM

École doctorale n°521

SCIENCES ET MÉTIERS DE L'INGÉNIEUR

Spécialité MÉCANIQUE

Soutenue par **Nicolas Guéninchault**
le 24 Mars 2017

Dirigée par:
Henry Proudhon,
Wolfgang Ludwig,
Samuel Forest.

COMPOSITION DU JURY :

Pr. Henning Friis POULSEN
Danmarks Tekniske Universitet ,Rapporteur

Pr. Andreas BORBELY
Mines St Étienne, Rapporteur

Dr Andrew KING
Synchrotron Soleil, Examinateur

Pr. Stéphane BERBENNI
Université de Lorraine, Président

Pr. Samuel FOREST
Mines Paristech, Examinateur

Pr. Wolfgang LUDWIG
INSA Lyon, Examinateur

Dr. Henry PROUDHON
Mines Paristech, Examinateur

A Elley, Léo, Noah, Baptiste,
Clément, Charlie, Stephen et Lisa,
avec tout mon amour.

Remerciements

Je tiens à remercier en premier lieu mes encadrants, Henry Proudhon, Samuel Forest et Wolfgang Ludwig. Vous avez su me supporter au fil des années, et avez toujours été présents lorsque j'en avais besoin, ce qui est assez difficile pour être souligné quand on connait vos agendas. Merci à Wolfgang pour m'avoir formé aux techniques expérimentales sur grands instruments, et à toute la famille Ludwig pour les moments passes à la montagne. Je regrette vraiment de n'avoir pas pu être plus souvent sur ID11. Merci à Samuel, pour sa passion et pour avoir passé un nombre plus que conséquent d'heures avec moi dans le "money time". Cela a vraiment été une chance de travailler avec quelqu'un d'aussi brillant, et nos innombrables discussions m'ont énormément enrichi tant sur le plan scientifique que sur le plan personnel. Enfin, merci à Henry. Merci pour m'avoir pris sous ton aile lorsque je n'étais qu'un "jeune" apprenti ingénieur, et d'avoir vu en moi un potentiel « padawan ». Merci d'avoir eu à cœur de me former jour après jour et d'avoir initié mon projet de thèse. La liste des mercis pourrait être très longue, alors simplement merci pour tout. Je me sens vraiment chanceux d'avoir été aux cotés de trois brillants scientifiques, mais aussi de formidables personnes, comme vous.

Merci à Luc Chevalier, pour m'avoir enseigné les bases de la mécanique, mais aussi et surtout pour avoir su m'orienter quand j'en avais besoin. Certaines personnes changent le cours de votre vie, et vous êtes certainement de ceux-là.

Merci à l'école des mines de Paris, MinesParistech, pour le financement de mes travaux, C'est une réelle chance d'avoir eu une liberté totale lors de mes recherches.

Je remercie mon jury, Henning Poulsen et Andras Borbely pour les rapporteur, Andrew King et Stéphane Berbenni pour les examinateurs. Cela à été un réel honneur d'avoir été adoubé par de telles références dans le domaine de la science des matériaux.

Je remercie aussi mille fois tout le personnel du centre des matériaux avec qui j'ai eu l'occasion de travailler. Une mention spéciale pour René pour s'être rendu disponible et pour sa gentillesse, et à Sylvain et Abdenour pour leur expertise technique, qu'ils ont essayé de me transmettre. Merci aussi à Odile, pour son

aide plus que précieuse lors de mes recherches bibliographiques.

Un grand merci aux thésards du centre avec qui converser et passer du temps a été un plaisir. Et plus particulièrement Quentin, Juan, François, Thibault, Nathan, Clément, Guillaume, Hayat, David, Pierre-Alexis pour les fous rires, les discussions plus ou moins sérieuses et les soirées. Merci aussi à mes compagnons du bureau, Sicong, Arina, Erembert et Jia pour l'aide que vous m'avez apporté.

Je tiens à remercier Erik Lauridsen pour m'avoir fait rejoindre Xnovo Technology, ainsi qu'à toute l'équipe pour l'accueil que vous m'avez réservé. Vous avez su me pousser dans la dernière ligne droite.

Je remercie aussi mes amis de Copenhague, et tout particulièrement Anh, Neil, Mat, Alex, Robin, Carl, Kenth et Anders. Vous m'avez donné de la chaleur et de la force pour terminer la rédaction pendant le terrible hiver danois !

Une grosse dédicace à Xlaw, mes dingos. Merci pour tout, les fous rires, les voyages, les soirées. Merci de m'avoir accueilli au sein de votre famille !

A mes amis les plus "fit", Valérie, Sébastien, Zouzou, Stéphanie, Caroline, Lloyd, Virginie, Yann, Mélanie, Thibault, Florent, Laura, merci pour tout, les rires, les repas, les voyages, tout !

Un grand merci à mes amis de longue date qui ont contribué de près ou de loin à faire de moi ce que je suis aujourd'hui. Teddy, Steward, Émilie, Lionel, Kelly, Damien, les honneurs sont aussi pour vous.

Comment est-il possible de remercier en quelques lignes Auriane et Jackson, qui ont toujours été à mes cotes et ont su trouver les mots lorsque j'en avais besoin ? Merci tout simplement pour votre amour. Vous faites de mois une personne meilleure jour après jour, et je ne serai probablement pas en train d'écrire ces lignes à cette heure-ci sans vous.

Enfin, merci à ma famille. Je pense particulièrement à mon grand-père et Andrée, pour leur soutien, et sans qui je n'aurais pas pu arriver jusque-là. Je ne pourrais jamais vous remercier assez. Et surtout, à ma mère, pour son amour et soutien inconditionnel. Tu es la meilleure, merci infiniment !

Summary

Abstract

Understanding the intimate details of plastic deformation in polycrystalline materials is an important issue to improve material design and ultimately produce safer structural parts with less impact on the environment. This understanding is presently limited by our ability to observe both the microstructure of the material and the deformation processes in three dimensions (3D) at small length scales and inform mechanical simulations with physical deformation mechanisms of the crystal lattice. Considerable progress has been made in the last decade with surface observation (eg EBSD coupled to digital image correlation) which led to numerous studies combining experimental observations and simulations from the surface microstructure. However, an accurate comparison without knowing the underlying microstructure remain challenging. In this work, we propose a new methodology which allows a quantitative comparison between the observation of deformation mechanisms, the evolution of the grain lattice curvature and the simulated mechanical fields.

For that purpose, a mechanical stress rig dedicated for synchrotron 4D diffraction imaging experiments has been designed, and used to deform an Aluminium-Lithium specimen under tension. The 3D grain map has been obtained by diffraction contrast tomography analysis, and a cluster of three grains within the bulk has been selected to be the region of interest of the 4D observation by X-ray topotomography. The appearance and evolution of 3D crystalline defects as a function of the applied load has been observed to be located along well defined crystallographic planes. All three grains showed plastic activity on along two different set of planes, which is not always coherent with a macroscopic Schmid Factor analysis. The change of the amplitude and the orientation of the average grain curvature has been measured with an unprecedented level of detail by means of 3D rocking curve analysis.

In parallel, crystal plasticity finite element (CPFE) simulations have been carried using the 3D grain map measured experimentally. Tension loading was applied to reproduce the experiment numerically and compare the plastic activity on a grain by grain basis. The slip system activity predicted by the model matches in most cases the observed two slip system scenario. A mathematical framework

to predict the local Bragg angle based on the stretch and rotation of the crystal lattice by the elastic strain tensor was derived. Post-processing the intragranular strains fields from the CPFE results allowed to simulate 3D rocking curves, showing excellent agreement with the experimental measurements. This result confirms that in situ X-ray topotomography is a promising tool to study the early stage of polycrystal plasticity within the bulk of millimetric material specimens.

Résumé

La compréhension des mécanismes de déformation dans les matériaux polycristallins est un problème important, qui conditionne notre capacité à concevoir et à produire des pièces de structure plus sures et avec un impact environnemental moindre. Cette compréhension est aujourd'hui limitée par notre capacité à observer à la fois la microstructure du matériau et ses mécanismes de déformation en trois dimensions (3D) aux petites échelles, et à informer les simulations mécaniques à partir des mécanismes physique de déformations du réseau cristallin. Des progrès considérables ont été faits dans les dernières décennies avec les observations de surfaces (i.e. technique EBSD associée a de la corrélation d'image) qui a permis de nombreuses études combinant des observations expérimentales à des simulations, à partir de la surface de la microstructure. Cependant, une comparaison précise sans connaitre la microstructure sous-jacente reste un défi. Dans ce travail, nous proposons une nouvelle méthodologie basée d'une part sur des mesures couplant la tomographie et la diffraction des rayons X, et d'autre part sur des simulations mécaniques de platicité cristalline. Cette approche permet une comparaison quantitative en volume entre les mécanismes de déformation, l'évolution de la courbure du réseau cristallin et les champs mécaniques simulés.

Pour ce faire, une machine de traction dédiée aux expériences 4D d'imagerie par diffraction sur grands instruments a été conçue, et utilisée pour déformer en tension un échantillon d'Aluminium Lithium. La cartographie 3D de la microstructure a été obtenue par tomographie par contraste de diffraction, et un agrégat de trois grains dans le volume de l'échantillon a été choisi comme région d'intérêt pour des observation 4D par topotomographie. L'apparition des premières bandes de glissement en volume et leur évolution au cours du chargement ont été observées le long de plans cristallographiques bien définis. Les trois grains ont montré une activité plastique le long de deux familles de plans différents, pas toujours en accord avec une analyse macroscopique du facteur de Schmid, ce qui est attribué à l'influence du voisinage sur l'activation des systèmes de glissement. Les changements d'amplitude et d'orientation de la courbure moyenne des grains ont été mesures avec un niveau de détail sans précédent, par une analyse tridimensionnelle des courbes de reflexions.

En parallèle, des simulations de la plasticité cristalline par éléments finis (CPFE) ont été menées utilisant la cartographie tridimensionnelle de la microstructure mesurée expérimentalement. Un chargement uniaxial de traction a été applique pour reproduire numériquement l'expérience, et comparer grain par grain l'activité plastique. L'activité des systèmes de glissement prédite par le modèle est conforme aux observations expérimentales d'une activité plastique le long de deux plans. Un cadre mathématique pour prédire l'angle de Bragg local en fonction des déformations et des rotations du réseau cristallin a été formulé. Un post-traitement des champs intragranulaires de déformation à partir des résultats des simulations CPFE a montré une excellente concordance avec les résultats expérimentaux. Ce résultat confirme que la topotomographie in-situ aux rayons X est un outil prometteur pour l'étude des premiers stades de la plasticité cristalline en volume.

Introduction

Les matériaux polycristallins composent une grande partie des pièces de structure des moyens de transport modernes ou de production d'énergie. Il est dont important de disposer des connaissances nécessaires a la conception de ces dernières. L'arrangement spatial, la forme, l'orientation des différents cristaux (grains) qui le compose le polycristal influe grandement sur les propriétés mécaniques du matériau. Les mécanismes de plasticité dans ces matériaux sont spécifiques, et la déformation plastique se produit par le mouvement des dislocations. Souvent, ces défauts s'organisent en structures, comme des bandes de glissement.

Les récents progrès des techniques expérimentales on permettent aujourd'hui d'observer les défauts individuellement ou les structures de dislocations, en 2D, 3D, ou 4D. Ces observations peuvent être utilisées comme données d'entrée pour des simulations du comportement mécanique du matériau, et des modèles prenant en compte les mécanismes particuliers de la déformation plastiques dans les cristaux permettent de prédire les champs locaux de contrainte et de déformation, ainsi que l'orientation locale du cristal ainsi que les paramètres de mailles. Comparer ces études 4D et les simulations reste un défi, mais apparait comme une voie prometteuse pour améliorer notre compréhension des mécanismes de déformations et nos modèles.

Le premier chapitre de ce travail s'attache a faire une revue des différentes techniques d'analyses de la microstructure des matériaux actuelles. Le second chapitre expose les caractéristiques du matériau utilise dans le cadre de cette étude, ainsi que les techniques expérimentales utilisées. Le troisième chapitre détaille une expérience originale menée a l'ESRF, qui a permis d'observer en trois dimension l'apparition et l'évolution de défauts cristallins dans trois différents grains. Enfin, une simulation numérique du comportement mécanique de l'échantillon étudié expérimentalement est menée. à la fois expérimentalement ou numériquement.

As early as prehistoric times, human being have shaped stones to make weapons, and be able to hunt. Now, we are capable to confine a 5 million degrees plasma in the *Tokamak* toroidal chamber. We constantly use materials with shapes and applications more and more complex. Materials have evolved with mankind through history, when they were not the factor that took a civilization to the next one, as shown by ages of civilization named after materials.

Among these materials, metals had a special place in History and they were the vector of modernity for several civilizations. The development of metallurgy and the industry of bronze $\sim$ 8000 years b.c. has been the starting point of deep upheaval of the socio-economic world. In the XIX^{e} century, the industrial revolution has been permitted by the new capabilities in terms of production and machining of steel. Since then, metals have been the most widely used components in structures for the modern ways of of transportation, energy production and construction. Precious metals, integrated in the most recent micro-electronic systems, were part of the transformation of our world into a society of information. By their inner structure, metallic materials are very specific. The atomic arrangement is both long range and short range ordered, which gives them very interesting physical (mechanical, electrical, etc.) properties. The use of this class of interestingly materials are dictated by the defect structures. Particular applications require a high crystal purity, like Nickel based superalloys monocrystalline turbine blades used in modern jet turbines, decreasing the amount of creep in high temperature applications. Others use defects to produce specific effects, like Ni-Ti shape memory alloys (SMAs) using the reversible movement of twins, allowing to produce self-expanding stents. Understanding how these defects are generated, move, and interact is essential to better predict the life cycle of structural part (improving safety and reducing the ecological impact) or to optimize the performance linked to a specific use. Therefore, it is important to be able to understand and model the behavior of crystalline materials based on the physical mechanisms of deformation.

In polycrystalline materials, the microstructure composed by the grain shapes, orientations, sizes and spatial arrangement, controls the macroscopic properties such as the yield stress. The plastic deformation by dislocation motion is the principal deformation mechanism and lead to the formation of defects in the crystal structure. Crystal slip is often observed to be localized in slip bands which organize in complex 3D patterns. This has been observed at the surface of metallic specimens for a long time but until now, direct observations of plasticity in the bulk of a three-dimensional polycrystalline microstructure relied on transmission electron microscopy, limited to thin foils and destructive.

Recent experimental progress have allowed to measure the 3D grain maps, giving for each grain its shape, position and orientation. This 3D characterization of the inner structure of these materials can be achieved either destructively

using serial sectioning techniques in combination with surface imaging (electron or light microscopy) or non-destructively by the use of X-rays or neutron beams. The most advanced techniques are now capable to measure in 3D the local orientation field, the full strain tensor and the full dislocation density tensor, giving a more accurate picture of the microstructure. The non destructive nature of X-ray characterization and the high brilliance of third generation synchrotron sources allow for low acquisition times, and therefore time-resolved (4D) studies. It is then possible not only to take a snapshot of the microstructure and its defects, but to monitor its evolution.

The obtained 3D grain maps can be used as input for mechanical simulations, and allow to understand the local deformation mechanisms like deformation incompatibilities between two neighboring grains. Using crystal plasticity finite element modeling (CPFEM), the local strain and stress fields in the polycrystal can be extracted, as well as the evolution of the local crystal orientation and its lattice parameters. Bringing together 4D studies and simulations remains a challenge, but is a promising route to better understand the deformation mechanisms in a polycrystal and improve our constitutive material models.

First, a bibliographical chapter will focus on the current capabilities in terms of imaging for material analysis. It deals from basic microstructural imaging features to the most modern techniques, with an emphasis to the analysis of both the grain structures and intragranular defects analysis.

The second chapter focuses on the material and methods specifically used in this study. A first section introduce the Aluminum Lithium alloys, their mechanical behavior and the microstructural features that developed in the case of monotonic applied stress. A second section expose on two of three dimensional X-ray diffraction techniques that will be used in the next chapter, namely diffraction contrast tomography and topotomography, examples of applications and their limits. Finally, a published paper of a miniature tensile rig named Nanox specifically designed for 3D diffraction studies and used in the experiment mentioned further is included.

The third chapter details an original in-situ 3D diffraction experiment conducted at the ESRF. It shows how by the combined use of the stress rig and the two experimental techniques described before, it is possible to reconstruct in 3D the evolution and the localization of crystal defects within the bulk of a AlLi sample for a three grain cluster. An analysis in terms of 3D rocking curves which is a measure of the intragranular orientation spread, is carried out, to be compared with the results of the numerical simulation performed in the next chapter.

The last chapter of this study shows crystal plasticity finite element simulations performed on a realistic microstructure, extracted from the results of the experiment of the previous chapter. Individual slip system activities in the grains of interest are directly compared to the experimental observations. A theoretical

framework is developed to process the simulated data and extract corresponding rocking curves. This synthetic is thereafter compared to the experimental data and shows excellent agreement.

Conclusions about the present work, and outlook are given in a final part.

Chapter 1

State of the art: From standard characterization techniques to 4D microstructural studies

Une revue des différentes techniques permettant d'observer la structure internes des matériaux est effectuée. L'accent est mis sur les possibilités de détecter l'apparition et d'observer l'évolution des défauts cristallins (imagerie tridimensionnelle résolue en temps).
Tout d'abord, les différentes possibilités de révéler la microstructure polycristalline grâce à la microscopie optique sont étudiées. Ensuite, l'accent est mis sur les deux techniques de microscopie électronique (microscopie électronique en transmission et détection des électrons rétrodiffusés) largement répandues dans les laboratoires de recherche permettant de mesurer les caractéristiques locales du réseau cristallin. Enfin, Les techniques basées sur l'interaction rayons X-matière et permettant de reconstruire en trois dimensions la microstructure des polycristaux sont passées en revue.

From light microscopy, the most widely used and available technique to observe the microstructure of materials, to XFELs one of today most advanced instruments for material characterization, scientists have extensively used different characterization techniques to observe and quantify the structure of materials. In this review, we focus on the standard characterization techniques available at most of the material science laboratories (i.e. electron microscopy), and on microstructure characterization techniques available at synchrotron facilities. Each time, we will provide the basics of the techniques, and then focus on studies from 2D to 4D, when possible.

1.1 Optical microscopy

Metallography is the simplest, the oldest and the easiest solution to observe the microstructure of materials. In this section, we limit the study to light microscopy, because quite often, this is the first observation made. An overview of electron microscopy techniques can be found further in this chapter. In his pioneering work of [Sorby, 1863], taught himself how to prepare specimens and vary illumination mode [Vander Voort, 1993]. Indeed, the quality of visible light metallography is strongly dependent on how well the surface specimen has been prepared. The illumination mode must be chosen carefully, and depends on what is the nature of the feature to be observed.

Surface preparation involves grinding, polishing, and chemical etching. Mechanical preparation is the most widely used technique. Abrasive surfaces with hard particles are used, to remove a moderate volume of the sample surface. Particles employed are iteratively finer and finer, until the surface requirements are achieved. Etching is the process to reveal features that cannot be observed by simply polishing the specimen surface. Both chemical etching and electroetching are used in metallography. In chemical etching, the etchant selectively corrodes microstructural features. In electrolytic etching, the specimen is immersed in an electrolyte and used as the anode, the cathode being a highly insoluble, but conductive material. The reduction reaction will produce contrasts at the surface. The nature of the etchant and the time of immersion depends on the materials to be imaged. For example, for Aluminum alloys, the common procedure is to use Keller agent during 10 to 20 seconds. To achieve high quality images, the surface must be as flat as possible since the depth of the field is very limited. Confocal microscopy is an extension of the technique which can be used to image non-flat areas[Hovis and Heuer, 2010].

In optical microscopy, the observation involves visible light, and the image can be directly seen by the human eye. The surface image is magnified by using at least one lens, and optical microscopes use a CCD camera to record images. The

ultimate achievable spatial resolution is limited by the diffraction of the light and is $0.3\,\mu m$ as stated by [Abbe, 1873][1]. In a light microscope, the user can switch between different modes, increasing the contrast on the structure of interest. A full review of the different modes will not be provided here, but examples of polycrystalline materials imaging will be discussed in the next paragraphs. A review of the important achievements is available in [Evanko et al., 2011] and [Murphy, 2002] provide a full review of the different modes.

The use of polarized light can reveal the polycrystalline nature of the specimen as well. Here a polarizer is positioned in the light path, and because of the interaction between this polarized light and a birefringent material, grains can (mostly) be uniquely identified as shown in Fig. 1.1 (left). Using etching techniques,grain boundaries can be specifically visualized through optical microscopy. They are more severely attacked by the etchant. This results in image contrasts because of the topographic differences, which will reflect the light differently. [Couling and Pearsall, 1957, Larson and Picklesimer, 1966] have demonstrated the possibility to determine the orientation of the c-axis in hexagonal crystal structures.

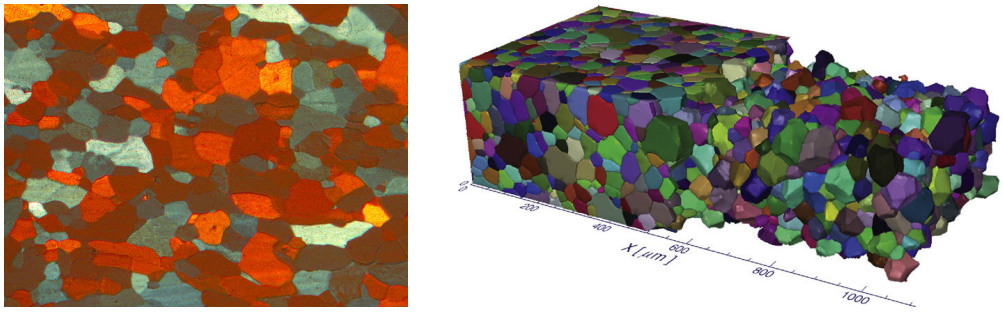

Figure 1.1 – Grain microstructure of a AlLi 2.5wt recrystallized alloy revealed by polarized light microscopy (left) and reconstruction of 4380 grains in a $1115 \times 516 \times 300\,\mu m^3$ big volume of β-Ti alloy built from a stack of 200 serial sections ($1.5\,\mu m$ spacing) by [Rowenhorst et al., 2010] (right).

A three-dimensional (3D) extension of the surface characterization is available through serial sectioning. By repeating observation and the surface preparation procedure, it is possible to reconstruct a 3D map of the microstructure. In a study by [Rowenhorst et al., 2010], 201 raw images were taken in a four weeks time frame. The final reconstruction of the volume, shown in Fig. 1.1 (right), grains have been segmented using dedicated image analysis routines exploiting the etching contrast at the grain boundaries. This is obviously a time-

[1] Super resolution microscopy techniques are now available. A review of these techniques can be found in [Neice, 2010]

consuming method, and cannot be extensively used in the present from, but efforts have been made to completely automate the serial sectioning process. In [Spowart et al., 2003, Spowart and Mullens, 2008], the team at the USAF laboratory demonstrates how with a specifically designed robot, it is possible to significantly increase the slice rate, up to 20 slices per hour. This automated process reduce significantly the difficulty of the image registration using a LVDT [Alkemper and Voorhees, 2001].

Optical microscopy, as well as other surface characterization techniques do not allow for time resolved 3D studies (4D studies), because of the destructive nature of the serial sectioning process.

1.2 Electron microscopy

Electron microscopes use a beam of electrons to illuminate the sample and a detector to measure the quantity of re-emitted electrons from this point. The first electron microscope was built in 1932 by [Knoll and Ruska, 1932] achieving a $\times$ 400 magnification, soon followed by the first supermicroscope (overcoming the resolution limit of the visible light) in [Ruska, 1934] with a $\times$ 12000 magnification (see Fig. 1.2 (left)).

Nowadays, electron microscopes have become a basic and widely used tool in most research laboratories for material characterization, and can mainly be categorized in two categories: Scanning Electron Microscopes (SEM) and Transmission electron microscopes. In TEMs, an electron beam that went through the sample is magnified, to get a picture of the structure in the sample. In SEMs, electrons reflected from the surface by a focused beam are detected, while a rectangular grid of the sample is scanned[2]. Users can switch between different modes, that depend on what type of electrons (Auger, secondary, backscattered, etc.) are used to generate the image (see Fig. 1.2 (right)). 10 times more SEMs are available compared to TEMs..

The next two sections will deal with *Transmission Electron Microscopy* (TEM) and with *Electron BackScatter Diffraction* (EBSD), two techniques capable of revealing the crystalline structure of the materials and its defects. *Secondary Electrons* (SE) and *BackScattered Electrons* (BSE) modes are capable to reveal most of the grain boundaries, with a sample properly prepared[3], but cannot give quantitative essential information about the crystal such as its orientation, and will not be discussed here.

[2] A comparable mode exists for TEM, where the transmitted electron from a focused beam are detected, called Scanning Transmission Electron Microscope (STEM).

[3] A sample prepared by chemical or electro chemical etching will exhibit facets. As the etching is sensitive to the orientation of the crystal.

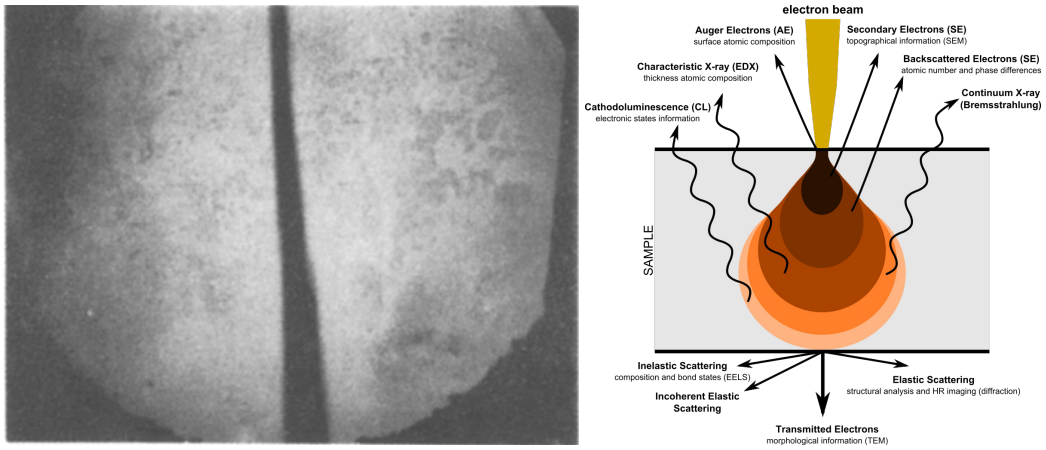

Figure 1.2 – One of the first image by an electron supermicroscope, a cotton thread magnified approximately $800\times$ from [Ruska, 1934] (left), and the diagram of the interaction between electrons and matter (courtesy of Claudionico, commons wiki).

1.2.1 Transmission electron microscopy

TEM, for *Transmission Electron Microscopy*, uses a transmitted beam of electrons through a very thin (typically $\simeq 100\,\mathrm{nm}$) specimen, to generate an image. The electrons emitted by an emission gun interact strongly with the matter, and the analysis of the images thus requires an appropriate theoretical background to be properly analyzed. Since the forward-thinking speech of R. Feynman in 1959 *There is Plenty of Room at the Bottom*, where he stated *The electron microscope is not quite good enough, with the greatest care and effort, it can only resolve about 10 angstroms ... Is there no way to make the electron microscope more powerful?*, progress in the optics have permitted to reach resolutions up to $50\,\mathrm{pm}$ have been reached [Erni et al., 2009, Kabius et al., 2009, Miao et al., 2016]. Thanks to TEM and its variants (in particular the high-resolution transmission electron microscopy (HREM) and the scanning electron transmission microscopy (STEM), huge advances have been made to the understanding of the behavior of materials at the nanoscale. The first ever direct image of a dislocation has been published by [Hirsch et al., 1956], and a remarkable review of the historical background leading to these breakthrough is available in [Hirsch, 1986].

Time resolve studies have been made with TEM, since the beginning of the development of the technique. Specifically designed stages, discussed in [Butler, 1979], capable of straining, heating, and cooling the observed samples have been designed. It allowed scientists to develop *in-situ* experiments, and observe the formation [Thomas and Whelan, 1961] and the dilution [Laird and Aaronson, 1966] of precipitates in an AlCu alloy, phase transforma-

tions in [Hull, 1962], radiation damage in [Eyre, 1962], or recrystallization in [Roberts and Lehtinen, 1972]. Essential observations for the understanding of the plastic deformation process have been allowed by the development of mechanical in-situ testing in TEM. The first movement of dislocations have been observed in [Hirsch et al., 1956] due to the beam heating of the sample. Early stages of plasticity have been studies by [Fujita, 1969] as well as fatigue in [Suga and Imura, 1976]. In-situ testing while taking images at a micrometer or nanometer scale is a difficult process. For TEM, [Martin and Kubin, 1978] discuss about the optimal setup for in-situ experiments.

With the availability of high voltage sources, the work of [Fujita, 1967] and colleagues have shown that the thickness of the sample is an important factor in the deformation behavior of the sample. Indeed, the main drawback of electron microscopes is to only allow observations in a very limited volume. Using substantial volumes, representative of the overall behavior at the scale of interest is of prime importance to get a representative picture.

Three-dimensional extensions of TEM (3D-TEM) have been first available for biological samples in the late 90ś, and rely on the same principles as those used in X-ray tomography. 2D projections are recorded with small increments of the angular position, over a wide angular range. If a specific diffraction condition is maintained, and with the adequate reconstruction procedure (realignment, etc. [Frank et al., 1996]), [Barnard et al., 2006] have demonstrated that one can produce a 3D map of crystal defects, like dislocations. Classic tomography reconstructions are also available from projections in imaging modes. Reconstructions of small objects such as nanometric Pd particles or a Silica bead topped with a nickel nanocrystal are shown in [Ersen et al., 2007].

Orientation imaging is also available in TEMs. In diffraction mode, it is possible to record diffraction patterns, from different tilts of the sample, and to index the Laue patterns to reconstruct the local crystallographic orientation. An EBSD like approach, called Automated Crystal Orientation and phase mapping in TEM (ACOM-TEM), can be adopted, where a nanofocused beam scans the sample and diffraction patterns are acquired rather than Kikuchi lines [Rauch and Véron, 2014]. Phase mapping is possible as well, and spatial resolutions down to $\sim 1\,\mathrm{nm}$ can be reached. The angular resolution is around 1° limited by the angular step size used to cover the orientation space, and ACOM-TEM is only relevant if the grain size is bigger than the thickness of the foil. The 3D extension of ACOM-TEM is presented in [Eggeman et al., 2015], where patterns are recorded pixel-by-pixel and tilt-by-tilt. The possibility to generate 3D orientation maps from TEM (without scanning the sample) in diffraction mode has been demonstrated in [Liu et al., 2011]. The authors have used simulated data and algorithms inherited from 3D X-ray diffraction (detailled further in this section) to prove that TEM diffraction patterns are relevant for 3D orientation

mapping without using a focused beam.

Finally, with the possibility to generate ultra short pulses of electrons, 4D studies have been released for electron microscopy. A 4D movie of the motion of a complex Carbone nanotube has been published in [Kwon and Zewail, 2010]. Here, the time scale (the pico second) used, is totally appropriate to observe the deformation behavior of materials and individual dislocation moving through the crystal lattice, and there is no doubt that in the near future formation of dislocations structure will be observed at the atomic scale in 3D.

1.2.2 Electron backscattered diffraction

The first EBSD patterns have been analyzed by [Coates, 1967], and the technique is now routinely used in materials science facilities. It provides fully automated [Wright and Adams, 1992, Kunze et al., 1993]. The technique is (typically) implemented in a conventionnal SEM, where diffraction patterns (Kikuchi patterns [Nishikawa and Kikuchi, 1928, Kikuchi, 1928]) originating from backscattered electrons, are collected on a dedicated high speed detector system consisting in a phosphor screen and a CCD camera. To maximize the back-scattered electrons signal, the sample is usually tilted at 70°. From the knowledge of the geometry and the crystalline phases existing in the sample, it is possible to generate a precise map of local crystallographic orientation and phase. EBSD is intrinsically a surface scanning technique, and the depth of the measurement, even though depending on the acceleration voltage and the atomic number of the material, is approximately $100\,\mathrm{nm}$ (but there is no general consensus and research is still conducted in this field [Wisniewski and Rüssel, 2015]).

The ultimate achievable spatial resolution of EBSD is $20\,\mathrm{nm}$, and its angular resolution approximately 0.5°. High resolution modes have been developed [Wilkinson et al., 2006], and angular resolutions down to 0.004° have been reported, allowing the calculation of the GNDs density tensor in [Maurice and Fortunier, 2008, Ruggles and Fullwood, 2013] and elastic strains down a precision of 10^{-4} in [Wilkinson et al., 2006].

In-situ experiments for EBSD have been developed, to provide 2D-time resolved studies. Specific tension rigs has been developed to fit EBSD requirements (and more generally electron microscopy requirements like vacuum and space constraints) like in [Chiron et al., 1997]. In [Bao et al., 2010], the authors present a study of the lattice rotation and the twinning of a Ti alloy, through several interrupted in-situ EBSD scans. In [Wright et al., 2016], the evolution of intragranular and overall lattice rotation is presented, as well as the variation of the local misorientation at grain boundaries due neighboring grains. As grains can be individually identified by EBSD, the recrystallization process can be monitored, like in [Zhu et al., 2005]. EBSD scans can be coupled to other techniques

to provide multi-channel data sets ("correlative microscopy"). As an example, EBSD coupled with digital image correlation of BSE images provides microextensometry [Doumalin and Bornert, 2000].

In [Lewis et al., 2006], the authors present a 3D reconstruction of an austenitic stainless steel. EBSD maps were taken every $33\,\mu m$ and the reconstructed volume was $250\,\mu m \times 250\,\mu m \times 160\,\mu m$, comprising 138 layers and served as an input for an image-based finite element model to simulate the mesoscale mechanical response of the real microstructure [Lewis and Geltmacher, 2006]. The alignment of the layers was made using Vickers indent marks. This process can now be automated, using robots, as mentioned earlier. The more recent development of dual beams instruments

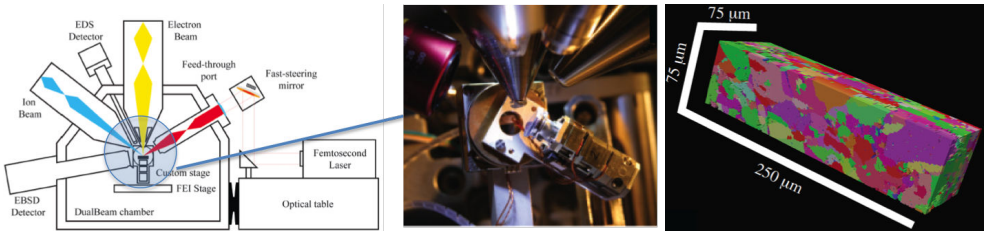

Figure 1.3 – Schematic of the principle of the tri-beam (left), and picture of the chamber of the microscope (middle). Reconstruction of a polycrystalline Nickel sample. From [Echlin et al., 2012].

(FIB[4]/SEM) extend the capability of a classical SEM instrument from 2D to 3D analysis. Thin layers (down to $50\,nm$) of the sample can be removed by the action of the FIB on the sample surface, and at each step, a comprehensive analysis taking advantage of the multimodal capabilities of the SEM (SE and BSE imaging, phase, orientation and composition analysis). The typical material removal rate by Ga ions drastically limits the volume of material which can be observed ($100\,\mu m \times 100\,\mu m \times 20\,\mu m$). Plasma-FIB may be a way forward soon [Burnett et al., 2016], enabling the imaging of larger volumes. More recently, the team of Pr. Tresa Pollock at UCSB has developed a tri-beam microscope, adding a pulsed femto second laser to the previously presented system (Fig. 1.3) [Echlin et al., 2011, Echlin et al., 2012]. This femtolaser focused into a $1\,\mu m$ spot provide micromachining capabilities by sequentially ablating the surface (compared to FIB micromachining, the material removal rate is several orders of magnitude higher, which allow to image a much larger volume of material).

[4]Focused Ion Beam

1.3 3D X-ray microstructure characterization techniques

While the serial sectioning techniques rely on sequentially removing thin layers of the samples to provide 3D data, the techniques presented in this section make use of the penetration power of X-rays through matter to provide non-destructive orientation or defect maps.

1.3.1 Laue micro diffraction

Laue diffraction is the oldest X-ray analysis technique. A polychromatic beam illuminates a crystalline sample giving rise to a diffraction pattern onto a detector (an X-ray sensitive photographic plates in the old times), see Fig. 1.4. Here the spatial resolution is linked to the focalization of the X-ray beam. Nowadays, with the great improvement of X-ray optics, polychromatic beams (typically within the range of 5 and $35\,\mathrm{keV}$[5]), beams can be focused down to about a $7\,\mathrm{nm}$ spot size [Mimura et al., 2010], although in DXWM $100\,\mathrm{nm}$ are rather used. With the acquisition of several Laue patterns, through an indexing and position refinement procedure, it is possible to retrieve not only crystal orientation, but the deviatoric elastic strain tensor. The accuracy of these analysis is respectively 0.1° and 10^{-4}. For the hydrostatic component of the elastic tensor, the energy of at least one reflection must be done, in addition to the white beam data [Robach et al., 2011]. For that purpose, the microlaue diffraction beamlines are equipped with specific optics which allow to switch between polychromatic and monochromatic modes. A direct application of the technique was the high-resolution grain mapping shown in [Tamura et al., 2002]. In situ testing of FIB milled single crystal micro pillars has been made in [Maaß et al., 2007]. Which confirmed the importance of preexisting strain gradients in the slip system activation.

A depth resolved variant of the technique allowing the analysis of bulk samples has been developed in [Larson et al., 2002, Robach et al., 2014], called *Differential aperture X-ray microscopy* (DAXM). It consists of the acquisition of diffraction patterns while an absorbing thin wire (typically made of tungsten) moves close to the sample surface. By analyzing the different images at each position of the beam, it is possible to perform a triangulation and therefore to know the origin of each diffraction spot. For optimal spatial and temporal resolutions, the wire should be placed close to the surface of the sample. This in turn complicates the extension to 4D studies, due to severe space constraints limiting the possibility to include a mechanical test rig into the setup. A reconstructed grain map

[5] High energy Laue microdiffraction has been reported in [Hofmann et al., 2010].

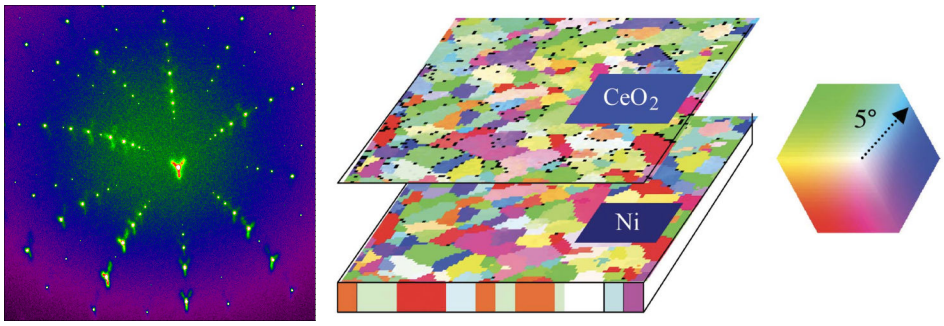

Figure 1.4 – A Laue diffraction pattern (left, courtesy of the ESRF), and a reconstructed microstructure of a CeO_2 film on a Ni substrate from [Ice et al., 2005].

is shown in Fig. 1.4 (right).

1.3.2 X-ray microtomography

From the pioneering work of [Cormack and Koehler, 1976, Hounsfield, 1980] and the first invention of a computed tomography (CT) scan, first applied to medical diagnosis, computed tomography has quickly grown up, thanks to the improvement of both sources and detectors, it is nowadays a widely used tool for materials science, enabling non-destructive, three-dimensional analysis of bulk samples. from the nanometer[6] to the millimeter range. Every synchrotron radiation facility now accept CT experiments, and plenty of manufacturers provide CT lab solutions, overcoming the intrinsically limited access to synchrotron beamlines. Here, we will focus on applications of synchrotron radiation CT.

Computed tomography, or more commonly named X-ray computed microtomography in the field of material science, is based on the acquisition of a set of 2D projections on a high resolution detector. The sample is fixed on a turntable and several images are taken for different angular positions. Although many different variants of reconstruction algorithms exist, 3D reconstructions are typically obtained via filtered back projection developed originally by [Feldkamp et al., 1984]. Synchrotron X-ray beams are partially coherent, which makes the detector image a combination of absorption and phase contrast, the later being dependent on the sample detector distance. Due to this, there are mainly three different acquisition modes available for material characterization [Salvo et al., 2003]. In the absorption mode, contrasts arise from the differences of density and atomic number of the material. In this case the detector is placed close to the sample (hence no phase contrast), this mode is not suitable if the

[6] $\sim 15\,\mathrm{nm}$ at best for soft X-rays, and $\sim 50\,\mathrm{nm}$ for hard X-rays.

difference of density between the components is too small. When the detector is placed further away (in the edge detection regime), contrasts in the projections as well as in the reconstructed volumes arise from the interferences, revealed by the refraction of the electromagnetic wave in the material. A phase retrieval algorithm for the reconstruction in the edge detection regime is described in [Paganin et al., 2002], but degrades the spatial resolution. In the later, the real part δ of the refractive index is reconstructed[7]. This technique is called Phase Contrast Tomography (PCT). By taking images at several propagation distances, and applying a special phase retrieval algorithm (inspired by the high-resolution electron microscopy) presented in [Cloetens et al., 1999] called holotomography, a quantitative analysis of the material density is possible. This latter mode is especially suited when previous modes fail to provide contrast. The difference between the different modes is shown in Fig. 1.5.

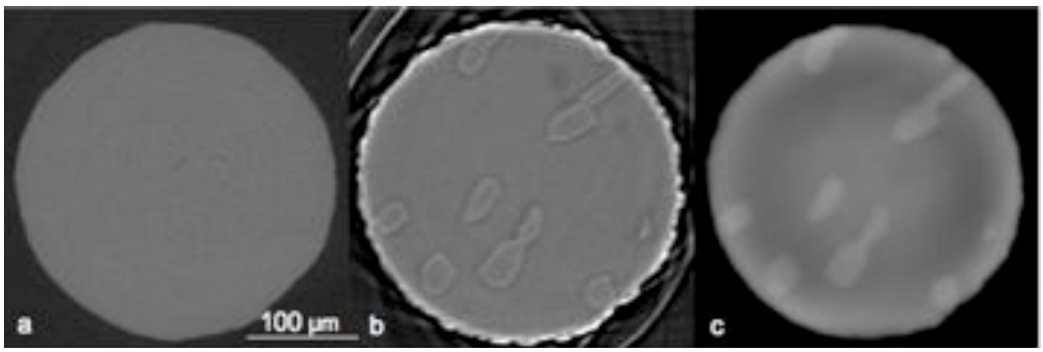

Figure 1.5 – Comparison of slices reconstructed by (a) absorption tomography, (b) phase contrast tomography, (c) holotomography. The sample was an austenitic/ferritic steel, from [Ludwig, 2010]

As monophasic polycrystalline materials do not exhibit contrasts between grains in term of electronic densities, the previous techniques are not suitable to provide insight into the grain structure. To reveal the grain boundaries, it is possible to decorate the grain boundaries with a liquid phase as demonstrated in [Nicholas and Old, 1979]. Liquid Gallium has been used in [Ludwig and Bellet, 2000] to reveal the grain microstructure of an Aluminum alloy, as well as interactions between a fatigue crack and grain boundaries in [Ludwig et al., 2003]. When infiltrated, the Gallium penetrates and diffuses along the grain boundaries which in turn can be reconstructed by means of absorption contrast. One important drawback of this method is that Gallium completely changes the mechanical properties, and makes metals like Al and Zn alloys brit-

[7]The refractive index for x-rays is given by $n = 1 - \delta + i\beta$

tle[8]. It is therefore not possible to perform in-situ studies with the Gallium embrittlement method. Another solution is to use the segregation of alloying elements at grain boundaries [Ludwig, 2010]. In some cases, GBs are preferred sites for phase transformations, and the contrast of layer-like GB precipitates can be retrieved by PCT as shown in [Dey et al., 2007], or in [Dake et al., 2016] where the GBs show a higher concentration of Cu and are observable by PCT. These methods will only work in a limited number of material systems and only provide the 3D grain morphologies without access to their orientation. Crystallographic orientations and defects play a major role in the mechanical behavior of materials, and for that purpose, there is a need for combined diffraction and imaging techniques, as exposed in [Ludwig, 2010]. This will be covered in the next subsections.

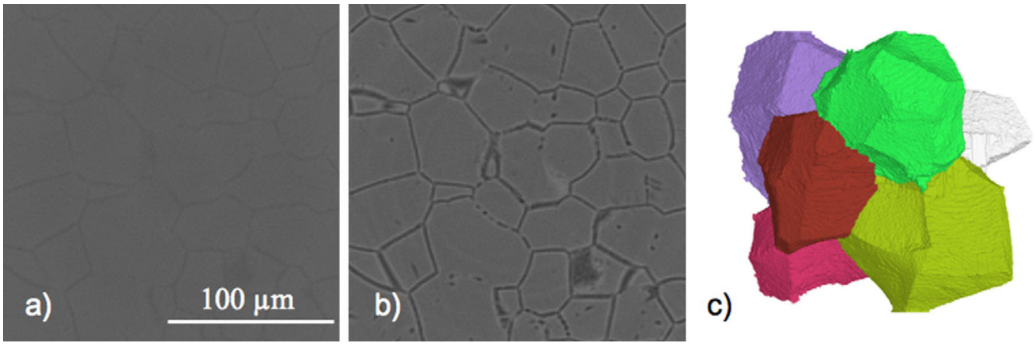

Figure 1.6 – Tomographic reconstruction in the absorption regime (a), and the phase contrast regime (b) of sample made from a metastable β-Ti alloy. Volume rendering of the grains from the segmentation (c). The alloying layer-like precipitation of α-Ti at the grain boundaries is visible in the phase contrast regime. From [Ludwig et al., 2009b].

1.3.3 X-ray diffraction topography

Overview of X-ray topography

Images of the surface or the interior of a single crystal formed by X-ray Bragg reflected from its lattice planes provide information about lattice misorientations and defects in a unique way [Lang, 1993]. X-ray diffraction topography has been widely used since the first topographic experiment has been published by [Berg, 1931, Barrett, 1931], which have respectively observed plastic deformation on rock salt and elastic strains in quartz crystals. The capability of

[8]Gallium was used during the WWII to sabotage metallic structures like airplane wings.

the different topographic techniques to reveal defects in crystalline structures has been of prime interest, especially when crystal quality is crucial like for the semi-conductor industry. The technique consists in recording on a 2D detector, the Bragg (or Laue[9]) reflection of a crystal (single crystal or a grain embedded in a polycrystal). Different imaging modes can be used: polychromatic [Ramachandran, 1944, Guinier and Tennevin, 1949], or monochromatic as Berg in 1931, and with both X-rays produced by conventional X-ray tubes or synchrotron radiation [Tuomi et al., 1974]. From the analysis of the intensity variations in the reflections (see below for more details on the physical processes involved), it is possible to determine the spatial location of defects like dislocations. For instance, studies have been carried out in neutron irradiated [Young Jr et al., 1965] and deformed [Young Jr and Sherrill, 1972] Copper samples. Many different setups exist, and have been reviewed in [Black and Long, 2004].

In synchrotron X-ray topography, both transmission and (back)reflection geometries are used, and defects like precipitates, stacking faults, voids and dislocations have been observed. The main assets of synchrotron topography are the high flux allowing low exposure times, and the long source to sample distance increasing drastically the spatial resolution. The ultimate geometric resolution r is given in [Tuomi, 2002] as:

$$r = \frac{s}{L} w \tag{1.1}$$

with s the sample to detector distance, L the source to sample distance, and w the size of the source. For the monochromatic case, a previous indexing of the crystal thanks to a Laue pattern is required, or the crystal can be aligned to fulfill the Bragg condition by the method exposed in [Ludwig et al., 2007a] consisting in the determination of the diffracted vector by taking images of a reflection at different sample to detector distances.

Contrasts in the topographs

Different mechanisms can give rise to contrasts arising within the 2D topographs, an example of some of them is given in Fig. 1.7 (right). First extinction contrast in high quality (like recrystallized) crystals might occur due to dynamical diffraction. When the grain, or the sub-grain, size is comparable to or bigger than the Pendelloesung period, dynamical diffraction can occur and contrasts arise in the topographs. For example, in an aluminum crystal illuminated with

[9] It depends if the setup uses reflection geometry (Bragg case) or transmission geometry (Laue case)

a $40\,\mathrm{keV}$ radiation, the Pendellöesung period will be around $70\,\mu\mathrm{m}$ for the (111) reflection in the Laue case.

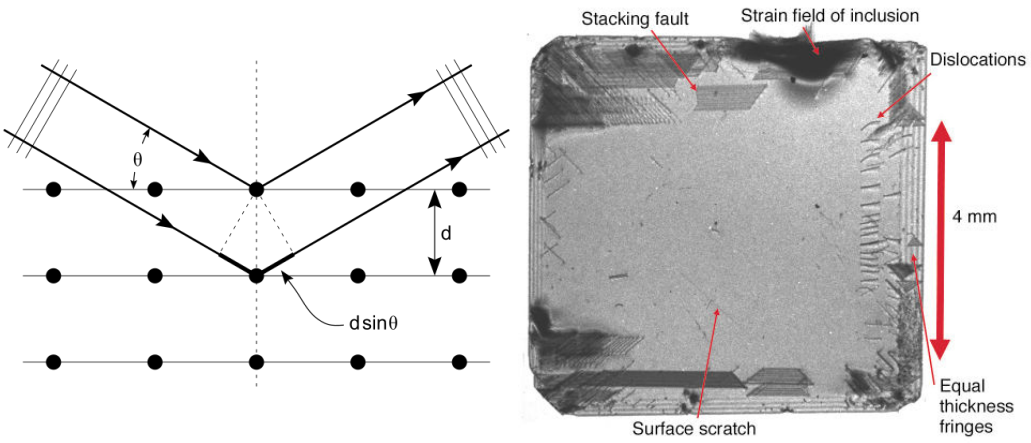

Figure 1.7 – Schematic of the Bragg diffraction (left, courtesy of wikimedia commons) and identification of the contrasts in an X-ray topography of a diamond single crystal (right, courtesy of the ESRF).

In deformed crystals, orientation contrasts may arise due to local modifications of the Bragg condition. In polycrystals, a strong heterogeneity of elastic and plastic strains arise under loading. Elastic strains lead to local variations of the interplanar distance and angles, which in turn can result in a modification of the Bragg condition, see Fig. 1.7 (left). Plastic strains can lead to even higher lattice rotations. To ensure the geometrical compatibility of the material subvolumes, geometrically necessary dislocations (GNDs) densities arise, as well as lattice curvatures [Ashby, 1971]. Locally, the crystal is not exactly oriented as the rest of the grain, and this leads again to a local modification of the Bragg condition.

A variety of other effects can lead to contrasts in topographs. Dislocations for example generate a contrast under certain geometrical conditions ($\underline{\boldsymbol{g}}.\underline{\boldsymbol{b}} = 0$) between the Burgers vector $\underline{\boldsymbol{b}}$ of the dislocation and the scattering vector $\underline{\boldsymbol{g}}$. Generally speaking, two types of contrasts can be identified in topographs: orientation contrasts explained by the Bragg law (local variations of the directions of the diffracted beams), and defect contrasts, explained by means of the kinematical and the dynamical diffraction theory [Zachariasen, 2004]. A comprehensive review of the contrast mechanisms in topographs can be found in [Tanner, 1976].

Variants of X-ray diffraction topography

Two variants of X-ray diffraction topography shall be presented in more details. They both consist in imaging the defect structure of crystalline materials. They are based on the classical Bragg imaging (monochromatic diffraction topography) presented previously, and can be extended to provide 3D maps of the defects.

Rocking curve imaging (RCI) is based on the simple idea that if a crystal is illuminated by a wide (2D) monochromatic beam and fulfills the Bragg condition, topographs can be recorded for different tilt angles of the rocking curve (RC). It is then possible to provide a space resolved map of rocking curves. This is a combination of X-ray topography and X-ray diffractometry, and the development of this technique has been possible thanks to the improvement of synchrotron sources and imaging detectors, decreasing drastically the exposure time for each image. It is possible with such data to analyze local variations of the lattice parameters by taking images for different reflections, and measuring the deviation of the peak positions of the RC. The full width at half maximum (FWHM) of these RCs is linked to the intragranular orientation spread of the crystal, giving information about the GND density. RCI imaging provides a map of these quantities. Studies of the quality of crystals have been published this way, in [Hoszowska et al., 2001] for diamond single crystals, or [Lübbert et al., 2000, Mikulík et al., 2003] for GaAs wafers. A 3D variant exists for this technique, called three-dimensional rocking curve imaging (3D-RCI), published in [Kluender et al., 2011, Kluender, 2011]. Here a line beam delimited by a slit, will illuminate the sample. By applying the previously presented method (diffraction topography) for different slices, it is possible to reconstruct a 3D map of the rocking curves. In this study, with another variant called *pinhole topography*, the authors add the possibility to scan the lateral deflection of the beam out of the diffracting plane. The method has been successfully applied to an ice tri-crystal, and an in-situ study has shown in [Philip et al., 2013] the formation of a subgrain boundary after applying a compressive load to the ice sample (see Fig. 1.8).

Another variant of topography is the Dark Field X-ray Microscopy (DFXM). This time, the principle is to magnify the diffracted beam by placing between the sample and the detector a set of compound refractive lenses (CRL, [Snigirev et al., 1996]) (the latter are more suitable for energies used to scan samples of interest in the field of engineering, above $15\,\mathrm{keV}$, than Fresnel Zone plates). The image on the detector is a magnified projection of the grain in the direct space. The grain can either be illuminated by a line beam (1D) or a box beam (2D). The sample is mounted on a 4-circles diffractometer, and is aligned in a way that a grain fulfills the Bragg condition. The imaging lenses are mounted on a

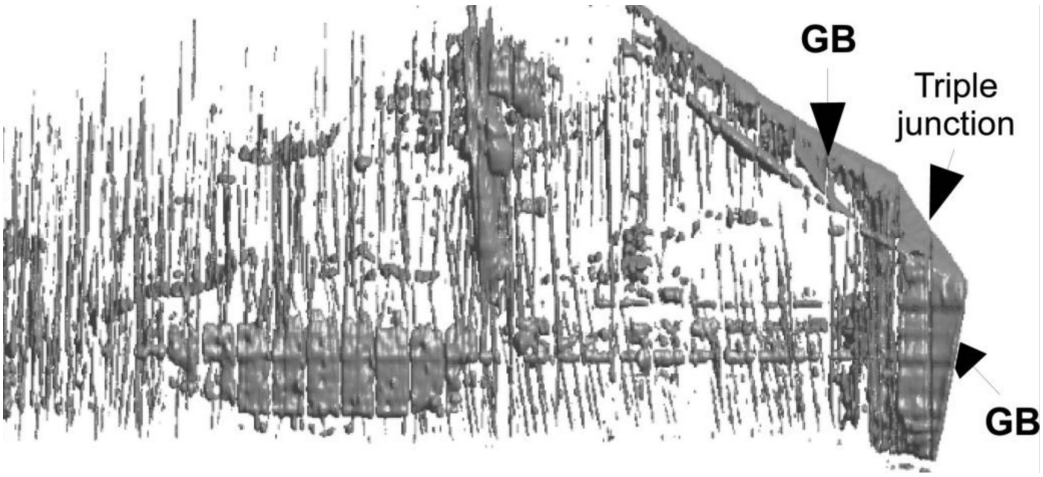

Figure 1.8 – 3D rendering of the dislocation structures within an ice tri-crystal, imaged by 3D-RCI, from [Philip et al., 2013].

multi axis rotation and translation stage to ensure a proper alignment. The small numerical aperture (less than 4×10^{-4}) of the CRLs allows to filter diffracted beams from locally misoriented subvolumes of grain. The use of CRLs allows spatial resolutions down to $100\,\mathrm{nm}$ ($20\,\mathrm{nm}$ are expected in the future with the use of Multi Laue lenses [Simons et al., 2016]) and angular resolutions better than $1\,\mathrm{mrad}$. Then, by scanning the different tilts of the sample goniometer, a map of the local orientation within the grain can be produced. A schematic of the setup is presented in Fig. 1.9 (left).

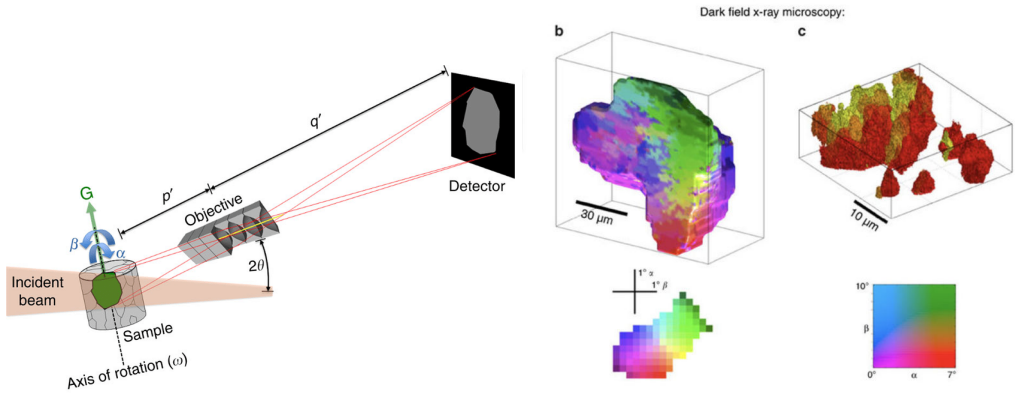

Figure 1.9 – Principle of the DFXM (left), and 3D rendering of local orientation in a grain (middle) and its subgrains (right). From [Simons et al., 2015a].

The recovery of aluminum has been studied with this technique in [Simons et al., 2015a, Ahl et al., 2015], see Fig. 1.9 (right). The three-dimensional

characterization has been conducted by scanning different slices of the grain and merging them. The imaging of individual ferro-electric domains was also studied [*Simons,not published*], as well as individual embedded dislocations in a diamond single crystal [Jakobsen et al., 2016]. This method is non-destructive, and allows for in-situ studies, both during thermal and mechanical loading. Alongside the in-situ device presented in Chap. 2, a tiny compressive rig (not presented here) suited for in-situ DFXM studies has been developed in the frame of the present work.

1.3.4 Three-dimensional X-ray diffraction

The term of "Three-dimensional X-ray diffraction" (3DXRD) refers to a variety of techniques based on the monochromatic rotation method, starting from the pioneering work of [Poulsen et al., 2001, Lauridsen et al., 2001a, Poulsen, 2004a]. Although different variants exist, the basic principle remains the same: a polycrystalline sample is illuminated by a monochromatic beam (most of the 3DXRD setups use the illumination by a laterally extended 1D line beam, and repeat acquisitions for several slices of the sample.). At each angular position of the ω-rotation stage, a subset of grains fulfilling the Bragg condition give rise to diffraction spots on a far field 2D detector. In the near-field variant, the acquisition may have to be repeated at several distances to measure the diffraction vector of a given spot (or the use of a 3D detector -structured scintillator- as in [Olsen et al., 2009], which allows ray tracing) see Fig. 1.10. By indexing the spots, it is possible to know the orientation, and the position of the center of mass of the grains of the illuminated sample volume. The technique has continuously evolved during the past 15 years, in term of setups, reconstruction algorithms, and its ability to measure additional physical quantities such as strain. It will be developed in the next paragraphs.

In [Lauridsen et al., 2001b] the authors published the first monochromatic beam indexing algorithm applicable to polycrystals called GRAINDEX. It is based on the detection of spots recorded at two or three different detector distances (see Fig. 1.10) matching criteria in terms of size and intensity. Due to its mosaicity, a grain can give rise to spots over a certain ω range. These detected spots at different distances are grouped into reflections, and a ray tracing algorithm identifies the possible diffraction vectors associated. To index the different grains of the sample, the algorithm groups them into grains, the intersection of the diffraction vectors being at the center of mass of a grain. The orientation of a grain is calculated by scanning the orientation space and choosing the best fit given the diffraction vectors associated to the given grain.

With these very first experiments, it was possible to extract a grain map from the diffraction data, giving for each grain the average orientation of the crystal

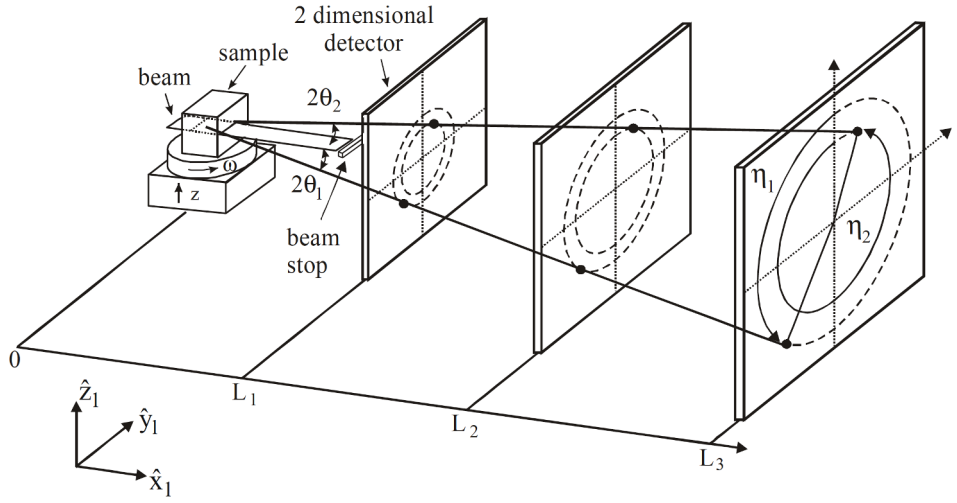

Figure 1.10 – Sketch of the principle of a 3DXRD experiment, from [Lauridsen et al., 2001b, Poulsen, 2004b].

and the average strain state. To reconstruct the shape of the grains, back projections of the diffraction spots close to the pole were used in [Poulsen et al., 2001]. This idea was extended to algebraic reconstruction procedures to take into account more spots for each grain, and increase the accuracy of this reconstruction in [Fu et al., 2003, Fu et al., 2006]. New computational capabilities allow the reconstruction of the orientation to be associated with forward modeling algorithm. By simulating the diffraction spots for all possible orientations, these algorithms simulate a diffraction pattern, compare it with the experimental data, and iterate to minimize the differences. Several of these algorithms have been implemented, like GRAINSWEEPER (Søren Schmidt, DTU) or [Li and Suter, 2013a] at LLNL and CMU. An example from the work of [Li, 2011] is shown in Fig. 1.11. A near field variant of the 3DXRD technique, called diffraction contrast tomography (DCT) which has been used in this work, is presented in more details in Sec. 2.3.1.

One direct application of 3DXRD was the study of recrystallization. In [Schmidt et al., 2004] it was shown how it is possible to watch the morphology of a single grain growing during recrystallization (see Fig. 1.12), and how these observations are in contradiction with the established knowledge. [Lauridsen et al., 2006] studied the kinetic of the recrystallization of individual grains, and [Hefferan et al., 2012] used the new possibilities provided forward modeling approach to identify the growth of new grains related to intragranular microstructures. The plastic deformation of polycrystalline samples has

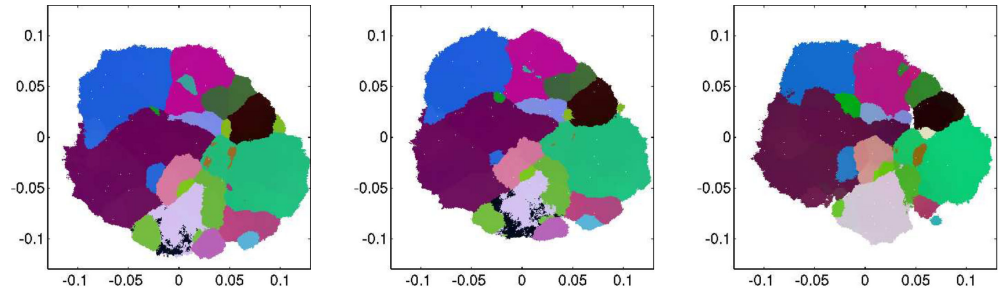

(a) S0 (b) S1 (c) S2

Figure 1.11 – Orientation maps of a high purity Ni sample, reconstructed by a forward modelling approach, for three different applied loads. From [Li, 2011].

been studied in [Margulies et al., 2001] who compared the grain rotations induced by the deformation with the Taylor model. By studying the intensity distribution in the reciprocal space, [Jakobsen et al., 2008, Pantleon et al., 2009] were able to identify the formation of dislocation structures, and the formation of subgrains. Fatigue of engineering materials has also been studied. In [Obstalecki et al., 2014], the authors show the effect of cyclic deformation on the spread over η and ω of the spots. Strain and stress fields within a polycrystal have been extensively studied using this method, as in [Oddershede et al., 2012, Sedmák et al., 2016].

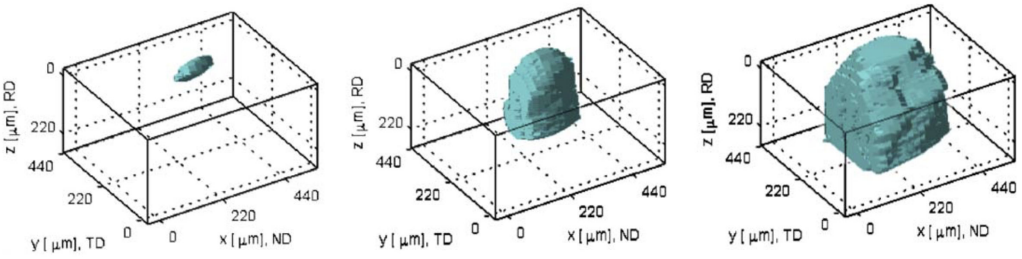

Figure 1.12 – Grain growth imaged by 3DXRD, from [Schmidt et al., 2004].

Most of the previous mentioned studies are time-lapse studies (interrupted in-situ). The main asset of these techniques is the use of the penetration power of X-rays, allowing non-destructive analysis. It is then possible to observe the evolution of physical parameters (crystal orientation, grain size and shape, strain, etc.). Space constraint as well as required accuracy make the use of in-situ mechanical stress rig difficult. In the US, a joint effort of CHESS, APS, and the Air Force National Laboratory lead to the design of a rotational and axial motion

system [Blank et al., 2016]. It allows the sample to rotate under load within the required accuracy and take advantage of the robust load frame from MTS. In Chap. 2, a new design adapted to the DCT geometry and allowing for 4D studies of polycrystalline specimen will be presented.

Chapter 2

Materials and methods

Ce chapitre décrit le matériau et les techniques expérimentales utilisées dans le cadre de ce travail.
Premièrement, une revue historique, et une revue du comportement mécanique des alliages d'Aluminium-Lithium est faite. Les caractéristiques du matériau choisit pour ce travail, un alliage binaire d'Aluminium contenant 2,5% de Lithium sont exposées.
Dans une seconde partie, les deux techniques expérimentales sur lesquelles reposent ce travail sont détaillées : la tomographie par contraste de diffraction et la topo-tomographie. La tomographie par contraste de diffraction permet de connaitre la position, la forme, et l'orientation des grains qui composent un polycristal. Avec la topotomographie, l'attention est portée sur un grain en particulier. La technique permet de reconstruire en trois dimensions les défauts cristallins qui perturbent la diffraction du cristal.
Enfin, afin de disposer d'un moyen d'essai mécanique adaptée aux techniques précédemment exposées, une machine de traction miniature appelée Nanox a été développée. L'article, publié dans Journal of synchrotron radiation, traite de ces développements est inclu est attache dans la troisième partie de ce chapitre.

2.1 Introduction

This chapter provides the necessary details on the material and the methods used throughout this work. First, a short review on Aluminum-Lithium (AlLi) alloys is given, with a focus on the metallurgy and the deformation behavior of binary AlLi alloys. The second part of this chapter shows how it is possible to study microstructural evolutions of polycrystalline materials with two different three-dimensional diffraction techniques namely diffraction contrast tomography and topotomography. At the end, the design of a specific tensile rig allowing for 4D diffraction studies is detailed. This last part was published in [Gueninchault et al., 2016].

2.2 Material: Review of the properties of binary AlLi alloys

2.2.1 Developments of AlLi alloys

Structural weight reduction is a very efficient way to improve aircraft performance [Joshi, 2005]. To this end, AlLi alloys with their low density and their good mechanical properties, are of high interest for the aeronautical industry. Most of the developments for these alloys were led by the need of greener and safer planes, as the traffic has increased from 106 million in 1960 to more than 6 billion passengers-kilometers in 2016 (ICAO statistics). Extensive reviews of the development of these alloys can be found in the work of [Proton, 2012, Cerutti, 2014, Delacroix, 2011] as well as in [Lavernia and Grant, 1987] for the microstructural and the mechanical behavior of AlLi alloys.

AlLi alloys have been widely used in aircraft structures since the 1920s [Prasad et al., 2013], and mainly four phases in the development of the AlLi alloys can be distinguished since the fifties:

- The first phase, beginning in the 1950s, with the development of the AA2020[1] alloy from ALCOA and the VAD20 from the USSR industry. They were developed mainly for fighter aircraft applications (the F20 tigershark program of the US department of defense for the AA2020 alloy, later abandoned for the famous F16). This first generation of AlLi alloys was withdrawn because of their low toughness and low ductility.

- The second generation of alloys began with the oil shock of 1970-1980 [Cerutti, 2014] and the design of supersonic aircrafts like *le Concorde*

[1] this alloy has the following composition: Al 1.1Li 4.5Cu 0.5Mn 0.2Cd.

[Starke and Staley, 1996] and resulted in the development of the AA2090, AA2091, AA8090 and AA8091 alloys. But low toughness and excessive anisotropy of mechanical properties [Campbell, 2008] have limited their commercial success, and restrained them mainly for military applications like in the MIG29 aircraft.

- During the 1990s a third generation of alloys have emerged with the AA2094 used for the space shuttle[2]. This generation of alloys was also used for the B19 stringer of the F16, and presents enhanced fatigue properties. It achieved a greater commercial success, notably thanks to new alloying techniques, reducing the technical difficulties and production costs.

- Fiber reinforced composite materials were once thought to take over most of the structural part of an aircraft but the high costs of production and difficulties in the maintenance process have motivated the metallurgical industry to pursue the innovation in AlLi alloys. *Constellium* has recently (2013) achieved great success in it, with the commercialization of *AIRWARE™* integrated by *Bombardier* in their CS program or *SpaceX* for their reusable rocket launcher.

This evolution of the use of AlLi alloys has been achieved thanks to continuous improvement of the knowledge of the microstructural properties and their link to the behavior of the alloy under working conditions. These aspects are reviewed in the next sections.

2.2.2 Effects of Lithium addition to Aluminum

Lithium is the third element of the periodic table and the lightest metal with an atomic mass of $6.94\,\mathrm{u}$. This is almost $4\times$ lighter than Aluminum ($26.98\,\mathrm{u}$). Furthermore, Lithium has the highest solubility in Aluminum [Starke and Staley, 1996]. Up to 4%, every added percent of Lithium to Aluminum decreases by 4% the density of the alloy and increases by 3% the stiffness [Noble et al., 1982, Sankaran and Grant, 1981]. The stiffness is both increased by the Lithium in solid solution and the second phase $\delta'(Al_3Li)$. Up to 4% wt. Lithium can be dissolved to reach a $86\,\mathrm{GPa}$ Young modulus, increasing by 30% the stiffness compared to pure Aluminum [Noble et al., 1982].

The strengthening of the AlLi alloys is mostly due to the large presence of δ' precipitates. This phase is an ordered $L1_2$ superlattice structure, and the preferred positions for the Lithium atoms are in the corners of the Aluminum

[2]The use of this alloys allowed a weight saving of $3.4\,\mathrm{t}$ out of a total weight of the shuttle tank of $27\,\mathrm{t}$.

FCC cell as shown in Fig. 2.1. [Noble et al., 1982] has shown that δ' precipitates have a Young modulus of $89\,\mathrm{GPa}$, are coherent with the Aluminum matrix and are spherical. They present a cube-cube orientation and remain coherent up to $300\,\mathrm{nm}$ [Lavernia and Grant, 1987]. The precipitates are shearable up to a diameter of $30\,\mathrm{nm}$, from where Orowan looping would be energetically more efficient [Ashby, 1968]. The precipitation of Lithium is not homogeneous through

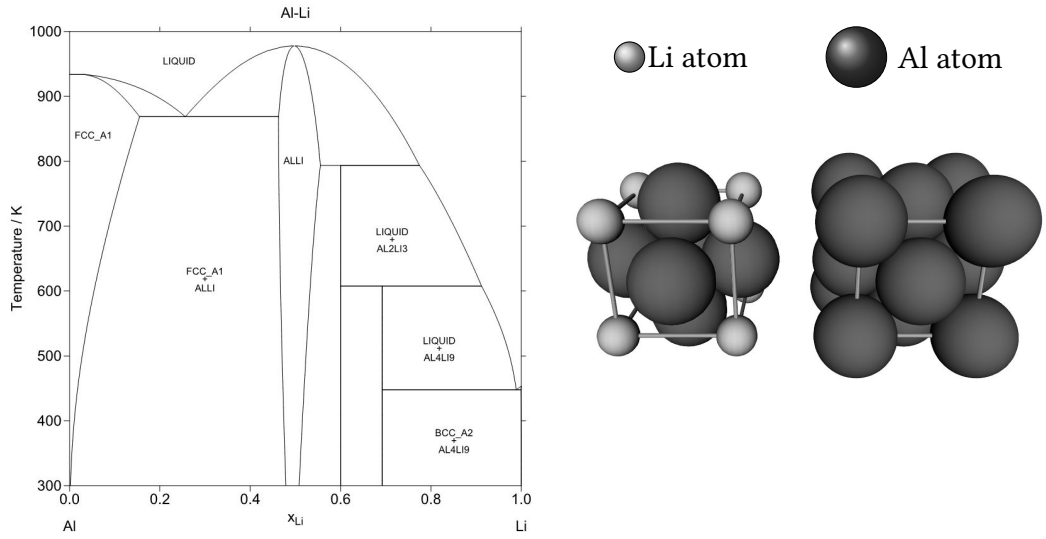

Figure 2.1 – The Al/Li phase diagram (left), the Al_3Li unit cell (center) and the FCC Aluminum unit cell (right).

the matrix, and due to the highest solubility of Lithium and the precipitation of δ (AlLi) phase at the grain boundaries, development of precipitates free zones can occur (see Fig. 2.8 for an illustration). In [Radmilovic et al., 1989], the authors show that PFZs can be up to $0.5\,\mu\mathrm{m}$ large and are strongly affected by ageing conditions.

2.2.3 Deformation behavior of binary AlLi alloys

At the grain level, deformation is achieved both by lattice distortions (elasticity) and by dislocation glide on the {111}<110> slip systems. Even if it is widely accepted that the precipitation of the δ' is the main strengthening mechanism, [Lavernia and Grant, 1987] state that the exact mechanism is not totally understood and some disagreements exist. When the size of the precipitates is below $30\,\mathrm{nm}$, the precipitates are sheared by dislocation glide, resulting in a local reduction of the strengthening effect. In [Cohen, 1969], the author states that *When an alloy with only local order is deformed, the passage of dislocations across a slip*

plane reduces the local order across this plane by about 20 %, but does not destroy it completely. These local softer areas are subject to stronger dislocation motion and concentration of slip as shown in Fig. 2.2. The presence of PFZs with their local low critical resolved shear stress (CRSS) leads to strong strain localization close to GBs. Micrographs from [Sanders and Starke, 1982] shown further in this work demonstrate that strain localization occurs along glide planes and lead to well defined slip bands. In AlLi alloys, dislocations are supposed to move in pairs to minimize the energy of the disorder created, resulting in a fine planar slip. But when sufficient disorder has been created, strain localization and coarse slip occur [Sanders and Starke, 1982, Allen and Cahn, 1979].

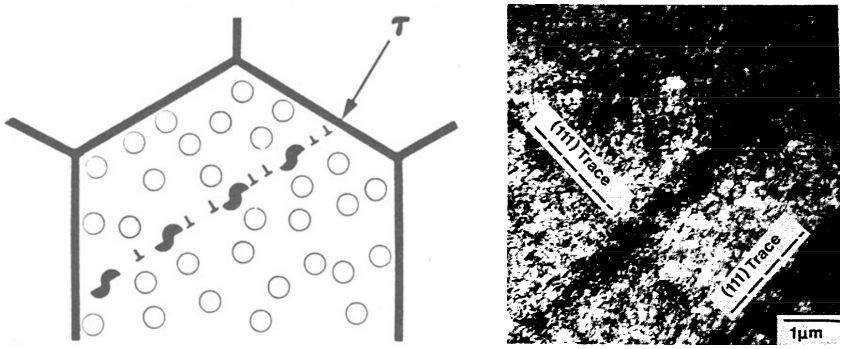

Figure 2.2 – Schematic of the softening mechanism (left) and micrograph of plastic strain localization in AlLi alloy from [Sanders and Starke, 1982].

2.2.4 Conclusion: material used for the study

In this work, the aim is not to improve an AlLi alloy itself, but to provide new methods for the characterization of the evolution of crystalline defect structures, through 3D X-ray characterization techniques presented in the next section. For that, binary AlLi alloys are perfect candidates. As shown in the previous sections, they are subject to strong plastic strain localization, and X-ray absorption at energies around $40\,\mathrm{keV}$ (Fig. 2.3) remains small. This allows for short exposure times, making it a good candidate for time-lapse observations in 4D diffraction imaging experiments.

The alloy chosen is a binary AlLi alloy with 2.5% wt. of Lithium. Specimen used in this work were machined from a cold rolled $6\,\mathrm{mm}$ plate ordered from MATECK subjected to a 45% reduction to reach an approximate final thickness of $3\,\mathrm{mm}$. To guarantee a strain free structure, the samples have been recrystallized $20\,\mathrm{min}$ at $530\,^{\circ}\mathrm{C}$ after machining to reach a grain size from $20\,\mu\mathrm{m}$ to $200\,\mu\mathrm{m}$ and then water quenched. The obtained microstructure is perfectly equiaxed with no

particular texture with a mean grain equivalent diameter of $55\,\mu m$ as measured by EBSD on a $8 \times 2\ mm^2$ sample. To improve the mechanical properties of the samples, all specimens have been aged 4 hours at $100\,°C$, and they are expected to have a mean δ' precipitate size of $\simeq 8\,nm$ [Brechet and Livet, 1987]. These precipitates are well below the $30\,nm$ limit which make them shearable by the dislocations.

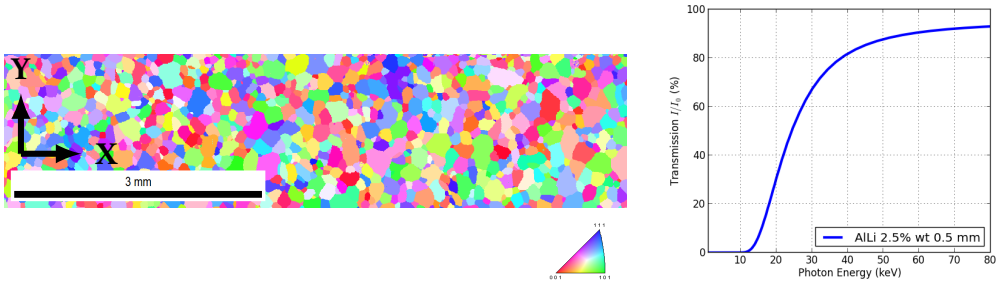

Figure 2.3 – Microstructure of a recrystallized AlLi 2.5wt sample measured by EBSD (left), IPF coloring of the Z axis, in this case the rolling direction is Y, and X-ray transmission of a $500\,\mu m$ thick sample as a function of the X-ray energy (right).

2.3 Experimental methods: 3D X-ray diffraction imaging techniques

In this section we introduce two 3D X-ray diffraction methods developed by the team of W. Ludwig at the ESRF. First, Diffraction Contrast tomography (DCT) allows to measure the 3D map of the grain microstructure of a sample, in terms of grain shape, position and mean orientation. Then topotomography (TT) is presented. This technique enables focus on a particular grain, to give a map of crystalline defects in 3D.

2.3.1 Diffraction contrast tomography

Principle

X-ray diffraction contrast tomography (DCT) is a near field variant of the 3DXRD (see Sec. 1.3.4) concept developed by [Poulsen, 2004b], which has been constantly improved since then. Here, the sample is illuminated by a monochromatic 2D (box) X-ray beam and a high resolution 2D X-ray detector is placed

close (typically $5\,\mathrm{mm}$) to the sample. During the experiment the sample is rotated continuously around a vertical (perpendicular to the beam) ω-axis and images are recorded for every $\delta\omega$ increment (typically 0.1° which leads to 3600 images over a full rotation of the sample). Two interlaced turns are used to make sure the intensity missed during the readout time of the camera is captured during the second turn. The key is to use a field of view larger than the sample to capture both the transmitted direct beam and the multitude of diffracted beams coming from the sample. In that sense, this is a combined diffraction-imaging technique.

At a given ω position, a grain will give rise to a diffraction spot onto the detector if one of its lattice planes fulfills the Bragg condition as shown in Fig. 2.4. The diffracted intensity leads to an extinction spot in the direct beam image. The first version of the code presented in [Ludwig et al., 2008] was based on the segmentation of these extinction spots. Overlap in the direct beam limited this version to multicrystalline samples with a limited number of grains (several tens). In [Johnson et al., 2008], the authors presented an improvement of the direct beam case to overcome this limitation by using the shape of the diffraction spots (combined case). The most recent version of the reconstruction code is

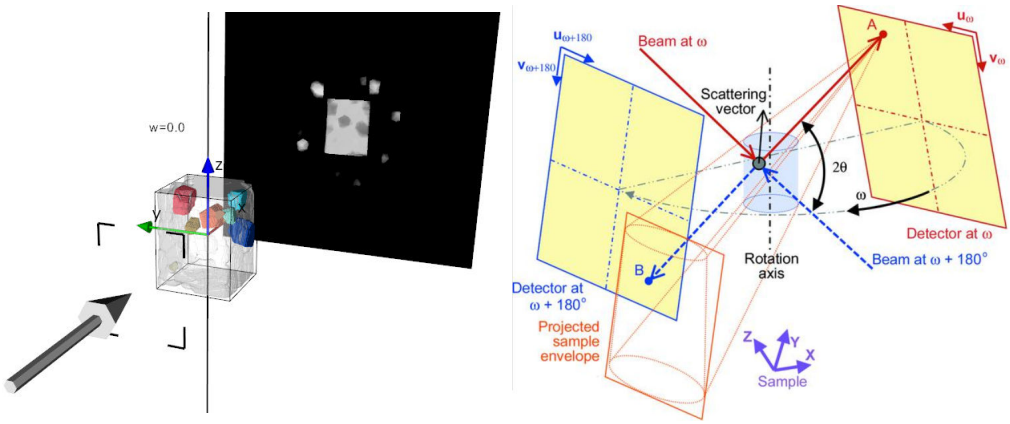

Figure 2.4 – Principle of the DCT experiment (left). The grains fulfilling the Bragg condition are highlighted and give rise to a diffraction spot onto the detector, as well as an extinction spot in the direct beam. Schematic of the Friedel pair analysis from [Reischig et al., 2013] (right). The line connecting Friedel pairs of diffraction spots passes through the grain in diffraction condition.

uniquely based on the use of diffraction spots. Diffraction vectors are derived from Friedel pairs of diffraction as presented in [Ludwig et al., 2009c]. The indexation process (determination of the orientation of a grain by the knowledge of its diffraction vector(plane normals)) assigns different pairs of spots by means of size, shape, intensity, interplanar angles, ω spread and position. The different

steps of the reconstruction process are described in [Reischig et al., 2013] and summarized in Fig. 2.5:

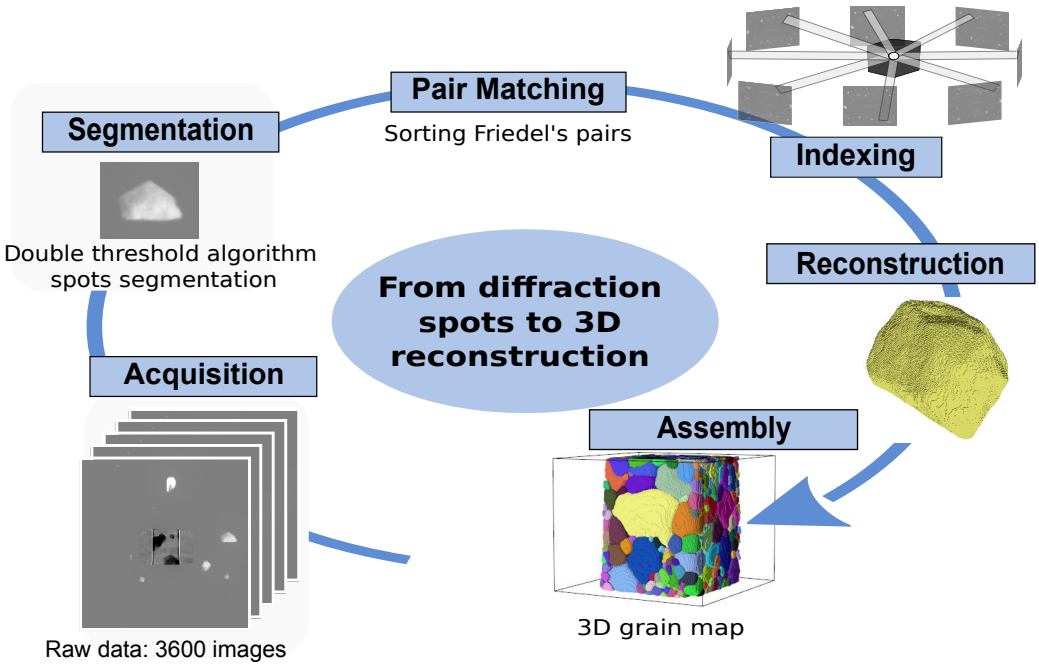

Figure 2.5 – Steps of the reconstruction process of DCT data.

- the images are preprocessed. A flat field correction is applied, and the direct beam image is separated from the rest. The position of the rotation axis is calculated here;
- the diffraction spots are individually identified. Peaks of intensity above a certain threshold are set as seeds and the outlines of the spots are determined by a second threshold linearly dependent on the first one. A three dimensional morphological operation is then applied, and the final diffraction blob (the 3D diffraction spot[3]) is labeled and stored in a database. This is a critical step, the quality of the final 3D reconstruction of the volume is directly linked to the quality of the segmentation;
- the diffraction spots are then associated in pairs. If a (hkl) set of lattice planes fulfills the Bragg condition at a position ω of the sample, the $(\bar{h}\bar{k}\bar{l})$ planes will give rise to another diffraction spot at $\omega + 180°$. The grain of

[3]Whereas a diffraction spot is an integrated (2D) variation of intensity on the (u, v) detector space, a diffraction blob is characterized in the 3D (u, v, ω) space.

origin of this pair lies on the diffracted beam path as shown in Fig. 2.4. The use of Friedel pairs has shown high accuracy in the measurement of diffraction angles in the near field mode. Extension of this method to far field data is available in [Moscicki et al., 2009]. From the knowledge of the pair position, a calibration procedure of the experimental geometry (detector position, tilts, etc) is executed to refine the initial parameters filled by the user through an optimization algorithm;

- the indexation process based on the iterative algorithm called *INDEXTER*. The algorithm searches through the list of pairs, and identifies consistent sets of pairs by means of crystallographic and geometric selection criteria. By iteratively decreasing tolerances, grains are merged if needed and extra pairs and diffraction spots are added to them[4];

- each grain is individually reconstructed by an algebraic iterative reconstruction algorithm. A set of suitable spots (no overlap) is used, and the diffraction geometry (diffraction vector, position of the detector) associated to each spot is calculated. This information is used to perform oblique angle reconstruction using the ASTRA tomography library presented in [Palenstijn et al., 2013]. After reconstructing, the different grains are segmented and assembled in a single volume. The small gaps between neighboring grains can be eliminated in an optional dilation step to ensure continuity at the grain boundaries.

Applications of DCT

The first published DCT volume was a Al1050 recrystallized multicrystalline sample, illustrating the capabilities and limitations of the technique in [Ludwig et al., 2008]. Even if metals are the most natural candidates for DCT, [Reischig et al., 2013] have successfully reconstructed the microstructure of a ceramic, whereas [Roscoat et al., 2011] used an ice sample. Minerals have been successfully reconstructed as well, even if not yet published. Since then, about 50 experiments have been allocated at the ESRF to DCT experiments through the proposal process, and many more experiments have been carried out in the framework of in-house research at ID11. The main interest of getting 3D maps of the microstructure by DCT is either to be associated or to other experimental techniques or to monitor microstructural evolutions in 4D experiments or to validate predictions made by image based numerical simulations. Compared to slice beam acquisition techniques, DCT is about 1 to 2 orders of magnitude faster. A (non exhaustive) list of uses of the DCT is given below:

[4] An exhaustive description of the indexing process can be found in [Reischig et al., 2013].

- Fatigue failure of materials may lead to dramatic events. It is of prime importance that scientists provide engineers improved lifetime models of materials which in turn allow for optimized and safe design of critical components. As the stage of short fatigue cracks may takes up to 90% of the lifetime [Nowack and Lutjering, 1996], it is important to understand the physical processes underlying the initiation and propagation in relation with the crystallographic microstructure of the material. In [Herbig et al., 2011], the authors propose a study of fatigue crack growth in a Ti-β-21S sample by combining DCT (to characterize the microstructure) and phase contrast tomography (to monitor the crack growth). One of the advantage of DCT is the possibility to switch between diffraction and imaging mode with the same setup. The sample was mounted on a fatigue rig developed at INSA Lyon. A DCT scan was first performed and several PCT scans were performed at regular intervals of applied fatigue loading cycles. It was then possible to analyze the crack growth path with respect to the crystallographic orientation of the relevant grains. A correlation between the slip planes and the fracture surface orientation has been established;

- Grains sizes and morphologies evolve when specific thermal treatments are applied. The knowledge and prediction of these microstructural evolutions are essential since it will impact the mechanical behavior of polycrystalline materials, governed by the intrinsic elastic and plastic anisotropy of crystalline materials. In [Syha et al., 2013a], the authors propose a study of the recrystallization of a sintered strontium titanate sample. From the DCT data, it was possible to analyze the grain boundary shape and grain orientation for two successive high temperature annealing steps (and to individually identify pores and monitor their shapes). This data was then compared to a mesoscale grain growth model. An extensive comparison in terms of grain shape and orientation accuracy between a Tri-beam dataset and DCT has been made for the same sample in [Lenthe et al., 2015]. The DCT takes advantage of the extension by the TriBeam of the well established EBSD technique to confirm the accuracy of its grain map;

- DCT can be used as an input for 3D CP-FEM simulations. In [Proudhon et al., 2016], the authors show how from the DCT data it is possible to build suitable meshes and perform finite element simulations of the micromechanical behavior. As grain morphology, shape and orientation play a major role in the microstructural evolution of mechanical fields, it is essential to have access to realistic microstructures. The proposed methodology is a clear improvement compared to Voronoi tessellations based com-

putations. A grain by grain comparison of mechanical quantities that can be retrieved from DCT, such as elastic strains, has been achieved. This is a promising way to validate predictive models. Moreover, crystal plasticity FE calculations were used to simulate the short crack growth observed by DCT and PCT in [Proudhon et al., 2017].

Limitations of DCT

Even though DCT has proven to be a powerful technique giving access to the 3D grain microstructure of polycrystalline materials, there are some intrinsic limitations:

- Diffraction spots are summed over ω, and if there is too much orientation spread within the grain (if the grain is plastically deformed), spot overlap might occur. As the pair matching and the indexation process are based on the diffraction spot metadata (position, intensity, etc.), these overlaps can compromise the quality and consistency of the grain maps;

- Sample volumes with too many illuminated grains can lead to spot overlap too, with the same problems as exposed before. It is possible to decrease the number of grains by reducing the illuminated area of the sample with slits, but if too many grains are present in a horizontal section of the sample, it could be a difficult issue to overcome. Reducing the $\delta\omega$ step may be a solution for undeformed materials, but comes with an increasing acquisition and data processing time. Mixed far-field/near field approaches are under development to allow the reconstruction of samples with higher number of grains;

- The availability of the beam time is a problem, since only selected experiments are allowed to be performed at the ESRF. In [King et al., 2013, McDonald et al., 2015], the authors show the possibility to adapt the technique to laboratory microtomography setups, with the evident asset of better accessibility. A dedicated software package, called *LabDCT*, is now commercialized by Zeiss with the Xradia 520 Versa microtomograph;

- By nature, DCT gives information averaged over the grain volume. For most studies, it is of prime interest to have access to the intragranular mechanical fields. A six dimensional framework has been developed at the ESRF and shows promising results described in [Viganò et al., 2013, Viganò et al., 2016, Viganò et al., 2016, Viganò et al., 2014]. It will be further discussed in Chap. 4.6.4.

2.3.2 Topotomography

Principle of topotomography

Whereas DCT gives average information about all the grains of a sample, topotomography focuses on a selected grain, and can give a 3D map of the defects within this grain. The first topotomography was performed on a diamond single crystal in [Ludwig et al., 2001b]. The extension to a single grain within the bulk of a polycrystal has been demonstrated six years later in [Ludwig et al., 2007b] and more recently has been combined with dark field X-ray microscopy [Simons et al., 2016]. Topotomography combines the concepts of X-ray diffraction topography with X-ray absorption tomography and enables three-dimensional characterization of crystals, using two different contrast mechanisms [Ludwig, 2010].

In a topotomography experiment, the normal $\underline{\boldsymbol{n}}$ of a given set of (hkl) planes is aligned parallel to the ω axis of rotation of the tomographic rotation stage as described in Sec. 2.4. This alignment can be achieved thanks to a goniometer stage mounted on top of the tomographic rotation stage exposed in Fig. 2.7. Once aligned, the whole setup is tilted by the Bragg angle of the selected reflection by a third rotation stage, called the *base tilt* T_0, to set the Bragg angle for the reflection. Whereas in the DCT setup a given reflection will satisfy this Bragg condition only for a small subset of ω positions, here the diffraction condition is maintained during the rotation of ω. Due to the orientation spread within the grain, a small azimuthal rocking scan over Θ, the base tilt angle, must be performed in order to integrate the full crystal reflection curve. Typically, the relative energy bandwidth on ID11 is $\frac{\Delta\lambda}{\lambda} = 10^{-3}$, and subvolumes where lattice rotation higher than the value defined further by Eq. 2.3 lead to the Bragg condition not to be fulfilled in the entire grain which is why the rocking scan is needed[5]. By integrating the diffracted intensity over Θ, it is possible to get a full projection of the selected grain as illustrated in Fig. 2.6. The acquisition of a large number of projections over ω allow for the 3D reconstruction of the grain by means of analytical cone beam filtered backprojection or SIRT algebraic reconstruction as used for DCT.

The critical step here is the alignment of the reciprocal lattice vector with the rotation axis. In [Ludwig et al., 2007b], the authors exposed how by moving back and forward the detector it is possible to calculate the diffraction vector of a suitable[6] reflection. These is a basic approach (no knowledge which grain aligned), and a more powerful approach using the knowledge of the microstruc-

[5]The divergence of the beam in a third generation synchrotron is very low, and topotomographic experiment are not sensitive to that.

[6]By suitable we mean that the grain could be aligned with the motors of the id11 diffractometer, since they have a limited range of motion.

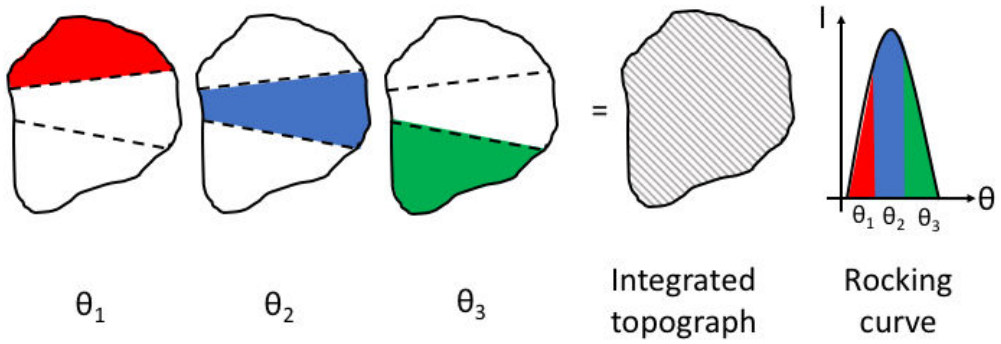

Figure 2.6 – Shematic of the topographs for a grain diffracting for three different angles of the base tilt. The grain projected outline is in black solid line. The illuminated area of the detector is in color and the corresponding integrated topograph is in grey. The corresponding rocking curve is illustrated on the right.

ture (grain orientation) gained from an initial DCT scan makes the alignment procedure much easier, since from the orientation of a grain, a simple trigonometric equation needs to be solved to determine exactly the goniometer tilts required to align this grain. Given the diffractometer geometry exposed in Fig. 2.7, $\underset{\sim}{\boldsymbol{g}}^{-1}$ the orientation of the grain, and $\begin{pmatrix} p \\ q \\ r \end{pmatrix} = \underset{\sim}{\boldsymbol{g}}^{-1} \begin{pmatrix} h \\ k \\ l \end{pmatrix}$ the components in the sample reference system of the scattering vector $(h, k, l)^t$ to be aligned, one can compute the upper tilt (ut) and the lower tilt (lt) as[7]:

$$ut = \arctan \frac{-p}{r} \tag{2.1}$$

$$lt = \arctan \frac{q}{-p\sin(ut) + r\cos(ut)} \tag{2.2}$$

2.3.3 Interpretation of the contrast

Strain localization in Al-Li alloys has been widely studied during the 80's. The presence of shearable δ́precipitates strengthen the β coherent matrix by increasing the frictional drag of dislocation motion [Fisher, 1954]. Once sheared, the size of the precipitates is below the critical size and the precipitates are dissolved

[7]This is only valid if the tilts are set to (0,0) before alignment.

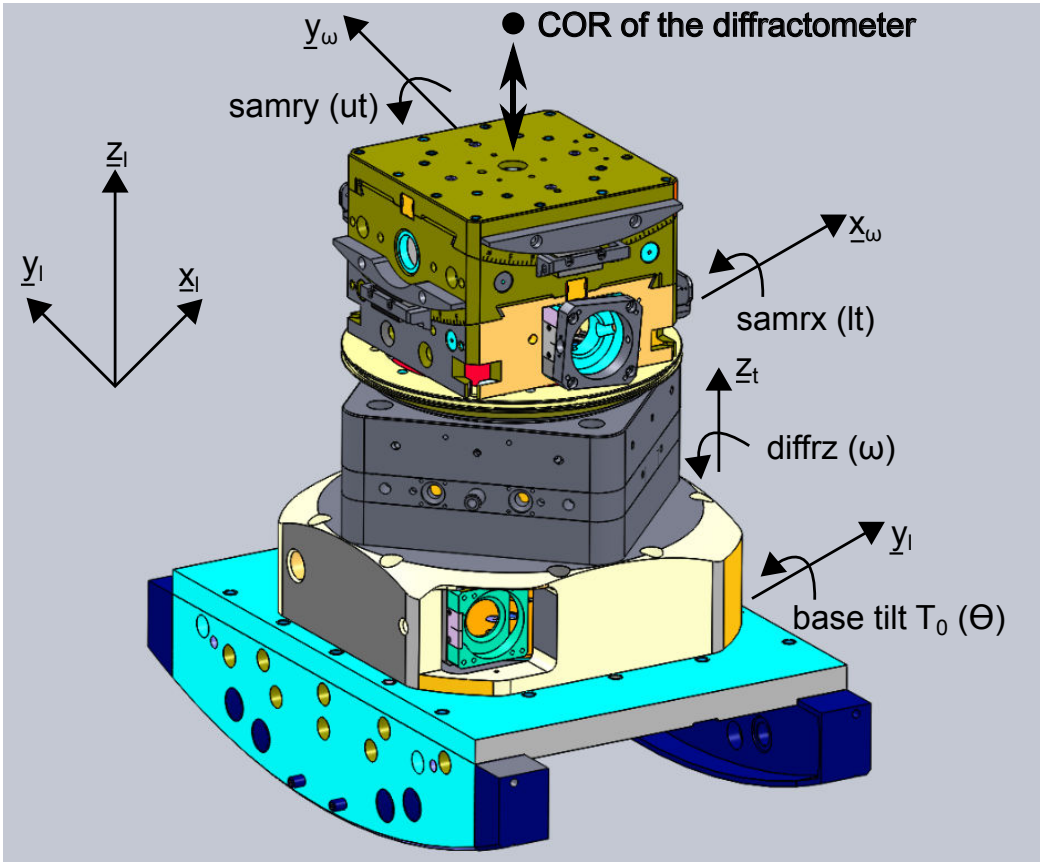

Figure 2.7 – Simplified CAD model of the ID11 diffractometer. Each rotation axis passes through the diffractometer center of rotation (COR). Axis of rotation are drawn close to their motors for sake of simplicity. l indices refer to the laboratory coordinate system, t indices to the tilted coordinate system and ω indices to the rotated coordinate system. A full description of the different coordinate systems is given in Chap. 4.

[Brechet et al., 1987] or at least the local order is perturbed [Cohen, 1969]. There is a local softening due to the lower concentration of precipitates and plastic slip will localize along crystallographic {111} directions, see Fig. 2.2(right). In these dislocation bundles, the local order of the lattice is widely disrupted. In fatigue, [Bréchet, 1987] has demonstrated that the local lack of precipitates leads to the formation of persistent slip bands (PSBs), preferred sites for crack initiation

In aged binary Al-Li alloys, vacancy depletion or solute depletion mechanisms lead to precipitates free zones (PFZ) close to the grain boundaries [Pashley et al., 1967, Starke, 1970]. These local soft areas are embedded in a harder matrix, and are subject to higher stresses and plastic flow.

These zones where the plastic deformation is localized exhibit higher lattice rotations compared to the rest of the grain. The bandwidth of the ID11 monochromator is $\frac{\Delta\lambda}{\lambda} = 10^{-3}$. From that we can compute the absolute angular sensitivity of the instrument for $\lambda = 0.309\,95$ Å, and $d_{hkl} = 4.04/\sqrt{3} = 0.58$ Å:

$$\Delta\theta = \tan\theta \frac{\Delta\lambda}{\lambda} = 6.6 \times 10^{-2}\,\mathrm{mrad} \tag{2.3}$$

Material subvolumes subject to a lattice rotation superior to this value will no longer satisfy the Bragg condition and will generate contrasts on the topographs. This is the orientation contrast as described by [Tanner, 1976] and illustrated in Fig. 2.8.

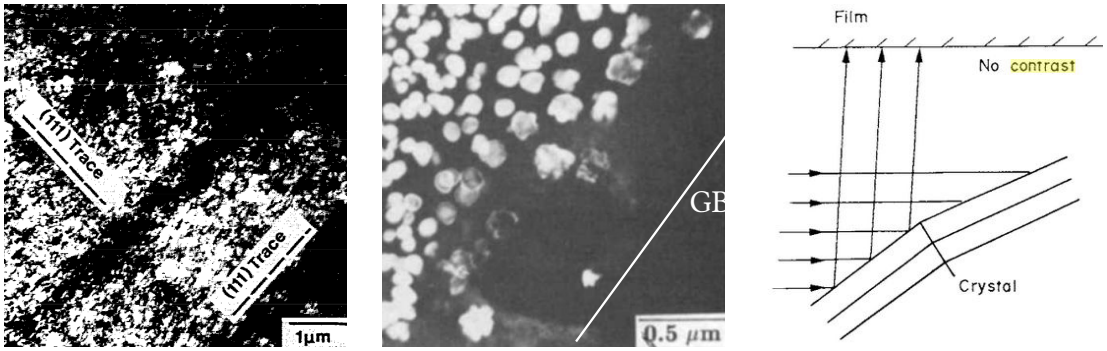

(a) (b) (c)

Figure 2.8 – Dislocation bundles from [Sanders and Starke, 1982] (a), PFZ from [Jha et al., 1987] (b), and schematic of the orientation contrast mechanism from [Tanner, 1976] (c).

2.3.4 Applications of topotomography

Except the present work, and dark field X-ray microscopy variants of the topotomography, the previous application of topotomography was the study of recrystallization in [Van Boxel et al., 2014, Van Boxel et al., 2010]. In these studies, topotomography allowed the authors to monitor non-destructively the migration of the grain facets during the recrystallization process, as well as the grain shape evolution during abnormal grain growth [*Yubin, Zhang, in preparation*]. In [Kawado et al., 2004], the authors show the dislocation network of a lithium fluoride single crystal, and the possible extension to lab sources. A topotomographic study of LiF single crystal by laboratory X-ray topo-tomography has been presented in [Zolotov et al., 2011].

2.4 Nanox: a miniature tensile rig specifically designed for 4D diffraction studies

With the advent of high brilliance third generation X-ray sources, scan times have decreased drastically. It is now possible to perform several scans of the same sample in one shift of beamtime. It is then possible to monitor microstructural evolutions within the bulk of a sample, from both in-line imaging (PCT) and diffraction imaging (DCT and topotomography). To perform extensive 4D studies in both modes, a very specific tensile rig called *Nanox* has been developed and is described here. Special care has been taken to facilitate further numerical simulations with the experiment results, by using two pins as grips. These two pins ensure auto-alignment, making easy to set boundary conditions for finite element simulations (the force pass through the pins, because of the geometry). To be able to mount samples with a very low yield limit, a special system for the upper grip was designed. To fulfill the severe space constraints imposed by diffraction imaging (the sample has to be located at the centre of rotation (COR), see Fig. 2.7). That specification ensures that the COR of the experiment and the center of the sample coincide but made the design more difficult. Indeed, no commercially available load cell has the right dimension to fit on that design, with the special shape that allow a very small sample to detector distance (it allows diffracted intensity from higher hkl families to be detected and a better reconstruction). The choice was made to use a homemade sensor, with a full Wheatstone bridge strain gauges stuck on a Titanium axis. This solution lead to not reproductive load measurements. A modification of the design has been made, and will benefit the next experiment on ID11.

This work was published in the Journal of synchrotron radiation, and the text of the paper is reprinted here.

JOURNAL OF SYNCHROTRON RADIATION

ISSN 1600-5775

Received 26 April 2016
Accepted 29 August 2016

Edited by G. E. Ice, Oak Ridge National Laboratory, USA

Keywords: miniature stress rig; X-ray diffraction contrast tomography; topotomography; crystal plasticity; *in situ*.

Supporting information: this article has supporting information at journals.iucr.org/s

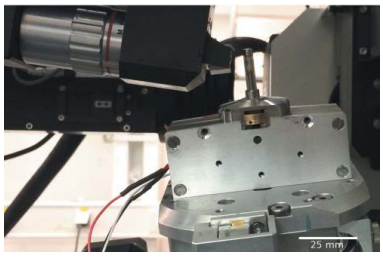

Nanox: a miniature mechanical stress rig designed for near-field X-ray diffraction imaging techniques

N. Gueninchault,[a]* H. Proudhon[a] and W. Ludwig[b,c]

[a]MAT – Centre des Materiaux, CNRS UMR 7633, PSL – Research University, BP 87, 91003 Evry, France, [b]MATEIS, INSA Lyon, CNRS UMR5510, 25 Avenue Jean Capelle, 69621 Villeurbanne Cedex, France, and [c]ESRF – The European Synchrotron, 71 Rue des Martyrs, 38000 Grenoble, France.
*Correspondence e-mail: nicolas.gueninchault@mines-paristech.fr

Multi-modal characterization of polycrystalline materials by combined use of three-dimensional (3D) X-ray diffraction and imaging techniques may be considered as the 3D equivalent of surface studies in the electron microscope combining diffraction and other imaging modalities. Since acquisition times at synchrotron sources are nowadays compatible with four-dimensional (time lapse) studies, suitable mechanical testing devices are needed which enable switching between these different imaging modalities over the course of a mechanical test. Here a specifically designed tensile device, fulfilling severe space constraints and permitting to switch between X-ray (holo)tomography, diffraction contrast tomography and topotomography, is presented. As a proof of concept the 3D characterization of an Al–Li alloy multicrystal by means of diffraction contrast tomography is presented, followed by repeated topotomography characterization of one selected grain at increasing levels of deformation. Signatures of slip bands and sudden lattice rotations inside the grain have been shown by means of *in situ* topography carried out during the load ramps, and diffraction spot peak broadening has been monitored throughout the experiment.

1. Introduction

After more than ten years of development, three-dimensional (3D) X-ray diffraction (3DXRD) techniques now routinely provide orientation maps of polycrystalline materials. Far-field variants of 3DXRD give access to grain center of mass and orientation information in sample volumes containing up to thousands of grains. Employing two-dimensional diffraction detectors positioned some hundreds of millimeters behind the sample, they usually provide ample space for sample environment like stress rigs or furnaces and have been used for time-lapse studies of grain rotations (Margulies *et al.*, 2001), evolution of strain tensors during tensile loading (Martins *et al.*, 2004; Oddershede *et al.*, 2011) or for the observation of grain coarsening processes (Wu & Jensen, 2012). Near-field diffraction imaging techniques, on the other hand, employ high-resolution X-ray imaging detector systems and provide access to spatially resolved orientation maps and 3D grain morphologies. Since the diffracted beams have to be captured on a high-resolution screen positioned a few millimeters behind the sample position, severe space constraints apply to the design of the auxiliary sample environment in this case. For that reason, the majority of studies involving 3D grain mapping coupled with repeated observations of samples as they evolve as a function of strain (King *et al.*, 2008) or load cycles (Herbig *et al.*, 2011; King *et al.*, 2011) were conducted in such a way that the grain microstructure of the sample was

mapped without the auxiliary equipment first, whereas subsequent phase contrast observations at increasing levels of strain or fatigue cycles were performed at higher sample-to-detector distances, imposed by the size of the equipment. This procedure is not without problems since it requires 3D image registration of dissimilar volume data sets (phase contrast and diffraction contrast). The minimum distance imposed by the auxiliary equipment may also compromise the optimum settings, even for phase-sensitive imaging techniques (cracks may give rise to strong artifacts in edge-enhanced phase contrast imaging when working at too large propagation distances). A micro-mechanical testing device compatible with the space constraints imposed by diffraction imaging techniques would solve these problems and enable multi-modal observation such as holotomography (Cloetens *et al.*, 1999) and diffraction contrast tomography (Ludwig *et al.*, 2009*a*) during (interrupted) load tests whilst maintaining the loading conditions throughout the test, since no unmounting/remounting of the sample is required.

In this work we present a compact design for a tensile testing device and show first results obtained during a tensile test on an Al alloy sample. A combination of near-field diffraction imaging techniques was used to study the onset of plastic deformation in a sample made from a binary Al–Li alloy. As crystalline materials are strongly subject to strain localization either under monotonic or dynamic loading (Ewing & Humfrey, 1903), there is a renewed interest in non-destructive *in situ* analysis of strain fields and lattice rotations in bulk grains, using non-destructive characterization capabilities provided by hard-X-ray diffraction techniques. Indeed, strain localization has been studied by electron microscopy, scanning electron microscopy and electron back-scatter diffraction (Abuzaid *et al.*, 2012), and appears as a precursor and critical physical process in cracking. However, strain localization is intrinsically a 3D phenomenon, depending on the crystal orientation, the grain morphology and the grain neighborhood (Echlins *et al.*, 2015). With the combination of monochromatic synchrotron X-ray diffraction imaging techniques and tomographic reconstruction methods, these types of studies are now possible for bulk grains, in 3D (King *et al.*, 2010; Li *et al.*, 2012; Pokharel *et al.*, 2014).

3DXRD microscopes are now available at the ESRF, APS, Petra III, CHESS and SPring-8. Resolving local lattice orientations inside a crystal and/or determining average elastic strain tensors of individual grains inside a polycrystalline sample are non-trivial tasks, and several teams are working on different ways to tackle these problems. One can mention the work of Oddershede *et al.* (2011) at DTU, Denmark, of Suter *et al.* (2006; see also Li & Suter, 2013) at Carnegie Mellon and APS, of Miller *et al.* (2012) at Cornell and CHESS, of Bernier *et al.* (2011) at LLNL and Viganò *et al.* (2014) at the ESRF. Taking advantage of well established and optimized experimental setups, one can now consider four-dimensional (time-lapse) studies, capturing the evolution of the microstructure during a mechanical load test. Several near-field diffraction imaging studies have been performed to probe grain coarsening during grain growth or recrystallization (McKenna *et al.*, 2014), but performing a clean mechanical test without transferring the sample between an external load frame and the experiment is still challenging. For the purpose of tomographic imaging during a load test there are mainly two types of design providing full 360° visibility of the sample, as required for optimum imaging results. In the first case only the sample is rotating during the experiment, *e.g.* the micropress developed for bone studies at European Synchrotron Radiation Facility (ESRF) (Bleuet *et al.*, 2004) or the RAMS mechanical load frame with air bearings available at CHESS as described by Shade *et al.* (2015) or, alternatively, designs where the whole frame is rotating like that described by Buffière *et al.* (1999). The main drawback of these designs is that they are not especially suited to the more stringent space and weight constraints imposed by X-ray diffraction contrast tomography and topotomography. Indeed, during a DCT experiment one has to position the detector at distances comparable with the field of view of the detector, and for a topotomography experiment the entire tomographic sample stage has to be tilted (rocking curve scan) around a second axis, perpendicular to the beam and the tomographic rotation axis. Thus, a specific design is needed to enable repeated observations based on a combination of these near-field diffraction imaging techniques during a mechanical load test. In this paper we propose a design fully compatible with the 3DXRD microscope at the ESRF and fulfilling the above-mentioned requirements for four-dimensional observations including phase contrast tomography, diffraction contrast tomography and topotomography imaging modalities.

These four-dimensional studies are essential to validate micromechanical simulations. But while models are now capable of simulating some of the physical processes, capturing them within the bulk of polycrystalline microstructures is still very challenging. Recent works by Proudhon *et al.* (2016), Miller *et al.* (2008) and Oddershede *et al.* (2012) have shown the possibility of using initial microstructures as determined by 3DXRD techniques as input to predict the evolution of experimental microstructures upon loading. Comparison of these simulations with four-dimensional experimental observations provides unique possibilities for further refinement and optimization of the models used in the simulations.

2. Full-field diffraction imaging techniques for polycrystalline materials

Three-dimensional X-ray diffraction-based tomography techniques combine the classical tomographic approach [acquisition of a set of projection images at different angles, and reconstruction by suitable algorithms like filtered back-projection or algebraic approaches (Kak & Slaney, 1988)] and Bragg kinematical diffraction. Unlike in absorption micro-tomography (μCT) where contrasts arise from variations of the attenuation coefficient within the material, diffraction-based imaging techniques exploit Bragg diffraction signals from crystalline domains inside the material. Two of these methods are briefly reviewed in the following sections.

2.1. Diffraction contrast tomography

Diffraction contrast tomography (DCT) (Ludwig *et al.*, 2009*a*; Reischig *et al.*, 2013) is a variant of 3D X-ray diffraction (Poulsen, 2004), using an experimental setup identical to classical absorption micro-tomography. DCT is capable of providing the 3D grain shape, average orientation and elastic strain tensor for every grain of a polycrystal. However, some limitations exist in terms of texture, total number of grains and intragranular orientation spread of the grains which can be analyzed with this technique. Higher values for the combination of these parameters will promote diffraction spot overlap on the detector and will eventually lead to failure of the indexing procedure and not space-filling grain maps. Just like in conventional tomography, the sample is rotated around a single axis and illuminated by an extended, monochromatic beam as shown in Fig. 1. During the rotation, each grain will fulfill several times the Bragg condition, and the diffracted beams (hereafter called diffraction spots) can be recorded, segmented and indexed using automated analysis procedures developed at the ESRF (Ludwig *et al.*, 2009*b*; Reischig *et al.*, 2013). DCT has, for instance, been used to track grain growth processes in metals (Johnson *et al.*, 2012) and ceramics (Syha, 2014) and has been coupled with phase contrast tomography to observe the process of stress corrosion cracking (King *et al.*, 2008) and the propagation of fatigue cracks in metals (Herbig *et al.*, 2011; King *et al.*, 2011). A recently implemented six-dimensional extension of the reconstruction framework (Viganò *et al.*, 2014) now enables studies for moderately deformed materials and gives access to the local orientation within the grains (Viganò *et al.*, 2016*a*,*b*).

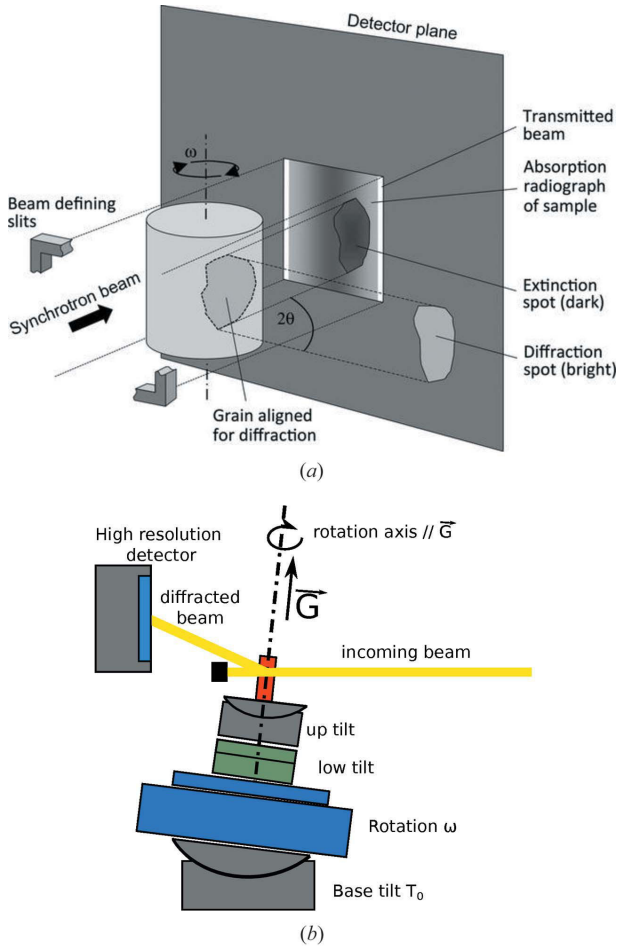

Figure 1
Schematic of a diffraction contrast tomography experiment (from Ludwig *et al.*, 2009*a*) (*a*) and of a topotomography experiment (updated from Ludwig *et al.*, 2007) (*b*).

2.2. Topotomography

In X-ray topography, a two-dimensional projection image of the 3D crystal is recorded on a high-resolution detector system. The technique is sensitive to local variations of the crystal orientation (or deviations from a perfect lattice) and can reveal defects like dislocations, slip bands and stacking faults in rather perfect crystals (Tanner, 1996). In X-ray topotomography, a crystal is mounted on a dedicated four-circle diffractometer stage (Fig. 1) and aligned such that the normal of a diffracting lattice plane (a reciprocal lattice vector $\underline{G}$) is parallel to the axis of the rotation stage and the grain is located in the center of rotation of the diffractometer stage. To put the grain in the diffraction condition, the tomographic rotation axis $\underline{\omega}$ is inclined by the Bragg angle θ by means of the base tilt goniometer T_0. At each rotation position ω a rocking scan covering the width of the crystal reflection curve is recorded by scanning this outer rotation axis [perpendicular to the plane of Fig. 1(*b*)]. By integrating these images of the rocking scan, one obtains a two-dimensional projection topograph of the diffracting grain. The 3D grain volumes of (undeformed) grains can be then reconstructed from a series of tomographic (ω) projection angles, using oblique angle algebraic reconstruction algorithms, available in the *ASTRA* toolbox (Palenstijn *et al.*, 2011).

This combination of X-ray topography and tomography can be used to extract qualitative information about the 3D arrangement of lattice defects like dislocations in single crystals (Ludwig *et al.*, 2001) and precipitates in metallic alloys (Ludwig *et al.*, 2007). Moreover, since the position of the diffraction spot does not change during rotation of a grain aligned for topotomography, one can 'zoom' on individual grains using an optimized optical configuration of the detector system or by placing magnifying X-ray optics in the diffracted beam (Simons *et al.*, 2015).

For structural materials, the combination of DCT and topotomography opens interesting new possibilities for detailed observations of individual grains and grain neighborhoods at the onset of plastic deformation. Defect structures like slip bands and kink bands in metallic alloys can be revealed due to topographic orientation contrast which becomes visible at favorable ω and θ rotation positions during the topotomographic scanning procedure. However, the four-circle diffractometer configuration required for topotomography puts some stringent requirements on the size and weight of the auxiliary sample environment which can be used for this purpose.

3. A new compact design compatible with synchrotron X-ray transmission and diffraction imaging

Generally speaking, integration of an auxiliary sample environment on a synchrotron beamline requires a device to observe severe space constraints, the space around the sample being crowded by detectors, cameras and motorized positioning stages. Geometrical constraints are even more severe for near-field diffraction experiments where the sample needs to be positioned a few millimeters from the high-resolution imaging detector and/or in the center of rotation of the instrument (topotomography). The design presented in the current work targets a tensile specimen, with a cross section typically around 0.5–1 mm^2.

Specifications were as follows:

(i) Tensile load up to 500 N.

(ii) Apply tensile cyclic load up to a frequency of 100 Hz.

(iii) Load measurement accuracy and stability of 1 N.

(iv) Compatibility with the ID11 diffractometer (*i.e.* maximum 63 mm height from the base plate to the sample position).

(v) The high-resolution imaging detector may approach the rotation center as close as 3 mm.

(vi) Allow 360° rotation for full visibility during tomographic scan acquisition.

A specifically modified piezoelectric actuator (from DSM, USA) was used to fulfill the space constraints imposed by the instrument (63 mm from the mounting interface to the sample/beam position). The actuator is based on a flexure design, has a maximum travel range of 500 µm and can carry up to 650 N of load. A cylindrical quartz tube is used as the load frame which takes place in a mechanical preloading system (fine thread with 0.5 mm pitch). The dog-bone-shaped samples are held in place by two cylindrical pins providing an auto-alignement feature with the steel shaft. The shaft was instrumented with a full Wheatstone bridge of semiconductor strain gauges (Texense, France). The strain gauge signal is amplified and conditioned (tunable gain and offset) to generate a 0–10 V signal over 12 bits. This custom load cell can be calibrated on the force range 0–500 N using a classical electromechanical tensile testing machine thanks to machined adaptor parts. Measured load precision and repeatability is 1 N. The actual displacement of the steel shaft is not precisely known and will vary as a function of applied voltage and the effective stiffness of the load chain formed by the metallic housing, quartz capillary, sample, steel shaft and piezoelectric actuator. The determination of the deformation has therefore to rely on digital image (or 3D volume) correlation techniques applied to the X-ray projections (or 3D volumes, respectively). This is further illustrated in §4.2.

The main benefits of using a 1 mm-thick amorphous quartz tube are related to full sample visibility over 360° rotation, the absence of diffraction peaks and its high stiffness and radiation hardness as compared with polymers. The homogeneity and constant absorption allow for high-quality tomographic reconstructions. The weak scattering from the amorphous quartz matrix gives rise to a constant background with smooth spatial variations, which can be easily substracted from the diffraction images.

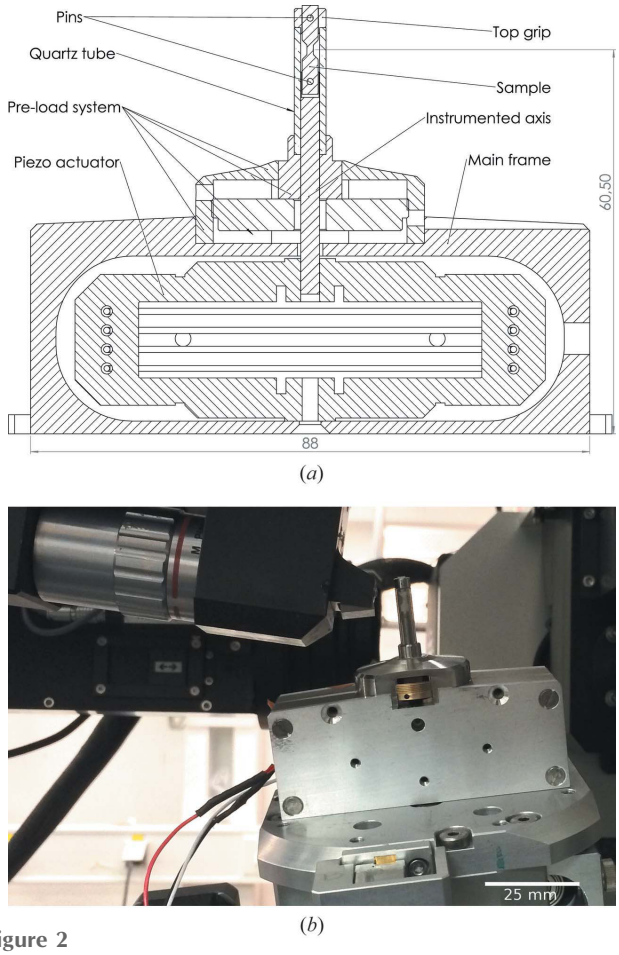

Figure 2
Schematic drawing of Nanox (*a*), and photograph of the device installed on the 3DXRD instrument at ID11, ESRF (*b*).

With the present design (see Fig. 2), the ID11 high-resolution detector systems can be as close as 2.6 mm to the center of rotation (0.1 mm from the quartz tube), thereby enabling high-spatial-resolution acquisitions with pixel size down to 0.7 µm.

4. Application to an *in situ* topotomography experiment on a Al–Li polycrystal

The Nanox device was tested successfully for a combined DCT and topotomography diffraction imaging experiment during the onset of plastic deformation in a binary Al–Li alloy.

4.1. Experimental setup

The experiment was performed at the ID11 beamline of the ESRF, France. An Al–Li 2.5 wt% multicrystal sample with 0.7 mm × 0.7 mm cross section was mounted in Nanox, itself mounted on the four-circle diffractometer. This instrument is installed in the third experimental hutch, situated at a distance of about 90 m from the in-vacuum undulator insertion device of the beamline. The X-ray beam was monochromated by a

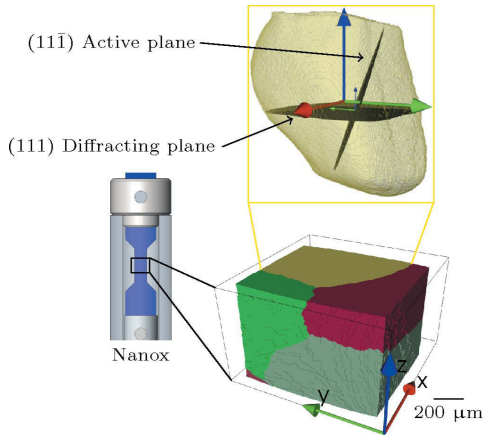

Figure 3
Bottom: 3D rendering of the multicrystal reconstructed by DCT (grain 1 is in yellow). Top: semi-transparent visualization of the outline of grain 1, as obtained from topotomography. The orientation of the diffracting lattice planes and the active slip plane are materialized in black.

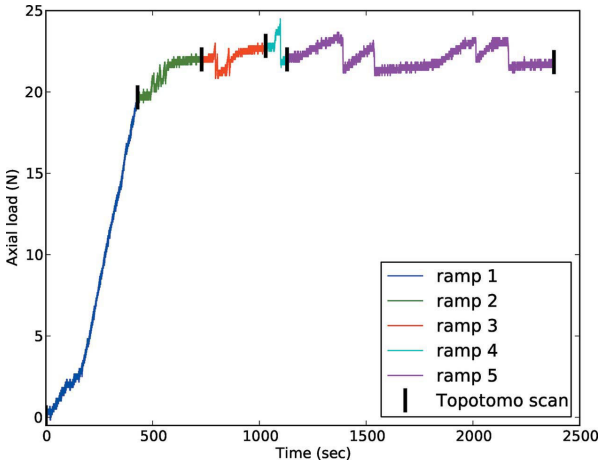

Figure 4
Load history of the sample. Each load ramp is represented by a different color, and the black lines indicate when topotomography scans were performed. For the sake of clarity, the constant load signal during acquisition of the topotomography scans has been removed. Note that ramp 5 itself is composed of four load ramps.

bent Laue–Laue Si 111 double-crystal monochromator delivering a relative bandwidth of about 3×10^{-3}. The energy was set to 41.8 keV.

The sample was carefully mounted into the device, to avoid any initial deformation, and a DCT scan, comprising 3600 equally spaced projections over 360°, was recorded before any loading. The diffraction images were recorded on a 2048 × 2048 pixel high-resolution detector system based on a 50 µm-thick transparent luminiscent screen made from GGG (Martin & Koch, 2006), optically coupled to an ESRF Frelon camera (Labiche *et al.*, 1996). The effective pixel size of this system was 1.5 µm.

Following the usual steps of diffraction spot segmentation, Friedel pair matching and indexing, the orientation and position of all grains in the illuminated sample volume were determined using the DCT analysis code (Ludwig *et al.*, 2009*b*) (Fig. 3, bottom). Knowing the orientation of the grains, it is then possible to calculate the list of reflections and associated diffractometer tilt angles for aligning these grains and reflections for subsequent characterization by topotomography. Here we selected a grain for which one of the reflections of the {111} family was accessible within the travel range (±20° and ±15° for the upper and the lower tilt motors, respectively) of the ID11 sample goniometer stages.[1] Once the diffraction vector was exactly aligned with the rotation axis of the tomography stage, the latter was inclined by the corresponding Bragg angle of $\theta = 3.66°$ and integrated projection topographs using the previously described scanning procedure (see §2.2) were recorded on a second high-resolution detector system, featuring 1040 × 1376 pixels and an effective pixel size of 0.65 m. The complete experiment was a repetition of the following routine:

(i) The displacement imposed on the sample was incremented by ramping up the voltage of the piezoelectric actuator in constant steps of 1 V (sensitivity: 1 V = 3.33 µm in unloaded condition). This corresponded to a deformation of about 0.22% in the gauge length of the sample. The load ramps were divided into 0.33 µm steps, applied while recording diffraction topographs at $\omega = 152°$ and the nominal Bragg angle.

(ii) The width of the reflection curve was updated[2] and a topotomography scan with 180 projections in ω, covering the full width of the reflection curve in equidistant intervals of 0.1° in θ, was recorded.

The orientation of the chosen grain resulted in sample goniometer tilt values of 12.95° and 10.68° to align the (111) plane normal collinear to the ω rotation axis of the instrument. The major part of the grain fulfills the diffraction condition at $\theta = -3.53°$. In total, five load ramps were performed covering both elastic and plastic regimes, as shown on Fig. 4. Observing the loading curve reveals strong instabilities during the load ramps after reaching the elastic limit at about 41 MPa, which is consistent with a critical resolved shear stress around 20 MPa as evaluated from the Taylor factor and the 67 MPa value for this alloy as measured by Rao & Ritchie (1992). Here the lower yield point is caused by the large grain number 1 which spread over the majority of the cross section, and is favorably oriented for slip (Schmid factor 0.43); see §5.

4.2. Inferring strain from image correlation

The measurement of macroscopic strain applied to the sample is a critical requirement for the conduction of micromechanical tests. Given the space constraints of the miniature design, we rely on the use of image correlation techniques in order to measure the elongation of the sample in the observation zone. In the simplest case, a virtual extensometer consisting of two absorbing objects [*e.g.* small Pb spheres

[1] Given these tilt ranges, most grains can only be aligned for a limited sub-set of *hkl* reflections.

[2] With increasing deformation, the orientation spread in the grain increases and the angular range of the rocking scan has to be enlarged in order to cover the full grain volume.

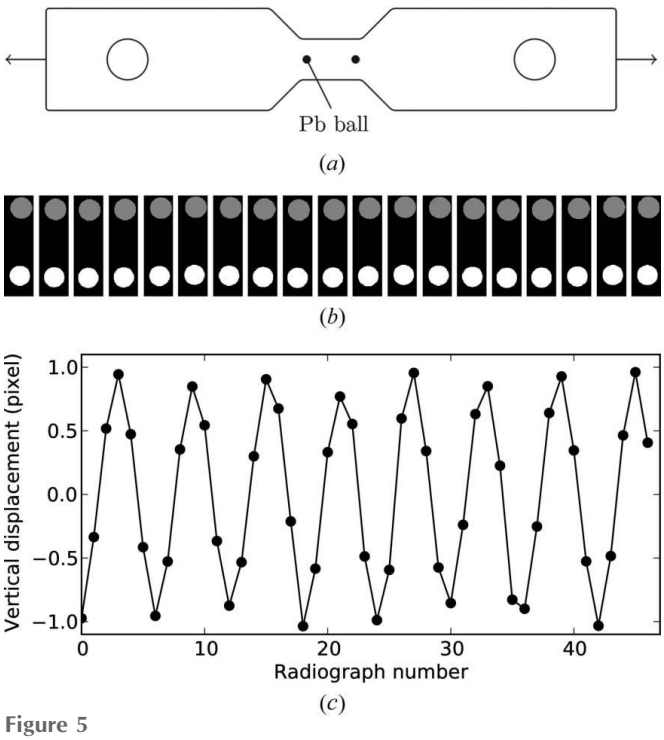

Figure 5
X-ray virtual extensometer. (*a*) Small 316LN tomographic sample with two 50 µm lead balls glued at each end of the gauge length. (*b*) A 100 N cyclic load is applied at 0.1 Hz; X-ray radiographs are recorded every 0.2 s and processed automatically. (*c*) Measured relative displacement in micrometers.

glued on the sample surface; see Fig. 5(*a*)] can be implemented. The relative position of these objects can be tracked by X-ray radiography as a function of applied load and time. The radiographs are automatically processed by a Python script, determining the center of mass position of the objects and computing the relative displacement (Fig. 5*b*). A test was performed with a 316LN steel sample mounted on the device, and one can use those values to verify the calibration of the system by calculating the apparent Young's modulus from the measured values for load and deformation. For instance, in the example presented here, the load was 100 N with a section of 0.45 mm × 0.45 mm. The measured displacement was 1.9 pixels over a gauge length of 769 pixels ($\varepsilon = 0.0025$), which results in a modulus of $E = 199$ GPa (Fig. 5*c*), very close to the known value for this material. These results allowed us to validate this method and generalize it to further experiments. If full tomographic scans are available at each deformation step, digital volume correlation would be a more advanced solution, if the material exhibits sufficient internal contrast (Réthoré *et al.*, 2008).

5. Results and analysis

In this section, ($\underline{X}$, $\underline{Y}$, $\underline{Z}$) refers to the orthogonal right-handed laboratory basis, $\underline{X}$ being along the X-ray beam and $\underline{Z}$ the vertical direction. {*hkl*}, (*hkl*) and [*hkl*] refer to plane families, plane normals and directions expressed in the crystal coordinate system with Millers indices, respectively.

5.1. Topographs

As seen in Fig. 6, in the first scan the grain exhibits only a small intragranular orientation spread (mosaicity) and this orientation spread is observed to increase with increasing levels of plastic deformation. Another interesting observation is the apparition and reinforcement of band-like topographic image contrast, best visible at favorable ω rotation positions, resulting in 'edge-on' projections of the active slip plane, as illustrated in Fig. 3 and in the supporting information. The topographs of Fig. 6 were recorded in this particular configuration. The inclination of these structures corresponds exactly to the projected trace of the $(11\bar{1})$ planes in the observed grain and that plane belongs to the slip system with

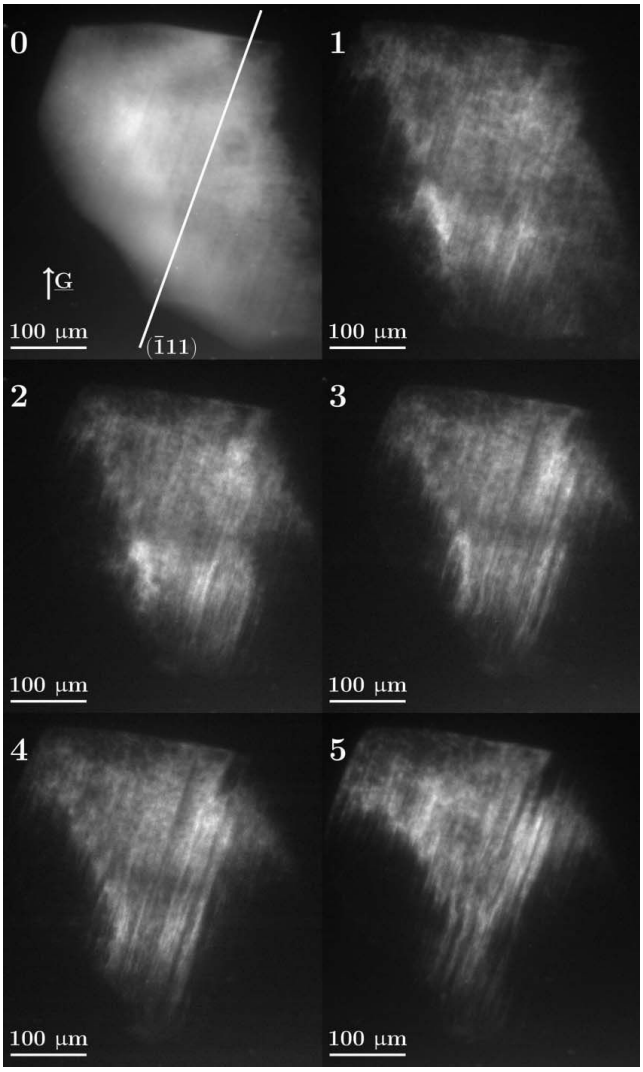

Figure 6
(111) projection Bragg topographs of grain 1 at $\omega = 152°$ and $\theta = 3.80°$ acquired at each load step. The band-like topographic contrast increases with the applied deformation and increasing subvolumes of the grain rotate out of the Bragg condition. The white line in topograph 0 materializes the intersection of the $(11\bar{1})$ lattice plane with the detector. For this specific ω rotation, this plane is imaged 'edge-on' to the detector screen.

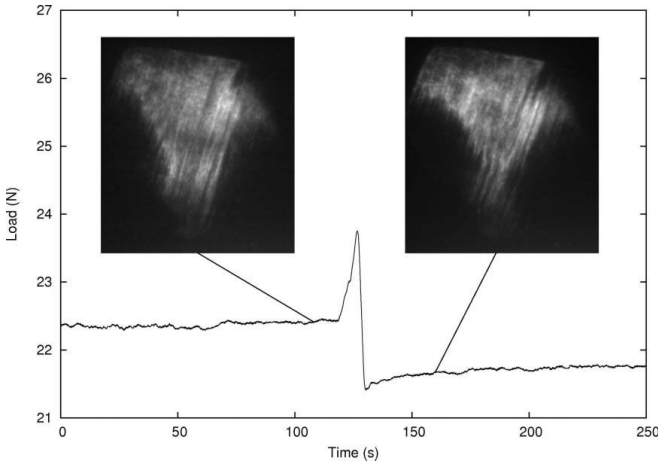

Figure 7
Evolution of the load during the fifth load ramp, and two Bragg topographs at $\omega = 152^\circ$ and $\theta = 3.80^\circ$.

the highest Schmid factor, and should therefore be the most easily activated one.

Monitoring these topographic contrasts during the actual load ramp reveals another interesting phenomenon: as the load increases, nothing appears to happen, but at one moment the load decreases suddenly by 0.5 N, and at the same time a large part of the grain is no longer in the diffraction condition; see Fig. 7. This could very well be direct evidence of a 'Portevin–Le Chatelier'-like effect due to plastic instabilities, and the extinction of the grain is probably due to a spatial rearrangement of dislocation structures, inducing rotation of part of the grain volume.

5.1.1. Reconstructed volume. At initial stages of deformation, a large fraction of the grain volume occupies a small volume in orientation space, and, for a perfectly aligned setup, this undeformed part of the grain volume would fulfill the Bragg condition at the same base tilt value $\theta_{\rm Bragg}$ for each of the ω rotation positions. In practice, the plastic deformation and rigid body rotations of the sample upon loading result in a precession of the scattering vector associated with this part of the grain volume around the rotation axis. The highest intensity for a given ω is thus observed at different values of θ which in turn vary as $\sin(\omega)$. This slight misalignment ($\sim 0.15^\circ$) between the rotation axis and the scattering vector has been accounted for in the reconstruction process. As described by Ludwig *et al.* (2001), topographs were corrected to improve the quality of the reconstruction, by correcting pixel values for constant background. The 3D reconstruction of the main intensity was performed using the *ASTRA* toolbox (Palenstijn *et al.*, 2011), which can handle arbitrary projection geometries, like the one encountered in topotomography, where the rotation axis is not perpendicular to the directions of the incoming or diffracted beams.

[3] The slip system $(11\bar{1})[011]$ has a Schmid factor of 0.43, the highest for the {111} family of this grain.

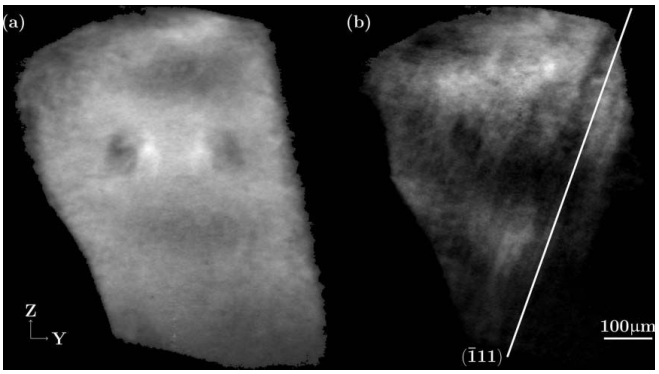

Figure 8
Reconstructed *YZ* slices of the volume, (*a*) before loading, (*b*) after the five load ramps.

The reconstructed grain volumes before deformation and after five load ramps are shown in Fig. 8. The deformed volume exhibits band-like contrast parallel to the trace of the $(11\bar{1})$ plane, in accordance with the observation in the topographs. Since the reconstruction is based on partially integrated topographs (*i.e.* the image with maximum intensity in the rocking-curve scan), larger parts of the grain, corresponding to subvolumes misoriented by more than 0.1°, are no longer reconstructed.

5.1.2. Rocking curves. The four-dimensional topotomography experiment consists of taking images of the grain of interest at different ω and θ values for different load (σ) states. The amount of diffracted photons for a given triplet (θ, ω, σ) is proportional to the subvolume of the grain fulfilling the Bragg condition, and could be represented as a scalar value I, the integrated intensity over the detector range. The width of the $I = f(\theta)$ curve for a given (ω, σ) position is a measure of the quality of a crystal (Lübbert *et al.*, 2000). Contrary to far-field measurements, one cannot directly extract 3D maps or 2D projections of the reciprocal space intensity distribution from images acquired with the near-field acquisition geometry described in this work.[4] On the other hand, the near-field diffraction imaging described in this article allows for direct identification of the active slip system from the topographic (orientation) contrast, visible in a sub-set of the projection images. Note that the visibility of this contrast varies as a function of the rotation angle[5] and reaches a maximum for ω rotation positions close to the 'edge-on' configuration depicted in Fig. 3.

We propose a simplified analysis, whereby plotting the full width at 10% of the maximum of the reflection curves as a function of ω we determine the convex hull of the reciprocal space intensity distribution (integrated along the strain

[4] One could envisage the reconstruction of 2D projections from a series of integrated near-field intensity profiles $I(\theta)$ acquired at different ω rotation positions. This leads to an inverse problem, similar to the one of image reconstruction from projections, and has not been further considered in this work.

[5] The lattice rotation giving rise to this orientation contrast may very well be linked to the presence and accumulation of dislocations on different slip systems, interacting and piling up in the vicinity of the band structures created by the dominant system.

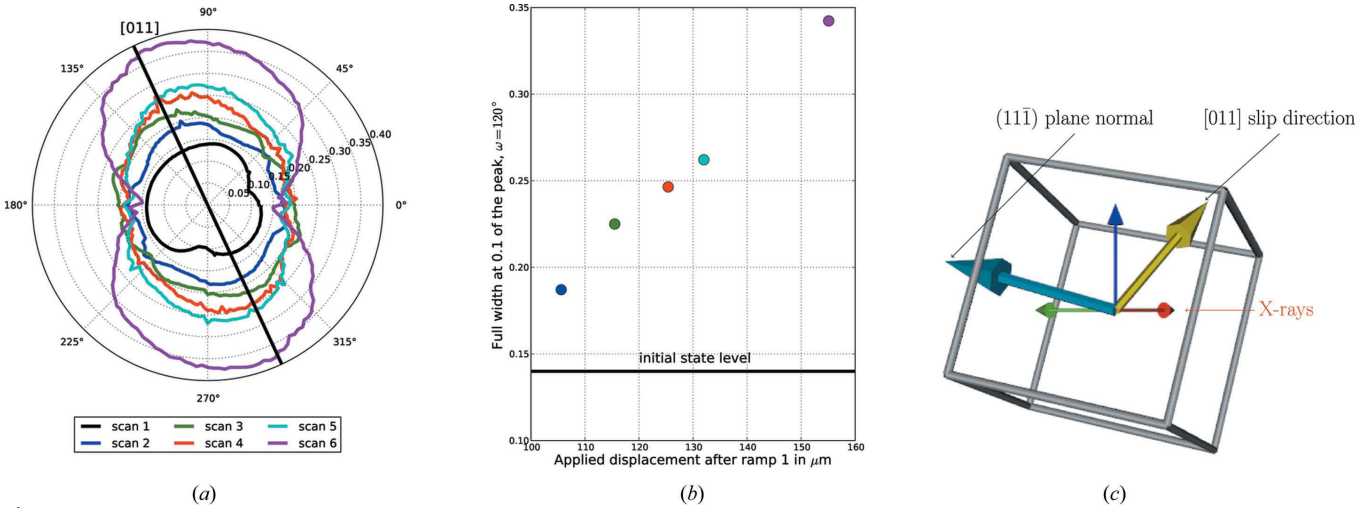

(*a*) (*b*) (*c*)

Figure 9
(*a*) Full width at 10% maximum as a function of ω and of the scan. The black line indicates when the [011] direction of the crystal is within the XZ plane. (*b*) Width evolution at $\omega = 120^\circ$ as a function of the scan. (*c*) Crystal configuration at $\omega = 120^\circ$. $\underline{X}$ is along the beam while $\underline{Y}$ is along the base tilt axis $\underline{T}_0$. The beam direction, the vertical direction and the slip direction (yellow arrow) are coplanar.

direction). The resulting contours have an elliptical shape and are plotted for each ω and each load state in Fig. 9. The ellipsis tends to widen in a specific direction (at a preferential ω value). This ω value corresponds to the configuration where the slip direction $\underline{d}$ lies in the plane ($\underline{X}$; $\underline{Z}$), being the direction of the incoming X-rays beam, and $\underline{Z}$ being the vertical axis. In other words, at this particular ω, the slip direction $\underline{d}$ of the active slip system is included in the ($\underline{k}_i$; $\underline{G}$) plane, with $\underline{k}_i$ the incoming beam direction and $\underline{G}$ the reciprocal lattice vector. This widening of the ellipsis shows a continuous increase when plotted in this particular direction (Fig. 9). In this plot, the initial 100 m displacement corresponds to the clearance of the mechanical play between the specimen and the loading pins.

The width of the rocking curves is directly linked to the mosaicity in the crystal. As the load increases, dislocation densities increase too, both at grain boundaries to accommodate the strain and in the grain bulk (dislocation forest and dislocations pile-ups). Stress fields around these dislocations structures generate crystal rotations, which modify locally diffraction conditions as explained by Hull & Bacon (1984). Depending on the type (screw or edge) and the Burger's vector of the dislocation, the impact on fulfilling Bragg's law will not be equivalent. An edge dislocation will bend the crystal, and generate a lattice rotation field, around its line vector. The widening of the rocking curve along the [011] direction observed in Fig. 9 could be seen as an indirect observation of a pile-up of edge dislocations with the Burger's vector perpendicular to this [011] slip direction.

6. Discussion

As diffraction imaging techniques give access to the 3D grain microstructure at the micrometer length scale, it is possible to create realistic meshes of polycrystalline microstructures as encountered in common structural materials like metals and their alloys. Combining real microstructure (image) based numerical computations and four-dimensional observations of the same microstructure evolving as a function of strain or temperature offers unique possibilities to corroborate predictions from material models like crystal plasticity or phase field. Note that conventional 3D observations based on destructive serial sectioning techniques can only provide a snapshot of the state of the sample at a given time. Regarding plastic deformation of polycrystalline aggregates, it is well known that misorientations between grains lead to strain incompatibilities and result in a complex heterogeneous response of the material to mechanical loading (Ashby, 1970). Access to local crystallographic orientation would allow advanced models of material constitutive behavior to be tested and validated, like strain-gradient plasticity (Forest & Guéninchault, 2013), where dislocations densities are linked to the local lattice rotations (Nye, 1953). Moreover, if the microstructure provides sufficient contrast in the reconstructed tomographic image, the crystallographic information can be complemented with 3D deformation fields, *via* digital volume correlation. Using phase-sensitive imaging techniques, one can also follow the evolution of damage (porosity, cracks) and again these observations can be compared with model predictions. Last, mechanical computations could be used to constrain the solution space and to improve the quality of the tomographic reconstruction in diffraction experiments.

More efforts are needed to increase experimental capabilities to directly compare with simulations of crystal deformations. Indeed, the latter can routinely compute both local and global variables (*e.g.* average stress tensor of a grain and local stresses inside the grain), whereas it is currently possible to access the local (intragranular) strain and stress variations with the help of full-field diffraction imaging techniques.[6]

[6] Polychromatic and monochromatic scanning microdiffraction techniques can provide access to this type of information but currently involve acquisition times which are incompatible with *in situ* studies of extended 3D sample volumes.

7. Conclusion

We have presented a compact design for a miniature tensile stress rig, compatible with the space and weight constraints imposed by near-field diffraction imaging techniques. The device can carry tensile loads up to 500 N and is driven by a piezoelectric actuator which can work in a static and dynamic regime up to frequencies of 100 Hz.

The design allows for minimum sample-to-detector distances of 2.6 mm and to position the sample in the center of rotation of the four-circle 3DXRD instrument at beamline ID11. Whereas the former is a prerequisite for full-field grain mapping in small grained materials (10–30 µm), the latter allows for observations of individual grains and grain neighborhoods by means of topotomography, revealing the early stages of plastic activity and associated diffraction peak broadening. The capacity to combine diffraction contrast tomography (3D mapping of grain microstructure), topotomography (high-resolution mapping of individual grains, localized plastic activity, peak broadening) and holotomography (internal surfaces, crack initiation) on the same instrument and without unmounting the sample opens new perspectives for studying the early stages of plasticity and damage in polycrystalline materials (*e.g.* formation of persistent slip bands).

As an illustration of the combined multi-modal observation capabilities of the device, we present *in situ* observations of plastic instabilities, slip band formation and diffraction peak broadening at increasing levels of tensile strain in a selected grain of a grain-mapped multicrystal prepared from Al 2.5 wt%–Li alloy.

Acknowledgements

The ESRF and staff at beamline ID11 are acknowledged for providing beam time and technical assistance during the experiment. We thank Pascal Bernard for providing precious knowledge and advice for the design of the device.

References

Abuzaid, W. Z., Sangid, M. D., Carroll, J. D., Sehitoglu, H. & Lambros, J. (2012). *J. Mech. Phys. Solids*, **60**, 1201–1220.
Ashby, M. (1970). *Philos. Mag.* **21**, 399–424.
Bernier, J., Barton, N., Lienert, U. & Miller, M. (2011). *J. Strain Anal. Engin. Des.* **46**, 527–547,
Bleuet, P., Roux, J.-P., Dabin, Y. & Boivin, G. (2004). *Optical Science and Technology, SPIE 49th Annual Meeting*, pp. 129–136. International Society for Optics and Photonics.
Buffière, J.-Y., Maire, E., Cloetens, P., Lormand, G. & Fougères, R. (1999). *Acta Mater.* **47**, 1613–1625.
Cloetens, P., Ludwig, W., Baruchel, J., Van Dyck, D., Van Landuyt, J., Guigay, J. P. & Schlenker, M. (1999). *Appl. Phys. Lett.* **75**, 2912–2914.
Echlins, M. P., Straw, M., Randolph, S., Filevich, J. & Pollock, T. M. (2015). *Mater. Charact.* **100**, 1–12.
Ewing, J. A. & Humfrey, J. C. W. (1903). *Philos. Trans. R. Soc. London. Ser. A*, **200**, 241–250.
Forest, S. & Guéninchault, N. (2013). *Acta Mech. Sin.* **29**, 763–772.
Herbig, M., King, A., Reischig, P., Proudhon, H., Lauridsen, E. M., Marrow, J., Buffière, J.-Y. & Ludwig, W. (2011). *Acta Mater.* **59**, 590–601.
Hull, D. & Bacon, D. J. (1984). *Introduction to Dislocations.* Oxford: Pergamon Press.
Johnson, A., Poulsen, S., King, A., Ludwig, W., Rule, D., Patterson, B., Voorhees, P. & Lauridsen, E. (2012). *2012 TMS Annual Meeting and Exhibition*, 11–15 March 2012, Orlando, FL, USA.
Kak, A. C. & Slaney, M. (1988). *Principles of Computerized Tomographic Imaging.* New York: IEEE Press.
King, A., Johnson, G., Engelberg, D., Ludwig, W. & Marrow, J. (2008). *Science*, **321**, 382–385.
King, A., Ludwig, W., Herbig, M., Buffière, J.-Y., Khan, A., Stevens, N. & Marrow, T. (2011). *Acta Mater.* **59**, 6761–6771.
King, A., Reischig, P., Martin, S., Fonseca, J. F., Preuss, M. & Ludwig, W. (2010). *31st Risø International Symposium on Materials Science: Challenges in materials science and possibilities in 3D and 4D characterization techniques.*, Roskilde, Denmark.
Labiche, J. C., Segura-Puchades, J., Van Brussel, D. & Moy, J. P. (1996). *ESRF Newsl.* **25**, 41–43.
Li, S. F., Lind, J., Hefferan, C. M., Pokharel, R., Lienert, U., Rollett, A. D. & Suter, R. M. (2012). *J. Appl. Cryst.* **45**, 1098–1108.
Li, S. F. & Suter, R. M. (2013). *J. Appl. Cryst.* **46**, 512–524.
Lübbert, D., Baumbach, T., Härtwig, J., Boller, E. & Pernot, E. (2000). *Nucl. Instrum. Methods Phys. Res. B*, **160**, 521–527.
Ludwig, W., Cloetens, P., Härtwig, J., Baruchel, J., Hamelin, B. & Bastie, P. (2001). *J. Appl. Cryst.* **34**, 602–607.
Ludwig, W., King, A., Reischig, P., Herbig, M., Lauridsen, E., Schmidt, S., Proudhon, H., Forest, S., Cloetens, P., du Roscoat, S. R., Buffière, J., Marrow, T. & Poulsen, H. (2009*a*). *Mater. Sci. Eng. A*, **524**, 69–76.
Ludwig, W., Lauridsen, E. M., Schmidt, S., Poulsen, H. F. & Baruchel, J. (2007). *J. Appl. Cryst.* **40**, 905–911.
Ludwig, W., Reischig, P., King, A., Herbig, M., Lauridsen, E., Johnson, G., Marrow, T. & Buffière, J.-Y. (2009*b*). *Rev. Sci. Instrum.* **80**, 033905.
McKenna, I., Poulsen, S., Lauridsen, E., Ludwig, W. & Voorhees, P. (2014). *Acta Mater.* **78**, 125–134.
Margulies, L., Winther, G. & Poulsen, H. F. (2001). *Science*, **291**, 2392–2394.
Martin, T. & Koch, A. (2006). *J. Synchrotron Rad.* **13**, 180–194.
Martins, R. V., Margulies, L., Schmidt, S., Poulsen, H. F. & Leffers, T. (2004). *Mater. Sci. Eng. A*, **387–389**, 84–88.
Miller, M., Park, J.-S., Dawson, P. & Han, T.-S. (2008). *Acta Mater.* **56**, 3927–3939.
Miller, M. P., Suter, R. M., Lienert, U., Beaudoin, A. J., Fontes, E., Almer, J. & Schuren, J. C. (2012). *Synchrotron Radiat. News*, **25**, 18–26.
Nye, J. (1953). *Acta Metall.* **1**, 153–162.
Oddershede, J., Camin, B., Schmidt, S., Mikkelsen, L. P., Sørensen, H. O., Lienert, U., Poulsen, H. F. & Reimers, W. (2012). *Acta Mater.* **60**, 3570–3580.
Oddershede, J., Schmidt, S., Poulsen, H. F., Margulies, L., Wright, J., Moscicki, M., Reimers, W. & Winther, G. (2011). *Mater. Charact.* **62**, 651–660.
Palenstijn, W., Batenburg, K. & Sijbers, J. (2011). *J. Struct. Biol.* **176**, 250–253.
Pokharel, R., Lind, J., Kanjarla, A. K., Lebensohn, R. A., Li, S. F., Kenesei, P., Suter, R. M. & Rollett, A. D. (2014). *Annu. Rev. Condens. Matter Phys.* **5**, 317–346.
Poulsen, H. F. (2004). *Three-Dimensional X-ray Diffraction Microscopy: Mapping Polycrystals and their Dynamics*, Vol. 205 of *Springer Series Tracts in Modern Physics.* Berlin: Springer.
Proudhon, H., Li, J., Wang, F., Roos, A., Chiaruttini, V. & Forest, S. (2016). *Int. J. Fatigue*, **82**, 238–246.
Rao, K. V. & Ritchie, R. (1992). *Intl Mater. Rev.* **37**, 153–186.
Reischig, P., King, A., Nervo, L., Viganó, N., Guilhem, Y., Palenstijn, W. J., Batenburg, K. J., Preuss, M. & Ludwig, W. (2013). *J. Appl. Cryst.* **46**, 297–311.
Réthoré, J., Tinnes, J.-P., Roux, S., Buffière, J.-Y. & Hild, F. (2008). *CR Mécan.* **336**, 643–649.

Shade, P. A., Blank, B., Schuren, J. C., Turner, T. J., Kenesei, P., Goetze, K., Suter, R. M., Bernier, J. V., Li, S. F., Lind, J., Lienert, U. & Almer, J. (2015). *Rev. Sci. Instrum.* **86**, 093902.
Simons, H., King, A., Ludwig, W., Detlefs, C., Pantleon, W., Schmidt, S., Snigireva, I., Snigirev, A. & Poulsen, H. F. (2015). *Nat. Commun.* **6**, 6098.
Suter, R., Hennessy, D., Xiao, C. & Lienert, U. (2006). *Rev. Sci. Instrum.* **77**, 123905.
Syha, M. (2014). Dissertation. Karlsruher Institut für Technologie, Germany.
Tanner, B. (1996). *X-ray and Neutron Dynamical Diffraction*, pp. 147–166. Berlin: Springer.
Viganò, N., Ludwig, W. & Batenburg, K. J. (2014). *J. Appl. Cryst.* **47**, 1826–1840.
Viganò, N., Nervo, L., Valzania, L., Singh, G., Preuss, M., Batenburg, K. J. & Ludwig, W. (2016*a*). *J. Appl. Cryst.* **49**, 544–555.
Viganò, N., Tanguy, A., Hallais, S., Dimanov, A., Bornert, M., Batenburg, K. J. & Ludwig, W. (2016*b*). *Sci. Rep.* **6**, 20618.
Wu, G. & Jensen, D. J. (2012). *Philos. Mag.* **92**, 3381–3391.

Chapter 3

Experimental observations of the early stages of plasticity by synchrotron X-ray insitu topotomography

Une étude expérimentale en volume des premiers stades de la plasticité a été menée a l'ESRF. La cartographie 3D de la microstructure a été obtenue par tomographie par contraste de diffraction, et un agrégat de trois grains dans le volume de l'échantillon a été choisi comme région d'intérêt pour des observation 4D par topotomographie. L'apparition des premières bandes de glissement en volume et leur évolution au cours du chargement ont été observées le long de plans cristallographiques bien définis. Les trois grains ont montré une activité plastique le long de deux familles de plans différents, pas toujours en accord avec une analyse macroscopique du facteur de Schmid, ce qui est attribué à l'influence du voisinage sur l'activation des systèmes de glissement. Les changements d'amplitude et d'orientation de la courbure moyenne des grains ont été mesurés avec un niveau de détail sans précédent, par une analyse tridimensionnelle des courbes de reflexions.

3.1 Introduction: Goal and overview of the experiment

The concept here (summarized in Fig. 3.1) is to use the information provided by a first DCT scan in the initial undeformedstate to analyze the microstructure on the fly and choose a set of grains to perform several series of topotomographic (TT) scans during an interrupted tensile test. The DCT scan provides the full grain map of the sample while TT scans provide a more detailed insight into the bulk of selected grains. The interest of the DCT scan in the initial state is twofold. First, this data is needed as an input to calculate which reflections are accessible for alignment in topotomography (the tilt motors used for the topotomographic alignment have a limited range of motion). Second, it is the main input to perform 3D CPFEM calculations, as exposed in Chap. 4.

3.1.1 The experimental setup

The ma2285 experiment was carried out in November 2014 at the materials science beamline (ID11) at the ESRF. An Al-Li 2.5 % wt. sample with dimensions exposed in Fig. 3.2 was carefully mounted in the Nanox device (item 0 in Fig. 3.1). The hour-glass shaped cross section (down to $0.25\,\mathrm{mm}^2$) allows to define precisely the region of interest. This sample geometry induces a small stress concentration in the middle of the gage length and ensures that the first plastic events will occur in the observed region. The light source is an in-vacuum undulator, and the beam is focused by an in-vacuum transfocator [Vaughan et al., 2011]. The distance between the source and the sample is $94\,\mathrm{m}$. The diffractometer depicted in Fig. 2.7 and in Sec. 2.4 has been used for this combined diffraction imaging experiment. The beam energy was set to $40\,\mathrm{keV}$ ($0.309\,95\,$Å) thanks to the bent Laue-Laue Si 111 double crystal monochromator. The relative bandwidth delivered was about 3×10^{-3}.

3.1.2 Sequence of the experiment

As explained previously, the experiment was split into two parts. First, a 3D characterization of the complete microstructure of the gage length was carried out by DCT (item 1 in Fig. 3.1). The reconstructed volume and the analysis of the sample microstructure in terms of grain size are presented later in Sec. 3.2. The camera used for the DCT scans was a Frelon Atmel 2k with an objective-revolver as presented in [Douissard et al., 2012]. A $10\times$ Olympus objective was placed behind the $50\,\mu\mathrm{m}$ thick GGG luminescent screen yielding to an effective pixel size of $1.4\,\mu\mathrm{m}$. Three different and partly overlapping DCT scans were

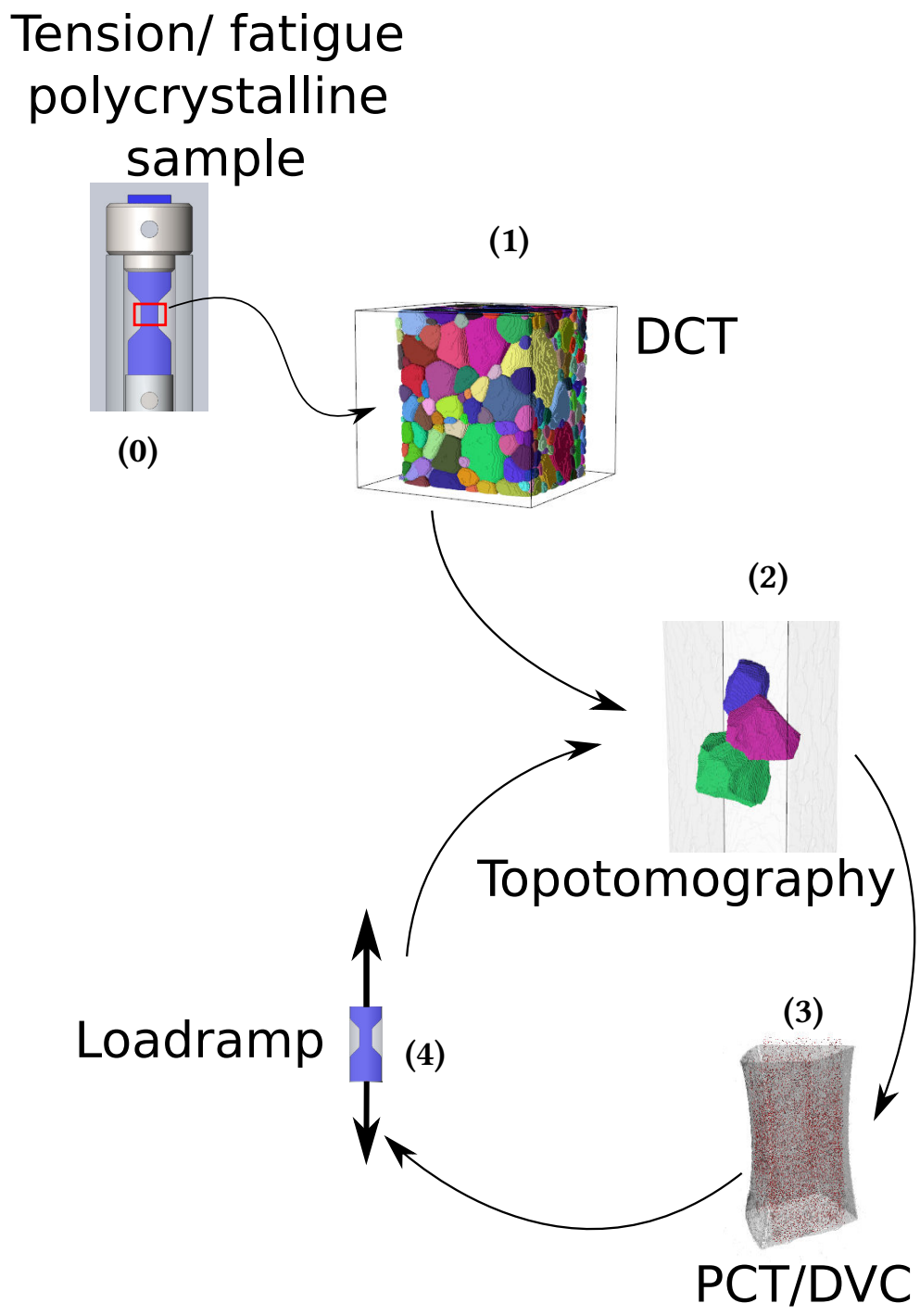

Figure 3.1 – Sequence of the ma2285 experiment. After being mounted into the nanox device (0), a series of 3DCT scan is performed (1). Then 13 cycles of (2) topotomography scans applied to a three grains cluster, (3) phase contrast tomography scan, followed by a (4) small increment of load were executed.

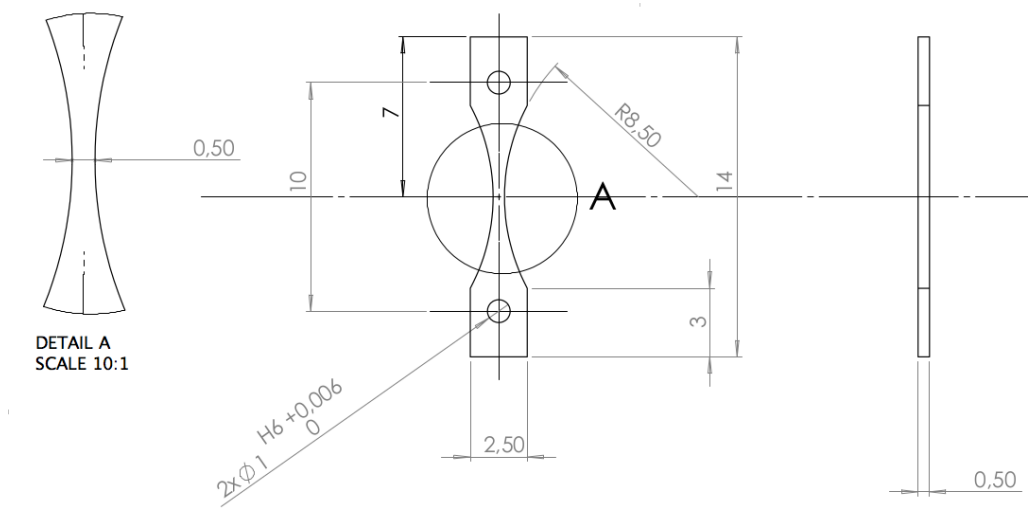

Figure 3.2 – Geometry of the sample used during the ma2285 experiment.

performed, with 3600 projections integrated over $0.1°$ and with an exposure time for each image of $300\,\mathrm{ms}$. The resulting acquisition time per scan was 1 h.

From the knowledge of the grain positions and orientations, it was possible to select three neighboring grains forming a small cluster, within the bulk of the sample. These grains were selected because it was possible to align the scattering vector of one of their reflections with the ω tomographic rotation axis. The selected reflexions and the tilts required for alignment of those reflections are presented in Tab. 3.3. Images were taken at different Θ positions of the base tilt motor to scan the rocking curve, every $\omega = 4°$. The same type of CCD camera as detailed above was used, with a $2\times$ magnification eyepiece, and an Olympus $10\times$ objective for a final pixel size of $0.7\,\mu\mathrm{m}$. The frame transfer mode of the camera was used, where only half of the pixels were read, the second half serving as a memory buffer. A black mask was put directly onto the CCD sensor to avoid illumination of this buffer by diffracted beams which would corrupt the data. In this mode, the readout time is reduced to $4\,\mu\mathrm{s}$, and allows for continuous scans with almost perfect integration instead of going forth and back each time to integrate over a small range of Θ. It is important to note that after each loading sequence, the angular range of the rocking curve had to be increased to capture the whole orientation spread of the grains.

Matlab routines were written to automate the process. First, rough rocking curves were taken at 4 different ω values ($\omega = \{0°, 22°, 45°, 67°\}$), to determine the ideal limit values of the base tilt for a given grain and a given scan. Due to the increasing deformation applied on the sample, topotomography scans (item 2 in Fig. 3.1) were ranged from 900 images (10 different Θ positions with $\Delta\Theta =$

$0.0056°$) to 9270 images (103 different Θ positions with $\Delta\Theta = 0.011°$). Each image was integrated during approximately $110\,\mathrm{ms}$.

After each topotomographic scan series of the cluster, a phase contrast tomography (PCT) scan with $0.7\,\mu\mathrm{m}$ effective pixel size with a binning of 2×2 (item 3 in Fig. 3.1) is performed. Surface features can be used as a virtual extensometer as exposed in Chap. 2. But here, instead, very small pores close to the surface of the sample will be used (see Sec. 3.1.3) as a natural speckle for digital volume correlation (DVC) over the scanned volume with a total height of $1.4\,\mathrm{mm}$.

Scan number	0	1	2	3	7	10	12	14	17	18	19	20	21	23
Color														

Table 3.1 – Color code used to identify the topotomographic scans.

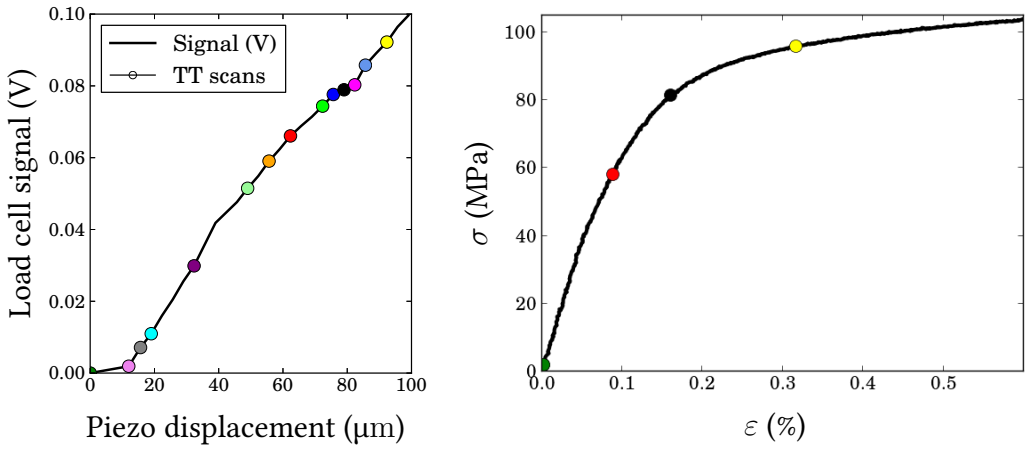

Figure 3.3 – Acquired load cell signal during the experiment as a function of displacement applied (left). The dots show where topotomography scans were recorded for all 3 grains. Macroscopic tensile curve of a macroscopic sample (right). The 4 dots were placed in function of the applied strain measured by DVC.

After steps (2) and (3), a loadramp was applied to the sample (4). As the piezo-actuator displacement is a linear function[1] of the imposed voltage, it was

[1] $150\,\mathrm{V}$ corresponds to $500\,\mu\mathrm{m}$ in the absence of external load

possible to control the displacement applied to the sample through the beamline control system[2] (SPEC) and completely automate the (2)-(3)-(4) series. The load versus displacement curve of the experiment is presented in Fig. 3.3. It shows clearly that most of the first loadramp displacement was used to clear the settling of the sample in the system. In the end it turned out that the load measurements appeared to be not reliable and the different loading series are identified by a specific color, as depicted in Tab. 3.1.

3.1.3 Displacement fields measurements by Digital Volume Correlation (DVC)

The analysis has been carried out by Clément Jailin, PhD student at LMT Cachan. To measure the displacement applied the sample, digital volume correlation (DVC) has been used. It uses the very small pores present in the sample (represented in red in Fig. 3.1 as a natural speckle. The DVC analysis has been carried out using an algorithm developed by the team of Pr. Roux from LTM Cachan. It uses a regularization by finite elements as in [Hild et al., 2011, Bouterf et al., 2014] called Global DVC.

The results shown in Tab. 3.2 show the average axial strain applied to the sample gage length. For that, the displacements measured by DVC on the tomographic reconstructions were averaged over the top and the bottom facet and divided by $l_0 = 1.4\,\mathrm{mm}$. In Fig. 3.3 (right), the strain measurements obtained via DVC on the miniature synchrotron sample are represented as dots on a (ε, σ) curve obtained by a macroscopic tensile test presented in Fig. 4.6.

Scan number	0	14	18	23
Applied strain	0	8.87×10^{-4}	1.61×10^{-3}	3.17×10^{-3}

Table 3.2 – Mean applied strain as measured by the digital volume correlation.

[2]The piezo-actuator of nanox behaves like any other motor of the beamline in this case.

3.2 Pre-characterization by DCT

Three different DCT scans were carried out, to reconstruct the full gage length of the sample. For each scan, the area illuminated by the beam was $870\,\mu m$ wide and $580\,\mu m$ high. The sample stage was moved by about $500\,\mu m$ between each scan, ensuring sufficient overlap to prevent any mismatch of the final merged reconstructed data. The grains belonging to two different scans were identified using a criterion based on both the grain orientation and the grain position. these grains were renumbered giving the priority to the numbering of the central scan. The merged data of the three different scans is presented in Fig 3.4. 737 different grains were reconstructed and the merged 3D data set had a dimension of $400 \times 435 \times 1122$ voxels.

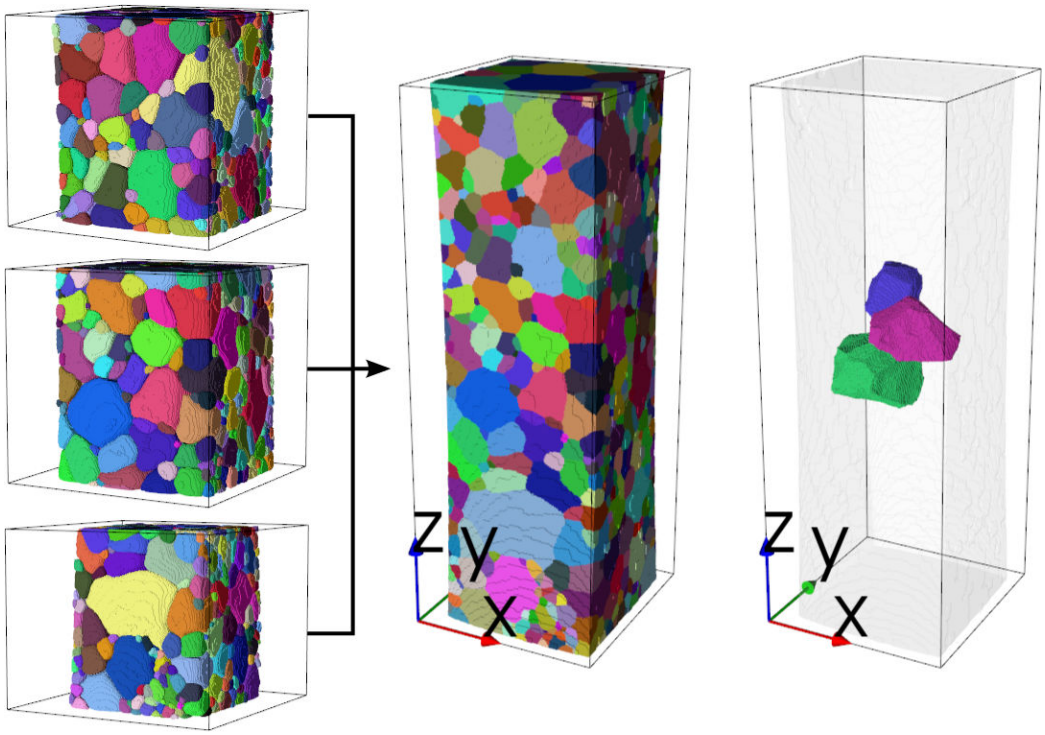

Figure 3.4 – 3D rendering of the reconstruction of the DCT scans. The three (top, center, bottom) volumes were scanned independently (left), and merged to constitute the "Sam8" sample (middle). The three grains cluster characterized by repeated tomographic scans is represented on the right, green, pink, and purple voxels denote respectively grain 4, 10 and 18.

The sample exhibits two different populations of grains. The 140 bigger grains (17.6% of the population) represent almost 90% of the volume (see Fig. 3.5). It is interesting to note that the large grains are located within the bulk of the

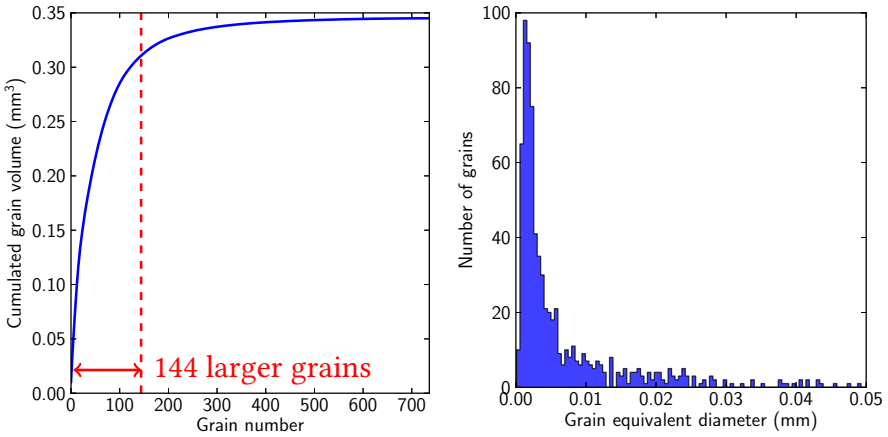

Figure 3.5 – Cumulated grain volume versus grain number (grains are numbered by their size from the largest to the smallest). The larger grain population is indicated in red (left). Histogram of the equivalent grain diameter (right).

sample, whereas the smaller ones are mostly located at the surface of the sample (Fig. 3.6).This can be explained by the specimen preparation process mentioned in Sec. 2.2.4, i.e. higher deformation on the surface due to machining lead to more recrystallization germs, and to a strong variability in the grain size. The material does not exhibit any particular texture, for both populations (Fig. 3.7).

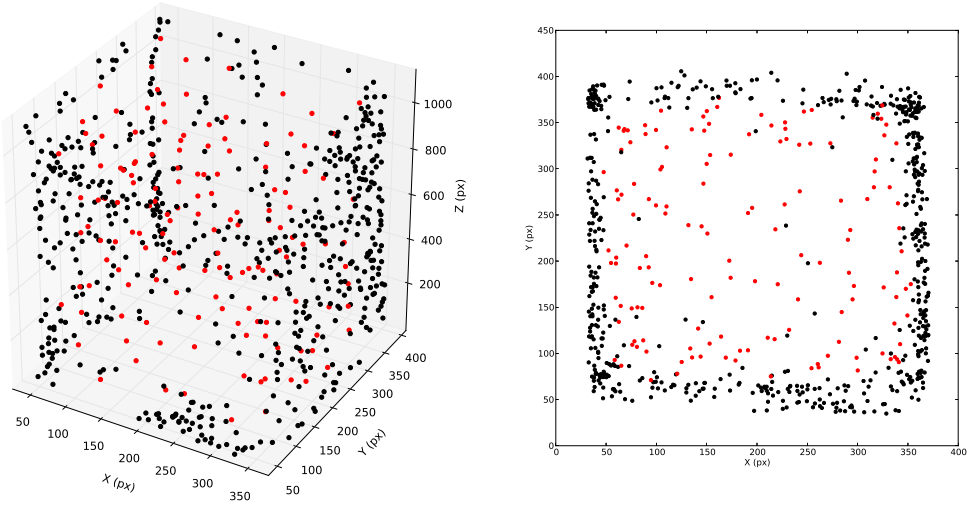

Figure 3.6 – 3D plot of the position of center of mass of the 732 grains of the sample (left) and 2D projection onto the XY plane of these positions (right). The red dots denote grains from the "large grains" population.

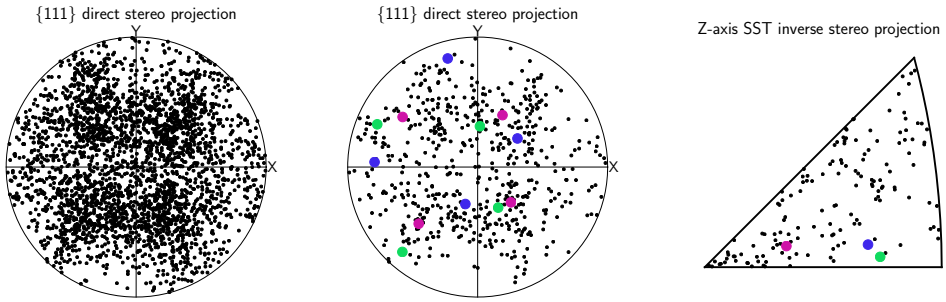

Figure 3.7 – {111} direct stereographic projections for Sam8 (left), {111} direct stereo projections for the large grain population (middle), and Z axis inverse stereo projection for the large grain population (right). When present, colors indicate the grain in the cluster as in Fig. 3.4.

3.2.1 The three grains cluster

The three grains cluster selected for the present study is represented in Fig. 3.4. The essential topotomographic information ((hkl) reflection of grain, grain size, aligned grain orientation, Bragg angle, and tilts) for each grain are listed in Tab. 3.3. The inverse pole figure representation of each grain is shown in Fig. 3.7 (right).

A (202) reflection with a Bragg angle of $6.21°$ was aligned for grains 4 and 18, whereas a (002) reflexion with a Bragg angle of $4.39°$ was aligned for grain 10. In the present study, each grain of the cluster is identified by a specific color as indicated in Fig. 3.7: grain 4, grain 10, grain 18.

Grain 4 is the largest grain of the cluster with an equivalent diameter of $113.3\,\mu m$, grains 10 and 18 have an equivalent diameter of $66.7\,\mu m$ and $48.8\,\mu m$ respectively. As shown in Fig. 3.4, the three-grains cluster is located approximately in the center of the sample. Its coordinates are $(247, 160, 568)$ in a $400 \times 435 \times 1122$ volume (pixels).

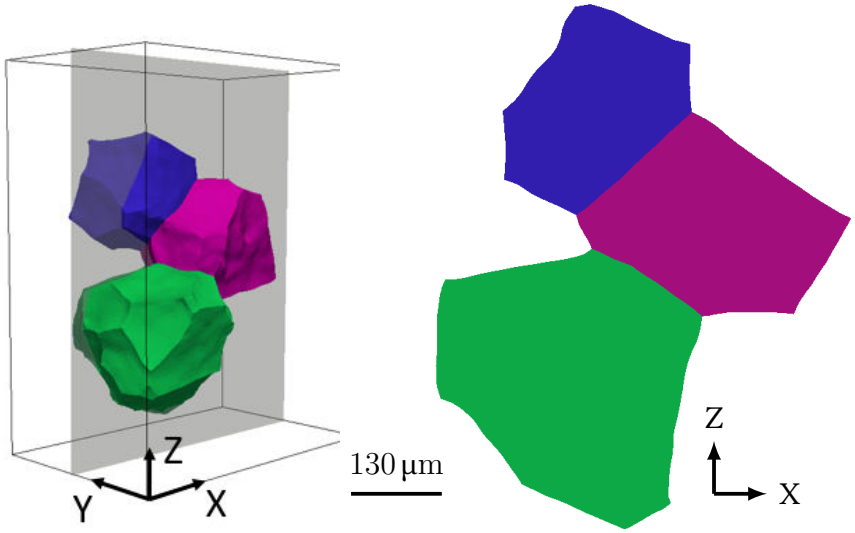

Figure 3.8 – 3D rendering of the cluster (left). The clipping plane is drawn in grey. 2D slice of the cluster, with reference to the clipping plane (right).

	Grain 4	Grain 10	Grain 18
Equivalent diameter	113.3 µm	66.7 µm	48.8 µm
COM position (px)	(240, 133, 513)	(235, 219, 605)	(285, 148, 667)
Rodrigues vector	[0.050, -0.305, 0.104]	[-0.028, -0.145, 0.062]	[-0.135, -0.272, -0.333]
Aligned plane normal	(202)	(002)	(202)
θ_{Bragg}	6.21	4.39	6.21
Tilts (up, low) in °	(11.04 ,0.53)	(-16.62, 2.24)	(12.84, -4.93)
ω for $\{111\}$ "edge-on" configuration:			
(111)	(176, 338)	(34 ,220)	(29,229)
$(1\bar{1}1)$	(159, 356)	(124, 310)	(209, 46)
$(\bar{1}11)$	(113, 293)	(130, 304)	(163, 343)
$(11\bar{1})$	(42, 222)	(40, 214)	(92, 272)
Schmid factors:			
$(111)[\bar{1}01]$	0.16	0.32	0.17
$(111)[0\bar{1}1]$	**0.46**	**0.49**	**0.49**
$(111)[\bar{1}10]$	0.31	0.16	0.31
$(1\bar{1}1)[\bar{1}01]$	0.15	0.36	0.19
$(1\bar{1}1)[011]$	**0.48**	**0.47**	**0.46**
$(1\bar{1}1)[110]$	0.33	0.11	0.27
$(\bar{1}11)[0\bar{1}1]$	0.10	0.25	0.09
$(\bar{1}11)[110]$	0.07	0.05	0.05
$(\bar{1}11)[101]$	0.17	0.30	0.14
$(11\bar{1})[\bar{1}10]$	0.05	0.10	0.10
$(11\bar{1})[101]$	0.13	0.39	0.22
$(11\bar{1})[011]$	0.08	0.27	0.12

Table 3.3 – Essential information about the three grains cluster. Red cells indicate systems with the highest SF and having a plane visible in the topographs. Bold characters indicate the two highest Schmid factor.

3.3 Topography analysis

The present analysis aims at identifying contrasts arising at particular ω positions of the tomographic rotation stage as a function of the load. These contrasts were first analyzed in [Gueninchault et al., 2016] and identified as signs of the activity of certain slip systems. The main asset of the present study is the observation of the evolution of these contrasts, for the three neighboring grains.

Topographs are 2D oblique projections of a diffracting grain. In this study, contrasts will only be analyzed as orientation contrasts, while intensity may vary because of gradients of structure factor or extinction contrast within the framework of dynamical diffraction. A more complete description of contrasts mechanisms can be found in Sec. 1.3.3. When defects accumulate on a particular slip system, the local Bragg condition is modified, producing orientation contrasts on the detector. These perturbations of the crystal lattice are often localized in slip bands, and the latter may only be visible at certain ω angles, the so call *edge-on* configuration when the diffraction direction is contained in the plane. Tab. 3.4 shows topographs for each grain at ω positions where the plane of the most active system is in the "edge-on" configuration as defined in Chap. 2.4 .

3.3.1 In-situ topography analysis

Integrated topographs at particular ω and at given load levels are shown in Fig. 3.4. "Band-like" contrasts are visible and appear first for grain 10, then grain 18 and grain 4. These sets of bands are parallel. A second set of bands appears also for each grain of the cluster. These bands are located along particular crystallographic planes, which could be identified as (the most) activated slip system, shown in Fig. 3.9.

It is worth noting that in the undeformed state, the topographs exhibit another type of contrast. Due to the pristine quality of the crystals and the relatively large size of the three grains, dynamical diffraction occurs. These contrasts, particularly visible for grain 10, quickly disappear when the sample is deformed.

Applied strain (%)	**Grain 4**	**Grain 10**	**Grain 18**
	$\omega = 180°$	$\omega = 40°$	$\omega = 32°$
0	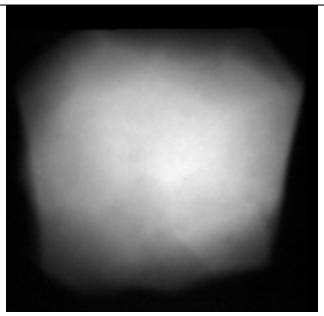	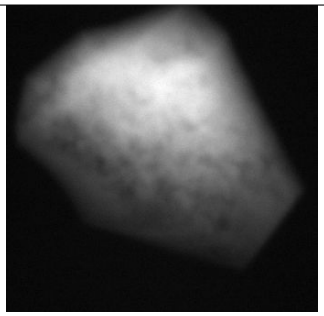	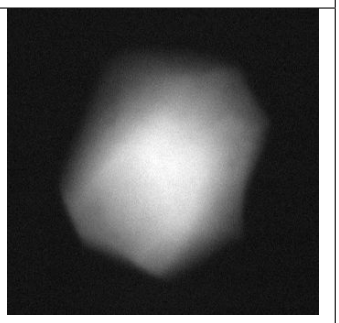
0.089	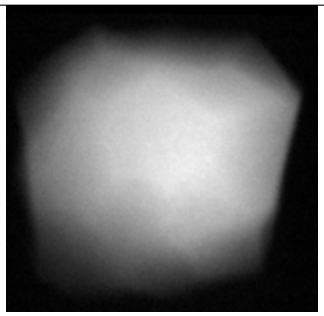	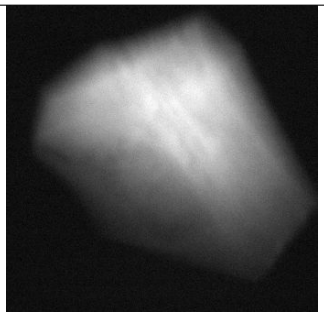	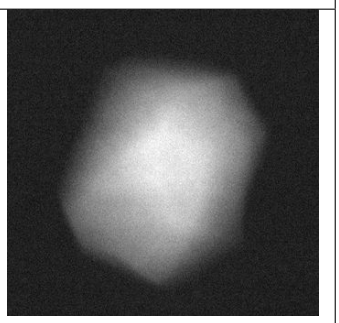
0.16	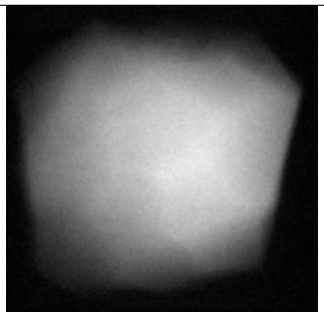	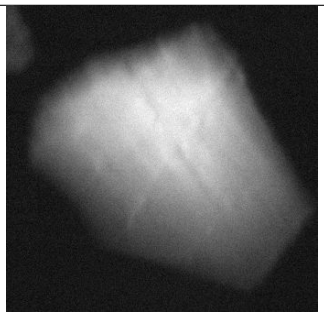	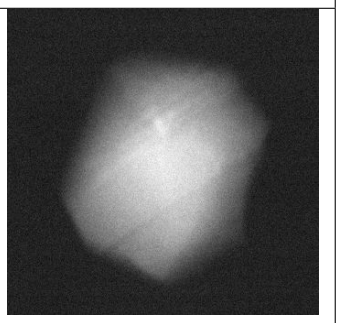
0.32	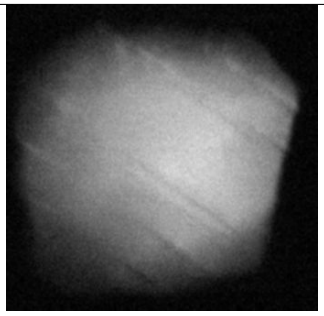	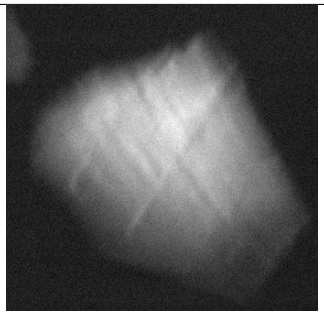	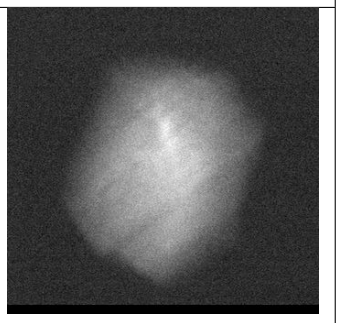

Table 3.4 – Integrated Topographs over Θ for each grain of the cluster, and different load levels.

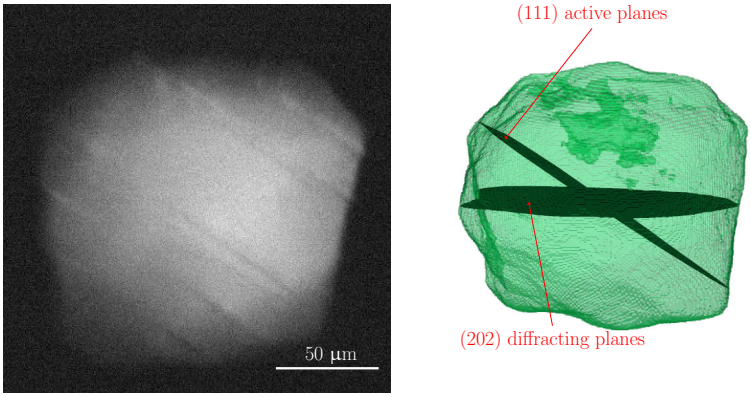

(a) Grain 4, $\omega = 180°$

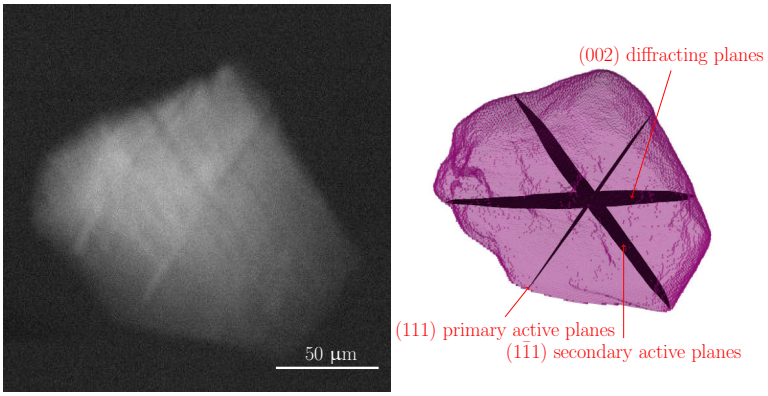

(b) Grain 10, $\omega = 40°$

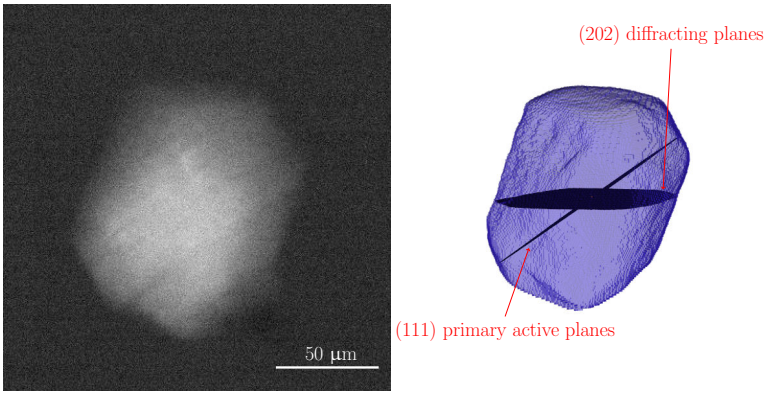

(c) Grain 18, $\omega = 32°$

Figure 3.9 – Planes identification on integrated topographs (right) with 3D plane visualization (right), for (a) grain 4, (b) grain 10, and (c) grain 18. At this particular ω, two sets of bands are visible for grain 10.

The order of appearance of the bands in the topographs seems partly correlated to the Schmid factors of the slip systems of the grains. Grain 10 shows the earliest appearance of bands at $0.0887\,\%$ strain ((111) plane with SF=0.49), while at $0.161\,\%$ bands are visible in the topographs of grain 18 ((111) plane with SF =0.46). At this load level, a second set of bands appears in grain 10 ($(1\bar{1}1)$ plane with SF=0.39. Note that due to the specific orientation of grain 10, both edge on configuration for the (111) and the $(1\bar{1}1)$ planes are very close ($32°$ vs $40°$. Because of that, both sets of bands are visible in single topographs represented at $\omega = 40°$). Grain 4 shows band-like contrasts only at the end of the experiment at $0.317\,\%$ strain, along both (111) and $(1\bar{1}1)$ planes as shown in Fig. 3.10. A second set of bands is visible at the end of the experiment for the grain 18, identified as activity along the $(1\bar{1}1)$ plane, as well. They are visible at $\omega = 160°$ for grain 4 and $\omega = 40°$ for grain 18.

For grain 4, the active plane is (111). In grain 10 (111) is the primary plane while $(11\bar{1})$ is the secondary. For grain 18, the (111) set of planes has been identified as active. The angle between the two sets of bands of grain 10 is $70°$, consistent with the identification of $\{111\}$ planes. As expected for FCC crystals, slip localization occurs along planes which can be identified as {111}.

It is noticeable that the most active plane for grain 4 belongs to the system with the second highest Schmid factor, and its Schmid factor (0.46) is below the Schmid factor of the active systems of grains 10 and 18 (0.49). The secondary set of planes of grain 10 belongs to the system with the third highest Schmid factor. Plane activation is therefore not only guided by the Schmid factor of the slip systems, but neighborhood effects are probably involved in the process of strain localization. All Schmid factors have been calculated from the macroscopic loading conditions.

As mentioned earlier, grain 10 is the softest grain and is easily activated. Grain 10 has 7 of its 12 systems with a Schmid factor above 0.3, and even if they are not visible in the topographs, the slip activity in this grain is probably more complex than just 2 active systems.

The contrast in the topographs comes from local lattice rotations and distortions. As seen on Fig. 2.8 (right), it is propagation based, and because of that the width of the bands cannot be directly and quantitatively taken as slip bands width. However, their evolution and their spacing may still be interpreted qualitatively. Measurements of band width and position are available in App. C. Here the methodology used was first to rotate the topograph, so that the bands of interest are horizontal. Then the bands positions are manually identified, and the intensity of the image is integrated over a limited area (30 pixels horizontally). Bands are fitted by a Gaussian function, and the width of the band is calculated by means of the FWHM of the Gaussian curve.

Five sets of bands are identifiable for the grain 4 at the end of the experiment.

Those bands range from $2.5\,\mu m$ to $7.5\,\mu m$ width. In the band #2, two distinct sub-bands are visible, but they are too close to be separated. The mean band width is $5\,\mu m$, and the mean space between two bands is $42.7\,\mu m$.

For grain 18, two bands are identifiable. They are respectively $6.7\,\mu m$ and $4.8\,\mu m$ wide. The distance between the bands is $44\,\mu m$.

For grain 10, more data is available, and the bands for the primary system are visible since scan #14. Even if several bands are visible, only one can be clearly discriminated after scan #17. This band is $6\,\mu m$ wide in scan #17 and grown to $7\,\mu m$ at the end of the experiment (scan #23). The contrast is more pronounced when more load is applied, and this is the sign of increasing lattice rotations due to the storage and accumulation of dislocations. For the secondary set of bands of grain 10, two bands are clearly distinguishable, and they are respectively 4 and $7\,\mu m$ wide. The distance between the bands is $51\,\mu m$.

The resolution here ($0.7\,\mu m$ per pixel) is too low to distinguish single slip bands, supposed to be approximately $1\,\mu m$ wide in this alloy (see Sec 2.2.3). The strong contrasts are most probably due to bundles on individual bands. The distance between the contrast in each grain of the cluster is of the same order of magnitude, approximately $50\,\mu m$.

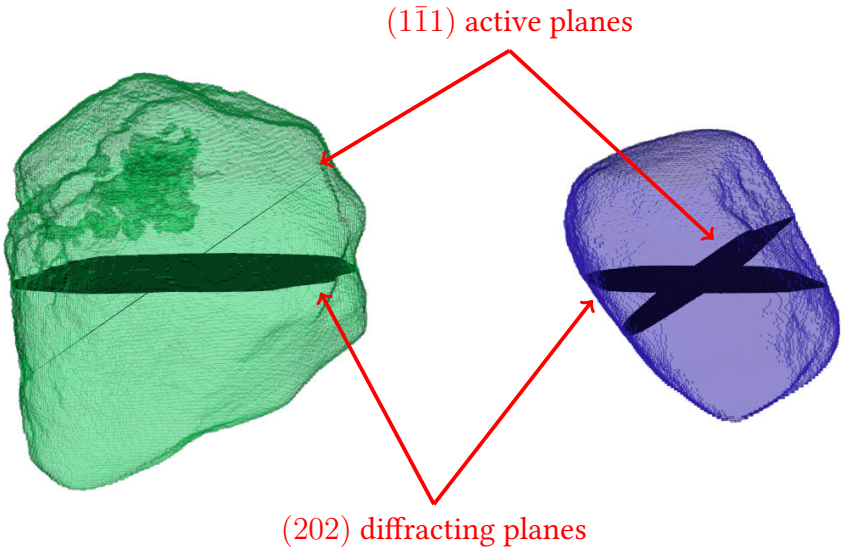

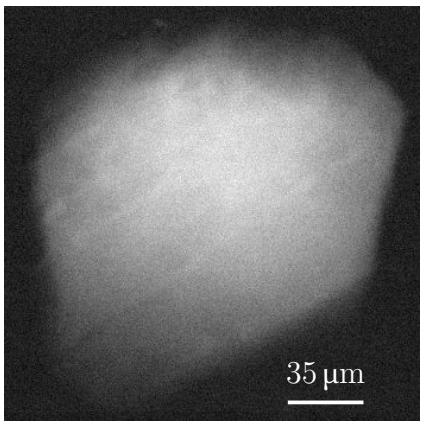

grain 4, $\omega = 160°$

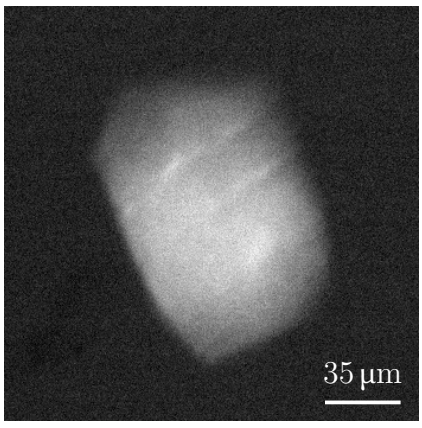

grain 18, $\omega = 40°$

Figure 3.10 – (202) topographs (left) grain 4and (right) grain 18, showing a second set of bands, visible at $\omega = 160°$ and $\omega = 40°$. The contrasts have been identified to be along to the $(1\bar{1}1)$ plane for both grains.

3.4 Topotomography analysis

The present analysis is an extension of the in-situ topography analysis, including the reconstruction of 3D volumes. While a given grain is aligned in the topotomography mode, it is possible to record a large number of topographs, at different ω positions. With the methodology exposed in [Ludwig et al., 2001a], it is possible to reconstruct the spatial arrangement of the defects giving rise to the observed image contrasts.

3.4.1 Reconstruction methodology

For the reconstructions, topographs were integrated along θ, at each of the 90 ω positions of the diffractometer. The routine takes four vectors (12 variables) as an input: the $\underline{\boldsymbol{u}}$ and $\underline{\boldsymbol{v}}$ directions of the detector, the detector position, and the direction of the projection $\underline{\boldsymbol{K}}$. Given D the distance between the rotation axis and the detector (and presuming that the scattering is aligned with this rotation axis) and ω, the diffracted beam vector $\underline{\boldsymbol{K}}$ associated to a topograph can be written as follows:

$$\underline{\boldsymbol{K}} = \begin{bmatrix} \cos\theta & 0 & \sin\theta \\ 0 & 1 & 0 \\ -\sin\theta & 0 & \cos\theta \end{bmatrix} \begin{bmatrix} \cos\omega & -\sin\omega & 0 \\ \sin\omega & \cos\omega & 0 \\ 0 & 0 & 1 \end{bmatrix} \begin{bmatrix} D \\ 0 \\ D\tan(2\theta) \end{bmatrix} \tag{3.1}$$

From this geometric information, an oblique SIRT reconstruction, involving repeated forward and backward projection operations along $\underline{\boldsymbol{K}}$ using the Astra toolbox [Palenstijn et al., 2013] is performed. Viewed in the sample system, the grain is considered immobile and the detector performs a rotation around the grain. The reconstruction was performed on a single node GPU with 16 CPU and 768 GB of memory with 50 iterations on the nice cluster of the ESRF.

3.4.2 Reconstructed volumes

3D volumes were reconstructed for both undeformed and deformed states. The size of each volume is $450 \times 450 \times 371$ voxels encoded in float 32 bits. After the reconstruction process, the volumes were converted into 8 bits data sets. The isotropic voxel size of the reconstructed volume depends on the pixel size of the detector used during the acquisition and was $0.7\ \mu\mathrm{m}$.

Contrasts are visible inside the topographs as the load increases, and it is possible to spatially resolve defects along planes in the reconstructed volumes. Comparisons between two slices at the same position within a grain at different load levels are presented for each grain in Fig. 3.11. Contrasts are more pronounced for grain 10 than for the two other grains. This observation is consistent with the topographs in Sec. 3.3.1. Indeed, grain 10 is the one with the highest visible slip activity. The volume reconstructed for the undeformed state exhibits some contrasts, which can probably be attributed to dynamical diffraction extinction primary effects in the almost perfect grains, as exposed before.

In Fig. 3.11(a) grain 4 shows the highest activity near the grain boundaries which could be an indication of strain localization in precipitates free zones (PFZ) as explained earlier in Sec. 2.3.3, while grain 10 shows contrasts crossing the whole grain volume. These bands appear to be from $1.4\,\mu\mathrm{m}$ to $2.8\,\mu\mathrm{m}$ wide in the reconstruction. They are in reality probably thinner. Since the orientation contrast seen in the topographs evolves as a function of the grain-detector distance. A 6D reconstruction would be needed for a quantitative analysis, linking the contrasts to local rotations of the crystal lattice. unfortunately this type of analysis is not yet available for the topotomographic geometry. Similar bands have been observed in binary Al-Li alloys for monotonic loading in [Sanders and Starke, 1982]. In the reconstruction of grain 10, the secondary slip system seems to bend the traces of the primary slip system. It could indicate that the secondary slip system was piling up onto a dislocation structure formed by the primary slip system activity.

Contrasts are barely visible in the reconstruction of grain 18, even though they are visible in the topographs. The lower (~ 1.5) signal to noise ratio of the topographs of this grain affects the quality of the reconstruction, as explained later in Sec. 3.4.3.

The contrasts visible in the reconstructed volumes are identified in Fig. 3.11 again along specific crystallographic directions as in Fig. 3.9 in the two dimensional analysis. Even if individual dislocations cannot be observed with the present analysis, and to the best of the authors knowledge, this is one of the first in-situ 3D observation of the apparition of dislocation structures within the bulk of grains of a mm-sized polycrystalline specimen.

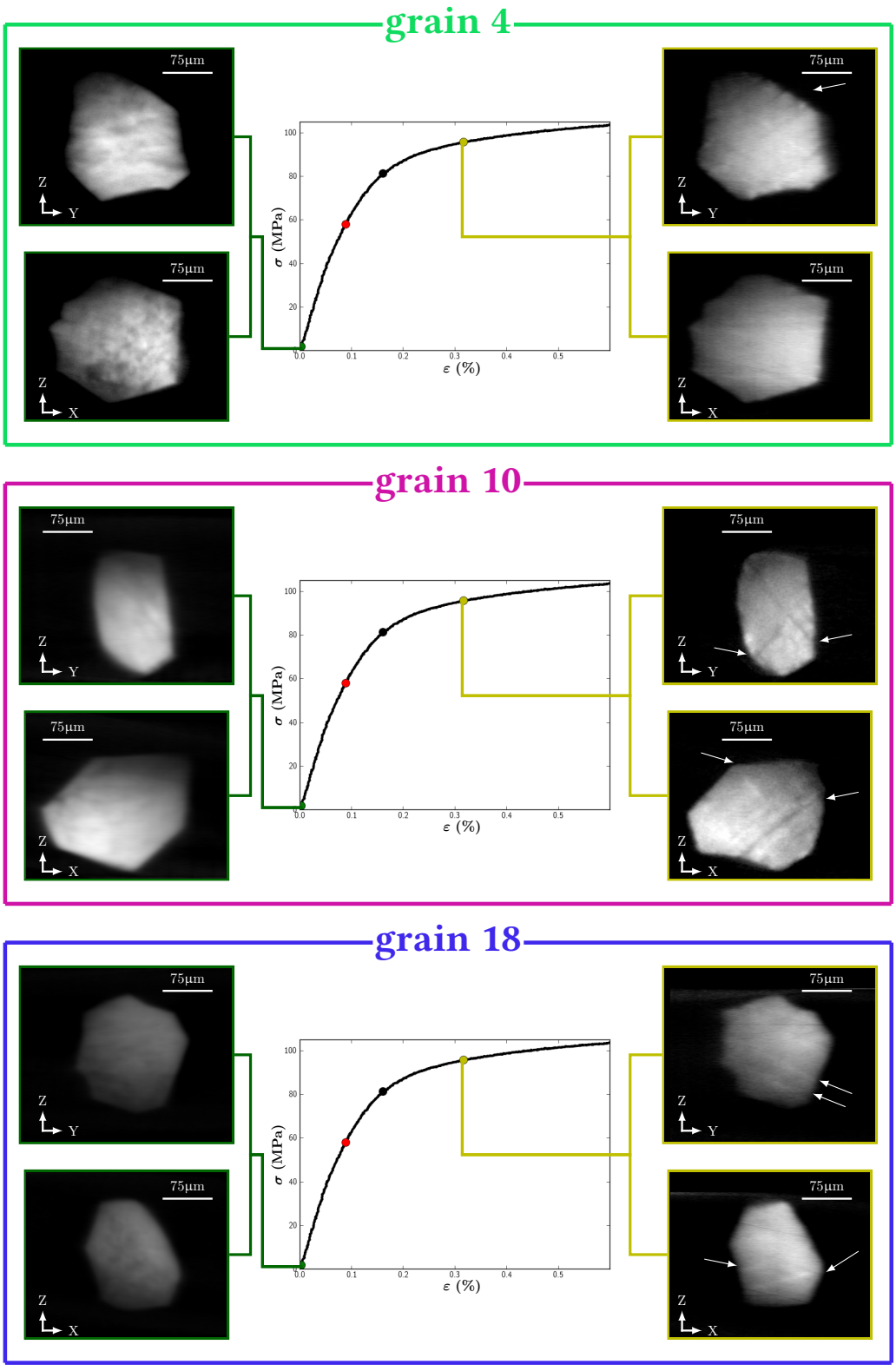

Figure 3.11 – Visualization of contrasts in the reconstructed volumes for (top) grain 4, (middle) grain 10, (bottom) grain 18. White arrows indicate the bands.

3.4.3 Quality of the reconstruction

For 3D insitu imaging techniques, the quality of the 2D projection data is essential. During the experiment, the exposure time of each topograph was set at $110\,\mu s$ and remained constant. In the kinematic approximation, the quantity of photons diffracted by a given grain is proportional to its volume, and for a given acquisition time, a larger grain will generate a more intense spot on the detector. For a given grain volume, the diffracted intensity depends on the squared modulus of the structure factor $\|F_{hkl}\|^2$. Higher order reflections of a grain will diffract less photons. For an Aluminum FCC crystal we have $\|F_{002}\|^2 = 1.4377 \times 10^5$ and $\|F_{202}\|^2 = 0.9960 \times 10^5$.

Topographs, integrated over ω and θ are shown in Fig. 3.12 for scans 0 and 23, and for each grain. Profiles of the intensity of these integrated images along a line passing through the point with the highest intensity are plotted. From this data it is possible to perform a rough analysis of the quality of the acquired topographs for the purpose of 3D topotomographic reconstructions.

Because a (002) reflexion was used for the topotomographic imaging of grain 10, its signal to noise ratio (SNR) is relatively correct for both undeformed (~ 7) and deformed (~ 3.75) states. As grain 4 is relatively large (the fourth biggest grain of the sample), its SNR in the undeformed state is ~ 7 and decreases to ~ 2.8 when deformed.

The situation is less favorable for grain 18. The grain is imaged through a (202) reflection, diffracting less (40%) photons than grain 10 and its (002) reflection, and it is the smallest grain of the cluster ($12\times$ smaller volume than grain 4, and $2.5\times$ smaller than grain 10). Furthermore it is a relatively soft grain (the maximum Schmid factor is 0.49) where misorientation will arise quickly. Due to the combination of these factors, the grain exhibits the worst SNR of the cluster for both undeformed (~ 4) and deformed (~ 1.6) states. The low SNR in the undeformed state leads to noisy 3D reconstructions, which explains why contrasts are barely visible within the volumes.

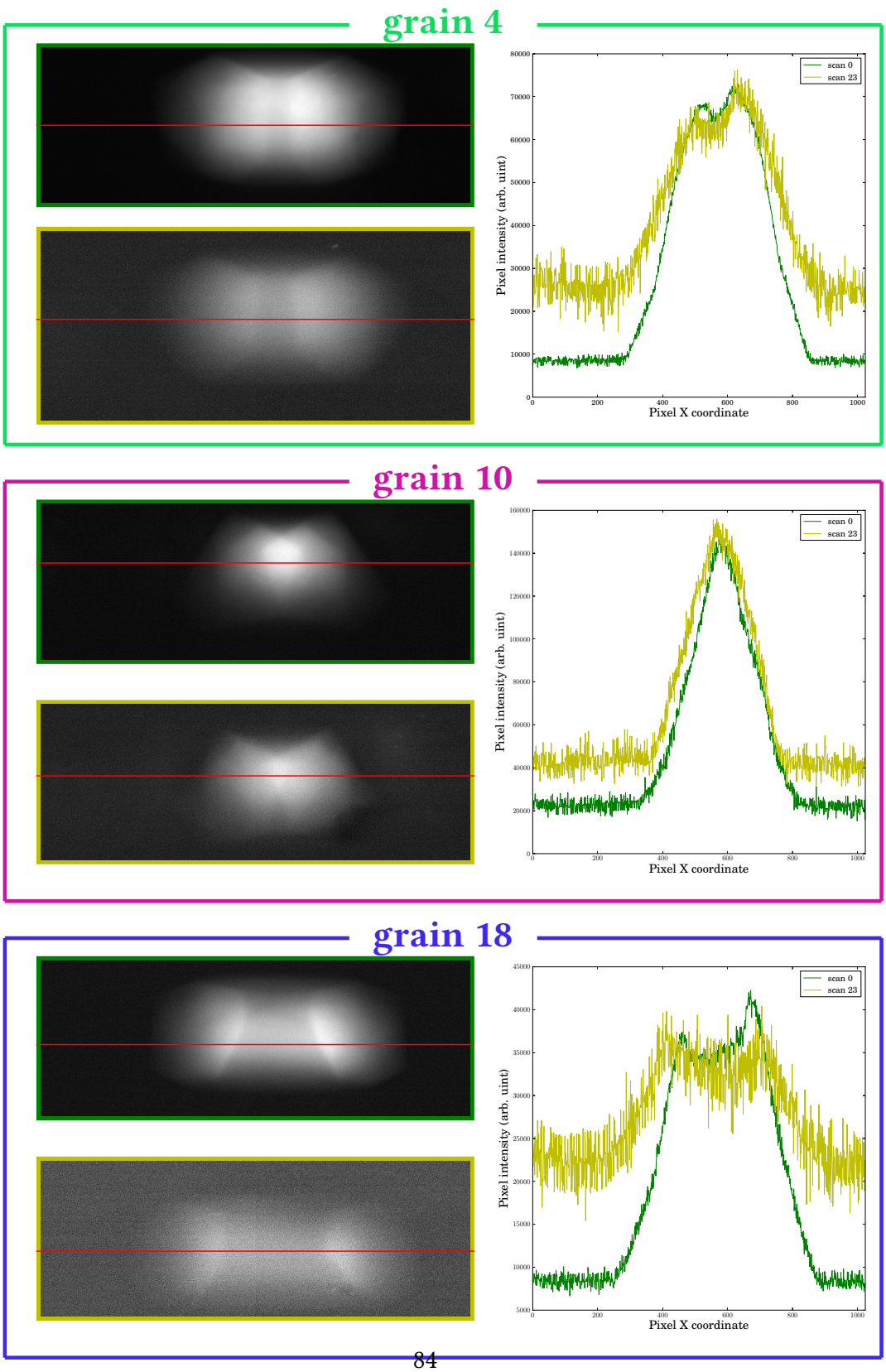

Figure 3.12 – Integrated topographs over ω (left) and intensity profiles along the red lines (right) for scan 0 and 23.

3.5 Rocking curves

While the previous sections dealt with a spatial (from topographs, integrated over the Bragg angle (θ)) analysis of the presence and the evolution of crystalline defects within the bulk of a grain, the present section aims at the analysis of the variation of intensity in the (ω, θ) space, but integrated over the grain volume. *Rocking curve analysis* has been widely used for over 80 years to measure the quality of crystals, in particular in the field of semi-conductors. For polycrystals, a detailed methodology, where plastic activity is deduced from far-field data, can be found in [Borbély and Ungár, 2012].

3.5.1 2D rocking curves analysis

Rocking curves (RC), plotted as function of strain are presented in Fig. 3.13, for each grain and for scans 0, 12, 18, and 23, were the applied strains have been measured by DVC. The ω position of the diffractometer was $180°$, $40°$, $32°$ for grains 4, 10 and 18 respectively. These values correspond to the configuration of the diffractometer previously chosen for the topotomography analysis presented in Tab. 3.4.

Grain 4 exhibits a simple behavior, as only two systems have been identified as active during the experiment. With the onset of plasticity, the rocking curves start to widen. The position of the peak drifts slightly to lower values of $|\theta|$. This indicates an increase of the d_{202} interplanar spacing, a sign that the grain is under tension or of a small overall rotation, and could also be the sign of a rigid body motion due to asymmetric loading conditions.

Two (or more) systems appear to be active in grain 10 as shown in Fig. 3.9. For the first two rocking curves (green and red) where no or only one slip system is active, the RC simply starts to widen as for grain 4. But as soon as the second (or more) slip systems become active, the RC loses its typical shape, sign of a more complex orientation distribution inside the grain.

Again only 2 systems were identified as active in grain 18, but the RCs show a more complex behavior than grain 4. The $(1\bar{1}1)[011]$ system has a relatively high (0.46) Schmid factor, comparable to the Schmid factor of the slip system of grain 4. It is then possible that the other systems not identified in the topographs are active without a strong localization along a specific direction and in that case no strong contrast within the topographs or the topotomographies would be visible.

The two dimensional analysis of rocking curves appears to be complementary to the in-situ topography and topotomography analysis, which correlates the slip activity of a grain with image contrasts in topotomographies.

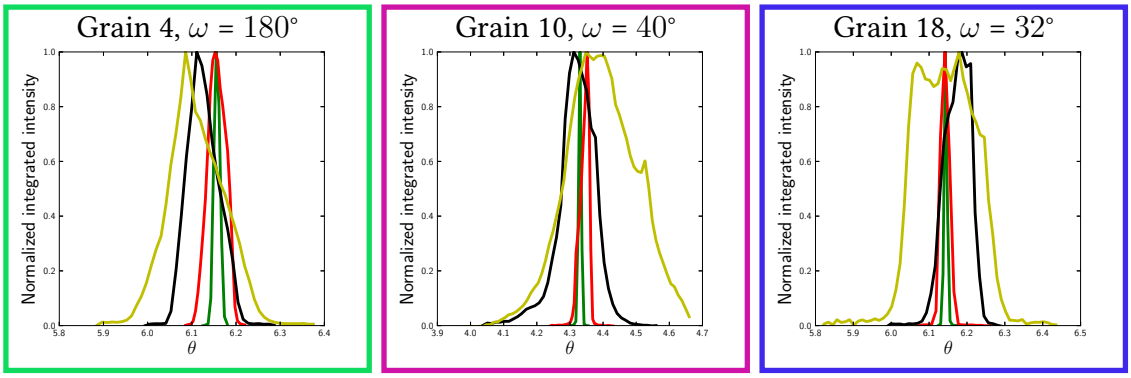

Figure 3.13 – Normalized two-dimensional rocking curves for each grain of the cluster, for scans 0, 12, 18 and 23, see Tab 3.3 for scan color code. The configuration of the diffractometer is the same as for the topographs presented in Tab. 3.4.

3.5.2 3D rocking curves analysis

As grains are aligned in a topotomographic sense, it is possible to measure rocking curves at every ω position. The benefit of rocking curves at different omega positions is to be sensitive not only to the amount of curvature of a crystal[3] but to the orientation of this curvature in real space as illustrated in Fig. 3.14(left).

In the ideal case of a crystal bent by an edge dislocation, the outer surface of the rocking curve can be easily deduced by solving the rotating crystal equation (see Appendix C). This gives the characteristic shape of Fig 3.14(right). To measure the intragranular orientation spread revealed by a rocking curve, we introduce $\delta_{0.1}$ the width of the RC at 10% of the peak of the normalized intensity. This value is a direct measure of the orientation spread, the *effective misorientation*, around the axis defined by the base tilt. This measure is available for each ω position and is plotted for every cycle of the experiment in Fig. 3.16. We called these plots *FWEM - Full width of the effective misorientation* as a function of ω.

As explained in [Gueninchault et al., 2016], activity on a single slip plane can be idealized as a dislocation pile-up of edge dislocations. These dislocations would bend the crystal around their line vector, and lead to the very specific shape observed in Fig. 3.16(left). As the dislocation density along the specified slip system increases, the FWEM tends to widen while keeping the dumbbell-like shape.

Again, the situation for grains 10 and 18 is more complex. During the first steps of the experiment, the shape of the MS for both grains is like the typical

[3]The shape and the width of a rocking curve are related to the crystal defects leading to orientation gradients within a crystal.

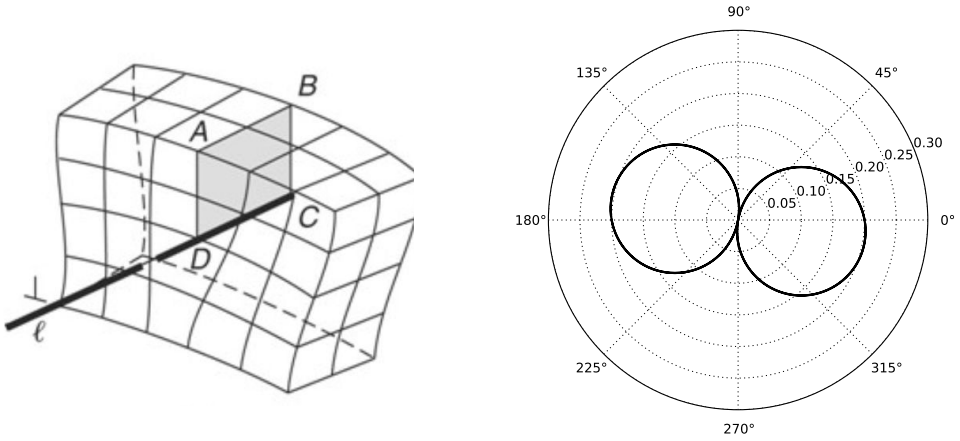

Figure 3.14 – Schematic of an edge dislocation bending a crystal (left). The bold line indicates the line vector. Ideal FWEM generated for a crystal bent by a network of edges dislocations, and a total curvature of $0.2°$. The aligned hkl set of planes was (111). The width of the FWEM is maximum when the X-rays beam is set perpendicular to the line vector of the dislocations.

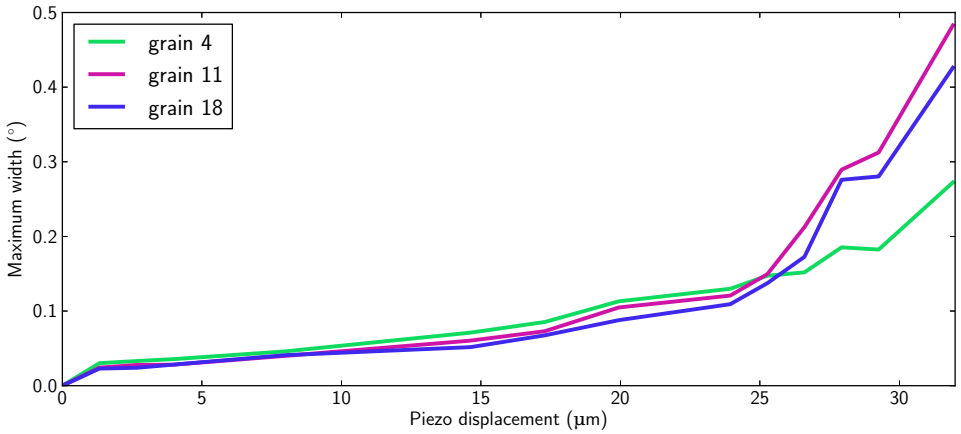

Figure 3.15 – Maximum width of the FWEM as a function of the displacement applied.

dumbbell observed for grain 4. When a second slip system starts to be active, the MS loses its shape and the preferred orientation is less pronounced. Again, this is the sign of multiple slip activity.

An interesting phenomenon is observed for grain 10. After losing its shape, the MS starts to turn whereas for grain 4 and 18 the main curvature of the grain remains along the same direction (Fig. 3.15(right)). One could speculate that the activity on the second system prevails and almost creates a dumbbell in the new direction, and more advanced experimental techniques should be used to get a very accurate picture of the orientation distribution inside the grain volume, in this case. Dark Field X-ray microscopy would have been the method of choice. Unfortunately the sample was destroyed due to a collision on the instrument.

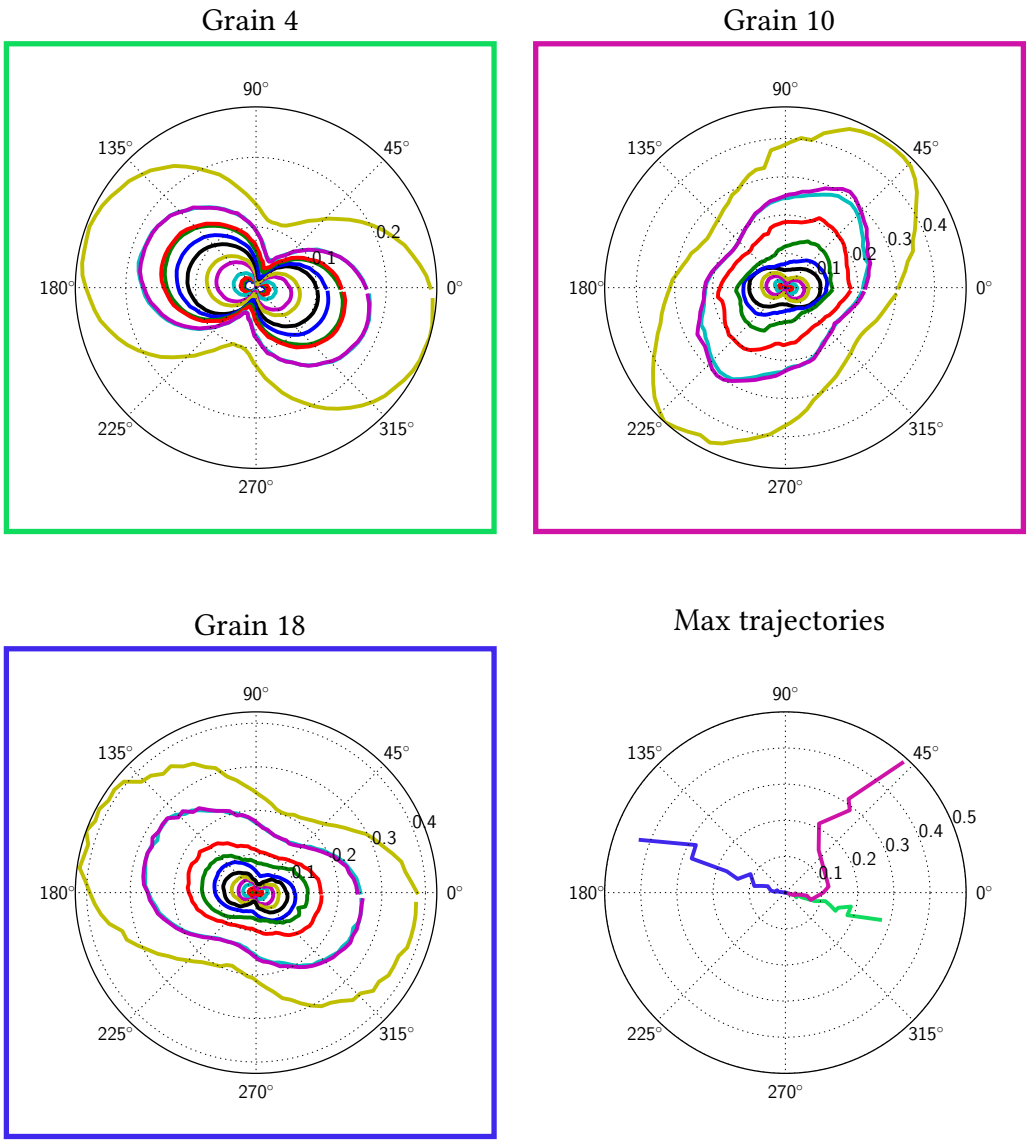

Figure 3.16 – In-situ FWEM for each grain of the cluster, and trajectories of the maximum of the FWEM (bottom right).

Chapter 4

Numerical analysis of early stage plasticity by CPFEM

En parallèle, des simulations de la plasticité cristalline par éléments finis (CPFE) ont été menées utilisant la cartographie tridimensionnelle de la microstructure mesurée expérimentalement. Un chargement uniaxial de traction a été appliqué pour reproduire numériquement l'expérience, et comparer grain par grain l'activité plastique. L'activité des systèmes de glissement prédite par le modèle est conforme aux observations expérimentales d'une activité plastique le long de deux plans. Un cadre mathématique pour prédire l'angle de Bragg local en fonction des déformations et des rotations du réseau cristallin a été formulé. Un post-traitement des champs intragranulaires de déformation à partir des résultats des simulations CPFE a montré une excellente concordance avec les résultats expérimentaux. Ce résultat confirme que la topotomographie in-situ aux rayons X est un outil prometteur pour l'étude des premiers stades de la plasticité cristalline en volume.

In this chapter, a regular character, a, denotes scalars (zero-order tensors), while $\underline{\boldsymbol{a}}$ denotes a vector (first-order tensors) and $\underset{\sim}{\boldsymbol{a}}$ denotes a second-order tensor.

4.1 Constitutive equations for crystal plasticity modelling

The full continuum crystal plasticity theory is presented in Appendix A. A shorter description of the model used in the computations is given in the next sections.

In order to analyze the microplastic behavior of an AlLi polycrystal, an elasto-visco-plastic crystal plasticity model was selected from [Besson et al., 2009]. Numerical computations were performed using the Z-set software (see [Besson and Foerch, 1997]). The modelling is formulated in the framework of finite strains, which gives access to both lattice distortions and rotations.

4.1.1 Continuum crystal plasticity theory

The following model is based on the multiplicative decomposition of the deformation gradient, $\underset{\sim}{\boldsymbol{F}}$, into an elastic part, $\underset{\sim}{\boldsymbol{E}}$, and a plastic part, $\underset{\sim}{\boldsymbol{P}}$:

$$\underset{\sim}{\boldsymbol{F}}(\underline{\boldsymbol{X}}) = \underset{\sim}{\mathbf{1}} + \frac{\partial \underline{\boldsymbol{u}}}{\partial \underline{\boldsymbol{X}}} = \underset{\sim}{\mathbf{1}} + \boldsymbol{\nabla}_X \underline{\boldsymbol{u}}\,, \quad \underset{\sim}{\boldsymbol{F}}(\underline{\boldsymbol{X}}) = \underset{\sim}{\boldsymbol{E}}(\underline{\boldsymbol{X}}).\underset{\sim}{\boldsymbol{P}}(\underline{\boldsymbol{X}}) \tag{4.1}$$

The initial coordinates of the material point in the reference configuration are denoted by $\underline{\boldsymbol{X}}$ and $\boldsymbol{\nabla}_X$ denotes the gradient operator with respect to initial coordinates. The current position of the material point in the current configuration is $\underline{\boldsymbol{x}}$. The displacement vector is $\underline{\boldsymbol{u}} = \underline{\boldsymbol{x}} - \underline{\boldsymbol{X}}$. The multiplicative decomposition (4.1) is associated with the definition of an intermediate configuration for which the elastic part of the deformation gradient is removed, see Fig. 4.1. The intermediate released configuration is uniquely determined up to a rigid body rotation which is chosen such that the lattice orientation in the intermediate configuration is the same as the initial one. [Mandel, 1973a] called it the *isoclinic* intermediate configuration. As a result, lattice rotation and distortion during elastoplastic deformation are contained in the elastic deformation part $\underset{\sim}{\boldsymbol{E}}$, as examined at the end of this section.

Plastic deformation is the result of slip processes according to a collection of N slip systems, each one characterised by the slip direction, $\underline{\boldsymbol{m}}^s$, and the normal

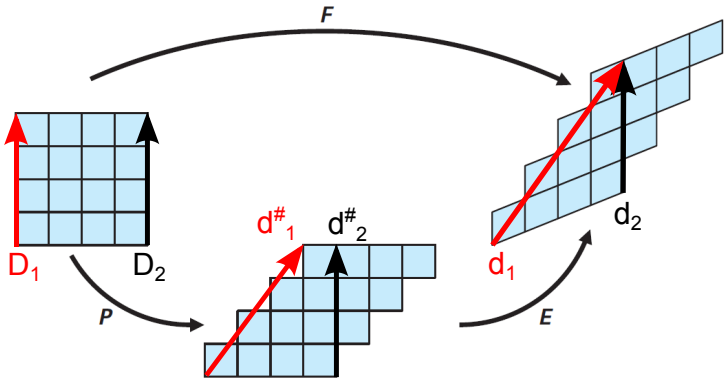

Figure 4.1 – Multiplicative decomposition of the deformation gradient into elastic and plastic parts. Red arrows denote a material line, while black arrows denote a particular crystallographic direction.

to the slip plane, $\underline{\boldsymbol{n}}^s$, in the intermediate configuration :

$$\dot{\underset{\sim}{\boldsymbol{P}}}.\underset{\sim}{\boldsymbol{P}}^{-1} = \sum_{s=1}^{N} \dot{\gamma}^s \underline{\boldsymbol{m}}^s \otimes \underline{\boldsymbol{n}}^s \tag{4.2}$$

Note that plastic deformation induced by dislocation glide is isochoric so that

$$J = \det \underset{\sim}{\boldsymbol{F}}, \quad J_p = \det \underset{\sim}{\boldsymbol{P}} = 1, \quad J_e = \det \underset{\sim}{\boldsymbol{E}} = J = \det \underset{\sim}{\boldsymbol{F}} \tag{4.3}$$

The slip rate on a given system s depends on the resolved shear stress τ^s in the glide direction. It is defined by a power law (here, no hardening is considered for the sake of brevity):

$$\dot{\gamma}^s = \left\langle \frac{|\tau^s| - \tau_0}{K} \right\rangle^n sign(\tau^s) \tag{4.4}$$

where τ_0 the critical resolved shear stress. Plastic slip will occur when the resolved shear stress reached τ_0. Hardening will be discussed in Sec. 4.1.4.

4.1.2 Lattice rotations

The previous continuum mechanical approach makes it possible to distinguish between the transformation of material and lattice directions. Material lines are made of material points that are subjected to the motion $\underline{\boldsymbol{u}}(\underline{\boldsymbol{X}})$. The tangent to a material line at $\underline{\boldsymbol{X}}$ is a material direction $\underline{\boldsymbol{D}}$ in the reference configuration that transforms into the material direction $\underline{\boldsymbol{d}}$ in the current configuration by means of the deformation gradient:

$$\underline{\boldsymbol{d}}_1 = \underset{\sim}{\boldsymbol{F}} \cdot \underline{\boldsymbol{D}}_1 \tag{4.5}$$

In contrast, lattice directions are not material insofar as they are not necessarily made of the same material points (atoms) in the initial and current configurations due to the passing of dislocations, but keep the same crystallographic meaning. According to the concept of isoclinic configuration, lattice directions are unchanged from the initial to the intermediate configuration of Fig. 4.1. Dislocations passing through a material volume element do not distort nor rotate the lattice, although material lines are sheared. According to the continuum theory of dislocations, statistically stored dislocations accumulating in the material volume element affect material hardening but do not change the element shape. Accordingly, an initial lattice direction $\underline{\boldsymbol{d}}^{\sharp}$ is transformed into $\underline{\boldsymbol{d}}$ by means of the elastic deformation:

$$\underline{\boldsymbol{d}}_1 = \underset{\sim}{\boldsymbol{E}}.\underline{\boldsymbol{d}}_1^{\sharp} \tag{4.6}$$

$$\underline{\boldsymbol{d}}_2 = \underset{\sim}{\boldsymbol{E}}.\underline{\boldsymbol{d}}_2^{\sharp} \tag{4.7}$$

According to the *polar decomposition theorem*, there is a unique decomposition of $\underset{\sim}{\boldsymbol{F}}$ into a rotation part $\underset{\sim}{\boldsymbol{R}}$ and a symmetric stretch part $\underset{\sim}{\boldsymbol{U}}$:

$$\underset{\sim}{\boldsymbol{F}} = \underset{\sim}{\boldsymbol{R}}\underset{\sim}{\boldsymbol{U}} \tag{4.8}$$

Similarly, polar decomposition exists for:

$$\underset{\sim}{\boldsymbol{E}} = \underset{\sim}{\boldsymbol{R}}^e\underset{\sim}{\boldsymbol{U}}^e \tag{4.9}$$

$$\underset{\sim}{\boldsymbol{P}} = \underset{\sim}{\boldsymbol{R}}^p\underset{\sim}{\boldsymbol{U}}^p \tag{4.10}$$

4.1.3 Lattice curvature and the dislocation density tensor

In his famous paper, [Ashby, 1971] made the statement that to accommodate non-homogeneous deformations, densities of so-called *Geometrically necessary dislocations* (GNDs) are required, contrary to homogeneous deformations leading to *statistically stored dislocations* (SSDs) with a zero net Burgers vector. These GNDs densities, expressed by a dislocation tensor $\underset{\sim}{\boldsymbol{\alpha}}$, arise either if the geometry of the loading (beding, torsion, ...) or the material (composites, polycrystals, ...) are non-homogenous [Fleck et al., 1994]. These statements are illustrated in Fig. 4.2. The dislocation density tensor was first defined by [Nye, 1953] as:

$$\sum_s \langle \underline{\boldsymbol{b}}^s \otimes \underline{\boldsymbol{\xi}} \rangle \tag{4.11}$$

with $\underline{\boldsymbol{b}}^s$ the burgers vector of a given s slip system, and $\underline{\boldsymbol{\xi}}$ its associated line vector.

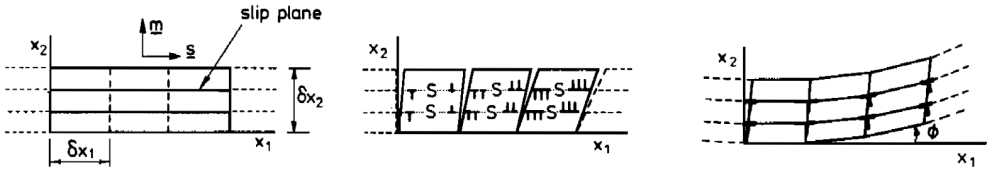

Figure 4.2 – Gradient of slips causing the apparition of GNDs densities, and leading to crystal curvature, from [Fleck et al., 1994]

It can be shown ([Cermelli and Gurtin, 2001b]) that this dislocation density can be expressed in terms of the elastic deformation[1]:

$$\underset{\sim}{\boldsymbol{\alpha}} = -\mathrm{curl}\,\underset{\sim}{\boldsymbol{E}}^{-1} = -\mathrm{curl}\,(\underset{\sim}{\boldsymbol{U}}^{e-1} \cdot \underset{\sim}{\boldsymbol{R}}^{eT}) \tag{4.12}$$

In the case of small elastic strain we have:

$$\underset{\sim}{\boldsymbol{\alpha}} \simeq -\mathrm{curl}\,\underset{\sim}{\boldsymbol{R}}^{eT} \tag{4.13}$$

In addition, if elastic rotations can be considered small, one have

$$\underset{\sim}{\boldsymbol{\alpha}} \simeq -\mathrm{curl}\,(\underset{\sim}{\mathbf{1}} - \underset{\sim}{\boldsymbol{\omega}}^e) = \mathrm{curl}\,\underset{\sim}{\boldsymbol{\omega}}^e \tag{4.14}$$

where ω^e is the skew-symmetric tensor. The small rotation axial vector is defined as

$$\overset{\times}{\underline{\boldsymbol{\omega}}}^{\,e} = -\frac{1}{2}\underset{\approx}{\boldsymbol{\epsilon}} : \underset{\sim}{\boldsymbol{\omega}}^e, \quad \underset{\sim}{\boldsymbol{\omega}}^e = -\underset{\approx}{\boldsymbol{\epsilon}} \cdot \overset{\times}{\underline{\boldsymbol{\omega}}}^{\,e} \tag{4.15}$$

or, in matrix notations,

$$[\underset{\sim}{\boldsymbol{\omega}}^e] = \begin{bmatrix} 0 & \omega_{12}^e & -\omega_{31}^e \\ -\omega_{12}^e & 0 & \omega_{23}^e \\ \omega_{31}^e & -\omega_{23}^e & 0 \end{bmatrix} = \begin{bmatrix} 0 & -\overset{\times}{\omega}{}_3^e & \overset{\times}{\omega}{}_2^e \\ \overset{\times}{\omega}{}_3^e & 0 & -\overset{\times}{\omega}{}_1^e \\ -\overset{\times}{\omega}{}_2^e & \overset{\times}{\omega}{}_1^e & 0 \end{bmatrix} \tag{4.16}$$

The gradient of the lattice rotation field delivers the lattice curvature tensor. In the small deformation context, the gradient of the rotation tensor is represented by the gradient of the axial vector:

$$\underset{\sim}{\boldsymbol{\kappa}} = \overset{\times}{\underline{\boldsymbol{\omega}}}^{\,e} \tag{4.17}$$

One can establish a direct link between $\mathrm{curl}\,\underset{\sim}{\boldsymbol{\omega}}^e$ and the gradient of the axial vector associated with $\underset{\sim}{\boldsymbol{\omega}}$. For that purpose, the matrix form of $\mathrm{curl}\,\underset{\sim}{\boldsymbol{\omega}}^e$ is derived

[1]The curl differential operator is defined by Eq. A.57 in the appendix.

according to (A.57):

$$[\mathrm{curl}\,\underset{\sim}{\boldsymbol{\omega}}^e] = \begin{bmatrix} \omega^e_{12,3} + \omega^e_{31,2} & -\omega^e_{31,1} & -\omega^e_{12,1} \\ -\omega^e_{23,2} & \omega^e_{12,3} + \omega^e_{23,1} & -\omega^e_{12,2} \\ -\omega^e_{23,3} & -\omega^e_{31,3} & \omega^e_{23,1} + \omega^e_{31,2} \end{bmatrix} \tag{4.18}$$

or equivalently

$$[\mathrm{curl}\,\underset{\sim}{\boldsymbol{\omega}}^e] = \begin{bmatrix} -\overset{\times}{\omega}{}^e_{3,3} - \overset{\times}{\omega}{}^e_{2,2} & \overset{\times}{\omega}{}^e_{2,1} & \overset{\times}{\omega}{}^e_{3,1} \\ \overset{\times}{\omega}{}^e_{1,2} & -\overset{\times}{\omega}{}^e_{3,3} - \overset{\times}{\omega}{}^e_{1,1} & \overset{\times}{\omega}{}^e_{3,2} \\ \overset{\times}{\omega}{}^e_{1,3} & \overset{\times}{\omega}{}^e_{2,3} & -\overset{\times}{\omega}{}^e_{1,1} - \overset{\times}{\omega}{}^e_{2,2} \end{bmatrix} \tag{4.19}$$

from which it becomes apparent that

$$\underset{\sim}{\boldsymbol{\alpha}} = \underset{\sim}{\boldsymbol{\kappa}}^T - (\mathrm{trace}\,\underset{\sim}{\boldsymbol{\kappa}})\underset{\sim}{\mathbf{1}}, \quad \underset{\sim}{\boldsymbol{\kappa}} = \underset{\sim}{\boldsymbol{\alpha}}^T - \frac{1}{2}(\mathrm{trace}\,\underset{\sim}{\boldsymbol{\alpha}})\underset{\sim}{\mathbf{1}} \tag{4.20}$$

This is a remarkable relation linking, within the context of small elastic strains[2] and rotations, the dislocation density tensor to lattice curvature. It is known as Nye's formula [Nye, 1953].

The edge dislocation case

To illustrate the previously stated model of GND density, let us take a crystal bent by n edge dislocations of Burgers vector $\underline{\boldsymbol{b}}$ and piercing the surface S, as illustrated in Fig. 4.3. By convention:

$$\underline{\boldsymbol{z}} = \frac{\underline{\boldsymbol{b}}}{b} \times \underline{\boldsymbol{\xi}} \tag{4.21}$$

The resulting Burgers vector is then:

$$\underline{\boldsymbol{B}} = \mathrm{n} b \underline{\boldsymbol{e}}_1 \tag{4.22}$$

$$= \underset{\sim}{\boldsymbol{\alpha}} \underline{\boldsymbol{e}}_3 S \tag{4.23}$$

with

$$\underset{\sim}{\boldsymbol{\alpha}} = \frac{\mathrm{n}}{S} \underline{\boldsymbol{b}} \otimes \underline{\boldsymbol{\xi}} \tag{4.24}$$

$$= -\rho^g \mathrm{b} \underline{\boldsymbol{e}}_1 \otimes \underline{\boldsymbol{e}}_3 \tag{4.25}$$

$$= \begin{bmatrix} 0 & 0 & \alpha_{33} \\ 0 & 0 & 0 \\ 0 & 0 & 0 \end{bmatrix} \tag{4.26}$$

$\rho^g = \mathrm{n}/S$ is the density of GNDs according to Ashby.

[2] and in fact of small gradient of elastic strain.

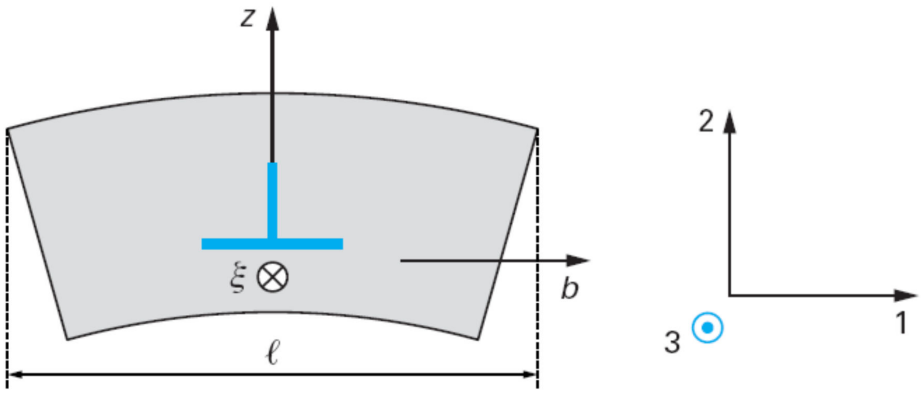

Figure 4.3 – Schematic of a crystal bent by n edge dislocations.

4.1.4 Hardening rule

A phenomenological isotropic hardening rule, as developed in [Méric et al., 1991], is used here. The Eq. 4.4 can be rewritten as follows:

$$\dot{\gamma}^s = \left\langle \frac{|\tau^s| - \tau_0 - r^s}{K} \right\rangle^n sign(\tau^s) \tag{4.27}$$

Here r^s, initially zero, increases with increasing plastic strain and hardens the system s since $|\tau|$ must be equal to $\tau_0 + r^s$ for plasticity on system s to be active. For the current study, a non-linear isotropic hardening was used:

$$r^s = Q \sum_{r=1}^{N} h^{sr}(1 - \exp(-bv^s)) \tag{4.28}$$

h^{sr} denotes the interaction matrix taking into account the relative influence of slip systems on each other. It includes the self and latent hardening, and only indirect and estimated quantitative information are available about the components of this matrix [Gérard, 2008] e.g. in [Franciosi et al., 1980] and [Wu et al., 1991]. Q and b are material parameters, v^s is defined by $\dot{v}^s = |\dot{\gamma}^s|$, is the cumulative plastic slip on the system s.

4.2 Identification of material parameters

In order to accurately simulate the local plastic field of the polycrystal, the elasto-plastic behavior of the Al-Li alloy must be identified. For that purpose, tensile tests at different strain rates were carried out with macroscopic tensile samples. From these experimental results, material parameters were identified through

	$B4$	$B2$	$B5$	$D4$	$D1$	$D6$	$A2$	$A6$	$A3$	$C5$	$C3$	$C1$
$B4$	h_1	h_2	h_2	h_4	h_5	h_5	h_5	h_6	h_3	h_5	h_3	h_6
$B2$		h_1	h_2	h_5	h_3	h_6	h_4	h_5	h_5	h_5	h_6	h_3
$B5$			h_1	h_5	h_6	h_3	h_5	h_3	h_6	h_4	h_5	h_5
$D4$				h_1	h_2	h_2	h_6	h_5	h_3	h_6	h_3	h_5
$D1$					h_1	h_2	h_3	h_5	h_6	h_5	h_5	h_4
$D6$						h_1	h_5	h_4	h_5	h_3	h_6	h_5
$A2$							h_1	h_2	h_2	h_6	h_5	h_3
$A6$								h_1	h_2	h_3	h_5	h_6
$A3$									h_1	h_5	h_4	h_5
$C5$										h_1	h_2	h_2
$C3$											h_1	h_2
$C1$												h_1

Table 4.1 – Interaction matrix for FCC crystals from [Franciosi et al., 1980]. The physical meaning of the h_i coefficients are described in [Gérard, 2008].

an optimization routine. The scale transition between the single crystal and the macroscopic behavior was performed with a extension of the self-consistent scheme for elastoplastic polycrystal as shown in [Berveiller and Zaoui, 1978].

4.2.1 Mechanical testing on macroscopic samples

Monotonic tensile tests were performed on five different macroscopic samples, at three strain rates. AlLi specimens were cut directly from the rolled plate (see Sec. 2.2.4) according to Fig. 4.4(a). Samples surfaces were roughly polished to eliminate the remaining burrs. These samples were recrystallized 20 minutes at 530 °C, and then water quenched and aged 4 hours at 100 °C.

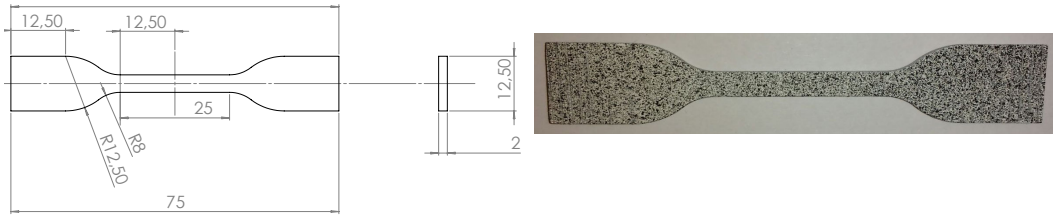

(a) (b)

Figure 4.4 – Drawings of the samples used for the tensile tests (a) and speckle on the sample (b).

The experiments were carried out using an INSTRON 5966 electro-

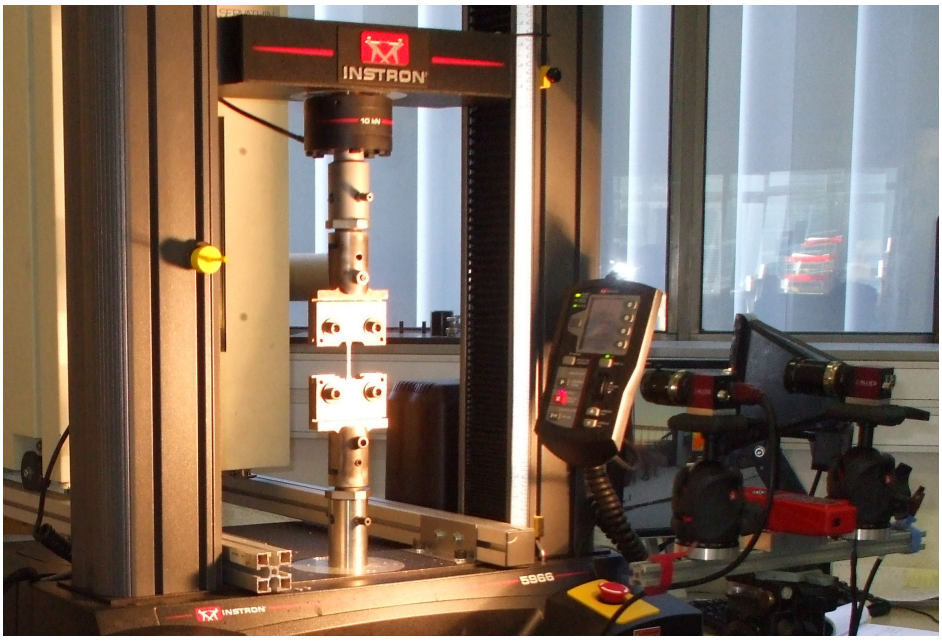

Figure 4.5 – Experimental setup for digital image stereo correlation.

mechanical table top machine. The applied strain was retrieved using digital image stereo correlation (see the experimental setup Fig 4.5) and a black and white speckle was applied on one surface of the sample (Fig. 4.4(b)). The angle between the two cameras was $18°$ and the sample-detector distance was $19\,\mathrm{cm}$. The cameras were equipped with $4.2\,\mathrm{Mpixels}$ CMOS (2048×2048 sensor), and with SCHNEIDER Xenoplan 2.8/50 objectives. Calibration and data analysis were performed using the VIC-3D software [Solutions, 2010]. The subset size used was $50\,\mu\mathrm{m}$, with a spatial resolution of $5\,\mu\mathrm{m}$. Strains were averaged over the gage length, and the data provided by the analysis could be seen as the results of a virtual extensometer.

Five different displacement controlled monotonic tensile tests were performed: two at $\dot{\varepsilon}_1 = 10^{-3}\,\mathrm{s}^{-1}$, two at $\dot{\varepsilon}_2 = 10^{-4}\,\mathrm{s}^{-1}$, and one at $\dot{\varepsilon}_3 = 5 \times 10^{-5}\,\mathrm{s}^{-1}$. The material exhibits an inverse sensitivity of the yield limit to the strain rate, and strong plastic instabilities are visible in Fig 4.6. This is a typical behavior of an alloy subject to the "Portevin-Le Chatelier" effect (more information can be found in Chap. 2).

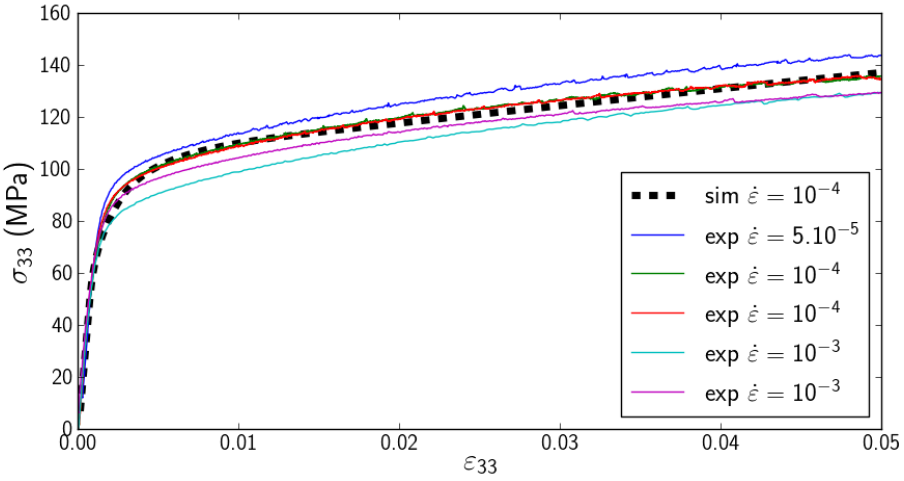

Figure 4.6 – Stress/strain curves from the macroscopic tensile tests (colored), and for the homogenized *Berveiller-Zaoui* behavior (dashed black).

K (MPa$^{1/n}$)	n	τ_0(MPa)	Q (MPa)	b	h_1	h_2	h_3	h_4	h_5	h_6
38	10	10.22	5.29	763.	0.2	0.3	0.3	0.3	0.4	0.1

Table 4.2 – Material parameters identified from the macroscopic tensile tests and coefficients of the interaction matrix h^{sr} from [Tabourot et al., 1997].

4.2.2 Identification with an homogenized behavior

A numerical optimization using Z-set implementation was performed to find the three parameters of the non-linear isotropic hardening law, (τ_0, Q, b) see Eq. 4.27 and 4.28. The results of these optimizations are presented in Tab. 4.2. The two parameters of the Norton law have not been identified, because of the observed inverse strain rate sensitivity of the yield limit. Modeling this effect requires a special model as developed in [Bertram et al., 2006]. For the interactions between dislocations, coefficients from [Tabourot et al., 1997] have been used. They are shown in Tab. 4.2

The comparisons between experimental data and fitted parameters are presented in Fig. 4.6. It is noticeable in Fig. 4.6 that the very smooth elasto-plastic transition of the material is difficult to fit perfectly with the simple model chosen here featuring only one hardening mechanism.

4.3 3D mesh from tomographic images

4.3.1 Meshing polycrystals from DCT data

DCT analysis performed on a polycrystaline sample provides a 3D map, composed of voxels, with labels. Each label corresponds to a grain. From there, as shown in [Proudhon, 2015], two different strategies are mainly used for mechanical computations:

- voxel based meshing;
- free meshing with tetrahedron.

The first strategy is the simplest one. It is straightforward to generate a structured mesh of hexahedrons from the voxelized data, but the number of nodes will be too high to be computationally efficient. A $500 \times 500 \times 500$ cube[3] will produce, by a direct meshing method, a 125751501 nodes mesh. The solution could be to downsample the data, but the spatial description of the curved regions like grain boundaries will be less accurate. Furthermore, the staircase nature of the grain boundaries will generate stress concentration, and will reduce the accuracy of the computation, even more if the data is downsampled.

In [Proudhon et al., 2015], the author shows the advantage of using a free meshing with tetrahedron instead of a regular grid. Beside a better geometrical description of the grain boundaries, one of the main advantages of free meshing is to obtain smaller elements around selected regions of interest, and a coarser mesh in the remaining parts (typically far away from the grains of interest).

4.3.2 Meshing strategy

A four step methodology has been developed to produce accurate meshes from the DCT data. First, the grain map produced by the DCT is dilated to ensure continuity at the grain boundaries as shown in Fig 4.7. This procedure is based on the dilate function of the MATLAB (The MathWorks Inc., Natick, MA, USA) image processing toolbox. It is noticeable that the high density of GNDs at the grain boundaries induce a strong curvature of the lattice. These gradients of orientation lead to badly reconstructed grain boundaries, but 6D reconstruction methods improve the reconstruction of grain boundaries as demonstrated in [Viganò et al., 2016]. The dilation process does not lead to significant differences between the real microstructure and the reconstructed grain map, as shown in a comparison between EBSD and DCT in [Syha et al., 2013b, Renversade et al., 2016].

[3] A cube with $500 \times 500 \times 500 = 125 \times 10^6$ voxels is approximately of the size of the sample of the ma2285 experiment analyzed in the previous chapter.

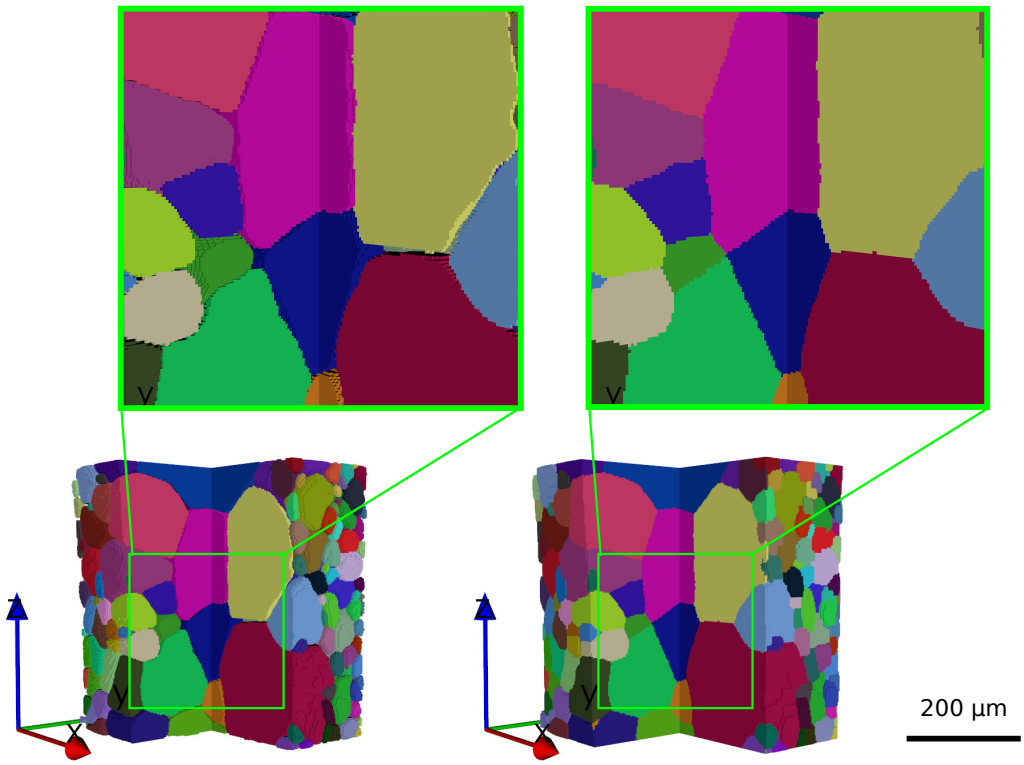

Figure 4.7 – Raw reconstructed volume (left) vs dilated reconstructed volume (right).

From this dilated volume, and for each set of voxels with the same label (each mapped grain), a surface mesh is generated using the Avizo software from FEI, through a "Multiple material marching cubes algorithm" developed by [Hege et al., 1997]. The method relies on the generation and then the meshing of isosurfaces coming from a space partitioning of the data. A Laplacian filter is applied to smooth grain boundaries to decrease the staircase effect [Wu and Sullivan, 2003].

The generated surface contains a very large number of triangles at this step. Mesh simplification is then applied using an iterative decimation approach, by means of an edge collapsing algorithm. Edges are collapsed into vertices, and the global shape of the domain is preserved through minimizing a certain error criterion. Several steps of simplifications can be required, in order to prevent surfaces of different domains to intersect. A special care must be taken for that check, a single intersection leading to a useless mesh. Surfaces from the last steps are filled using the volume mesh generator Ghs3D developed by Inria[4]. The volume mesh generated (element density, etc.) is governed by the properties of the surface mesh given as an input [George, 2004]. Grain boundaries are preserved, as every triangle present in the surface mesh will be a tetrahedron face.

As the next step, sets of elements must be identified as the grains of the DCT data. A special routine has been developed, assigning a set of elements of the mesh to a label of the voxellized DCT data, based on the center of mass (COM) of this set. Each domain of both datasets are reduced to a point, and by comparing the position of these points, a correlation is made between the set of voxels and the set of tetrahedron. During this process, the smallest grains can be lost, because the element size can be larger than the grain size.

At this point, the 3D mesh is usable for mechanical computations. If there is a particular region of interest (ROI) that needs to be analyzed, it could be efficient to have a *non homogeneous* element size toward the ROI. In our case, to analyze the local plastic fields, a smaller element size is required to mesh the three grains cluster. But a much more coarser mesh is sufficient far from the ROI. For that purpose, the meshadapt software from the Inria toolkit can be used to perform a mesh adaptation. The mesh density is modified, to fit a function of the euclidean distance d, referring to an element set, here the cluster of three grains. The function used here was $f(x, y, z) = 2. + 0.35d, \quad d = \sqrt{x^2 + y^2 + z^2}$.

[4]http://www.distene.com/

4.3.3 Results: Comparisons with the experimental DCT data

Comparison between the dilated reconstructed microstructure and the FE mesh generated following the previous steps is shown in Fig. 4.8. The resulting mesh is composed of 63329 nodes for 341687 C3D4 linear elements. As a comparison, the DCT data contains 125745506 voxels. The mesh generated was perfectly suitable for multithreading computations.

The mean tetrahedron volumes obtained are respectively $1.86 \times 10^{-7}\,\mathrm{mm}^3$, $1.69 \times 10^{-7}\,\mathrm{mm}^3$ and $1.68 \times 10^{-7}\,\mathrm{mm}^3$ for grain 4, grain 10, and grain 18. This is about 60 times the voxel volume of the reconstructed microstructure[5]. The gradation effect is visible on Fig. 4.9. Grains far from the cluster are meshed with large elements, while grains surrounding the cluster gradually have a finer mesh. The ratio between the minimum tetrahedron size and the maximum tetrahedron size is approximately 4000.

4.4 CPFEM computations on a realistic microstructure

crystal plasticity finite elements (CPFEM) calculations provide on each Gauss point of the mesh and for each time step (each map) the values of the different variables of the model developed in Sec. 4.1. In this section, the methodology and the direct[6] results of CPFEM simulations are detailed. These computations were carried out on a real microstructural mesh comprising all the grains of the gage length of our miniature tensile specimen, as explained in Sec. 4.3. Z-set uses numbers 1, 2 and 3 for the coordinate system such as $(\underline{\boldsymbol{x_1}}, \underline{\boldsymbol{x_2}}, \underline{\boldsymbol{x_3}})$. Care was taken to make the FEM coordinate system to match exactly the $(\underline{\boldsymbol{x}}, \underline{\boldsymbol{y}}, \underline{\boldsymbol{z}})$ coordinate system of the experiment. Grain orientations given by the DCT are therefore directly used in the calculations.

4.4.1 Computations methodology

The computations were performed on the *RAMA* linux cluster available at the *Centre des Matériaux*, on a single node with 256GB RAM and using 12 of the 16 cores. The integration of the constitutive equations is made using a *Runge-Kutta* scheme of second order with automatic time steps. A special element suitable for finite strain calculation available within the Zset software has been used here

[5]The volume of one voxel is $0.0014^3 = 2.744 \times 10^{-9}\,\mathrm{mm}^3 = 2.744\,\mu\mathrm{m}^3$.

[6]I consider direct results as raw the data which can be directly extracted from the computation files without further post-processing.

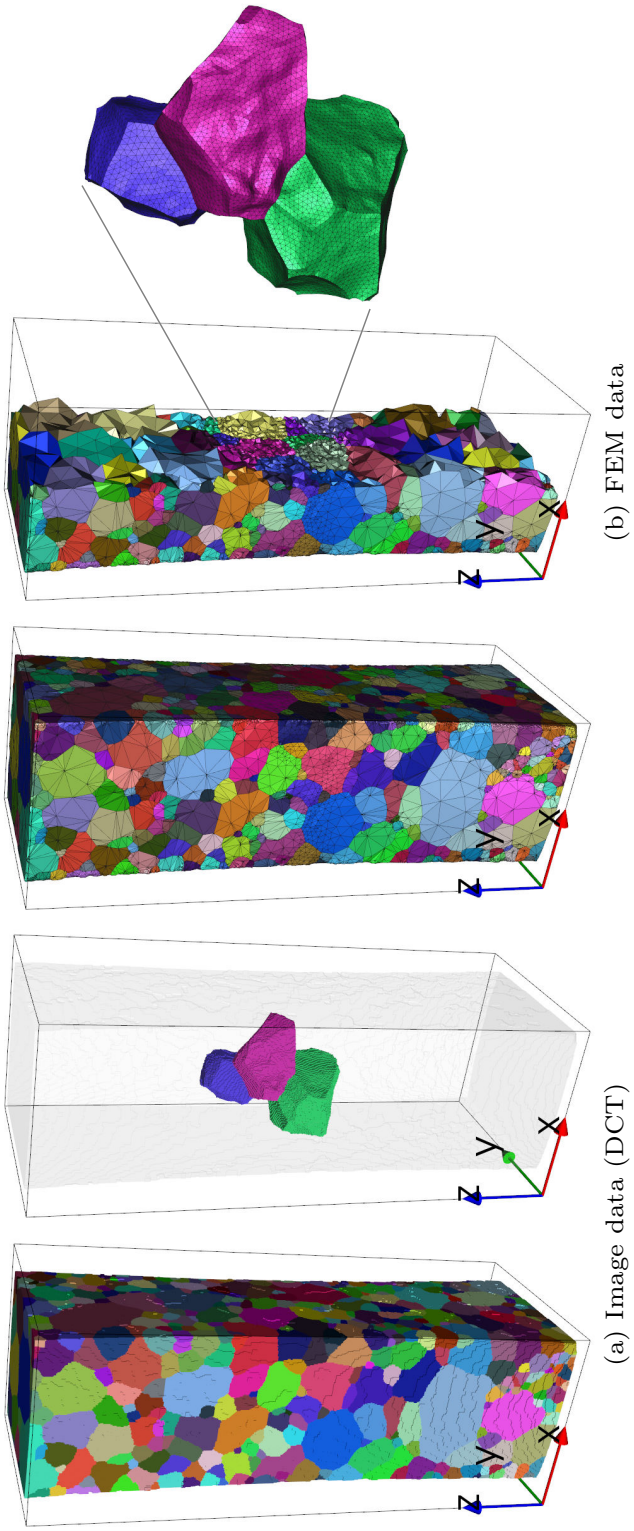

Figure 4.8 – Comparison between the DCT data (a) and the mesh generated (b). Grains have been colored by their label.

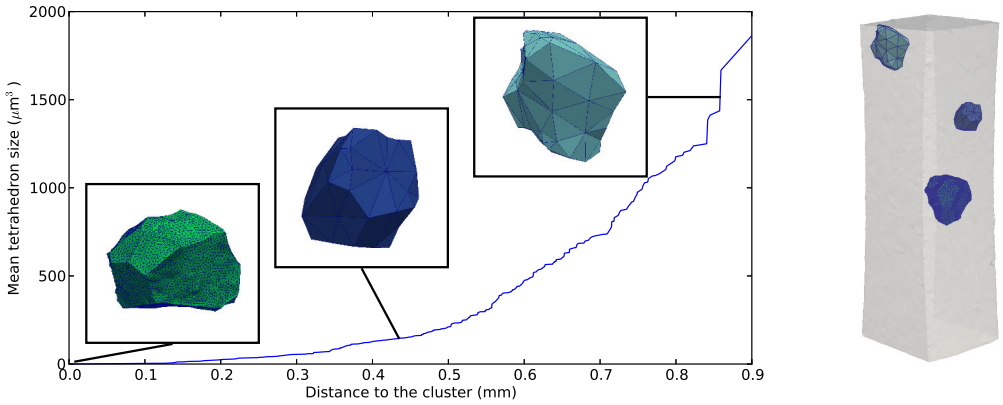

Figure 4.9 – Mean tetrahedron volume vs distance from the cluster with meshes of grain 4 (left), grain 80 (middle) and grain 506 (right). Their positions relative to the sample are shown on the right.

because it provides the value of lattice rotation. More information about the numerical framework used here can be found in [Besson et al., 2009].

A macroscopic displacement of $15.7\,\mu m$ has been applied to the upper surface of the mesh through 100 steps. It corresponds to a global strain ε_{33} of 1%. Suitable boundary conditions have been set on the lower surface of the sample to prevent any rigid body motion and lateral surfaces were free of stress.

$$u_3 = 15.7\,\mu m \text{ at } z = L \tag{4.29}$$
$$u_3 = 0\,\mu m \text{ at } z = 0 \tag{4.30}$$

4.4.2 Results

Macroscopic behavior

The simulated macroscopic behavior of the sample is presented in Fig. 4.10, with the label *Sam8*. This is the result of FE computations on the meshed microstructure, with the exact texture as measured during the DCT experiment. The result of the macroscopic tensile test as exposed in section 4.2.1 is labelled as *polycrystal*. Two other computations, using the same mesh, with random textures have been performed. They are presented in the same figure, with the labels *oligocrystal random 1* and *oligocrystal random 2*. It is clear that there is a strong effect of the texture on the computations and of the small number of grains in the sample sections. It partly explains that the simulated behavior of "Sam8" presents a

lower yield limit than the one observed with a macroscopic sample. The specific grain distribution within the sample could be another explanation. The presence of few large grains in the bulk of the sample could lead to early plasticity, especially if those grains have a "soft orientation". It is apparent that the considered sample is not a representative volume element (RVE) of the polycrystal. But this is not a problem here, since we are taking into account all the grains present in the gage length of the specimen[7].

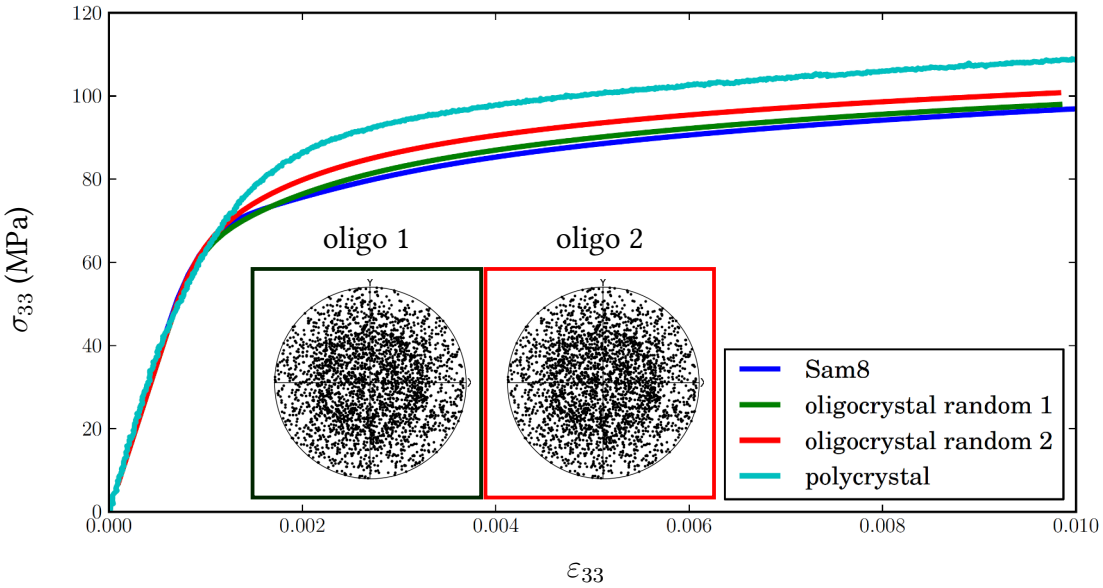

Figure 4.10 – Macroscopic behavior of the sample from CPFEM (Sam8) and macroscopic tensile tests (polycrystal). *oligocrystal 1* and *oligocrystal 2* represent the behavior of the Sam8 microstructure with random orientations. {111} direct pole figures of the 2 oligocrystalline samples are shown. The *Sam 8* pole figure was presented in Chap. 3., see Fig. 3.7

Local grain response

The averaged axial stress response over the volume of each grain of the cluster is shown in Fig. 4.11. The average stress is higher than the stress of the overall sample.

[7]Working with a non representative volume could lead to significant differences when comparisons are made with much more massive specimens, as shown further in this chapter.

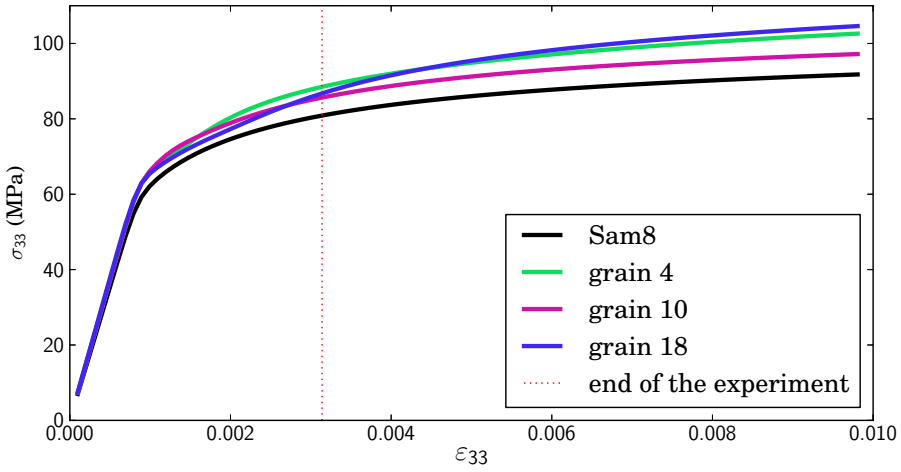

Figure 4.11 – Tensile curves of the three grains of the cluster, and the overall numerical behavior of the *Sam8* sample.

Slip system activity

The first validation of the numerical model is to compare the slip activity computed for each grain to the activity visible on the topographs for a particular ω position. The information provided by the CPFEM simulations is more complete, with the list of active normal and directions $(\underline{\boldsymbol{n}}, \underline{\boldsymbol{m}})$ pairs of active slip systems, and the amount of slip activity for each system[8] at each Gauss point for each time step.

The slip activity for each grain and each system is presented in Fig. 4.12. For grains 4 and 10 the model can predict which system is active in a perfect accordance with the observations made in Chap. 3. The sequential activation of two slip systems in grain 10 is also retrieved, but the model shows that the orientation of this grain is such that the slip state of this grain is more complex than double slip activation. It is possible that some active slip systems (in particular with the plane $(11\bar{1})$ with SF=0.47) are not visible in the topographs of the experiment.

Lattice rotations

It is possible to define a measure of the lattice rotation as follows:

$$\phi_c = \arccos\left[\frac{\mathrm{trace}\,(\underset{\sim}{\boldsymbol{R}}^e - \underset{\sim}{\mathbf{1}})}{2}\right] \tag{4.31}$$

[8] as opposed to the slip plane normal only identified in the experiment of Chap. 3

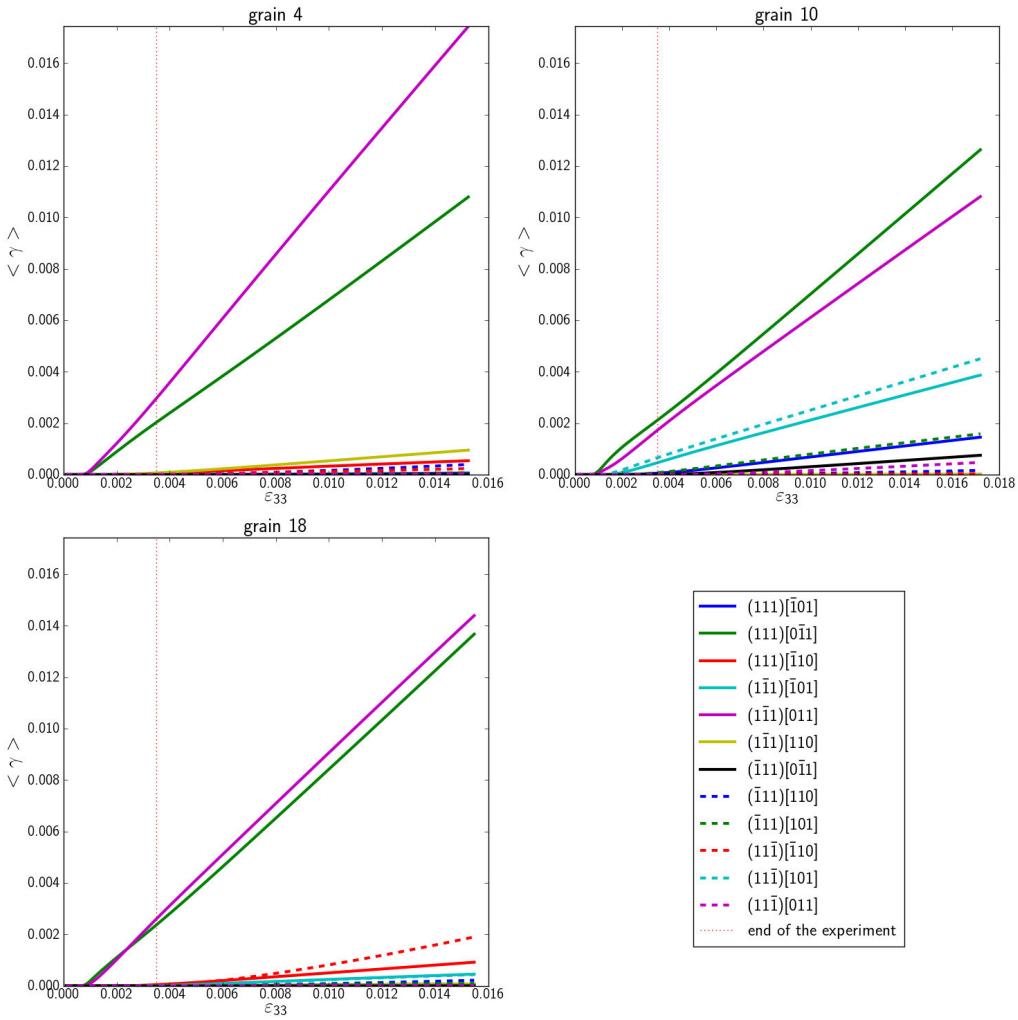

Figure 4.12 – Average slip activity on each of the 12 octahedral systems for the three grains of interest.

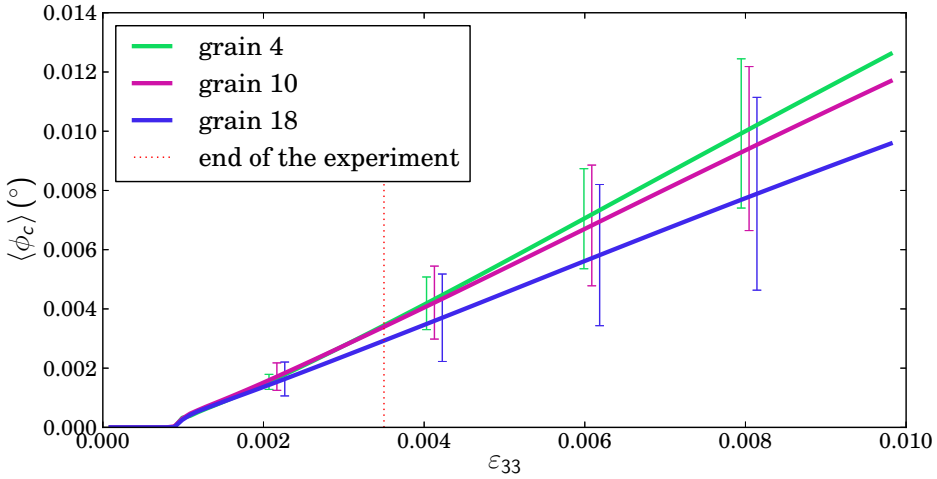

Figure 4.13 – Mean lattice rotation for each grain as a function of the applied strain. Plotted errorbars depict the standard deviation of ϕ_c due to the heterogeneities inside each grain which is linked to the grain misorientation.

This is the angle of the rotation (i.e. the norm of the Rodrigues vector and the angle defined further in Eq. 4.33) in the axis-angle representation of rotations. The mean lattice rotation for each grain of the cluster is presented in Fig. 4.13. The computed values are integrated over the grain volume. Two distinct domains are visible. First, within the elastic regime, the behavior of the three grains is similar and linear. During the plastic regime, each grain exhibits its own non-linear behavior, depending on the number of activated slip systems, and the amount of plastic slip accumulated on each of those systems. The figure shows that there is no direct link between ϕ_c and the number of slip systems activated. It could be due to the fact that the rotation induced by a slip system is counterbalanced by the activation of another one. The lattice rotation during the purely elastic regime is negligible.

As expected, the global misorientation whithin the grain increases with increasing strain. It is represented in Fig. 4.13 by the longer errorbars. One can observe that grain 4 shows a much smaller misorientation than grain 10 and 18, although the average lattice rotation is the same. Large misorientations are found later in grain 4.

Spatial variations of the mechanical fields

The spatial variation of the mechanical fields at $\varepsilon_{33} = 3.4 \times 10^{-3}$ is presented in Fig. 4.14. Each grain was oriented in a specific way, to be in the "edge-on" configuration as depicted in Fig. 3.9. The grains were clipped perpendicular to the X-rays direction, to reveal the fields inside the bulk of the grains. The fields presented here are respectively, from the left to the right, the deformation gradient along the vertical direction F_{33}, the sum of the plastic slip of all slip systems γ_{cum}, the plastic slip along the primary slip system γ_{PS}, and the lattice rotation ϕ_c.

Grain 4 exhibits a strong localization of the deformation in the upper right corner of the grain, due to the activity of the primary slip system $(111)[0\bar{1}1]$. The consequence is a relatively stronger lattice rotation in this area, leading to a locally new suborientation of the crystal. Grain 18 shows the formation of a local misoriented area as well. The plastic slip is generally higher in grain 10, due to the presence of "softer" slip systems. One grain boundary in the upper part of this grain is much more deformed than the rest of the grain. This is due to strain incompatibilities with an adjacent grain. Higher densities of GNDs are present in this area.

It is not possible, with this model, to exhibit localization along slip bands. The consideration of the PLC model could provide such localization effects, see [Graff et al., 2004, Marchenko et al., 2016].

4.5 Simulation of diffraction from CPFEM data

In this section, the results of the CPFEM computations presented previously are used to determine locally for which geometrical parameters the Bragg condition will be satisfied. The main idea of these post-processing steps is to generate synthetic rocking curves to be compared to those experimentally measured and presented in Chap. 3.

4.5.1 Definitions

Crystallographic orientation

A crystalline material exhibits a highly ordered structure. A reference crystal lattice composed of atoms, ions, or molecules can be repeated in the all three directions. Most materials are polycrystalline, composed of domains called "grains" where a unique crystallographic orientation is present. This crystallographic orientation refers to how the atomic planes are positioned relative to a fixed reference. The transformation between the crystal coordinates and the sample coor-

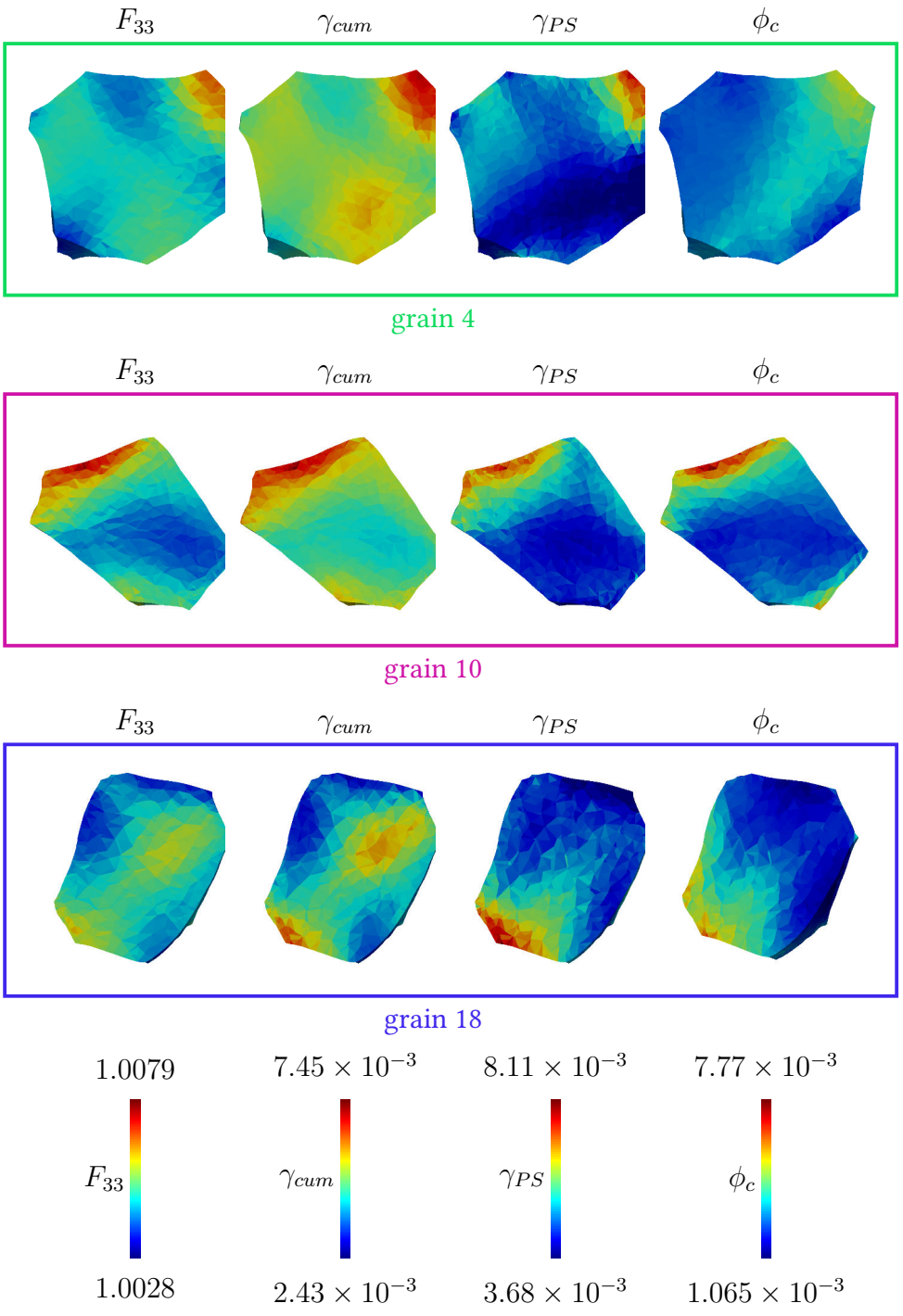

Figure 4.14 – Clips of grain 4, 10 and 18 when the applied strain $\varepsilon_{33} = 0.34\%$. The clip is made so that the direction of observation is along the same axis as in Fig. 3.9. The colors represent fields of F_{33}, cumulated plastic slip γ_{cum}, cumulated activity γ_{PS} on the primary slip system $(111)[0\bar{1}1]$, and the lattice rotation ϕ_c.

dinates is operated by a so-called *orientation matrix*, with nine non-independent parameters [Bunge, 2013]. At least five other ways are used to represent this orientation, and in [Rowenhorst et al., 2015] the authors try to give an exhaustive overview of the different methods while keeping consistency between them, a non trivial task. Here we define $\underset{\sim}{\boldsymbol{g}}$ the orientation matrix of a crystal[9] as:

$$[\underline{\boldsymbol{V}}]_c = \underset{\sim}{\boldsymbol{g}} \cdot [\underline{\boldsymbol{V}}]_s \tag{4.32}$$

where the *s* subscript refers to the *sample coordinate system* and *c* refers to the *Cartesian crystal coordinate system* B_{hkl}. This rotation can also be expressed with a sequence of three rotations (Euler angles), or by a single vector (Rodrigues vector, [Rodrigues, 1840]). Indeed, every rotation or sequence of rotations can be represented as a single rotation around a specified axis $\underline{\boldsymbol{r}}$, with an angle of magnitude θ_c. One can define a Rodrigues vector as:

$$\underline{\boldsymbol{R}} = \tan(\theta_c/2)\underline{\boldsymbol{r}} \tag{4.33}$$

This description is more suitable for computations compared to the rotation matrix, since it requires only three components to be stored instead of nine.

Diffractometer angles and reference systems

In a topotomography experiment, the sample lies onto a 4 circles diffractometer. It is essential to clearly define the different angles and coordinate systems associated with this setup. An exhaustive review of the geometry of a 3DXRD experiment is available in [Poulsen et al., 2009]. Given a vector $[\underline{\boldsymbol{V}}]_i$ expressed in the reference system called "B_i" with its three basis vectors $([\underline{\boldsymbol{x}}]_i, [\underline{\boldsymbol{y}}]_i, [\underline{\boldsymbol{z}}]_i)$, we have:

- the crystal reference system B_{hkl}, directly attached to the crystal lattice. The three vectors $([\underline{\boldsymbol{a}}]_{hkl}, [\underline{\boldsymbol{b}}]_{hkl}, [\underline{\boldsymbol{c}}]_{hkl})$ represent the translations of the crystal unit cell in the space and $[\underline{\boldsymbol{x}}]_{hkl} = \underline{\boldsymbol{a}}$,$[\underline{\boldsymbol{y}}]_{hkl} = \underline{\boldsymbol{b}}$, and $[\underline{\boldsymbol{z}}]_{hkl} = \underline{\boldsymbol{c}}$. B_{hkl} is not necessarily a orthonormal coordinate system, for instance for deformed cubic crystals, or orthorhombic systems;

- the Cartesian crystal coordinate system B_c is defined in [Poulsen, 2004b] and [Oddershede et al., 2010] as follows: $\underline{\boldsymbol{x}}_c = \frac{\underline{\boldsymbol{a}}}{\|\underline{\boldsymbol{a}}\|}$, and $\underline{\boldsymbol{y}}_c$ is the unit vector which belongs to the $(\underline{\boldsymbol{a}}, \underline{\boldsymbol{b}})$ plane, perpendicular to $\underline{\boldsymbol{x}}_c$. Then $\underline{\boldsymbol{z}}_c =$

[9] In this work, $\underset{\sim}{\boldsymbol{g}}^{-1}$ is more often used and $\underline{\boldsymbol{V}}_s = \underset{\sim}{\boldsymbol{g}}^{-1}\underline{\boldsymbol{V}}_c$

$\underline{\boldsymbol{x}}_c \wedge \underline{\boldsymbol{y}}_c$. Given a vector $\underline{\boldsymbol{V}}$, we have $[\underline{\boldsymbol{V}}]_c = \underset{\sim}{\boldsymbol{B}} \cdot [\underline{\boldsymbol{V}}]_{hkl}$, with[10] :

$$[\underset{\sim}{\boldsymbol{B}}]_{(c,hkl)} = \begin{bmatrix} a^* & b^*\cos(\gamma^*) & c^*\cos(\beta^*) \\ 0 & b^*\sin(\gamma^*) & -c^*\sin(\beta^*)\cos(\alpha) \\ 0 & 0 & c^*\sin(\beta^*)\sin(\alpha) \end{bmatrix}_{(c,hkl)} \tag{4.34}$$

- the sample reference system B_s is attached to the sample. The correspondence between the Cartesian crystal coordinate B_c system and the sample system B_s is given by the orientation matrix of the crystal. Given a vector $\underline{\boldsymbol{V}}$, we have $[\underline{\boldsymbol{V}}]_s = \underset{\sim}{\boldsymbol{g}}^{-1}.[\underline{\boldsymbol{V}}]_c$;
- the tilted reference system, B_t. In a topotomography experiment the normal vector of a given set of (hkl) planes needs to be aligned with the axis of the rotation stage. Two single circle goniometers with perpendicular axes of rotation are superimposed, with a coincident center of rotation. Given a vector $\underline{\boldsymbol{V}}$, with the ID11 configuration of the goniometer, and (ut, lt) (see Fig. 2.7) the respective values[11] of the upper and the lower tilts, we have :

$$[\underline{\boldsymbol{V}}]_t = \underset{\sim}{\boldsymbol{S}} \cdot [\underline{\boldsymbol{V}}]_s \tag{4.35}$$

$$[\underline{\boldsymbol{V}}]_t = \begin{bmatrix} 1 & 0 & 0 \\ 0 & \cos(lt) & -\sin(lt) \\ 0 & \sin(lt) & \cos(lt) \end{bmatrix} \begin{bmatrix} \cos(ut) & 0 & \sin(ut) \\ 0 & 1 & 0 \\ -\sin(ut) & 0 & \cos(ut) \end{bmatrix} [\underline{\boldsymbol{V}}]_s \tag{4.36}$$

$$[\underline{\boldsymbol{V}}]_t = \begin{bmatrix} \cos(ut) & 0 & \sin(ut) \\ \sin(lt)\sin(ut) & \cos(lt) & -\sin(lt)\cos(ut) \\ -\cos(lt)\sin(ut) & \sin(lt) & \cos(ut)\cos(lt) \end{bmatrix}_{(s,t)} [\underline{\boldsymbol{V}}]_s \tag{4.37}$$

- the rotated coordinate system B_ω, where the tilted reference system is rotated about an angle ω around an axis perpendicular to the rotation stage. Given a vector $\underline{\boldsymbol{V}}$, we have:

$$[\underline{\boldsymbol{V}}]_\omega = \underset{\sim}{\boldsymbol{\Omega}} \cdot [\underline{\boldsymbol{V}}]_t = \begin{bmatrix} \cos(\omega) & -\sin(\omega) & 0 \\ \sin(\omega) & \cos(\omega) & 0 \\ 0 & 0 & 1 \end{bmatrix}_{(\omega,t)} [\underline{\boldsymbol{V}}]_t \tag{4.38}$$

- the laboratory coordinate system B_l, where $\underline{\boldsymbol{x}}_l$ is along the X-ray beam, $\underline{\boldsymbol{z}}_l$ along the gravity and pointing up, and $\underline{\boldsymbol{y}}_c = \underline{\boldsymbol{z}}_c \wedge \underline{\boldsymbol{x}}_c$. B_ω is tilted by

[10] $(a, b, c, \alpha, \beta, \gamma)$ and $(a^*, b^*, c^*, \alpha^*, \beta^*, \gamma^*)$ respectively refer to the lattice parameters in the direct and the reciprocal space. It is illustrated in Fig. 4.17

[11] Note that in the case of a DCT scan $ut = lt = 0$

an angle Θ (the base tilt) around an axis parallel to $\underline{\boldsymbol{y}}_c$, and given a vector $\underline{\boldsymbol{V}}$ we have:

$$[\underline{\boldsymbol{V}}]_l = \underset{\sim}{\boldsymbol{T}} \cdot [\underline{\boldsymbol{V}}]_\omega = \begin{bmatrix} \cos(\Theta) & 0 & \sin(\Theta) \\ 0 & 1 & 0 \\ -\sin(\Theta) & 0 & \cos(\Theta) \end{bmatrix}_{(l,\omega)} \cdot [\underline{\boldsymbol{V}}]_\omega \tag{4.39}$$

The fundamental equation of the diffractometer can be therefore written as:

$$[\underline{\boldsymbol{V}}]_l = \left[\underset{\sim}{\boldsymbol{T}}\underset{\sim}{\boldsymbol{\Omega}}\underset{\sim}{\boldsymbol{S}}\underset{\sim}{\boldsymbol{g}}^{-1}\underset{\sim}{\boldsymbol{B}}\right][\underline{\boldsymbol{V}}]_{hkl} \tag{4.40}$$

4.5.2 Geometric principles of diffraction in 3D

In this section, it is assumed that a grain or a single crystal volume element is a perfect single crystal, without any orientation spread.

The general three-dimensional diffraction condition

We consider that a (hkl) set of planes illuminated by a X-ray radiation of wavelength λ and located at the origin of the laboratory reference system gives rise to a diffraction event, characterized by the angles pair $(2\theta, \eta)$ with reference to a plane detector as shown in Fig. 4.15. With the formalism of the Ewald sphere in Fig. 4.16, we define $\underline{\boldsymbol{G}}$ the scattering vector as followed:

$$\underline{\boldsymbol{G}} = \underline{\boldsymbol{K}} - \underline{\boldsymbol{X}} \tag{4.41}$$

with $\underline{\boldsymbol{X}}$ the incident wave vector, and $\underline{\boldsymbol{K}}$ the diffracted wave vector. They both have a norm of $1/\lambda$, one radius[12] of the sphere. $\underline{\boldsymbol{G}}$ is normal to the diffracting planes, and we define $\underline{\boldsymbol{H}} = \dfrac{\underline{\boldsymbol{G}}}{\|\underline{\boldsymbol{G}}\|}$ the normalized scattering vector.

From eq. 4.41 we have:

[12]Note that in numerous crystallographic books, as well in [Poulsen, 2004b], the radius of the Ewald's sphere is $\dfrac{2\pi}{\lambda}$.

$$\cos(\theta - \frac{\pi}{2}) = \frac{\underline{\boldsymbol{X}} \cdot \underline{\boldsymbol{G}}}{\|\underline{\boldsymbol{X}}\| \, \|\underline{\boldsymbol{G}}\|} \tag{4.42}$$

$$\sin\theta = \begin{bmatrix} 1 \\ 0 \\ 0 \end{bmatrix}_l \cdot \frac{\underline{\boldsymbol{G}}}{\|\underline{\boldsymbol{G}}\|} \tag{4.43}$$

$$\sin\theta = \frac{1}{\|\underline{\boldsymbol{G}}\|} \cdot \begin{bmatrix} 1 \\ 0 \\ 0 \end{bmatrix}_l \underset{\sim}{\boldsymbol{T}}\underset{\sim}{\boldsymbol{\Omega}}\underset{\sim}{\boldsymbol{S}}\underset{\sim}{\boldsymbol{g}}^{-1}\underset{\sim}{\boldsymbol{B}} \begin{bmatrix} h \\ k \\ l \end{bmatrix}_{hkl} \tag{4.44}$$

$$\|\underline{\boldsymbol{G}}\| \sin\theta = \left[\underset{\sim}{\boldsymbol{T}}\underset{\sim}{\boldsymbol{\Omega}}\underset{\sim}{\boldsymbol{S}}\underset{\sim}{\boldsymbol{g}}^{-1}\underset{\sim}{\boldsymbol{B}} \begin{bmatrix} h \\ k \\ l \end{bmatrix}_{hkl} \right]_1 \tag{4.45}$$

$$\frac{2\sin^2\theta}{\lambda} = \left[\underset{\sim}{\boldsymbol{T}}\underset{\sim}{\boldsymbol{\Omega}}\underset{\sim}{\boldsymbol{S}}\underset{\sim}{\boldsymbol{g}}^{-1}\underset{\sim}{\boldsymbol{B}} \begin{bmatrix} h \\ k \\ l \end{bmatrix}_{hkl} \right]_1 \tag{4.46}$$

This is the Bragg diffraction condition in 3D. Any (hkl) set of planes satisfying this condition will generate a diffraction event.

The DCT case

In a DCT experiment, $\Theta = ut = lt = 0$, the diffraction condition (4.46) can be written as:

$$\frac{2\sin^2(\theta)}{\lambda} = \left[\underset{\sim}{\boldsymbol{\Omega}}\underset{\sim}{\boldsymbol{g}}^{-1}\underset{\sim}{\boldsymbol{B}} \begin{bmatrix} h \\ k \\ l \end{bmatrix}_{hkl} \right]_1 \tag{4.47}$$

This relation is useful to predict the ω positions of the rotation stage where a grain with an orientation $\underset{\sim}{\boldsymbol{g}}^{-1}$ will fulfill the diffraction condition. Let us call p,q,r the components of the scattering vector expressed in the sample coordinate system $\underline{\boldsymbol{G}}_s$:

$$\underline{\boldsymbol{G}}_s = \underset{\sim}{\boldsymbol{g}}^{-1}\underset{\sim}{\boldsymbol{B}} \begin{bmatrix} h \\ k \\ l \end{bmatrix}_{hkl} = \begin{bmatrix} p \\ q \\ r \end{bmatrix}_s \tag{4.48}$$

The topotomographic case

In a topotomographic experiment the normal of a (hkl) set of planes is aligned with the rotation axis of the tomographic rotation stage ω. Given $\underline{\boldsymbol{H}}$ the normalized scattering vector as defined previously, we have:

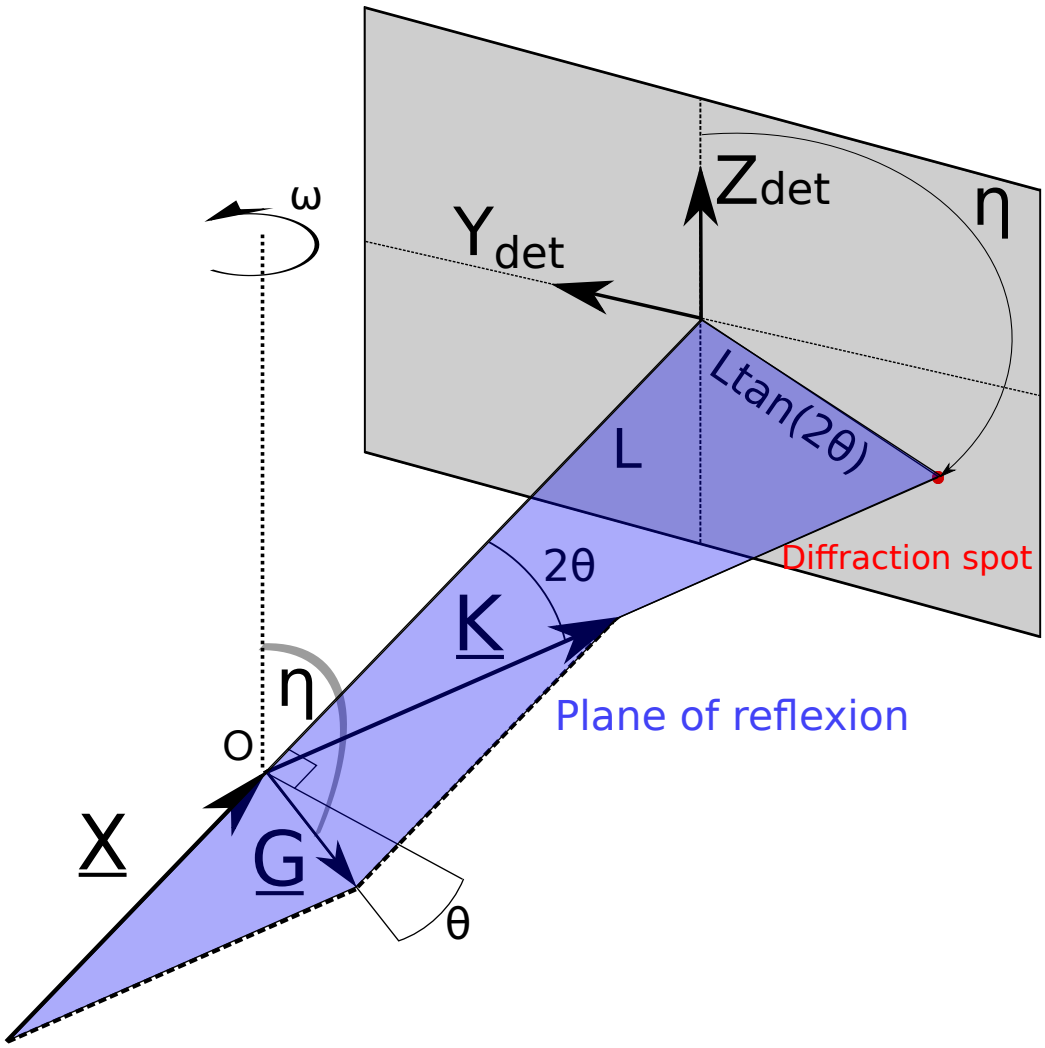

Figure 4.15 – The 3DXRD setup, adapted from [Poulsen, 2004b]. The Bragg condition is usually represented in the plane filled in blue.

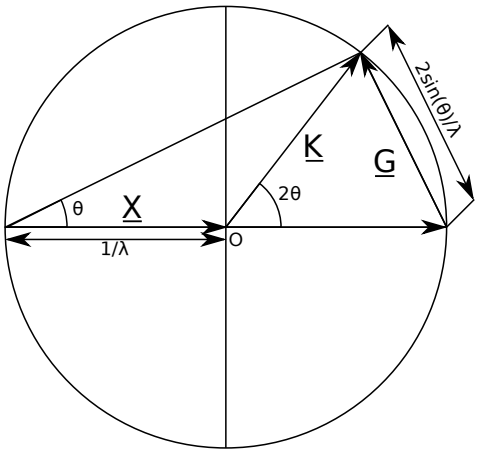

Figure 4.16 – The Ewald sphere of diffraction.

$$\underline{\boldsymbol{H}}_{\omega} = \underline{\boldsymbol{H}}_{t} = \begin{bmatrix} 0 \\ 0 \\ 1 \end{bmatrix}_{l} \tag{4.49}$$

If the orientation of a crystal is known, like after a DCT reconstruction, it is straightforward to determine the tilts angles needed to align the normal of a set of (hkl) planes and achieve Eq. 4.48:

$$\underline{\boldsymbol{G}}_{s} = \begin{bmatrix} p \\ q \\ r \end{bmatrix}_{s} = \left[\underset{\sim}{\boldsymbol{S}} \underset{\sim}{\boldsymbol{g}}^{-1} \underset{\sim}{\boldsymbol{B}} \right] \begin{bmatrix} h \\ k \\ l \end{bmatrix}_{hkl} \tag{4.50}$$

$$ut = \arctan(-\frac{p}{r}) \tag{4.51}$$

$$lt = \arctan\left[\frac{q}{-p\sin(ut) + r\cos(ut)} \right] \tag{4.52}$$

The two latter equations represent the fact that the alignment is made by two successive rotations, and they are valid for the ID11 goniometer configuration described previously. The first rotation (upper tilt) consists in bringing back the plane normal to the $(\underline{\boldsymbol{y}}_{\omega}, \underline{\boldsymbol{z}}_{\omega})$ plane, the second one (lower tilt) making the tilted normal and the rotation axis $\underline{\boldsymbol{z}}_{\omega}$ colinear.

With the tilt angles applied, the whole setup needs to be tilted with respect to the base tilt T_0. Then, the Bragg condition will remain valid for all the ω values, and $\Theta = \theta_{Bragg}$. The whole diffractometer configuration is shown in Fig. 2.7.

4.5.3 Generating 3D rocking curves

In this section, we consider a real crystal where mosaicity exists. The different dislocation densities, respectively the statistically stored dislocation density (ρ_{SSD}) and the geometrically necessary dislocation density (ρ_{GND} introduced by [Ashby, 1970] and presented in Sec. 4.1.3) develop because of the deformation. Due to the GNDs, gradients of crystal orientation arise, leading to local modification of the Bragg condition. It is therefore required to rock the sample with the base tilt motor to ensure that the whole volume of the grain will diffract. The next subsection shows how it is possible to correct the sample position with the base tilt to fulfill the Bragg condition with a locally homogeneously deformed subvolume of a grain. In the next subsection, we first consider a material point where the deformation induces only lattice rotation, and then consider the more general case, where both lattice rotation and lattice stretching take place. The 0 subscript refers to the undeformed lattice, whereas scalars, vectors, tensors without subscripts refer to the actual deformed state (i.e. $a, b, c, \alpha, \beta, \gamma$ refers to the deformed lattice parameters, $a_0, b_0, c_0, \alpha_0, \beta_0, \gamma_0$ refers to the undeformed lattice parameters).

Equations to solve to generate a rocking curve

Here we consider a grain with an orientation $\mathbf{g_0^{-1}}$ aligned in a topotomographic sense as previously described. Due to the deformation process deformation gradient arise, and locally the orientation of the crystal is[13] $\mathbf{g^{-1}}$. Since (ut, lt) are the angles to align a crystal with an orientation $\mathbf{g^{-1}}$, we have:

$$\left[\underset{\sim}{\boldsymbol{\Omega}}\underset{\sim}{\boldsymbol{S}}\underset{\sim}{\boldsymbol{g}}^{-1}\underset{\sim}{\boldsymbol{B}}\right]\begin{bmatrix}h\\k\\l\end{bmatrix}_{hkl} = \begin{bmatrix}p\\q\\r\end{bmatrix}_{l} \tag{4.53}$$

The problem consists in finding the Θ value where this misoriented material point will fulfill the Bragg condition. It is important to clearly understand the difference between Θ and θ_{Bragg}, since they differ in nature. Θ is the value of the tilt applied by the base tilt motor T_0, whereas θ_{Bragg} is a material parameter associated to a given d spacing and wavelength λ: $\theta = \arcsin\dfrac{\lambda}{2d}$. In the case of a perfect crystal, $\Theta = \theta_{Bragg}$. Referring to the 3D diffraction condition (4.46) we have:

[13] The sensitivity of the diffraction condition with respect to a given rotation is given by bandwidth of the source $\Delta\lambda/\lambda$.

$$\frac{2\sin^2(\theta)}{\lambda} = \left[\begin{bmatrix} \cos(\Theta) & 0 & \sin(\Theta) \\ 0 & 1 & 0 \\ -\sin(\Theta) & 0 & \cos(\Theta) \end{bmatrix} \begin{bmatrix} p \\ q \\ r \end{bmatrix}_{hkl}\right]_1 \tag{4.54}$$

$$\frac{2\sin^2(\theta)}{\lambda} = p\cos(\Theta) + r\sin(\Theta) \tag{4.55}$$

This trigonometric equation can be solved by the methodology exposed in (App. B), and one finds:

$$\Theta = 2\arctan\left[\frac{r \pm \frac{1}{2}\sqrt{p^2 + r^2 - \frac{\sin^4\theta}{\lambda}}}{p + 2\sin^2\lambda}\right] \tag{4.56}$$

The closest solution to θ_{Bragg} is kept to produce the rocking curves.

The stretched crystal case

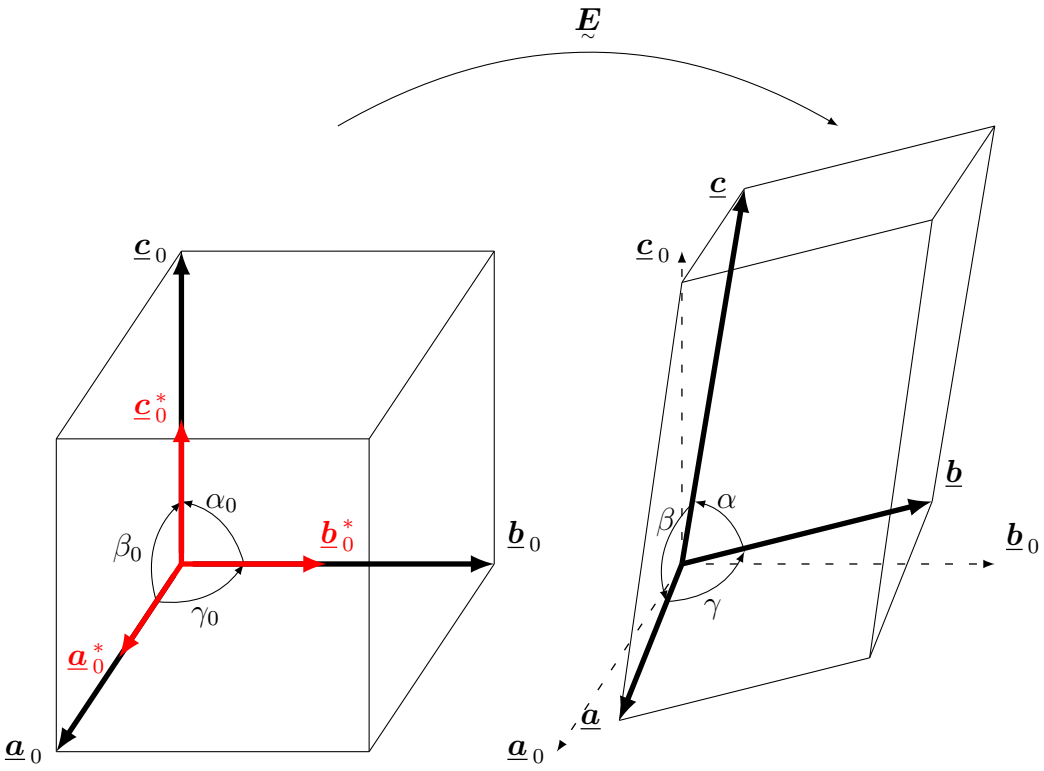

Figure 4.17 – Transformation of a cubic lattice cell by $\underset{\sim}{\boldsymbol{E}}$

In this section, we add the possibility that the elastic part of the deformation gradient $\underset{\sim}{\boldsymbol{E}}$ (see Eq. 4.1) maps real space lattice vectors[14] $(\underline{\boldsymbol{a}}_0, \underline{\boldsymbol{b}}_0, \underline{\boldsymbol{c}}_0)$ into $(\underline{\boldsymbol{a}}, \underline{\boldsymbol{b}}, \underline{\boldsymbol{c}})$ as shown in Fig. 4.17.

The previous equations of diffraction are valid for both the deformed and undeformed states. The stretches of the lattice are carried by the so-called $\mathbf{B}$ matrix as defined in Eq. 4.34. As shown in Fig. 4.1, only the elastic part $\underset{\sim}{\boldsymbol{E}}$ of $\underset{\sim}{\boldsymbol{F}}$ is involved in the distorsion of the lattice. The plastic part $\underset{\sim}{\boldsymbol{P}}$ will modify material directions, but will not change crystallographic directions. The six lattice parameters $(a_0, b_0, c_0, \alpha_0, \beta_0, \gamma_0)$ need to be updated to $(a, b, c, \alpha, \beta, \gamma)$ to compute the $\underset{\sim}{\boldsymbol{B}}$ matrix in the deformed state. The basic vectors in the deformed state can be expressed in function of $\underset{\sim}{\boldsymbol{E}}$ and of the initial ones:

$$\underline{\boldsymbol{a}} = \underset{\sim}{\boldsymbol{E}} \cdot \underline{\boldsymbol{a}}_0 \tag{4.57}$$

$$\underline{\boldsymbol{b}} = \underset{\sim}{\boldsymbol{E}} \cdot \underline{\boldsymbol{b}}_0 \tag{4.58}$$

$$\underline{\boldsymbol{c}} = \underset{\sim}{\boldsymbol{E}} \cdot \underline{\boldsymbol{c}}_0 \tag{4.59}$$

From [Shmueli, 2008], we define the reciprocal lattice vectors in the undeformed state:

$$\underline{\boldsymbol{a}}_0^* = \frac{\underline{\boldsymbol{b}}_0 \wedge \underline{\boldsymbol{c}}_0}{V_0} \text{ and } \underline{\boldsymbol{a}}^* = \frac{\underline{\boldsymbol{b}} \wedge \underline{\boldsymbol{c}}}{V} \tag{4.60}$$

$$\underline{\boldsymbol{b}}_0^* = \frac{\underline{\boldsymbol{c}}_0 \wedge \underline{\boldsymbol{a}}_0}{V_0} \text{ and } \underline{\boldsymbol{b}}^* = \frac{\underline{\boldsymbol{c}} \wedge \underline{\boldsymbol{a}}}{V} \tag{4.61}$$

$$\underline{\boldsymbol{c}}_0^* = \frac{\underline{\boldsymbol{a}}_0 \wedge \underline{\boldsymbol{b}}_0}{V_0} \text{ and } \underline{\boldsymbol{c}}^* = \frac{\underline{\boldsymbol{a}} \wedge \underline{\boldsymbol{b}}}{V} \tag{4.62}$$

where the volumes of both direct lattice and reciprocal lattice cells in the undeformed state are:

$$V_0 = (\underline{\boldsymbol{a}}_0 \wedge \underline{\boldsymbol{b}}_0) \cdot \underline{\boldsymbol{c}}_0 = \det[\underline{\boldsymbol{a}}_0, \underline{\boldsymbol{b}}_0, \underline{\boldsymbol{c}}_0] \tag{4.63}$$

$$V_0^* = (\underline{\boldsymbol{a}}_0^* \wedge \underline{\boldsymbol{b}}_0^*) \cdot \underline{\boldsymbol{c}}_0^* = \det[\underline{\boldsymbol{a}}_0^*, \underline{\boldsymbol{b}}_0^*, \underline{\boldsymbol{c}}_0^*] \tag{4.64}$$

It is then possible to compute these volumes in the deformed state. From [Forest et al., 2015], we know that $J_e = \det(\underset{\sim}{\boldsymbol{E}})$ is the volume variation of an elementary volume V_0:

$$V = \det(\underset{\sim}{\boldsymbol{E}}) V_0 = J_e V_0 \tag{4.65}$$

$$V^* = \frac{1}{V} \tag{4.66}$$

[14] All the 0 subscripts refer to the undeformed state.

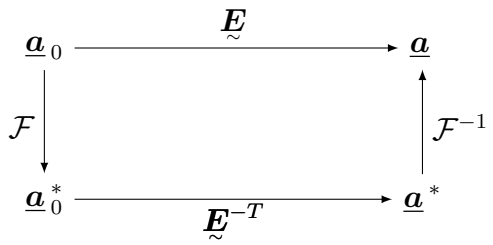

Figure 4.18 – Correspondence between the direct and reciprocal lattice vectors in both undeformed and deformed states. $\mathcal{F}$ denotes the Fourrier transform.

To compute the reciprocal lattice vectors in the deformed state, we need to define the vector product of two deformed lattice vectors. For that, we introduce a given vector $\underline{\boldsymbol{v}}$:

$$\begin{aligned}
(\underline{\boldsymbol{b}} \wedge \underline{\boldsymbol{c}}) \cdot \underline{\boldsymbol{v}} &= \det[\underline{\boldsymbol{b}}, \underline{\boldsymbol{c}}, \underline{\boldsymbol{v}}] \\
&= \det[\underset{\sim}{\boldsymbol{E}} \cdot \underline{\boldsymbol{b}}_0, \underset{\sim}{\boldsymbol{E}} \cdot \underline{\boldsymbol{c}}_0, \underline{\boldsymbol{v}}] \\
&= J_e \det[\underline{\boldsymbol{b}}_0, \underline{\boldsymbol{c}}_0, \underset{\sim}{\boldsymbol{E}}^{-1} \cdot \underline{\boldsymbol{v}}] \\
&= J_e (\underline{\boldsymbol{b}}_0 \wedge \underline{\boldsymbol{c}}_0) \cdot (\underset{\sim}{\boldsymbol{E}}^{-1} \cdot \underline{\boldsymbol{v}}) \\
&= J_e V_0 \underline{\boldsymbol{a}}_0^* \cdot (\underset{\sim}{\boldsymbol{E}}^{-1} \cdot \underline{\boldsymbol{v}}) \\
&= J_e V_0 (\underset{\sim}{\boldsymbol{E}}^{-T} \cdot \underline{\boldsymbol{a}}_0^*) \cdot \underline{\boldsymbol{v}}
\end{aligned} \tag{4.67}$$

We can now write the reciprocal lattice vectors in the deformed state[15]. The correspondence between the different lattice vectors in the different configurations is summed up in Fig. 4.18:

$$\underline{\boldsymbol{a}}^* = \frac{\underline{\boldsymbol{b}} \wedge \underline{\boldsymbol{c}}}{V} = \underset{\sim}{\boldsymbol{E}}^{-T} \cdot \underline{\boldsymbol{a}}_0^* \tag{4.68}$$

$$\underline{\boldsymbol{b}}^* = \frac{\underline{\boldsymbol{c}} \wedge \underline{\boldsymbol{a}}}{V} = \underset{\sim}{\boldsymbol{E}}^{-T} \cdot \underline{\boldsymbol{b}}_0^* \tag{4.69}$$

$$\underline{\boldsymbol{c}}^* = \frac{\underline{\boldsymbol{a}} \wedge \underline{\boldsymbol{b}}}{V} = \underset{\sim}{\boldsymbol{E}}^{-T} \cdot \underline{\boldsymbol{c}}_0^* \tag{4.70}$$

$$\tag{4.71}$$

Now we can compute the lattice parameters in the deformed state. The norm of a deformed lattice vector is:

$$a^2 = \underline{\boldsymbol{a}} \cdot \underline{\boldsymbol{a}} = \underline{\boldsymbol{a}}_0 \cdot (\underset{\sim}{\boldsymbol{E}}^T \cdot \underset{\sim}{\boldsymbol{E}}) \cdot \underline{\boldsymbol{a}}_0 = \underline{\boldsymbol{a}}_0 \cdot \underset{\sim}{\boldsymbol{U}}^{e2} \cdot \underline{\boldsymbol{a}}_0 \tag{4.72}$$

$$a^{*2} = \underline{\boldsymbol{a}}^* \cdot \underline{\boldsymbol{a}}^* = \underline{\boldsymbol{a}}_0^* \cdot (\underset{\sim}{\boldsymbol{E}}^{-1} \cdot \underset{\sim}{\boldsymbol{E}}^{-T}) \cdot \underline{\boldsymbol{a}}_0^* = \underline{\boldsymbol{a}}_0^* \cdot \underset{\sim}{\boldsymbol{U}}^{e-2} \cdot \underline{\boldsymbol{a}}_0^* \tag{4.73}$$

[15] $\underset{\sim}{\boldsymbol{E}} = \underset{\sim}{\boldsymbol{R}}^e \cdot \underset{\sim}{\boldsymbol{U}}^e$ and $\underset{\sim}{\boldsymbol{E}}^{-T} = \underset{\sim}{\boldsymbol{R}}^e \cdot \underset{\sim}{\boldsymbol{U}}^{e-1}$.

and

$$b^2 = \underline{\boldsymbol{b}}_0 \cdot \underset{\sim}{\boldsymbol{U}}^{e2} \cdot \underline{\boldsymbol{b}}_0 \tag{4.74}$$

$$c^2 = \underline{\boldsymbol{c}}_0 \cdot \underset{\sim}{\boldsymbol{U}}^{e2} \cdot \underline{\boldsymbol{b}}_0 \tag{4.75}$$

$$b^{*2} = \underline{\boldsymbol{b}}_0^* \cdot \underset{\sim}{\boldsymbol{U}}^{e-2} \cdot \underline{\boldsymbol{b}}_0^* \tag{4.76}$$

$$c^{*2} = \underline{\boldsymbol{c}}_0^* \cdot \underset{\sim}{\boldsymbol{U}}^{e-2} \cdot \underline{\boldsymbol{c}}_0^* \tag{4.77}$$

Finally, we need to compute the (α, β, γ) angles. In the direct space, and from Eq. 4.67:

$$\sin\gamma = \frac{\|\underline{\boldsymbol{a}} \wedge \underline{\boldsymbol{b}}\|}{ab} = \frac{V \underset{\sim}{\boldsymbol{E}}^{-T} \underline{\boldsymbol{c}}_0^*}{ab} \tag{4.78}$$

$$= J_e \frac{\left\| \underset{\sim}{\boldsymbol{E}}^{-T} \cdot (\underline{\boldsymbol{a}}_0 \wedge \underline{\boldsymbol{b}}_0) \right\|}{\sqrt{\underline{\boldsymbol{a}}_0 \cdot \underset{\sim}{\boldsymbol{U}}^{e2} \cdot \underline{\boldsymbol{a}}_0} \sqrt{\underline{\boldsymbol{b}}_0 \cdot \underset{\sim}{\boldsymbol{U}}^{e2} \cdot \underline{\boldsymbol{b}}_0}} \tag{4.79}$$

$$\cos\gamma = \frac{\underline{\boldsymbol{a}} \cdot \underline{\boldsymbol{b}}}{ab} \tag{4.80}$$

$$= \frac{\underline{\boldsymbol{a}}_0 \cdot \underset{\sim}{\boldsymbol{U}}^{e2} \cdot \underline{\boldsymbol{b}}_0}{\sqrt{\underline{\boldsymbol{a}}_0 \cdot \underset{\sim}{\boldsymbol{U}}^{e2} \cdot \underline{\boldsymbol{a}}_0} \sqrt{\underline{\boldsymbol{b}}_0 \cdot \underset{\sim}{\boldsymbol{U}}^{e2} \cdot \underline{\boldsymbol{b}}_0}} \tag{4.81}$$

$$\sin\alpha = J_e \frac{\left\| \underset{\sim}{\boldsymbol{E}}^{-T} \cdot (\underline{\boldsymbol{b}}_0 \wedge \underline{\boldsymbol{c}}_0) \right\|}{\sqrt{\underline{\boldsymbol{b}}_0 \cdot \underset{\sim}{\boldsymbol{U}}^{e2} \cdot \underline{\boldsymbol{b}}_0} \sqrt{\underline{\boldsymbol{c}}_0 \cdot \underset{\sim}{\boldsymbol{U}}^{e2} \cdot \underline{\boldsymbol{c}}_0}} \tag{4.82}$$

$$\cos\alpha = \frac{\underline{\boldsymbol{b}}_0 \cdot \underset{\sim}{\boldsymbol{U}}^{e2} \cdot \underline{\boldsymbol{c}}_0}{\sqrt{\underline{\boldsymbol{b}}_0 \cdot \underset{\sim}{\boldsymbol{U}}^{e2} \cdot \underline{\boldsymbol{b}}_0} \sqrt{\underline{\boldsymbol{c}}_0 \cdot \underset{\sim}{\boldsymbol{U}}^{e2} \cdot \underline{\boldsymbol{c}}_0}} \tag{4.83}$$

$$\sin\beta = J_e \frac{\left\| \underset{\sim}{\boldsymbol{E}}^{-T} \cdot (\underline{\boldsymbol{c}}_0 \wedge \underline{\boldsymbol{a}}_0) \right\|}{\sqrt{\underline{\boldsymbol{c}}_0 \cdot \underset{\sim}{\boldsymbol{U}}^{e2} \cdot \underline{\boldsymbol{c}}_0} \sqrt{\underline{\boldsymbol{a}}_0 \cdot \underset{\sim}{\boldsymbol{U}}^{e2} \cdot \underline{\boldsymbol{a}}_0}} \tag{4.84}$$

$$\cos\beta = \frac{\underline{\boldsymbol{c}}_0 \cdot \underset{\sim}{\boldsymbol{U}}^{e2} \cdot \underline{\boldsymbol{a}}_0}{\sqrt{\underline{\boldsymbol{c}}_0 \cdot \underset{\sim}{\boldsymbol{U}}^{e2} \cdot \underline{\boldsymbol{c}}_0} \sqrt{\underline{\boldsymbol{a}}_0 \cdot \underset{\sim}{\boldsymbol{U}}^{e2} \cdot \underline{\boldsymbol{a}}_0}} \tag{4.85}$$

In the reciprocal space, and:

$$\begin{aligned}\sin\gamma^* &= \frac{\|\underline{\boldsymbol{a}}^* \wedge \underline{\boldsymbol{b}}^*\|}{a^* b^*} \\ &= J_e \frac{\|\underset{\sim}{\boldsymbol{E}} \cdot (\underline{\boldsymbol{a}}_0^* \wedge \underline{\boldsymbol{b}}_0^*)\|}{\sqrt{\underline{\boldsymbol{a}}_0^* \cdot \underset{\sim}{\boldsymbol{U}}^{e-2} \cdot \underline{\boldsymbol{a}}_0^*}\sqrt{\underline{\boldsymbol{b}}_0^* \cdot \underset{\sim}{\boldsymbol{U}}^{e-2} \cdot \underline{\boldsymbol{b}}_0^*}} \end{aligned} \tag{4.86}$$

$$\begin{aligned}\cos\gamma^* &= \frac{\underline{\boldsymbol{a}}^* \cdot \underline{\boldsymbol{b}}^*}{a^* b^*} \\ &= \frac{\underline{\boldsymbol{a}}_0^* \cdot \underset{\sim}{\boldsymbol{U}}^{e-2} \cdot \underline{\boldsymbol{b}}_0^*}{\sqrt{\underline{\boldsymbol{a}}_0^* \cdot \underset{\sim}{\boldsymbol{U}}^{e-2} \cdot \underline{\boldsymbol{a}}_0^*}\sqrt{\underline{\boldsymbol{b}}_0^* \cdot \underset{\sim}{\boldsymbol{U}}^{e-2} \cdot \underline{\boldsymbol{b}}_0^*}} \end{aligned} \tag{4.87}$$

and

$$\sin\alpha^* = J_e \frac{\|\underset{\sim}{\boldsymbol{E}} \cdot (\underline{\boldsymbol{b}}_0^* \wedge \underline{\boldsymbol{c}}_0^*)\|}{\sqrt{\underline{\boldsymbol{b}}_0^* \cdot \underset{\sim}{\boldsymbol{U}}^{e-2} \cdot \underline{\boldsymbol{b}}_0^*}\sqrt{\underline{\boldsymbol{c}}_0^* \cdot \underset{\sim}{\boldsymbol{U}}^{e-2} \cdot \underline{\boldsymbol{c}}_0^*}} \tag{4.88}$$

$$\cos\alpha^* = \frac{\underline{\boldsymbol{b}}_0^* \cdot \underset{\sim}{\boldsymbol{U}}^{e-2} \cdot \underline{\boldsymbol{c}}_0^*}{\sqrt{\underline{\boldsymbol{b}}_0^* \cdot \underset{\sim}{\boldsymbol{U}}^{e-2} \cdot \underline{\boldsymbol{b}}_0^*}\sqrt{\underline{\boldsymbol{c}}_0^* \cdot \underset{\sim}{\boldsymbol{U}}^{e-2} \cdot \underline{\boldsymbol{c}}_0^*}} \tag{4.89}$$

$$\sin\beta^* = J_e \frac{\|\underset{\sim}{\boldsymbol{E}} \cdot (\underline{\boldsymbol{c}}_0^* \wedge \underline{\boldsymbol{a}}_0^*)\|}{\sqrt{\underline{\boldsymbol{c}}_0^* \cdot \underset{\sim}{\boldsymbol{U}}^{e-2} \cdot \underline{\boldsymbol{c}}_0^*}\sqrt{\underline{\boldsymbol{a}}_0^* \cdot \underset{\sim}{\boldsymbol{U}}^{e-2} \cdot \underline{\boldsymbol{a}}_0^*}} \tag{4.90}$$

$$\cos\beta^* = \frac{\underline{\boldsymbol{c}}_0^* \cdot \underset{\sim}{\boldsymbol{U}}^{e-2} \cdot \underline{\boldsymbol{a}}_0^*}{\sqrt{\underline{\boldsymbol{c}}_0^* \cdot \underset{\sim}{\boldsymbol{U}}^{e-2} \cdot \underline{\boldsymbol{c}}_0^*}\sqrt{\underline{\boldsymbol{a}}_0^* \cdot \underset{\sim}{\boldsymbol{U}}^{e-2} \cdot \underline{\boldsymbol{a}}_0^*}} \tag{4.91}$$

All the lattice parameters in the deformed state for both direct and reciprocal spaces are now known, and it is possible to compute the diffraction condition for a deformed lattice cell.

Computation of the Bragg angle for deformed crystals

The last parameter needed to compute a 3D diffraction condition for a deformed crystal is the actual interplanar distance d^{hkl}. Under loading, the d^{hkl} changes lead to modifications of the Bragg angle. The scattering vector is defined by:

$$\underline{\boldsymbol{h}} = h\underline{\boldsymbol{a}}^* + k\underline{\boldsymbol{b}}^* + l\underline{\boldsymbol{c}}^* \tag{4.92}$$

$$= \underset{\sim}{\boldsymbol{E}}^{-T} \cdot (h\underline{\boldsymbol{a}}_0^* + k\underline{\boldsymbol{b}}_0^* + l\underline{\boldsymbol{c}}_0^*) \tag{4.93}$$

$$\underline{\boldsymbol{h}} = \underset{\sim}{\boldsymbol{E}}^{-T} \cdot \underline{\boldsymbol{h}}_0 \tag{4.94}$$

From the previous equation, the squared norm of the scattering vector is:

$$\|\underline{\boldsymbol{h}}\|^2 = (h\underline{\boldsymbol{a}}^* + k\underline{\boldsymbol{b}}^* + l\underline{\boldsymbol{c}}^*)^2 \tag{4.95}$$
$$= h^2a^{*2} + k^2b^{*2} + l^2c^{*2} \tag{4.96}$$
$$+ 2(hka^*b^*\cos\gamma^* + hla^*c^*\cos\beta^* + klb^*c^*\cos\alpha^*) \tag{4.97}$$

Given the initial interplanar distance d_0^{hkl}, we have:

$$d_{hkl} = \frac{1}{\|\underline{\boldsymbol{h}}\|} = \frac{1}{\left\|\underset{\sim}{\boldsymbol{E}}^{-T}\cdot\underline{\boldsymbol{h}}_0\right\|} = \frac{d^0_{hkl}}{\left\|\underset{\sim}{\boldsymbol{E}}^{-T}\cdot\frac{\underline{\boldsymbol{h}}_0}{\|\underline{\boldsymbol{h}}_0\|}\right\|} \tag{4.98}$$

And the strain along an (hkl) direction can be written:

$$\varepsilon_{hkl} = \frac{d_{hkl} - d^0_{hkl}}{d^0_{hkl}} = \frac{\|\underline{\boldsymbol{h}}\|^{-1} - \|\underline{\boldsymbol{h}}_0\|^{-1}}{\|\underline{\boldsymbol{h}}_0\|^{-1}} = \frac{\|\underline{\boldsymbol{h}}_0\|}{\left\|\underset{\sim}{\boldsymbol{E}}^{-T}\cdot\underline{\boldsymbol{h}}_0\right\|} - 1 \tag{4.99}$$

The Bragg angle in the deformed crystal is:

$$\theta = \arcsin\frac{\lambda}{2d_{hkl}} = \arcsin\frac{\lambda\left\|\underset{\sim}{\boldsymbol{E}}^{-T}\cdot\underline{\boldsymbol{h}}_0\right\|}{2} \quad \text{with} \quad \|\underline{\boldsymbol{h}}_0\|^{-1} = d^0_{hkl} \tag{4.100}$$

Resolution strategy and algorithm

The algorithm used to generate synthetic rocking curves is based on the determination of Θ_n, for each element n of a grain meshed by N tetrahedron, by solving Eq. 4.56. The main assumption of the present study is that under kinematical diffraction, the intensity of the diffracted beam is proportional to the diffracting volume. Knowing, the exact position of the base tilt motor T_0 needed to fulfill the Bragg condition (the Θ angle) for each subvolume (here an element of the mesh), it is possible to generate a histogram representing the diffracted intensity over the Θ position, which is strictly equivalent to a rocking curve measured at a synchrotron beamline during a diffraction experiment. The flow chart of the script is shown in Fig. 4.19.

A Z-set postprocessing script computes for each time step, and for each element of the selected meshed grain, the components of the $\underset{\sim}{\boldsymbol{E}}$ and $\underset{\sim}{\boldsymbol{R}}^{\mathbf{e}}$ tensors, and the volume of this element. These values are stored in an ASCII file, convenient to be read by a python routine. The routine needs information relative to the experiment. The λ wavelength, the initial lattice parameters, $a_0, b_0, c_0, \alpha_0, \beta_0, \gamma_0$, and the initial grain orientation $\underset{\sim}{\boldsymbol{g}}_0$ will represent the material exposed to the X-ray radiations. Finally, the (hkl) set of planes must be given to simulate the topotomographic experiment. From these information, a (ut, lt) pair is calculated to have all the geometric parameters of the experiment.

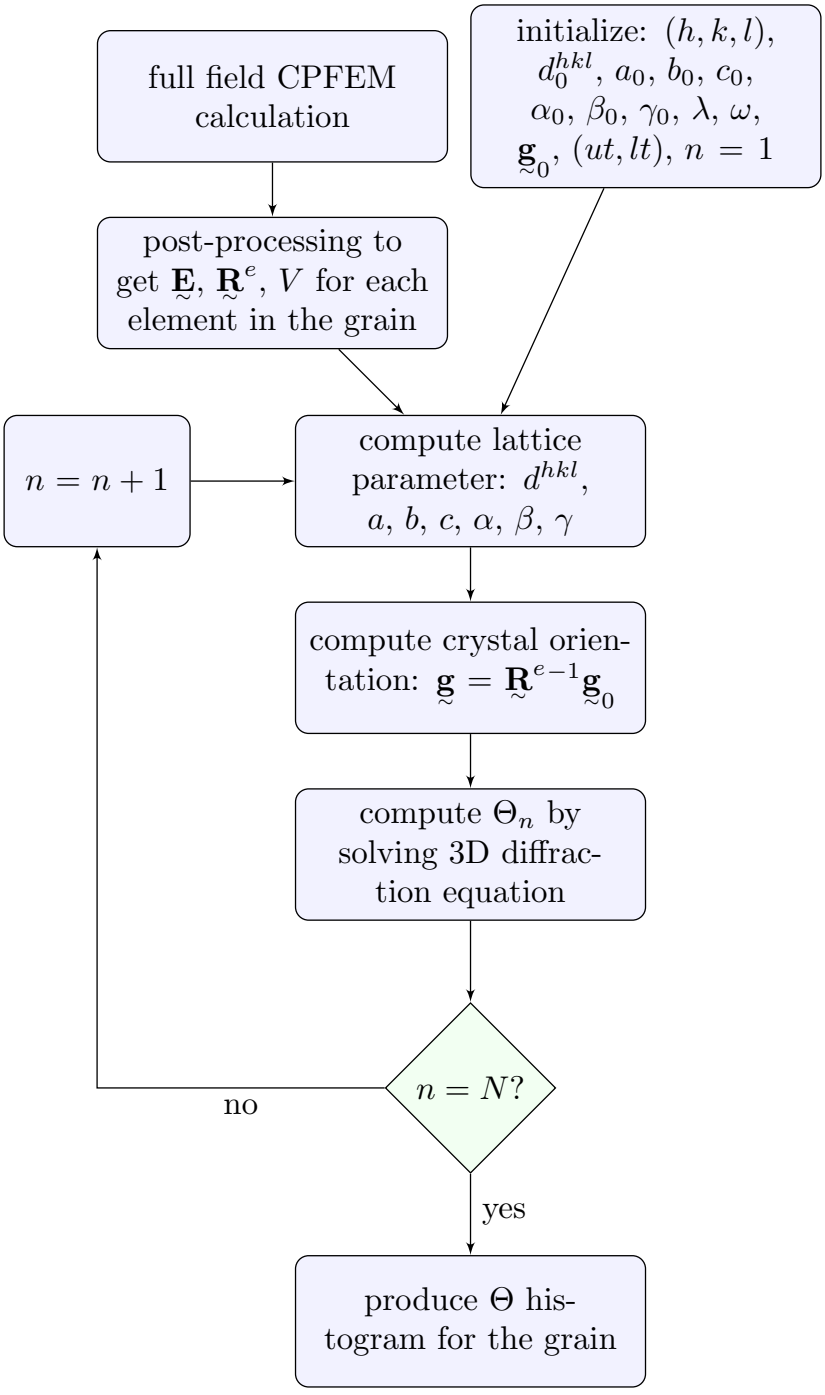

Figure 4.19 – Flow chart of the script used to produce synthetic rocking curves bases on the CPFEM computations. The loop presented here is for a certain level of applied strain on the sample, and a given ω, the position of the tomographic rotation stage as described in 4.39

For each material element, actual lattice parameters and orientation are computed from the initial and undeformed state using tensors $\underset{\sim}{\boldsymbol{E}}$ and $\underset{\sim}{\boldsymbol{R}}$. Lattice distorsions lead to lose the initial crystal symmetry and will affect the $\mathbf{B}$ matrix. Local rotations and the increasing density of geometrically necessary dislocations, can change locally the diffraction condition, and must be taken into account. In the 6D-DCT framework, as described in [Viganò et al., 2016], only these rotations are measured, and the assumption that the lattice distortions are negligible compared crystal rotations has been made. We will test this assumption at the end of this chapter.

When all the local geometrical and material parameters are known, the local (i.e. for a given crystal subvolume numbered "n") diffraction equation (4.56) can be solved, and the Θ_n value with its associated V_n volume is stored. From all the (Θ_n, V_n) doublets, a weighted histogram is generated, the equivalent of a rocking curve. The rocking curves are generated for a given ω angle, and the routine must be repeated to get the rocking curves at every position of the tomographic rotation stage.

4.6 Results of synthetic rocking curves generation

The post-processing results of the numerical simulations, using the framework exposed previously are presented here. The aim of this section is to compare the numerical simulations to the experimental results.

4.6.1 Rocking curves

The generated rocking curves for each grain of the cluster are plotted in Fig. 4.20, at $\omega = 165°$. The simulated diffracted intensity is normalized by the maximum value, to be consistent with the experimental results in Chap. 3. The first observation is that the rocking curves shift to lower Θ values due to the increase of the interplanar distance during the loading. There is a little broadening due to the heterogenous strain field within the grain. This is typical of a rocking curve of a crystal within the elastic regime. When one or several slip systems start to be active, this widening is more pronounced, and the rocking curve starts to be distorted.

The two distinct peaks visible in Fig. 4.20(a) for grain 4 could be explained by the tendency to form a subgrain. This is correlated by the observations of the mechanical fields in Fig. 4.14. Grain 10 exhibits much more misorientation than grain 4 and 18 ($0.5°$ compared to $0.25°$ and $0.3°$) and its rocking curves are much more distorted, losing very early the typical "Gaussian shape". It is

explained by the numerous slip systems with relatively high Schmid factors, leading to multiple slip activity and causing curvature, as visible in Fig. 4.14. This effect has been studied both experimentally and numerically for instance by [Barabash and Klimanek, 1999].

4.6.2 Misorientation surfaces

The same methodology as exposed in Chap. 2 and 3 is used to generate FWEM from the simulated rocking curves. Surfaces are plotted from the undeformed state to an applied strain of $\varepsilon_{33} = 3.4 \times 10^{-3}$. The typical shape of these surfaces is very well described by the simulation results. Surfaces starts as disks at the beginning of the experiment, and then become dumbbells oriented in a special direction. The surface of grain 10 does not seem to be deformed by the activation of several slip systems as visible in the experimental data. There is a correlation between the amount of cumulated plastic strain in the grain and the length of the principal axis of the surface. The surface area of grain 10 is wider than the one of grain 4, because in grain 10 several slips systems are activated.

4.6.3 Comparative effects of $\mathbf{B}$ and $\mathbf{R^e}$

Both lattice rotations $\mathbf{R^e}$ and lattice distortions $\mathbf{U^e}$ can affect the diffraction, and thus the shape of the rocking curve. In the plastic regime, lattice distortions are negligible with respect to the lattice rotations. It is visible in Fig. 4.22 that there is no significant effect on the width of the rocking curve. The width taking only $\mathbf{B}$ into account is $0.04°$ while when $\mathbf{R}$ is used, the width is $0.25°$ for this particular ω. Without $\mathbf{R}$, the surface does not exhibit its typical dumbbell shape. But when only $\mathbf{R}$ is used, there is a $4°$ difference on the orientation of the main axis[16].

4.6.4 Comparison with the experimental data

Rocking curves

Comparison between rocking curves at $\omega = 162°$ are drawn in Fig. 4.23. The experimental and computed widths of the rocking curves of grain 4 and grain 18 show good matching. The split of the peak for grain 4 could indicate the presence of a subgrain or another dislocation structure, and is not present in the experimental rocking curve. This is probably due to the activation of secondary slip systems in the CPFEM computations which are not visible during

[16] Caution must be taken with the exact value, as the angular step used to generate the rocking curves was $4°$.

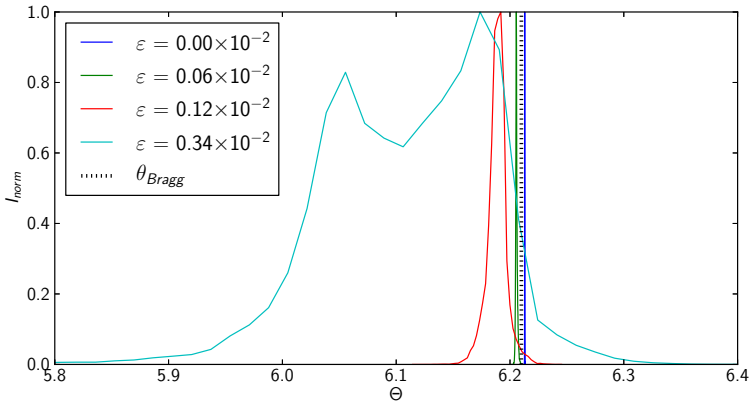

(a) grain 4

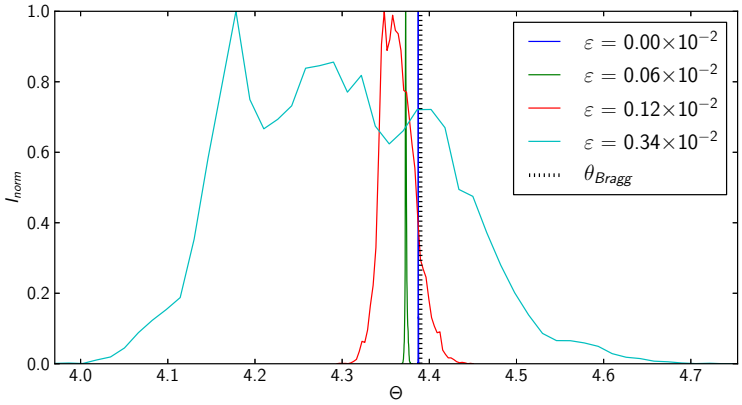

(b) grain 10

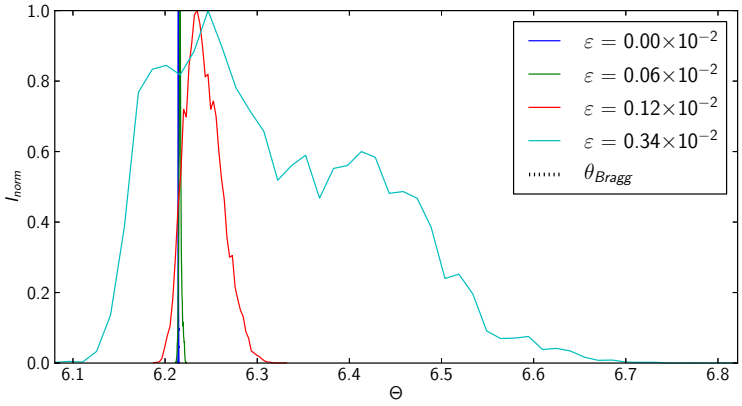

(c) grain18

Figure 4.20 – Simulated rocking curves at $\omega = 165°$ at four different strain levels for: grain 4 (a), grain 10 (b) and grain 18 (c).

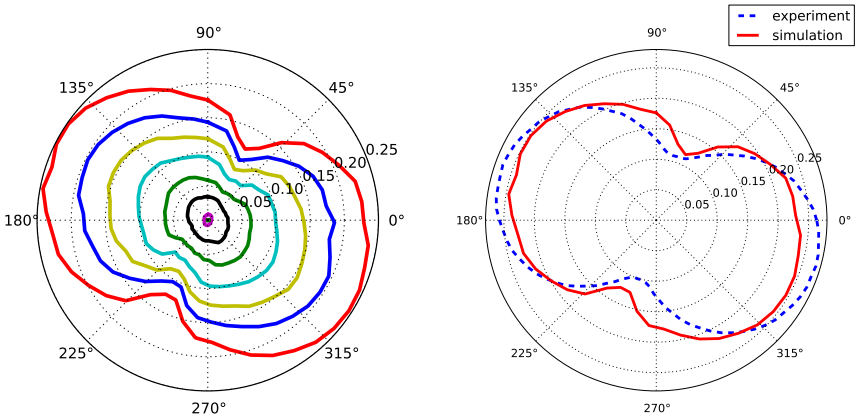

(a) grain 4

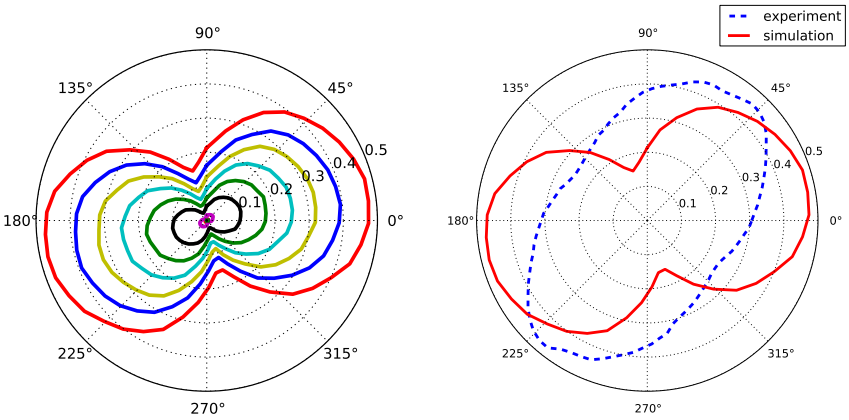

(b) grain 10

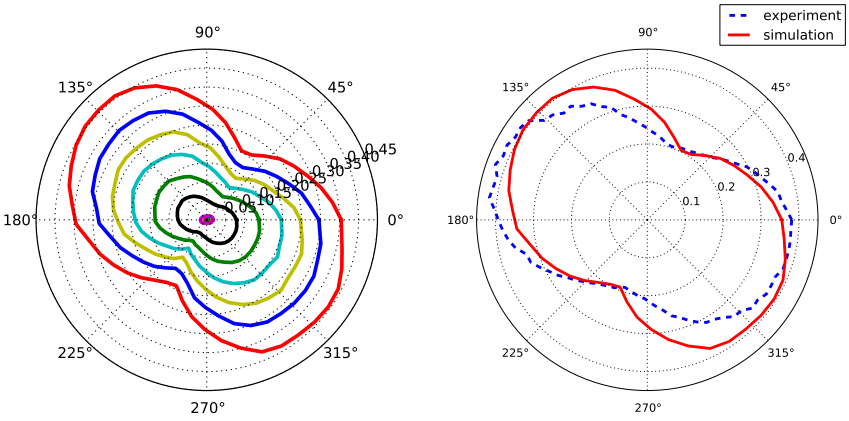

(c) grain18

Figure 4.21 – Synthetic FWEM for: grain 4 (a) and grain 10 (b) and grain 18 (c). Curves are plotted with increment of deformation of $\Delta\varepsilon_{33} = 2 \times 10^{-4}$.

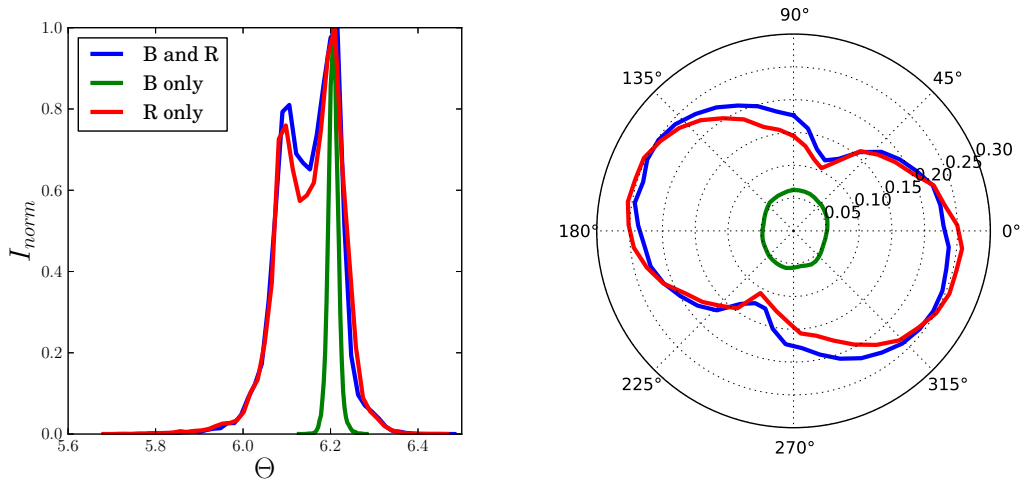

Figure 4.22 – Effect of $\mathbf{B}$ and $\mathbf{R}$ on the synthetic rocking curve generation. The blue lines denote the computation taking both $\mathbf{B}$ and $\mathbf{R}$, the red lines taking only $\mathbf{R}$ into account, and the green lines taking only $\mathbf{B}$ into account. (left) Rocking curve at $\omega = 162°$ and $\varepsilon_{33} = 3.4 \times 10^{-3}$ for grain 4 and (right) corresponding misorientation surfaces.

the experiment. Grain 18 displays a good agreement between simulated and experimental data, for both shape and width. The lower average Θ value for the experimental data is induced by the misalignment between the center of rotation of the diffractometer and the center of mass of the grain. The experimental and computed rocking curves differ for grain 10. The CPFEM computations predict a high number of active slip systems, that are not visible during the experiment. It induces more lattice rotations as observed experimentally, and explain the wider rocking curve for simulated data.

FWEM

Comparison between experimental FWEM and synthetic FWEM is presented in Fig. 4.21(right)(a,b,c). Synthetic surfaces are plotted for an applied strain of $\varepsilon_{33} = 0.0034$, and experimental surfaces are plotted for the last step of the topo-tomography experiment. Both surfaces are in very good agreement for grain 4 and grain 18, for both shape and orientation. For grain 10, the surface has the right amplitude but not the right direction. As explained is the previous section, too many slip systems are predicted active by the simulations, leading to a big mismatch between experimental and synthetic data.

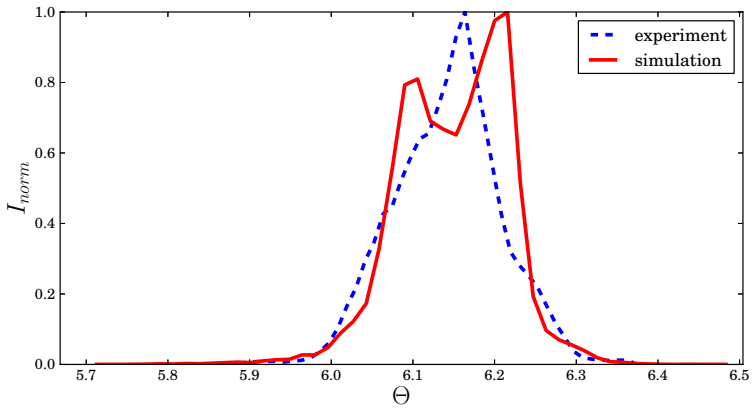

(a) grain 4

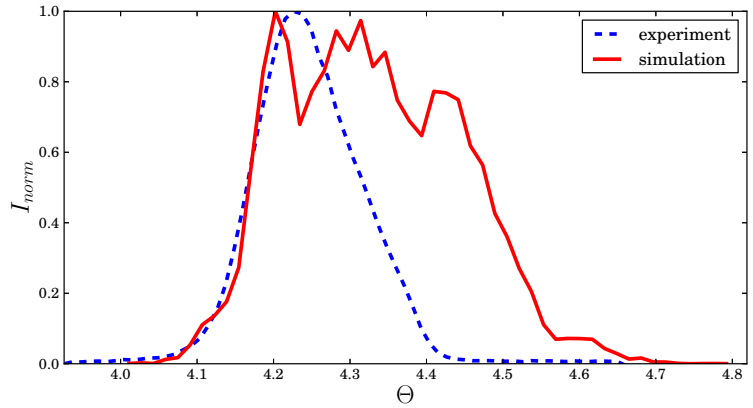

(b) grain 10

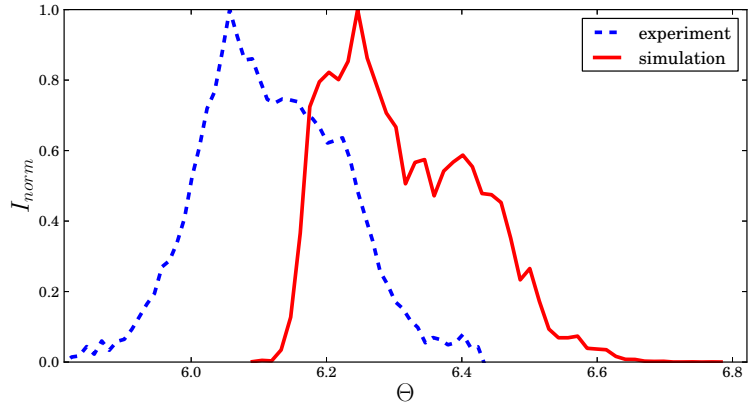

(c) grain18

Figure 4.23 – Comparison between experimental rocking curves and synthetic rocking curves at $\varepsilon_{33} = 2 \times 10^{-4}$ for grain 4 (a), grain 10 (b) and grain 18 (c).

Conclusion and outlook

L'objectif de ce travail a été de développer une nouvelle méthode pour l'étude de la plasticité dans les matériaux polycristallins, à la fois expérimentalement et numériquement. La partie expérimentale consiste en une caractérisation 3D de la microstructure polycristalline initiale grâce à la tomographie par contraste de diffraction, suivi de la caractérisation in situ des mécanismes de déformation par topo-tomographie et tomographie par contraste de phase. Le comportement mécanique de l'échantillon a été simulé par la méthode des éléments finis en utilisant un modèle de plasticité cristalline.. Les deux analyses montrent une très bonne concordance, et les simulations ont été capables de prédire avec précision les systèmes de glissement actifs, et l'amplitude de la rotation du cristal.
Plusieurs pistes sont proposées afin d'améliorer encore la compréhension des méca nismes de plasticité, à la fois expérimentalement ou numériquement.

Conclusion

The objective of this thesis was to develop a new method to study the development of plasticity inside the grains of crystalline materials, both experimentally and numerically. The experimental part is a combination of DCT and interrupted in-situ PCT and topotomographic scans. The mechanical behavior of the sample was then simulated using the Crystal Plasticity Finite Element Method. Both analyses were compared and show good agreement in predicting the active slip systems and the magnitude of the crystal rotation. To achieve this goal, the Ph.D. work was divided in three main parts:

- development of a tensile rig, specifically designed to fit with the requirements of in-situ synchrotron diffraction imaging experiments, especially topotomography,
- in-situ experimental characterization of the plastic strain localization in several grains, using the developed stress rig,
- simulation of the behavior of the polycrystal, using the experimental 3D microstructure from the diffraction experiment.

A binary AlLi alloy was chosen for this study. This material is especially suited for diffraction experiment. Its low Z number allow low exposure times, a big benefit regarding the number of images taken during the experiment (more than 100000). Second, this material exhibits the development of micrometric crystalline defect structures under stress, observable by the diffraction techniques (DCT and topotomography) used in this work. To get a grain size suited for the experiments, a specific process that involved several cold rolling passes and heat treatment has been iteratively identified.

An experimental campaign presented in Chap. 3 has been conducted during the second year of the work. The objective was to observe the localization of the plastic strain in AlLi samples under monotonic tension. Using the specifically developed rig has been used. The experiment was divided in two main phases. Three initial DCT scans were performed to get a representative grain map of the sample, in the region of interest where plastic strain localization was supposed to occur. A preliminary DCT reconstruction of the central volume, carried out during the experiment, was used as an input to select three grains of interest for topomographic scans. The knowledge of their orientation allowed to calculate the tilts required for the topomographic alignment. Moreover, the complete grain map, a concatenation of three overlapping subvolumes, served as an input for the numerical simulations presented in Chap. 4. Topotomographic scans were performed for a cluster of three grains, for 15 different load levels. It was

possible to observe strain localization along well defined from the topographs. These planes could be identified as {111} crystallographic planes. The orientation contrasts observed on the 2D projections could be reconstructed in 3D. These bands became more intense with increasing load. Integrating the intensity over the detector area, it was possible to compute rocking curves for each ω position of the diffractometer. The analysis of the width of these rocking curves for all ω positions measured during the experiment gave the effective misorientation for each grain. These FWEM plots showed that for grain 10, the main curvature not only increases like for the two other grains, but its orientation changes with the increasing load. This analysis was especially suited for comparison with the numerical simulations.

The objective of the third part of this work was to perform CPFEM simulations on the previously analyzed microstructure. For that purpose, the grain map from the DCT data was meshed using a special routine that ensures consistency between the experimental volume and the FE mesh, in terms of grain orientation, position, and numbering. Special care has been taken to ensure that the grain boundaries were suitable for FE computations. The three grains cluster has been meshed using finer elements, to optimize the computation time. Tensile tests have been carried out on macroscopic samples to identify the material parameters. The macroscopic simulated behavior exhibits a lower yield stress than identified. This can be explained by the presence of few large and soft grains in the bulk of the specimen. The slip system activity has been analyzed as well, and the slip systems identified as active in the experimental analysis are found to be active in the simulation. For grain 10, the predicted slip activity is more complex than the observed one. Slip systems not observed experimentally show activity in the simulation. The continuum crystal plasticity full field simulations do not predict strong localization along well defined planes. An equation for calculation of the scattered intensity has been derived for the deformed crystal case. From these it was possible to compute the diffraction condition for each element of a given grain as a function of the computed mechanical variables, and then generate synthetic rocking curves. These simulated rocking curves allow to observe that the influence of the lattice stretching is minor, whereas lattice rotations have a strong influence. Lattice deformations slightly modify the orientation of the main lattice curvature of the grain. With the FWEM analysis developed in this work, it was possible to make direct comparisons between experimental and simulated data. Individual rocking curves and FWEM show excellent agreement for grain 4 and 18, while for grain 10 there is a mismatch both in term of orientation. It may indicate that the numerical model has problems to make good predictions when a grain presents numerous soft slip systems, probably due to a poor description of the interaction between slip systems.

Prospects

This work has provided an insight into the coupling between numerical and experimental studies of plastic strain localization in FCC crystals, with the original association of different experimental and numerical methods. We now propose some directions that can be followed to pursue and improve this work.

Topotomographic imaging has proven to be well suited for the study of the deformation of crystalline materials under monotic loading. However, for highly strained materials, longer exposure times are needed, as well as wider tilt ranges, leading to prohibitive exposures times. Under cyclic loading, metals have the tendency to form ordered structures of intense deformation. For low stress amplitudes in easy cross-slip metals, Persistent Slips Bands (PSBs) appear, and are preferred sites for crack initiation. This process could be easily observed by topotomography, because strains remain low in average in the grain, but are localized in the PSBs, providing orientation contrast in topotomography.

In this Ph.D. project, the spatially resolved observations of the localization of the plastic strain localization in the bulk of crystals that have been made are only qualitative. Orientation mapping techniques lying on the optimization of the local reconstructed orientation and forward modeling of diffraction like in [Viganò et al., 2014] for the DCT technique and in [Li and Suter, 2013b] for HEDM, will allow to measure **quantitatively the local orientation field of the crystal**. From that, the curvature of the lattice can be deduced, and the dislocation density tensor as well. A 6D in-situ DCT experiment would provide for every grain of the sample the local orientation of the crystal as a function of the applied load. This approach (X-ray microscopy) could be limited in terms of spatial and angular resolution, and the use of X-ray optics in the diffracted beam as in [Simons et al., 2015b] is a possibility to scale down the experiment. It is then not possible to observe the full polycrystal, and topotomographic measurements must be made. To improve the accuracy of the 6D reconstructions, it could be interesting to extend its framework to include the data from topotomography, as a constraint for the reconstruction for example. Moreover, by scanning several reflections, the indetermination of the curvature around the diffraction vector can be solved.

The numerical simulation of the behavior of this binary AlLi alloy has been simplified and thus can be more finely tuned. First, the PLC effect has to be taken account, to reproduce the instabilities that have been observed during the experiment or the identification of the material behavior. Special numerical models like in [Perrin et al., 2010, Collard et al., 2010] can be implemented to take into account the discreteness of the intragranular slip. Generalized crystal plasticity is a promising way, and models such as [Fleck and Hutchinson, 1997, Forest, 2009, Forest and Guéninchault, 2013] are able to compute directly the dislocation den-

sity tensor, and could be directly compared to fine resolved orientation mapping experiments as described before. The coupling with other numerical simulation methods seems promising for multiscale studies as well. Coupling CPFEM computations with Discrete Dislocation Dynamics (DDD) as in [Xu et al., 2016] opens the possibility to perform full field simulations on the polycrystal and to simulate the local behavior of dislocations in a grain of interest.

The coupling between experiment and FEM simulation can be improved with the use of the finite element framework presented in [Roux et al., 2008] where the displacement field is decomposed over finite element shape functions and called global DVC. This method provides displacement fields that can be directly exploited as boundary conditions by the FEM code. The acquisition of data for DVC can be accelerated by acquiring only a few projections, as presented in [Taillandier-Thomas et al., 2016].

More generally speaking, upgrades of the third-generation synchrotrons will provide brighter and more coherent X-ray beams. It will lead to a significant improvement in terms of resolution and exposure time, and more extensive 4D studies will be available. New instruments like the "nanoscope" on ID11 and the hard X-ray microscope on ID06 will provide more detailed insight at length scales which start to overlap with established electron microscopy techniques. With the new brighter source, and with new high-speed X-ray detectors, it will be an fascinating way to get very local measurements from the bulk of deeply embedded grains.

Bibliography

[Abbe, 1873] Abbe, E. (1873). Beiträge zur theorie des mikroskops und der mikroskopischen wahrnehmung. *Archiv für mikroskopische Anatomie*, 9(1):413–418.

[Ahl et al., 2015] Ahl, S. R., Simons, H., Jakobsen, A. C., Zhang, Y. B., Stöhr, F., Juul Jensen, D., and Poulsen, H. F. (2015). Dark field X-ray microscopy for studies of recrystallization. *Proceedings of the 36th Risø International Symposium on Materials Science, IOP Conference Series: Materials Science and Engineering*, 89(1):012016.

[Alkemper and Voorhees, 2001] Alkemper, J. and Voorhees, P. (2001). Quantitative serial sectioning analysis. *Journal of microscopy*, 201(3):388–394.

[Allen and Cahn, 1979] Allen, S. M. and Cahn, J. W. (1979). A microscopic theory for antiphase boundary motion and its application to antiphase domain coarsening. *Acta Metallurgica*, 27(6):1085–1095.

[Ashby, 1968] Ashby, M. (1968). Oxide dispersion strengthening. In *Proc. 2nd Bolton Landing Conf., GS Ansell, ed., Gordon and Breach, New York, NY*, page 143.

[Ashby, 1970] Ashby, M. (1970). The deformation of plastically non-homogeneous materials. *Philosophical Magazine*, 21(170):399–424.

[Ashby, 1971] Ashby, M. (1971). The deformation of plastically non-homogeneous alloys. In Kelly, A. and Nicholson, R., editors, *Strengthening Methods in Crystals*, pages 137–192. Applied Science Publishers, London.

[Bao et al., 2010] Bao, L., Lecomte, J.-S., Schuman, C., Philippe, M.-J., Zhao, X., and Esling, C. (2010). Study of plastic deformation in hexagonal metals by interrupted in-situ ebsd measurement. *Advanced Engineering Materials*, 12(10):1053–1059.

[Barabash and Klimanek, 1999] Barabash, R. and Klimanek, P. (1999). X-ray scattering by crystals with local lattice rotation fields. *Journal of applied crystallography*, 32(6):1050–1059.

[Barnard et al., 2006] Barnard, J., Sharp, J., Tong, J., and Midgley, P. (2006). High-resolution three-dimensional imaging of dislocations. *Science*, 313(5785):319–319.

[Barrett, 1931] Barrett, C. S. (1931). Laue spots from perfect, imperfect, and oscillating crystals. *Physical Review*, 38(4):832.

[Berg, 1931] Berg, W. (1931). Über eine röntgenographische methode zur untersuchung von gitterstörungen an kristallen. *Naturwissenschaften*, 19(19):391–396.

[Bertram et al., 2006] Bertram, A., Böhlke, T., Brüggemann, C., Estrin, Y., and Lebyodkin, M. (2006). Modeling and simulation of the Portevin-Le Chatelier effect. *PAMM*, 6(1):353–354.

[Berveiller and Zaoui, 1978] Berveiller, M. and Zaoui, A. (1978). An extension of the self-consistent scheme to plastically-flowing polycrystals. *Journal of the Mechanics and Physics of Solids*, 26(5-6):325–344.

[Besson et al., 2009] Besson, J., Cailletaud, G., Chaboche, J.-L., Forest, S., and Blétry, M. (2009). *Non–Linear Mechanics of Materials*. Series: Solid Mechanics and Its Applications, Vol. 167, Springer, ISBN: 978-90-481-3355-0, 433 p.

[Besson and Foerch, 1997] Besson, J. and Foerch, R. (1997). Large scale object-oriented finite element code design. *Computer Methods in Applied Mechanics and Engineering*, 142(1):165–187.

[Bilby et al., 1957] Bilby, B., Bullough, R., Gardner, L., and Smith, E. (1957). Continuous distributions of dislocations iv: Single glide and plane strain. *Proc. Roy. Soc. London*, A236:538–557.

[Bittencourt et al., 2003] Bittencourt, E., Needleman, A., M.E., G., and Van der Giessen, E. (2003). A comparison of nonlocal continuum and discrete dislocation plasticity predictions. *Journal of the Mechanics and Physics of Solids*, 51:281–310.

[Black and Long, 2004] Black, D. R. and Long, G. G. (2004). X-ray topography.

[Blank et al., 2016] Blank, B. E., Schuren, J., Shade, P., and Turner, T. (2016). Rotational and axial motion system and methods of use. US Patent 20,160,047,722.

[Borbély and Ungár, 2012] Borbély, A. and Ungár, T. (2012). X-ray line profiles analysis of plastically deformed metals. *Comptes Rendus Physique*, 13(3):293–306.

[Bouterf et al., 2014] Bouterf, A., Roux, S., Hild, F., Adrien, J., Maire, E., and Meille, S. (2014). Digital volume correlation applied to x-ray tomography images from spherical indentation tests on lightweight gypsum. *Strain*, 50(5):444–453.

[Bréchet, 1987] Bréchet, Y. (1987). *Fatigue des alliages al-li : un exemple de localisation de la deformation plastique*. PhD thesis. Thèse de doctorat dirigée par Guyot, Pierre Sciences appliquées. Physique INP GRENOBLE 1987.

[Brechet and Livet, 1987] Brechet, Y. and Livet, F. (1987). Low cycle fatigue of binary al-li alloys: Iii-coalescence of δ'precipitates in fatigue: X-ray low angle scattering investigation. *Le Journal de Physique Colloques*, 48(C3):C3–717.

[Brechet et al., 1987] Brechet, Y., Louchet, F., Marchionni, C., and Verger-Gaugry, J. (1987). Experimental (tem and stem) investigation and theoretical approach to the fatigue-induced dissolution of δ' precipitates in a 2.5 wt% al-li alloy. *Philosophical Magazine A*, 56(3):353–366.

[Bunge, 2013] Bunge, H.-J. (2013). *Texture analysis in materials science: mathematical methods*. Elsevier.

[Burnett et al., 2016] Burnett, T., Kelley, R., Winiarski, B., Contreras, L., Daly, M., Gholinia, A., Burke, M., and Withers, P. (2016). Large volume serial section tomography by xe plasma fib dual beam microscopy. *Ultramicroscopy*, 161:119–129.

[Butler, 1979] Butler, E. (1979). In situ experiments in the transmission electron microscope. *Reports on Progress in Physics*, 42(5):833.

[Campbell, 2008] Campbell, F. C. (2008). *Elements of metallurgy and engineering alloys*. ASM International.

[Cermelli and Gurtin, 2001a] Cermelli, P. and Gurtin, M. (2001a). On the characterization of geometrically necessary dislocations in finite plasticity. *Journal of the Mechanics and Physics of Solids*, 49:1539–1568.

[Cermelli and Gurtin, 2001b] Cermelli, P. and Gurtin, M. E. (2001b). On the characterization of geometrically necessary dislocations in finite plasticity. *Journal of the Mechanics and Physics of Solids*, 49(7):1539–1568.

[Cerutti, 2014] Cerutti, X. (2014). *Numerical modelling and mechanical analysis of the machining of large aeronautical parts: Machining quality improvement.* PhD thesis, Ecole Nationale Supérieure des Mines de Paris.

[Chiron et al., 1997] Chiron, R., Fryet, J., and De Lesegno, P. V. (1997). In situ tensile testing machine and sample for a scanning electron microscope. US Patent 5,606,168.

[Cloetens et al., 1999] Cloetens, P., Ludwig, W., Baruchel, J., Van Dyck, D., Van Landuyt, J., Guigay, J., and Schlenker, M. (1999). Holotomography: Quantitative phase tomography with micrometer resolution using hard synchrotron radiation x rays. *Applied physics letters*, 75(19):2912–2914.

[Coates, 1967] Coates, D. (1967). Kikuchi-like reflection patterns obtained with the scanning electron microscope. *Philosophical magazine*, 16(144):1179–1184.

[Cohen, 1969] Cohen, J. (1969). A brief review of the properties of ordered alloys. *Journal of Materials Science*, 4(11):1012–1021.

[Collard et al., 2010] Collard, C., Favier, V., Berbenni, S., and Berveiller, M. (2010). Role of discrete intra-granular slip bands on the strain-hardening of polycrystals. *International Journal of Plasticity*, 26(2):310–328.

[Cordero et al., 2010] Cordero, N., Gaubert, A., Forest, S., Busso, E., Gallerneau, F., and Kruch, S. (2010). Size effects in generalised continuum crystal plasticity for two–phase laminates. *Journal of the Mechanics and Physics of Solids*, 58:1963–1994.

[Cormack and Koehler, 1976] Cormack, A. and Koehler, A. (1976). Quantitative proton tomography: preliminary experiments. *Physics in medicine and biology*, 21(4):560.

[Couling and Pearsall, 1957] Couling, S. and Pearsall, G. (1957). Determination of orientation in magnesium by polarized light examination.

[Dake et al., 2016] Dake, J. M., Oddershede, J., Sørensen, H. O., Werz, T., Shatto, J. C., Uesugi, K., Schmidt, S., and Krill, C. E. (2016). Direct observation of grain rotations during coarsening of a semisolid al–cu alloy. *Proceedings of the National Academy of Sciences*, 113(41):E5998–E6006.

[Delacroix, 2011] Delacroix, J. (2011). *Étude des mécanismes de fissuration en fatigue et/ou fretting d'alliages Al-Cu-Li.* PhD thesis, Lyon, INSA.

[Dey et al., 2007] Dey, S., Lauridsen, E., Ludwig, W., Rowenhorst, D., and Fonda, R. (2007). Study of microstructure evolution of grain boundary alpha phase during beta to alpha transformation in timetal 21s alloy. *Proceedings of Titanium*, pages 467–470.

[Douissard et al., 2012] Douissard, P.-A., Cecilia, A., Rochet, X., Chapel, X., Martin, T., van de Kamp, T., Helfen, L., Baumbach, T., Luquot, L., Xiao, X., et al. (2012). A versatile indirect detector design for hard x-ray microimaging. *Journal of Instrumentation*, 7(09):P09016.

[Doumalin and Bornert, 2000] Doumalin, P. and Bornert, M. (2000). Micromechanical applications of digital image correlation techniques. In *Interferometry in Speckle Light*, pages 67–74. Springer.

[Echlin et al., 2011] Echlin, M., Mottura, A., and Pollock, T. (2011). The tri-beam system: Femtosecond laser based tomography in a dual-beam fib. *Microscopy and Microanalysis*, 17(S2):958–959.

[Echlin et al., 2012] Echlin, M. P., Mottura, A., Torbet, C. J., and Pollock, T. M. (2012). A new tribeam system for three-dimensional multimodal materials analysis. *Review of Scientific Instruments*, 83(2):023701.

[Eggeman et al., 2015] Eggeman, A. S., Krakow, R., and Midgley, P. A. (2015). Scanning precession electron tomography for three-dimensional nanoscale orientation imaging and crystallographic analysis. *Nature communications*, 6.

[Erni et al., 2009] Erni, R., Rossell, M. D., Kisielowski, C., and Dahmen, U. (2009). Atomic-resolution imaging with a sub-50-pm electron probe. *Physical Review Letters*, 102(9):096101.

[Ersen et al., 2007] Ersen, O., Hirlimann, C., Drillon, M., Werckmann, J., Tihay, F., Pham-Huu, C., Crucifix, C., and Schultz, P. (2007). 3d-tem characterization of nanometric objects. *Solid State Sciences*, 9(12):1088–1098.

[Evanko et al., 2011] Evanko, D., Heinrichs, A., and Rosenthal, C. (2011). Milestones in light microscopy. *Nature*.

[Eyre, 1962] Eyre, B. (1962). Direct observations of neutron irradiation damage in α-iron. *Philosophical Magazine*, 7(84):2107–2113.

[Feldkamp et al., 1984] Feldkamp, L., Davis, L., and Kress, J. (1984). Practical cone-beam algorithm. *JOSA A*, 1(6):612–619.

[Fisher, 1954] Fisher, J. (1954). On the strength of solid solution alloys. *Acta Metallurgica*, 2(1):9 – 10.

[Fivel and Forest, 2004a] Fivel, M. and Forest, S. (2004a). *Plasticité cristalline et transition d'échelle : cas du monocristal.* Techniques de l'Ingénieur, M4016, 23 pages.

[Fivel and Forest, 2004b] Fivel, M. and Forest, S. (2004b). *Plasticité cristalline et transition d'échelle : cas du polycristal.* Techniques de l'Ingénieur, M4017, 11 pages.

[Fleck and Hutchinson, 1997] Fleck, N. and Hutchinson, J. (1997). Strain gradient plasticity. *Advances in applied mechanics*, 33:296–361.

[Fleck et al., 1994] Fleck, N., Muller, G., Ashby, M., and Hutchinson, J. (1994). Strain gradient plasticity: theory and experiment. *Acta Metallurgica et Materialia*, 42(2):475–487.

[Forest, 2009] Forest, S. (2009). Micromorphic approach for gradient elasticity, viscoplasticity, and damage. *Journal of Engineering Mechanics*, 135(3):117–131.

[Forest et al., 2015] Forest, S., Amestoy, M., Damamme, G., Kruch, S., Maurel, V., and Mazière, M. (2015). *Mécanique des milieux continus.* École des Mines de Paris.

[Forest and Guéninchault, 2013] Forest, S. and Guéninchault, N. (2013). Inspection of free energy functions in gradient crystal plasticity. *Acta Mechanica Sinica*, 29(6):763–772.

[Franciosi et al., 1980] Franciosi, P., Berveiller, M., and Zaoui, A. (1980). Latent hardening in copper and aluminium single crystals. *Acta Metallurgica*, 28(3):273–283.

[Frank et al., 1996] Frank, J., Radermacher, M., Penczek, P., Zhu, J., Li, Y., Ladjadj, M., and Leith, A. (1996). Spider and web: processing and visualization of images in 3d electron microscopy and related fields. *Journal of structural biology*, 116(1):190–199.

[Fu et al., 2006] Fu, X., Knudsen, E., Poulsen, H. F., Herman, G. T., Carvalho, B. M., and Liao, H. Y. (2006). Optimized algebraic reconstruction technique for generation of grain maps based on three-dimensional x-ray diffraction (3dxrd). *Optical Engineering*, 45(11):116501–116501.

[Fu et al., 2003] Fu, X., Poulsen, H., Schmidt, S., Nielsen, S. F., Lauridsen, E., and Jensen, D. J. (2003). Non-destructive mapping of grains in three dimensions. *Scripta materialia*, 49(11):1093–1096.

[Fujita, 1967] Fujita, H. (1967). Continuous observation of dynamic behaviors of dislocations in aluminum. *Journal of the Physical Society of Japan*, 23(6):1349–1361.

[Fujita, 1969] Fujita, H. (1969). The work-hardening process in metals. *Journal of the Physical Society of Japan*, 26(2):331–338.

[George, 2004] George, P. (2004). Tetmesh-ghs3d, tetrahedral mesh generator. *INRIA User's Manual, INRIA (Institut National de Recherche en Informatique et Automatique), France*, 83.

[Gérard, 2008] Gérard, C. (2008). *Mesures de champs et identification de modèles de plasticité cristalline*. PhD thesis, Université Paris-Nord-Paris XIII.

[Graff et al., 2004] Graff, S., Forest, S., Strudel, J.-L., Prioul, C., Pilvin, P., and Béchade, J.-L. (2004). Strain localization phenomena associated with static and dynamic strain ageing in notched specimens: experiments and finite element simulations. *Materials Science and Engineering: A*, 387:181–185.

[Gueninchault et al., 2016] Gueninchault, N., Proudhon, H., and Ludwig, W. (2016). Nanox: a miniature mechanical stress rig designed for near-field X-ray diffraction imaging techniques. *Journal of Synchrotron Radiation*, 23(6).

[Guinier and Tennevin, 1949] Guinier, A. and Tennevin, J. (1949). Sur deux variantes de la méthode de laue et leurs applications. *Acta Crystallographica*, 2(3):133–138.

[Gurtin, 2002] Gurtin, M. (2002). A gradient theory of single–crystal viscoplasticity that accounts for geometrically necessary dislocations. *Journal of the Mechanics and Physics of Solids*, 50:5–32.

[Hefferan et al., 2012] Hefferan, C. M., Lind, J., Li, S. F., Lienert, U., Rollett, A. D., and Suter, R. M. (2012). Observation of recovery and recrystallization in high-purity aluminum measured with forward modeling analysis of high-energy diffraction microscopy. *Acta Materialia*, 60(10):4311–4318.

[Hege et al., 1997] Hege, H.-C., STALLING, D., SEEBASS, M., and Zockler, M. (1997). A generalized marching cubes algorithm based on non-binary. Technical report, Citeseer.

[Herbig et al., 2011] Herbig, M., King, A., Reischig, P., Proudhon, H., Lauridsen, E. M., Marrow, J., Buffière, J.-Y., and Ludwig, W. (2011). 3-d growth of a short fatigue crack within a polycrystalline microstructure studied using combined diffraction and phase-contrast x-ray tomography. *Acta Materialia*, 59(2):590–601.

[Hild et al., 2011] Hild, F., Fanget, A., Adrien, J., Maire, E., and Roux, S. (2011). Three-dimensional analysis of a tensile test on a propellant with digital volume correlation. *Archives of Mechanics*, 63(5-6):1–20.

[Hirsch, 1986] Hirsch, P. (1986). Direct observations of moving dislocations: reflections on the thirtieth anniversary of the first recorded observations of moving dislocations by transmission electron microscopy. *Materials Science and Engineering*, 84:1–10.

[Hirsch et al., 1956] Hirsch, P., Horne, R., and Whelan, M. (1956). Lxviii. direct observations of the arrangement and motion of dislocations in aluminium. *Philosophical Magazine*, 1(7):677–684.

[Hofmann et al., 2010] Hofmann, F., Song, X., Jun, T.-S., Abbey, B., Peel, M., Daniels, J., Honkimäki, V., and Korsunsky, A. (2010). High energy transmission micro-beam laue synchrotron x-ray diffraction. *Materials Letters*, 64(11):1302–1305.

[Hoszowska et al., 2001] Hoszowska, J., Freund, A., Boller, E., Sellschop, J., Level, G., Burns, R., Rebak, M., Baruchel, J., et al. (2001). Characterization of synthetic diamond crystals by spatially resolved rocking curve measurements. *Journal of Physics D: Applied Physics*, 34(10A):A47.

[Hounsfield, 1980] Hounsfield, G. N. (1980). Computed medical imaging. *Journal of computer assisted tomography*, 4(5):665–674.

[Hovis and Heuer, 2010] Hovis, D. and Heuer, A. (2010). The use of laser scanning confocal microscopy (lscm) in materials science. *Journal of microscopy*, 240(3):173–180.

[Hull, 1962] Hull, D. (1962). Spontaneous transformation of metastable β-brass in thin foils. *Philosophical Magazine*, 7(76):537–550.

[Ice et al., 2005] Ice, G. E., Larson, B. C., Yang, W., Budai, J. D., Tischler, J. Z., Pang, J., Barabash, R., and Liu, W. (2005). Polychromatic x-ray microdiffraction studies of mesoscale structure and dynamics. *Journal of synchrotron radiation*, 12(2):155–162.

[Jakobsen et al., 2016] Jakobsen, A., Simons, H., Sonja, A., Detlefs, C., Haartwig, J., and Poulsen, H. (2016). Mapping of embedded dislocations in diamond with sub 200 nm resolution. Three dimensionnal material science.

[Jakobsen et al., 2008] Jakobsen, B., Lienert, U., Almer, J., Poulsen, H. F., and Pantleon, W. (2008). Direct observation of strain in bulk subgrains and dislocation walls by high angular resolution three-dimensional x-ray diffraction. *Materials Science and Engineering: A*, 483:641–643.

[Jha et al., 1987] Jha, S., Sanders, T., and Dayananda, M. (1987). Grain boundary precipitate free zones in al-li alloys. *Acta Metallurgica*, 35(2):473 – 482.

[Johnson et al., 2008] Johnson, G., King, A., Honnicke, M. G., Marrow, J., and Ludwig, W. (2008). X-ray diffraction contrast tomography: a novel technique for three-dimensional grain mapping of polycrystals. II. The combined case. *Journal of Applied Crystallography*, 41(2):310–318.

[Joshi, 2005] Joshi, A. (2005). Lithium aluminium alloys–the new generation aerospace alloys. *Indian Institute of Technology Bombay*.

[Kabius et al., 2009] Kabius, B., Hartel, P., Haider, M., Müller, H., Uhlemann, S., Loebau, U., Zach, J., and Rose, H. (2009). First application of cc-corrected imaging for high-resolution and energy-filtered tem. *Journal of electron microscopy*, 58(3):147–155.

[Kawado et al., 2004] Kawado, S., Taishi, T., Iida, S., Suzuki, Y., Chikaura, Y., and Kajiwara, K. (2004). Determination of the three-dimensional structure of dislocations in silicon by synchrotron white x-ray topography combined with a topo-tomographic technique. *Journal of synchrotron radiation*, 11(4):304–308.

[Kikuchi, 1928] Kikuchi, S. (1928). Diffraction of cathode rays by mica. *Proceedings of the Imperial Academy*, 4(6):271–274.

[King et al., 2013] King, A., Reischig, P., Adrien, J., and Ludwig, W. (2013). First laboratory x-ray diffraction contrast tomography for grain mapping of polycrystals. *Journal of applied crystallography*, 46(6):1734–1740.

[Kluender, 2011] Kluender, R. (2011). *3D resolved distortion measurements by Bragg diffraction imaging: application to ice crystals*. PhD thesis, Université de Grenoble.

[Kluender et al., 2011] Kluender, R. T., Philip, A., Meyssonnier, J., and Baruchel, J. (2011). Three-dimensional distortion measurements by section rocking curve imaging: Application to ice crystals. *physica status solidi (a)*, 208(11):2505–2510.

[Knoll and Ruska, 1932] Knoll, M. and Ruska, E. (1932). Das elektronenmikroskop. *Zeitschrift für Physik*, 78(5-6):318–339.

[Kröner, 1969] Kröner, E. (1969). Initial studies of a plasticity theory based upon statistical mechanics. In Kanninen, M., Adler, W., Rosenfield, A., and Jaffee, R., editors, *Inelastic Behaviour of Solids*, pages 137–147. McGraw-Hill.

[Kröner and Teodosiu, 1972] Kröner, E. and Teodosiu, C. (1972). Lattice defect approach to plasticity and viscoplasticity. In Sawczuk, A., editor, *Problems of Plasticity, International Symposium on Foundations of Plasticity, Warsaw*. Noordhoff International Publishing Leyden.

[Kunze et al., 1993] Kunze, K., Wright, S., Adams, B., and Dingley, D. (1993). Advances in automatic ebsp single orientation measurements. *Texture, Stress, and Microstructure*, 20(1-4):41–54.

[Kwon and Zewail, 2010] Kwon, O.-H. and Zewail, A. H. (2010). 4D electron tomography. *Science*, 328(5986):1668–1673.

[Laird and Aaronson, 1966] Laird, C. and Aaronson, H. (1966). Mechanisms of formation of θ and dissolution of θ' precipitates in an al-4% cu alloy. *Acta Metallurgica*, 14(2):171–185.

[Lang, 1993] Lang, A. (1993). The early days of high-resolution x-ray topography. *Journal of Physics D: Applied Physics*, 26(4A):A1.

[Larson et al., 2002] Larson, B., Yang, W., Ice, G., Budai, J., and Tischler, J. (2002). Three-dimensional x-ray structural microscopy with submicrometre resolution. *Nature*, 415(6874):887–890.

[Larson and Picklesimer, 1966] Larson, L. and Picklesimer, M. (1966). Determination of the basal-pole orientation in zirconium by polarized-light microscopy. *Trans. Met. Soc. AIME*, 236(ORNL-P-2016).

[Lauridsen et al., 2006] Lauridsen, E., Schmidt, S., Nielsen, S. F., Margulies, L., Poulsen, H., and Jensen, D. J. (2006). Non-destructive characterization of recrystallization kinetics using three-dimensional x-ray diffraction microscopy. *Scripta materialia*, 55(1):51–56.

[Lauridsen et al., 2001a] Lauridsen, E. M., Schmidt, S., Suter, R., and Poulsen, H. F. (2001a). Tracking: a method for structural characterization of grains in powders or polycrystals. *Journal of applied crystallography*, 34(6):744–750.

[Lauridsen et al., 2001b] Lauridsen, E. M., Schmidt, S., Suter, R. M., and Poulsen, H. F. (2001b). Tracking : a method for structural characterization of grains in powders or polycrystals research papers Tracking : a method for structural characterization of grains in powders or polycrystals. pages 744–750.

[Lavernia and Grant, 1987] Lavernia, E. J. and Grant, N. J. (1987). Aluminium-lithium alloys. *Journal of Materials Science*, 22(5):1521–1529.

[Lenthe et al., 2015] Lenthe, W. C., Echlin, M., Trenkle, A., Syha, M., Gumbsch, P., and Pollock, T. M. (2015). Quantitative voxel-to-voxel comparison of tribeam and dct strontium titanate three-dimensional data sets. *Journal of Applied Crystallography*, 48(4):1034–1046.

[Lewis et al., 2006] Lewis, A., Bingert, J., Rowenhorst, D., Gupta, A., Geltmacher, A., and Spanos, G. (2006). Two-and three-dimensional microstructural characterization of a super-austenitic stainless steel. *Materials Science and Engineering: A*, 418(1):11–18.

[Lewis and Geltmacher, 2006] Lewis, A. and Geltmacher, A. (2006). Image-based modeling of the response of experimental 3d microstructures to mechanical loading. *Scripta Materialia*, 55(1):81–85.

[Li and Suter, 2013a] Li, S. and Suter, R. (2013a). Adaptive reconstruction method for three-dimensional orientation imaging. *Journal of Applied Crystallography*, 46(2):512–524.

[Li and Suter, 2013b] Li, S. F. and Suter, R. M. (2013b). Adaptive reconstruction method for three-dimensional orientation imaging. *Journal of Applied Crystallography*, 46(2):512–524.

[Li, 2011] Li, S. F. F. (2011). Imaging of orientation and geometry in microstructures: development and applications of high energy x-ray diffraction microscopy.

[Liu et al., 2011] Liu, H., Schmidt, S., Poulsen, H. F., Godfrey, A., Liu, Z., Sharon, J., and Huang, X. (2011). Three-dimensional orientation mapping in the transmission electron microscope. *Science*, 332(6031):833–834.

[Liu and Hansen, 1997] Liu, Q. and Hansen, N. (1997). Micro structural study of deformation in grain boundary region during plastic deformation of polycrystalline aluminium. *Materials Science and Engineering: A*, 234:672–675.

[Livingston and Chalmers, 1957] Livingston, J. and Chalmers, B. (1957). Multiple slip in bicrystal deformation. *Acta Metallurgica*, 5(6):322 – 327.

[Lübbert et al., 2000] Lübbert, D., Baumbach, T., Härtwig, J., Boller, E., and Pernot, E. (2000). μm-resolved high resolution x-ray diffraction imaging for semiconductor quality control. *Nuclear Instruments and Methods in Physics Research Section B: Beam Interactions with Materials and Atoms*, 160(4):521–527.

[Ludwig, 2010] Ludwig, W. (2010). *Habilitation à diriger les recherches*. PhD thesis, Université de Lyon I.

[Ludwig and Bellet, 2000] Ludwig, W. and Bellet, D. (2000). Penetration of liquid gallium into the grain boundaries of aluminium: a synchrotron radiation microtomographic investigation. *Materials Science and Engineering: A*, 281(1):198–203.

[Ludwig et al., 2003] Ludwig, W., Buffière, J.-Y., Savelli, S., and Cloetens, P. (2003). Study of the interaction of a short fatigue crack with grain boundaries in a cast al alloy using x-ray microtomography. *Acta Materialia*, 51(3):585–598.

[Ludwig et al., 2001a] Ludwig, W., Cloetens, P., Härtwig, J., Baruchel, J., Hamelin, B., and Bastie, P. (2001a). Three-dimensional imaging of crystal defects by 'topo-tomography'. *Journal of Applied Crystallography*, 34(5):602–607.

[Ludwig et al., 2001b] Ludwig, W., Cloetens, P., Härtwig, J., Baruchel, J., Hamelin, B., and Bastie, P. (2001b). Three-dimensional imaging of crystal defects bytopo-tomography'. *Journal of applied crystallography*, 34(5):602–607.

[Ludwig et al., 2009a] Ludwig, W., King, A., Reischig, P., Herbig, M., Lauridsen, E., Schmidt, S., Proudhon, H., Forest, S., Cloetens, P., Rolland du Roscoat, S., Buffière, J., Marrow, T., and Poulsen, H. (2009a). New opportunities for 3D materials science of polycrystalline materials at the micrometre lengthscale by combined use of X–ray diffraction and X–ray imaging. *Materials Science and Engineering A*, 524:69–76.

[Ludwig et al., 2009b] Ludwig, W., King, A., Reischig, P., Herbig, M., Lauridsen, E. M., Schmidt, S., Proudhon, H., Forest, S., Cloetens, P., Du Roscoat, S. R., et al. (2009b). New opportunities for 3d materials science of polycrystalline materials at the micrometre lengthscale by combined use of x-ray diffraction and x-ray imaging. *Materials Science and Engineering: A*, 524(1):69–76.

[Ludwig et al., 2007a] Ludwig, W., Lauridsen, E. M., Schmidt, S., Poulsen, H. F., and Baruchel, J. (2007a). High-resolution three-dimensional mapping of individual grains in polycrystals by topotomography. *Journal of Applied Crystallography*, 40(5):905–911.

[Ludwig et al., 2007b] Ludwig, W., Lauridsen, E. M., Schmidt, S., Poulsen, H. F., and Baruchel, J. (2007b). High-resolution three-dimensional mapping of individual grains in polycrystals by topotomography. *Journal of Applied Crystallography*, 40(5):905–911.

[Ludwig et al., 2009c] Ludwig, W., Reischig, P., King, A., Herbig, M., Lauridsen, E., Johnson, G., Marrow, T., and Buffière, J.-Y. (2009c). Three-dimensional grain mapping by x-ray diffraction contrast tomography and the use of friedel pairs in diffraction data analysis. *Review of Scientific Instruments*, 80(3):033905.

[Ludwig et al., 2008] Ludwig, W., Schmidt, S., Lauridsen, E. M., and Poulsen, H. F. (2008). X-ray diffraction contrast tomography: a novel technique for three-dimensional grain mapping of polycrystals. i. direct beam case. *Journal of Applied Crystallography*, 41(2):302–309.

[Maaß et al., 2007] Maaß, R., Van Petegem, S., Van Swygenhoven, H., Derlet, P. M., Volkert, C. A., and Grolimund, D. (2007). Time-resolved laue diffraction of deforming micropillars. *Physical review letters*, 99(14):145505.

[Mandel, 1965] Mandel, J. (1965). Une généralisation de la théorie de la plasticité de W.T. Koiter. *Int. J. Solids Structures*, 1:273–295.

[Mandel, 1971] Mandel, J. (1971). *Plasticité classique et viscoplasticité*. CISM Courses and Lectures No. 97, Udine, Springer Verlag, Berlin.

[Mandel, 1973a] Mandel, J. (1973a). Equations constitutives et directeurs dans les milieux plastiques et viscoplastiques. *International Journal of Solids and Structures*, 9(6):725–740.

[Mandel, 1973b] Mandel, J. (1973b). Equations constitutives et directeurs dans les milieux plastiques et viscoplastiques. *Int. J. Solids Structures*, 9:725–740.

[Mandel, 1982] Mandel, J. (1982). Définition d'un repère privilégié pour l'étude des transformations anélastiques du polycristal. *J. de Mécanique théorique et appliquée*, 1:7–23.

[Marchenko et al., 2016] Marchenko, A., Mazière, M., Forest, S., and Strudel, J.-L. (2016). Crystal plasticity simulation of strain aging phenomena in α-titanium at room temperature. *International Journal of Plasticity*.

[Margulies et al., 2001] Margulies, L., Winther, G., and Poulsen, H. (2001). In situ measurement of grain rotation during deformation of polycrystals. *Science*, 291(5512):2392–2394.

[Martin and Kubin, 1978] Martin, J. and Kubin, L. (1978). Discussion on the limitations of "in situ" deformation experiments in a high voltage electron microscope. *Ultramicroscopy*, 3:215–226.

[Maurice and Fortunier, 2008] Maurice, C. and Fortunier, R. (2008). A 3d hough transform for indexing ebsd and kossel patterns. *Journal of microscopy*, 230(3):520–529.

[McDonald et al., 2015] McDonald, S., Reischig, P., Holzner, C., Lauridsen, E., Withers, P., Merkle, A., and Feser, M. (2015). Non-destructive mapping of grain orientations in 3d by laboratory x-ray microscopy. *Scientific reports*, 5.

[Méric et al., 1991] Méric, L., Poubanne, P., and Cailletaud, G. (1991). Single crystal modeling for structural calculations: part 1—model presentation. *Journal of Engineering Materials and Technology*, 113(1):162–170.

[Miao et al., 2016] Miao, J., Ercius, P., and Billinge, S. J. (2016). Atomic electron tomography: 3d structures without crystals. *Science*, 353(6306):aaf2157.

[Mikulík et al., 2003] Mikulík, P., Lübbert, D., Korytár, D., Pernot, P., and Baumbach, T. (2003). Synchrotron area diffractometry as a tool for spatial high-resolution three-dimensional lattice misorientation mapping. *Journal of Physics D: Applied Physics*, 36(10A):A74.

[Mimura et al., 2010] Mimura, H., Handa, S., Kimura, T., Yumoto, H., Yamakawa, D., Yokoyama, H., Matsuyama, S., Inagaki, K., Yamamura, K., Sano, Y., et al. (2010). Breaking the 10 nm barrier in hard-x-ray focusing. *Nature Physics*, 6(2):122–125.

[Moscicki et al., 2009] Moscicki, M., Kenesei, P., Wright, J., Pinto, H., Lippmann, T., Borbély, A., and Pyzalla, A. (2009). Friedel-pair based indexing method for characterization of single grains with hard x-rays. *Materials Science and Engineering: A*, 524(1):64–68.

[Murphy, 2002] Murphy, D. B. (2002). *Fundamentals of light microscopy and electronic imaging*. John Wiley & Sons.

[Neice, 2010] Neice, A. (2010). Methods and limitations of subwavelength imaging. *Advances in imaging and Electron Physics*, 163:117–140.

[Nicholas and Old, 1979] Nicholas, M. and Old, C. (1979). Liquid metal embrittlement. *Journal of Materials Science*, 14(1):1–18.

[Nishikawa and Kikuchi, 1928] Nishikawa, S. and Kikuchi, S. (1928). The diffraction of cathode rays by calcite. *Proceedings of the Imperial Academy*, 4(8):475–477.

[Noble et al., 1982] Noble, B., Harris, S. J., and Dinsdale, K. (1982). The elastic modulus of aluminium-lithium alloys. *Journal of Materials Science*, 17(2):461–468.

[Nowack and Lutjering, 1996] Nowack, H. and Lutjering, G. (1996). *Fatigue'96: Proceedings of the 6th International Fatigue Congress*. Pergamon.

[Nye, 1953] Nye, J. (1953). Some geometrical relations in dislocated crystals. *Acta Metall.*, 1:153–162.

[Obstalecki et al., 2014] Obstalecki, M., Wong, S. L., Dawson, P. R., and Miller, M. P. (2014). Quantitative analysis of crystal scale deformation heterogeneity during cyclic plasticity using high-energy x-ray diffraction and finite-element simulation. *Acta Materialia*, 75:259–272.

[Oddershede et al., 2012] Oddershede, J., Camin, B., Schmidt, S., Mikkelsen, L. P., Sørensen, H. O., Lienert, U., Poulsen, H. F., and Reimers, W. (2012). Measuring the stress field around an evolving crack in tensile deformed mg az31 using three-dimensional x-ray diffraction. *Acta Materialia*, 60(8):3570–3580.

[Oddershede et al., 2010] Oddershede, J., Schmidt, S., Poulsen, H. F., Sørensen, H. O., Wright, J., and Reimers, W. (2010). Determining grain resolved stresses in polycrystalline materials using three-dimensional x-ray diffraction. *Journal of Applied Crystallography*, 43(3).

[Olsen et al., 2009] Olsen, U. L., Schmidt, S., Poulsen, H. F., Linnros, J., Yun, S. H., Di Michiel, M., and Martin, T. (2009). Structured scintillators for x-ray imaging with micrometre resolution. *Nuclear Instruments and Methods in Physics Research Section A: Accelerators, Spectrometers, Detectors and Associated Equipment*, 607(1):141–144.

[Paganin et al., 2002] Paganin, D., Mayo, S., Gureyev, T. E., Miller, P. R., and Wilkins, S. W. (2002). Simultaneous phase and amplitude extraction from a single defocused image of a homogeneous object. *Journal of microscopy*, 206(1):33–40.

[Palenstijn et al., 2013] Palenstijn, W. J., Batenburg, K. J., and Sijbers, J. (2013). The astra tomography toolbox. In *13th International Conference on Computational and Mathematical Methods in Science and Engineering, CMMSE*, volume 2013.

[Pantleon et al., 2009] Pantleon, W., Wejdemann, C., Jakobsen, B., Lienert, U., and Poulsen, H. F. (2009). Evolution of deformation structures under varying

loading conditions followed in situ by high angular resolution 3dxrd. *Materials Science and Engineering: A*, 524(1):55–63.

[Pashley et al., 1967] Pashley, D., Jacobs, M., and Vietz, J. (1967). The basic processes affecting two-step ageing in an al-mg-si alloy. *Philosophical magazine*, 16(139):51–76.

[Perrin et al., 2010] Perrin, C., Berbenni, S., Vehoff, H., and Berveiller, M. (2010). Role of discrete intragranular slip on lattice rotations in polycrystalline ni: Experimental and micromechanical studies. *Acta Materialia*, 58(14):4639–4649.

[Philip et al., 2013] Philip, A., Meyssonnier, J., Kluender, R. T., and Baruchel, J. (2013). Three-dimensional rocking curve imaging to measure the effective distortion in the neighbourhood of a defect within a crystal: an ice example. *Journal of applied crystallography*, 46(4):842–848.

[Poulsen, 2004a] Poulsen, H. F. (2004a). *Three-dimensional X-ray diffraction microscopy: mapping polycrystals and their dynamics*, volume 205. Springer Science & Business Media.

[Poulsen, 2004b] Poulsen, H. F. (2004b). *Three-dimensional X-ray diffraction microscopy: mapping polycrystals and their dynamics*, volume 205. Springer.

[Poulsen et al., 2001] Poulsen, H. F., Nielsen, S. F., Lauridsen, E. M., Schmidt, S., Suter, R., Lienert, U., Margulies, L., Lorentzen, T., and Juul Jensen, D. (2001). Three-dimensional maps of grain boundaries and the stress state of individual grains in polycrystals and powders. *Journal of applied crystallography*, 34(6):751–756.

[Poulsen et al., 2009] Poulsen, H. F., Schmidt, S., Wright, J., Sørensen, H., Oddershede, J., and Alpers, A. (2009). 3dxrd and totalcryst geometry. Technical report, Technical report, SourceForge, 2009. cited on: 119.

[Prasad et al., 2013] Prasad, N. E., Gokhale, A., and Wanhill, R. (2013). *Aluminum-Lithium Alloys: Processing, Properties, and Applications*. Butterworth-Heinemann.

[Proton, 2012] Proton, V. (2012). Caractérisation et compréhension du comportement en corrosion de structures en alliage d'al-cu-li 2050 assemblées par friction stir welding (fsw).

[Proudhon, 2015] Proudhon, H. (2015). Three dimensional study of deformation and fracture in polycrystalline materials: from synchrotron x-ray investigations to computational mechanics. "Habilitation à diriger les recherches.

[Proudhon et al., 2015] Proudhon, H., Li, J., Reischig, P., Guéninchault, N., Forest, S., and Ludwig, W. (2015). Coupling diffraction contrast tomography with the finite element method. *Advanced Engineering Materials*.

[Proudhon et al., 2016] Proudhon, H., Li, J., Reischig, P., Guéninchault, N., Forest, S., and Ludwig, W. (2016). Coupling diffraction contrast tomography with the finite element method. *Advanced Engineering Materials*, 18(6):903–912.

[Proudhon et al., 2017] Proudhon, H., Li, J., Roos, A., Ludwig, W., and Forest, S. (2017). Simulation of short fatigue crack propagation in a 3D experimental microstructure. *Advanced Engineering Materials*, accepted for publication.

[Proudhon et al., 2010] Proudhon, H., Vaxelaire, V., Labat, S., Forest, S., and Thomas, O. (2010). Finite element simulations of coherent diffraction in elastoplastic polycrystalline aggregates. *Comptes Rendus Physique*, 11:293–303.

[Radmilovic et al., 1989] Radmilovic, V., Fox, A., Fisher, R., and Thomas, G. (1989). Lithium depletion in precipitate free zones (pfz's) in al-li base alloys. *Scripta Metallurgica*, 23(1):75 – 79.

[Ramachandran, 1944] Ramachandran, G. (1944). X-ray topographs of diamond. *Proceedings Mathematical Sciences*, 19(5):280–292.

[Rauch and Véron, 2014] Rauch, E. and Véron, M. (2014). Automated crystal orientation and phase mapping in tem. *Materials Characterization*, 98:1–9.

[Reischig et al., 2013] Reischig, P., King, A., Nervo, L., Viganò, N., Guilhem, Y., Palenstijn, W. J., Batenburg, K., Preuss, M., and Ludwig, W. (2013). Advances in x-ray diffraction contrast tomography: flexibility in the setup geometry and application to multiphase materials. *Journal of Applied Crystallography*, 46(2):297–311.

[Renversade et al., 2016] Renversade, L., Quey, R., Ludwig, W., Menasche, D., Maddali, S., Suter, R. M., and Borbely, A. (2016). Comparison between diffraction contrast tomography and high-energy diffraction microscopy on a slightly deformed aluminium alloy. *IUCrJ*, 3(1).

[Robach et al., 2014] Robach, O., Kirchlechner, C., Micha, J.-S., Ulrich, O., Biquard, X., Geaymond, O., Castelnau, O., Bornert, M., Petit, J., Berveiller, S., et al. (2014). Laue microdiffraction at the esrf. *Strain and Dislocation Gradients from Diffraction: Spatially-Resolved Local Structure and Defects*, page 156.

[Robach et al., 2011] Robach, O., Micha, J.-S., Ulrich, O., and Gergaud, P. (2011). Full local elastic strain tensor from laue microdiffraction: simultaneous laue

pattern and spot energy measurement. *Journal of applied Crystallography*, 44(4):688–696.

[Roberts and Lehtinen, 1972] Roberts, W. and Lehtinen, B. (1972). On the feasibility of in situ observations of recrystallization in the high voltage electron microscope. *Philosophical Magazine*, 26(5):1153–1166.

[Rodrigues, 1840] Rodrigues, O. (1840). Des lois géometriques qui régissent les déplacements d'un système solide dans l'espace et de la variation des coordonnées provenant de déplacements considérés indépendamment des causes qui peuvent les produire. *J Math Pure Appl*, 5:380–440.

[Roscoat et al., 2011] Roscoat, S. R. d., King, A., Philip, A., Reischig, P., Ludwig, W., Flin, F., and Meyssonnier, J. (2011). Analysis of snow microstructure by means of x-ray diffraction contrast tomography. *Advanced Engineering Materials*, 13(3):128–135.

[Roux et al., 2008] Roux, S., Hild, F., Viot, P., and Bernard, D. (2008). Three-dimensional image correlation from x-ray computed tomography of solid foam. *Composites Part A: Applied science and manufacturing*, 39(8):1253–1265.

[Rowenhorst et al., 2010] Rowenhorst, D., Lewis, A., and Spanos, G. (2010). Three-dimensional analysis of grain topology and interface curvature in a β-titanium alloy. *Acta Materialia*, 58(16):5511–5519.

[Rowenhorst et al., 2015] Rowenhorst, D., Rollett, A. D., Rohrer, G. S., Groeber, M., Jackson, M., Konijnenberg, P. J., and Graef, M. D. (2015). Consistent representations of and conversions between 3d rotations. *Modelling and Simulation in Materials Science and Engineering*, 23(8):083501.

[Ruggles and Fullwood, 2013] Ruggles, T. and Fullwood, D. (2013). Estimations of bulk geometrically necessary dislocation density using high resolution ebsd. *Ultramicroscopy*, 133:8–15.

[Ruska, 1934] Ruska, E. (1934). Über fortschritte im bau und in der leistung des magnetischen elektronenmikroskops. *Zeitschrift für Physik A Hadrons and Nuclei*, 87(9):580–602.

[Salvo et al., 2003] Salvo, L., Cloetens, P., Maire, E., Zabler, S., Blandin, J., Buffière, J.-Y., Ludwig, W., Boller, E., Bellet, D., and Josserond, C. (2003). X-ray micro-tomography an attractive characterisation technique in materials science. *Nuclear instruments and methods in physics research section B: Beam interactions with materials and atoms*, 200:273–286.

[Sanders and Starke, 1982] Sanders, T. and Starke, E. A. (1982). The effect of slip distribution on the monotonic and cyclic ductility of AlLi binary alloys. *Acta Metallurgica*, 30(5):927–939.

[Sankaran and Grant, 1981] Sankaran, K. and Grant, N. (1981). I98i in proc. 1st int. conf. *Aluminium-Lithium alloys (ed. TH Sanders, Jr & EA Starke, Jr)*, pages 205–227.

[Schmidt et al., 2004] Schmidt, S., Nielsen, S. F., Gundlach, C., Margulies, L., Huang, X., and Jensen, D. J. (2004). Watching the growth of bulk grains during recrystallization of deformed metals. *Science*, 305(5681):229–232.

[Sedmák et al., 2016] Sedmák, P., Pilch, J., Heller, L., Kopeček, J., Wright, J., Sedlák, P., Frost, M., and Šittner, P. (2016). Grain-resolved analysis of localized deformation in nickel-titanium wire under tensile load. *Science*, 353(6299):559–562.

[Shmueli, 2008] Shmueli, U. (2008). *International Tables for Crystallography, Reciprocal Space*. Springer Science & Business Media.

[Simons et al., 2016] Simons, H., Jakobsen, A. C., Ahl, S. R., Detlefs, C., and Poulsen, H. F. (2016). Multiscale 3d characterization with dark-field x-ray microscopy. *Mrs Bulletin*, 41(06):454–459.

[Simons et al., 2015a] Simons, H., King, A., Ludwig, W., Detlefs, C., Pantleon, W., Schmidt, S., Snigireva, I., Snigirev, A., and Poulsen, H. F. (2015a). Dark-field x-ray microscopy for multiscale structural characterization. *Nature communications*, 6.

[Simons et al., 2015b] Simons, H., King, A., Ludwig, W., Detlefs, C., Pantleon, W., Schmidt, S., Stöhr, F., Snigireva, I., Snigirev, A., and Poulsen, H. F. (2015b). Dark-field x-ray microscopy for multiscale structural characterization. *Nature communications*, 6.

[Snigirev et al., 1996] Snigirev, A., Kohn, V., Snigireva, I., and Lengeler, B. (1996). A compound refractive lens for focusing high-energy x-rays. *Nature*, 384(6604):49.

[Solutions, 2010] Solutions, C. (2010). Vic-3d manual. correlated solutions. *Inc., Columbia, SC*.

[Sorby, 1863] Sorby, H. C. (1863). On the microscopical structure of meteorites. *Proceedings of the Royal Society of London*, 13:333–334.

[Spowart and Mullens, 2008] Spowart, J. and Mullens, H. (2008). High speed and repeatability serial sectioning method for 3-d reconstruction of microstructures using optical microscopy. US Patent 7,319,916.

[Spowart et al., 2003] Spowart, J. E., Mullens, H. E., and Puchala, B. T. (2003). Collecting and analyzing microstructures in three dimensions: a fully automated approach. *Jom*, 55(10):35–37.

[Starke and Staley, 1996] Starke, E. and Staley, J. (1996). Application of modern aluminum alloys to aircraft. *Progress in Aerospace Sciences*, 32(2):131 – 172.

[Starke, 1970] Starke, E. A. (1970). The causes and effects of "denuded" or "precipitate-free" zones at grain boundaries in aluminum-base alloys. *JOM*, 22(1):54–63.

[Stoudt et al., 2011] Stoudt, M., Levine, L., Creuziger, A., and Hubbard, J. (2011). The fundamental relationships between grain orientation, deformation-induced surface roughness and strain localization in an aluminum alloy. *Materials Science and Engineering: A*, 530:107–116.

[Suga and Imura, 1976] Suga, H. and Imura, T. (1976). Dynamic behavior of dislocations in silver and silver base dilute alloy single crystals. *Transactions of the Japan Institute of Metals*, 17(10):605–614.

[Svendsen, 2002] Svendsen, B. (2002). Continuum thermodynamic models for crystal plasticity including the effects of geometrically-necessary dislocations. *J. Mech. Phys. Solids*, 50:1297–1329.

[Syha et al., 2013a] Syha, M., Bäurer, M., Rheinheimer, W., Ludwig, W., Lauridsen, E. M., Weygand, D., and Gumbsch, P. (2013a). Combining x-ray diffraction contrast tomography and mesoscale grain growth simulations in strontium titanate: An integrated approach for the investigation of microstructure evolution. *Developments in Strategic Materials and Computational Design III*, pages 127–137.

[Syha et al., 2013b] Syha, M., Trenkle, A., Lödermann, B., Graff, A., Ludwig, W., Weygand, D., and Gumbsch, P. (2013b). Validation of three-dimensional diffraction contrast tomography reconstructions by means of electron backscatter diffraction characterization. *Journal of applied crystallography*, 46(4):1145–1150.

[Tabourot et al., 1997] Tabourot, L., Fivel, M., and Rauch, E. (1997). Generalised constitutive laws for fcc single crystals. *Materials Science and Engineering: A*, 234:639–642.

[Taillandier-Thomas et al., 2016] Taillandier-Thomas, T., Jailin, C., Roux, S., and Hild, F. (2016). Measurement of 3d displacement fields from few tomographic projections. In *SPIE Photonics Europe*, pages 98960L–98960L. International Society for Optics and Photonics.

[Tamura et al., 2002] Tamura, N., MacDowell, A., Celestre, R., Padmore, H., Valek, B., Bravman, J., Spolenak, R., Brown, W., Marieb, T., Fujimoto, H., et al. (2002). High spatial resolution grain orientation and strain mapping in thin films using polychromatic submicron x-ray diffraction. *Applied Physics Letters*, 80(20):3724–3726.

[Tanner, 1976] Tanner, B. K. (1976). *X-Ray Diffraction Topography: International Series in the Science of the Solid State*, volume 10. Elsevier.

[Teodosiu, 1970] Teodosiu, C. (1970). A dynamic theory of dislocations and its applications to the theory of the elastic-plastic continuum. In Simmons, J., de Wit, R., and Bullough, R., editors, *Fundamental Aspects of Dislocation Theory*, pages 837–876. Nat. Bur. Stand. (US) Spec. Publ. 317, II.

[Teodosiu et al., 1993] Teodosiu, C., Raphanel, J., and Tabourot, L. (1993). Finite element simulation of the large elastoplastic deformation of multi-crystals. In Teodosiu, C. and Sidoroff, F., editors, *Large Plastic Deformations MECAMAT'91*, pages 153–158. Balkema, Rotterdam.

[Teodosiu and Sidoroff, 1976] Teodosiu, C. and Sidoroff, F. (1976). A theory of finite elastoviscoplasticity of single crystals. *Int. J. of Engng Science*, 14:165–176.

[Thomas and Whelan, 1961] Thomas, G. and Whelan, M. (1961). Observations of precipitation in thin foils of aluminium+ 4% copper alloy. *Philosophical Magazine*, 6(69):1103–1114.

[Tuomi, 2002] Tuomi, T. (2002). Synchrotron x-ray topography of electronic materials. *Journal of synchrotron radiation*, 9(3):174–178.

[Tuomi et al., 1974] Tuomi, T., Naukkarinen, K., and Rabe, P. (1974). Use of synchrotron radiation in x-ray diffraction topography. *physica status solidi (a)*, 25(1):93–106.

[Van Boxel et al., 2014] Van Boxel, S., Schmidt, S., Ludwig, W., Zhang, Y., Jensen, D. J., and Pantleon, W. (2014). Direct observation of grain boundary migration during recrystallization within the bulk of a moderately deformed aluminium single crystal. *Materials Transactions*, 55(1):128–136.

[Van Boxel et al., 2010] Van Boxel, S., Schmidt, S., Ludwig, W., Zhang, Y., Sørensen, H., Pantleon, W., and Juul Jensen, D. (2010). Monitoring grain boundary migration during recrystallization using topotomography. In N. Hansen, D. Juul Jensen, S. N. H. P. B. R., editor, *31st Risø International Symposium on Materials Science*, volume 31, pages 449–456, Roskilde, Denmark.

[Vander Voort, 1993] Vander Voort, G. F. (1993). *Metallography–past, Present, and Future: 75th Anniversary Volume*, volume 1165. ASTM International.

[Vaughan et al., 2011] Vaughan, G. B., Wright, J. P., Bytchkov, A., Rossat, M., Gleyzolle, H., Snigireva, I., and Snigirev, A. (2011). X-ray transfocators: focusing devices based on compound refractive lenses. *Journal of synchrotron radiation*, 18(2):125–133.

[Vaxelaire et al., 2010] Vaxelaire, V., Proudhon, H., Labat, S., Kirchlechner, C., Keckes, J., Jacques, V., Ravy, S., Forest, S., and Thomas, O. (2010). Methodology for studying strain inhomogeneities in polycrystalline thin films during in situ thermal loading using coherent x-ray diffraction. *New Journal of Physics*, 12:035018.

[Viganò et al., 2013] Viganò, N., Ludwig, W., and Batenburg, K. J. (2013). Discrete representation of local orientation in grains using diffraction contrast tomography. In *2013 8th International Symposium on Image and Signal Processing and Analysis (ISPA)*, pages 594–599. IEEE.

[Viganò et al., 2014] Viganò, N., Ludwig, W., and Batenburg, K. J. (2014). Reconstruction of local orientation in grains using a discrete representation of orientation space. *Journal of Applied Crystallography*, 47(6):1826–1840.

[Viganò et al., 2016] Viganò, N., Nervo, L., Valzania, L., Singh, G., Preuss, M., Batenburg, K. J., and Ludwig, W. (2016). A feasibility study of full-field x-ray orientation microscopy at the onset of deformation twinning. *Journal of Applied Crystallography*, 49(2).

[Viganò et al., 2016] Viganò, N., Tanguy, A., Hallais, S., Dimanov, A., Bornert, M., Batenburg, K. J., and Ludwig, W. (2016). Three-dimensional full-field x-ray orientation microscopy. *Scientific reports*, 6.

[Wilkinson et al., 2006] Wilkinson, A. J., Meaden, G., and Dingley, D. J. (2006). High-resolution elastic strain measurement from electron backscatter diffraction patterns: new levels of sensitivity. *Ultramicroscopy*, 106(4):307–313.

[Wisniewski and Rüssel, 2015] Wisniewski, W. and Rüssel, C. (2015). An experimental viewpoint on the information depth of ebsd. *Scanning*.

[Wright and Adams, 1992] Wright, S. I. and Adams, B. L. (1992). Automatic analysis of electron backscatter diffraction patterns. *Metallurgical and Materials Transactions A*, 23(3):759–767.

[Wright et al., 2016] Wright, S. I., Suzuki, S., and Nowell, M. M. (2016). In situ ebsd observations of the evolution in crystallographic orientation with deformation. *JOM*, 68(11):2730–2736.

[Wu et al., 1991] Wu, T.-Y., Bassani, J. L., and Laird, C. (1991). Latent hardening in single crystals i. theory and experiments. In *Proceedings of the Royal Society of London A: Mathematical, Physical and Engineering Sciences*, volume 435, pages 1–19. The Royal Society.

[Wu and Sullivan, 2003] Wu, Z. and Sullivan, J. M. (2003). Multiple material marching cubes algorithm. *International Journal for Numerical Methods in Engineering*, 58(2):189–207.

[Xu et al., 2016] Xu, Y., Balint, D., and Dini, D. (2016). A method of coupling discrete dislocation plasticity to the crystal plasticity finite element method. *Modelling and Simulation in Materials Science and Engineering*, 24(4):045007.

[Young Jr and Sherrill, 1972] Young Jr, F. and Sherrill, F. (1972). Burgers vector of dislocations generated by small stresses in copper crystals. *Journal of Applied Physics*, 43(7):2949–2950.

[Young Jr et al., 1965] Young Jr, F., Sherrill, F., and Wittels, M. (1965). Observations of dislocations in copper using borrmann transmission topographs. *Journal of Applied Physics*, 36(7):2225–2230.

[Zachariasen, 2004] Zachariasen, W. H. (2004). *Theory of X-ray Diffraction in Crystals*. Courier Corporation.

[Zhu et al., 2005] Zhu, K., Chaubet, D., Bacroix, B., and Brisset, F. (2005). A study of recovery and primary recrystallization mechanisms in a zr–2hf alloy. *Acta materialia*, 53(19):5131–5140.

[Zolotov et al., 2011] Zolotov, D., Buzmakov, A., Asadchikov, V., Voloshin, A., Shkurko, V., and Smirnov, I. (2011). Study of the internal structure of lithium fluoride single crystal by laboratory x-ray topo-tomography. *Crystallography reports*, 56(3):393–396.

Appendix A

Continuum crystal plasticity theory

From S. Forest Master course MAGIS.

Continuum crystal plasticity is a special class of anisotropic elastoviscoplastic behaviour of materials. It relies on the precise knowledge of the kinematics of plastic slip according to crystallographic slip systems and of the driving force for activation of plastic slip, namely the corresponding resolved shear stress. When the number of dislocations inside the material volume element is high enough, a continuum description of plastic deformation and hardening can be formulated as settled in [Mandel, 1965, Mandel, 1971, Mandel, 1973b] and [Teodosiu and Sidoroff, 1976].

The objective of this contribution is to establish the continuum mechanical framework for the formulation of constitutive equations for single crystals. The considered plastic deformation mechanism is crystallographic slip but the formulation can serve as a basis for extensions to climb or twinning since thermomechanical balances and most kinematic considerations are still valid.

There exists an extreme variety of possible constitutive equations for single crystals derived in the last 40 years but the thermomechanical foundation is unique and now clearly settled. We will consider the variety of constitutive laws by introducing generic internal variables without making specific choices. Only generic examples of evolution laws for such internal variables are provided and the reader is referred to [Fivel and Forest, 2004a], and references quoted therein, for a detailed discussion of best–suited constitutive laws for metal single crystals. Also the transition from single to polycrystal behaviour is not addressed here but rather in [Fivel and Forest, 2004b, Besson et al., 2009].

The most relevant internal variables for describing the work–hardening of single crystals are undoubtedly dislocation densities, ρ^s, defined as the total length of dislocations belonging to a slip system s divided by the volume of

the material volume element. Evolution equations for dislocations densities can be found in [Fivel and Forest, 2004a]. In the present contribution, we introduce general isotropic and kinematic hardening variables accounting for monotonic and cyclic responses of crystals. Dislocation densities are generally related to isotropic hardening through forest hardening but recent contributions also aim at establishing dislocation based kinematic hardening dislocation rules.

Another characterisation of the dislocation distribution is the dislocation density tensor introduced by [Nye, 1953]. It is defined in section A.2 and contributes to many size effects observed in crystalline solids: grain size or Hall–Petch effect, precipitate size effect, etc. The dislocation density tensor cannot be handled as a usual internal variable because it is related to the gradient of the plastic deformation field. As a result, higher order partial differential equations arise when hardening laws involve the dislocation density tensor. The development of constitutive models involving the dislocation density tensor is the realm of strain gradient plasticity. Such a strain gradient plasticity theory is proposed in section A.3. Even for the probably too simple constitutive equations presented here, the model shows that the dislocation density tensor is responsible for a size–dependent kinematic hardening component in the material behaviour.

A.1 Thermomechanics of single crystal behaviour

A.1.1 Balance equations

Mechanical equilibrium can be expressed in the form of the principle of virtual power

$$-\int_{\mathcal{D}} \underset{\sim}{\boldsymbol{\sigma}} : \underset{\sim}{\boldsymbol{D}}^* \, dv + \int_{\mathcal{D}} \rho(\underline{\boldsymbol{f}} - \underline{\boldsymbol{a}}) \cdot \underline{\boldsymbol{v}}^* \, dv + \int_{\partial\mathcal{D}} \underline{\boldsymbol{t}} \cdot \underline{\boldsymbol{v}}^* \, ds = 0 \tag{A.1}$$

for all virtual velocity fields and all subdomains, $\mathcal{D}$, of the current configuration Ω of the body. The Cauchy stress tensor is $\underset{\sim}{\boldsymbol{\sigma}}$ and $\underset{\sim}{\boldsymbol{D}}$ is the strain rate tensor. Volume and acceleration forces are denoted by $\underline{\boldsymbol{f}}$ and $\underline{\boldsymbol{a}}$, respectively, whereas $\underline{\boldsymbol{t}}$ is the traction vector. The principle of virtual power implies the following balance of momentum equation

$$\operatorname{div} \underset{\sim}{\boldsymbol{\sigma}} + \rho \underline{\boldsymbol{f}} = \rho \underline{\boldsymbol{a}} \tag{A.2}$$

The energy balance is the purpose of the first principle of thermodynamics

$$\int_{\mathcal{D}} \rho \dot{e} \, dv - \int_{\mathcal{D}} \rho(\underline{\boldsymbol{a}} - \underline{\boldsymbol{f}}) \cdot \underline{\boldsymbol{v}} \, dv = \int_{\partial\mathcal{D}} \underline{\boldsymbol{t}} \cdot \underline{\boldsymbol{v}} \, ds + \mathcal{Q} \tag{A.3}$$

or equivalently, after implementing the balance of momentum principle,

$$\int_{\mathcal{D}} \rho \dot{e}\, dv = \int_{\mathcal{D}} \underset{\sim}{\boldsymbol{\sigma}} : \underset{\sim}{\boldsymbol{D}}\, dv + \mathcal{Q} \tag{A.4}$$

where ρe is the volume density of internal energy. The heat production rate is assumed to take the form

$$\mathcal{Q} = -\int_{\partial\mathcal{D}} \underline{\boldsymbol{q}} \cdot \underline{\boldsymbol{n}}\, ds \tag{A.5}$$

The local form of the energy principle is then

$$\rho \dot{e} = \underset{\sim}{\boldsymbol{\sigma}} : \underset{\sim}{\boldsymbol{D}} - \operatorname{div} \underline{\boldsymbol{q}} \tag{A.6}$$

The second principle of thermodynamics stipulates that

$$\int_{\mathcal{D}} \rho \dot{\eta}\, dv + \int_{\partial\mathcal{D}} \frac{\underline{\boldsymbol{q}}}{T} \cdot \underline{\boldsymbol{n}}\, ds \geq 0 \tag{A.7}$$

where η is the mass density of entropy and T the temperature field. The validity of this principle with respect to all subdomain $\mathcal{D}$ leads to the local form of the entropy principle

$$\rho \dot{\eta} + \operatorname{div} \frac{\underline{\boldsymbol{q}}}{T} \geq 0 \tag{A.8}$$

Introducing the free energy density $\Psi := e - T\eta$ and taking the balance of energy into account, we are lead to the Clausius inequality

$$\underset{\sim}{\boldsymbol{\sigma}} : \underset{\sim}{\boldsymbol{D}} - \rho \dot{\Psi} - \rho \eta \dot{T} - \underline{\boldsymbol{q}} \cdot \frac{\boldsymbol{\nabla} T}{T} \geq 0 \tag{A.9}$$

A.1.2 Kinematics of single crystals

It is based on the multiplicative decomposition of the deformation gradient, $\underset{\sim}{\boldsymbol{F}}$, into an elastic part, $\underset{\sim}{\boldsymbol{E}}$, and a plastic part, $\underset{\sim}{\boldsymbol{P}}$:

$$\underset{\sim}{\boldsymbol{F}}(\underline{\boldsymbol{X}}) = \underset{\sim}{\mathbf{1}} + \frac{\partial \underline{\boldsymbol{u}}}{\partial \underline{\boldsymbol{X}}} = \underset{\sim}{\mathbf{1}} + \boldsymbol{\nabla}_X \underline{\boldsymbol{u}}, \quad \underset{\sim}{\boldsymbol{F}}(\underline{\boldsymbol{X}}) = \underset{\sim}{\boldsymbol{E}}(\underline{\boldsymbol{X}}).\underset{\sim}{\boldsymbol{P}}(\underline{\boldsymbol{X}}) \tag{A.10}$$

The initial coordinates of the material point in the reference configuration are denoted by $\underline{\boldsymbol{X}}$ and $\boldsymbol{\nabla}_X$ denotes the gradient operator with respect to initial coordinates. The current position of the material point in the current configuration is $\underline{\boldsymbol{x}}$. The displacement vector is $\underline{\boldsymbol{u}} = \underline{\boldsymbol{x}} - \underline{\boldsymbol{X}}$. The multiplicative decomposition (A.10) is associated with the definition of an intermediate configuration for

which elastic strain is unloaded, see figure 4.1. The intermediate released configuration is uniquely determined up to a rigid body rotation which is chosen such that the lattice orientation in the intermediate configuration is the same as the initial one. Mandel called it the *isoclinic* intermediate configuration. As a result, lattice rotation and distortion during elastoplastic deformation are contained in the elastic deformation part $\underset{\sim}{\boldsymbol{E}}$, as examined at the end of this section.

The multiplicative decomposition leads to the following partition of the velocity gradient

$$\boldsymbol{\nabla} \underline{\boldsymbol{v}} = \dot{\underset{\sim}{\boldsymbol{F}}} \cdot \underset{\sim}{\boldsymbol{F}}^{-1} = \dot{\underset{\sim}{\boldsymbol{E}}} \cdot \underset{\sim}{\boldsymbol{E}}^{-1} + \underset{\sim}{\boldsymbol{E}} \cdot \dot{\underset{\sim}{\boldsymbol{P}}} \cdot \underset{\sim}{\boldsymbol{P}}^{-1} \cdot \underset{\sim}{\boldsymbol{E}}^{-1} \tag{A.11}$$

We introduce the Cauchy–Green and Green–Lagrange elastic strain measures

$$\underset{\sim}{\boldsymbol{C}}^e := \underset{\sim}{\boldsymbol{E}}^T \cdot \underset{\sim}{\boldsymbol{E}}, \quad \underset{\sim}{\boldsymbol{E}}^e = \frac{1}{2}(\underset{\sim}{\boldsymbol{C}}^e - \underset{\sim}{\mathbf{1}}) \tag{A.12}$$

and note that

$$\begin{aligned} \dot{\underset{\sim}{\boldsymbol{E}}}^e &= \frac{1}{2}(\dot{\underset{\sim}{\boldsymbol{E}}}^T \cdot \underset{\sim}{\boldsymbol{E}} + \underset{\sim}{\boldsymbol{E}}^T \cdot \dot{\underset{\sim}{\boldsymbol{E}}}) = \frac{1}{2}\dot{\underset{\sim}{\boldsymbol{C}}}^e \\ &= \frac{1}{2}\underset{\sim}{\boldsymbol{E}}^T \cdot (\underset{\sim}{\boldsymbol{E}}^{-T} \cdot \dot{\underset{\sim}{\boldsymbol{E}}}^T + \dot{\underset{\sim}{\boldsymbol{E}}} \cdot \underset{\sim}{\boldsymbol{E}}^{-1}) \cdot \underset{\sim}{\boldsymbol{E}} = \underset{\sim}{\boldsymbol{E}}^T \cdot \left(\dot{\underset{\sim}{\boldsymbol{E}}}^e \cdot \underset{\sim}{\boldsymbol{E}}^{-1}\right)^{sym} \cdot \underset{\sim}{\boldsymbol{E}} \end{aligned} \tag{A.13}$$

where sym operator takes the symmetric part of the quantity in brackets. The mass density of the material point with respect to the current (resp. intermediate) configuration is denoted by ρ (resp. ρ_e). The volume density of internal forces with respect to the intermediate configuration is

$$\begin{aligned} J_e \underset{\sim}{\boldsymbol{\sigma}} : \underset{\sim}{\boldsymbol{D}} &= J_e \underset{\sim}{\boldsymbol{\sigma}} : (\dot{\underset{\sim}{\boldsymbol{F}}} \cdot \underset{\sim}{\boldsymbol{F}}^{-1}) = J_e \underset{\sim}{\boldsymbol{\sigma}} : (\dot{\underset{\sim}{\boldsymbol{E}}} \cdot \underset{\sim}{\boldsymbol{E}}^{-1}) + J_e \underset{\sim}{\boldsymbol{\sigma}} : (\underset{\sim}{\boldsymbol{E}} \cdot \dot{\underset{\sim}{\boldsymbol{P}}} \cdot \underset{\sim}{\boldsymbol{P}}^{-1} \cdot \underset{\sim}{\boldsymbol{E}}^{-1}) \\ &= J_e \underset{\sim}{\boldsymbol{\sigma}} : (\dot{\underset{\sim}{\boldsymbol{E}}} \cdot \underset{\sim}{\boldsymbol{E}}^{-1})^{sym} + J_e \underset{\sim}{\boldsymbol{\sigma}} : (\underset{\sim}{\boldsymbol{E}} \cdot \dot{\underset{\sim}{\boldsymbol{P}}} \cdot \underset{\sim}{\boldsymbol{P}}^{-1} \cdot \underset{\sim}{\boldsymbol{E}}^{-1}) \\ &= \underset{\sim}{\boldsymbol{\Pi}}^e : \dot{\underset{\sim}{\boldsymbol{E}}}^e + \underset{\sim}{\boldsymbol{M}} : \dot{\underset{\sim}{\boldsymbol{P}}} . \underset{\sim}{\boldsymbol{P}}^{-1} \end{aligned} \tag{A.14}$$

where $J_e = \det \underset{\sim}{\boldsymbol{E}}$ is the volume change from the intermediate to the current configuration, $\underset{\sim}{\boldsymbol{\Pi}}^e$ is the second Piola–Kirchhoff stress tensor with respect to the isoclinic intermediate configuration, and $\underset{\sim}{\boldsymbol{M}}$ is the Mandel stress tensor defined as :

$$\underset{\sim}{\boldsymbol{\Pi}}^e = J_e \underset{\sim}{\boldsymbol{E}}^{-1} . \underset{\sim}{\boldsymbol{\sigma}} . \underset{\sim}{\boldsymbol{E}}^{-T}, \quad \underset{\sim}{\boldsymbol{M}} = J_e \underset{\sim}{\boldsymbol{E}}^T . \underset{\sim}{\boldsymbol{\sigma}} . \underset{\sim}{\boldsymbol{E}}^{-T} = \underset{\sim}{\boldsymbol{C}}^e \cdot \underset{\sim}{\boldsymbol{\Pi}}^e \tag{A.15}$$

Plastic deformation is the result of slip processes according to N slip systems characterised by the slip direction, $\underline{\boldsymbol{m}}^{\,s}$, and the normal to the slip plane, $\underline{\boldsymbol{n}}^{\,s}$, in the intermediate configuration :

$$\dot{\underset{\sim}{\boldsymbol{P}}} . \underset{\sim}{\boldsymbol{P}}^{-1} = \sum_{s=1}^{N} \dot{\gamma}^s \underline{\boldsymbol{m}}^{\,s} \otimes \underline{\boldsymbol{n}}^{\,s} \tag{A.16}$$

Note that plastic deformation induced by dislocation glide is isochoric so that

$$J_p = \det \underset{\sim}{\boldsymbol{P}} = 1, \quad J_e = J = \det \underset{\sim}{\boldsymbol{F}} \tag{A.17}$$

A.1.3 Constitutive equations

Constitutive equations for elastoviscoplastic materials are based on the definition of two potential functions, namely the free energy density function and the dissipation potential. The specific energy density, $\Psi(\underset{\sim}{\boldsymbol{E}}^e, T, \alpha)$, is a function of elastic strain, temperature and internal variables accounting for hardening properties. Writing the Clausius–Duhem inequality (A.9) with respect to the intermediate isoclinic configuration amounts to multiplying (A.9) by $\rho_e/\rho = J_e$

$$J_e \underset{\sim}{\boldsymbol{\sigma}} : \underset{\sim}{\boldsymbol{D}} - \rho_e \dot{\Psi} - \rho_e \eta \dot{T} - \underline{\boldsymbol{Q}} \cdot \frac{\boldsymbol{\nabla}_X T}{T} \geq 0 \tag{A.18}$$

where $\underline{\boldsymbol{Q}} = J_e \underset{\sim}{\boldsymbol{F}}^{-T} \cdot \underline{\boldsymbol{q}}$. Expanding the time derivative of the free energy density, we obtain

$$\left(\underset{\sim}{\boldsymbol{\Pi}}^e - \rho_e \frac{\partial \Psi}{\partial \underset{\sim}{\boldsymbol{E}}^e} \right) : \dot{\underset{\sim}{\boldsymbol{E}}}^e - \rho_e (\eta + \frac{\partial \Psi}{\partial T}) \dot{T} + \underset{\sim}{\boldsymbol{M}} : \dot{\underset{\sim}{\boldsymbol{P}}} \cdot \underset{\sim}{\boldsymbol{P}}^{-1} - \rho_e \frac{\partial \Psi}{\partial \alpha} \dot{\alpha} - \underline{\boldsymbol{Q}} \cdot \frac{\boldsymbol{\nabla}_X}{\partial T} \geq 0 \tag{A.19}$$

The following state laws provide the hyperelasticity relation and the entropy density :

$$\underset{\sim}{\boldsymbol{\Pi}}^e = \rho_e \frac{\partial \Psi}{\partial \underset{\sim}{\boldsymbol{E}}^e} = \underset{\approx}{\boldsymbol{C}} : \underset{\sim}{\boldsymbol{E}}^e, \quad \eta = -\frac{\partial \Psi}{\partial T}, \quad X = \rho_e \partial \Psi / \partial \alpha \tag{A.20}$$

where a quadratic potential for elasticity has been proposed, thus introducing the fourth rank tensor of elasticity moduli, $\underset{\approx}{\boldsymbol{C}}$. Such an assumption is realistic for metals since elastic strain usually remains small, as discussed in the next subsection. The thermodynamic forces associated with the internal variables α are called X. The residual dissipation rate is

$$\underset{\sim}{\boldsymbol{M}} : \dot{\underset{\sim}{\boldsymbol{P}}} \cdot \underset{\sim}{\boldsymbol{P}}^{-1} - X \dot{\alpha} - \underline{\boldsymbol{Q}} \cdot \frac{\boldsymbol{\nabla}_X T}{T} \geq 0 \tag{A.21}$$

The first term is the plastic power. Part of it is stored due to the second contribution whereas the third one denotes thermal dissipation.

At this stage, a dissipation potential $\Omega(\underset{\sim}{\boldsymbol{M}}, X)$ is introduced from which the flow rule and the evolution equation for internal variables are derived

$$\dot{\underset{\sim}{\boldsymbol{P}}} . \underset{\sim}{\boldsymbol{P}}^{-1} = \frac{\partial \Omega}{\partial \underset{\sim}{\boldsymbol{M}}}, \quad \dot{\alpha} = -\frac{\partial \Omega}{\partial X} \tag{A.22}$$

Positivity of dissipation rate is ensured if the dissipation potential $\Omega(\underset{\sim}{\boldsymbol{M}}, X)$ exhibits specific convexity properties with respect to its arguments (convex with

respect to $\underset{\sim}{\boldsymbol{M}}$ and concave with respect to X) and if a Fourier type of heat conduction is chosen

$$\underline{\boldsymbol{Q}} = -\underset{\sim}{\boldsymbol{K}} \cdot \boldsymbol{\nabla}_X(\log T) \tag{A.23}$$

The dissipation potential is assumed to depend on $\underset{\sim}{\boldsymbol{M}}$ and X via the Schmid yield function

$$f^s(\underset{\sim}{\boldsymbol{M}}, X) = |\tau^s - x^s| - \tau_c^s, \quad \text{with} \quad \tau^s = \underset{\sim}{\boldsymbol{M}} : \underline{\boldsymbol{m}}^s \otimes \underline{\boldsymbol{n}}^s \tag{A.24}$$

where τ_c^s is the critical resolved shear stress for slip system s, which may evolve due to isotropic hardening. Kinematic hardening is accounted for by means of back-stress components x^s attached to each slip system. The resolved shear stress $\tau^s = \underline{\boldsymbol{m}}^s.\underset{\sim}{\boldsymbol{M}}.\underline{\boldsymbol{n}}^s$ on slip system s is the driving force for activation of slip. This corresponds to the specific choice of hardening variables: $X = (\tau_c^s, x^s)$. So we consider a function

$$\Omega(\underset{\sim}{\boldsymbol{M}}, X) = \sum_{s=1}^{N} \Omega^s(f^s(\underset{\sim}{\boldsymbol{M}}, X)) \tag{A.25}$$

It follows that

$$\dot{\underset{\sim}{\boldsymbol{P}}}.\underset{\sim}{\boldsymbol{P}}^{-1} = \frac{\partial \Omega}{\partial \underset{\sim}{\boldsymbol{M}}} = \sum_{s=1}^{N} \frac{\partial \Omega^s}{\partial f^s} \frac{\partial f^s}{\partial \underset{\sim}{\boldsymbol{M}}} = \sum_{s=1}^{N} \dot{\gamma}^s \underline{\boldsymbol{m}}^s \otimes \underline{\boldsymbol{n}}^s \tag{A.26}$$

where the slip rate is computed as

$$\dot{\gamma}^s = \frac{\partial \Omega^s}{\partial f^s} \operatorname{sign}(\tau^s - x^s) \tag{A.27}$$

Accordingly, the kinematics (A.16) is retrieved from the normality rule, showing that the crystal slip kinematics is associated with the Schmid law. Let us call (ρ^s, α^s) internal variables associated with the isotropic and kinematic hardening variables (τ_c^s, x^s). The hardening rules in (A.22) become

$$\dot{\rho}^s = -\frac{\partial \Omega}{\partial \tau_c^s} = \frac{\partial \Omega^s}{\partial f^s} = |\dot{\gamma}^s|, \quad \dot{\alpha}^s = -\frac{\partial \Omega}{\partial x^s} = \frac{\partial \Omega^s}{\partial f^s} \operatorname{sign}(\tau^s - x^s) = \dot{\gamma}^s \tag{A.28}$$

It is worth computing the plastic power after taking the previous relations into account

$$\underset{\sim}{\boldsymbol{M}} : \dot{\underset{\sim}{\boldsymbol{P}}}.\underset{\sim}{\boldsymbol{P}}^{-1} = \sum_{s=1}^{N} \tau^s \dot{\gamma}^s \tag{A.29}$$

Specific hardening laws including evolution equations for dislocation densities can be found for example in [Fivel and Forest, 2004a]. As an example, we consider here a power law potential

$$\dot{\gamma}^s = \frac{\partial \Omega}{\partial \tau^s} = \left\langle \frac{|\tau^s - x^s| - \tau_c}{K} \right\rangle^n \operatorname{sign}(\tau^s), \tag{A.30}$$

$$\Omega(\tau^s) = \sum_{s=1}^{N} \frac{K}{n+1} \left\langle \frac{|\tau^s - x^s| - \tau_c}{K} \right\rangle^{n+1} \tag{A.31}$$

The brackets $\langle x \rangle$ denote the positive part of x. Viscosity parameters are K and n in (A.30). They can be chosen such that plastic processes are almost rate–independent in a given range of applied strain rates. As an example, we give here simple nonlinear evolution rules for the isotropic and kinematic variables that are used for practical computations

$$\tau_c^s = \tau_c + q \sum_{r=1}^{N} h^{sr}(1 - \exp(-bv^r)), \quad \dot{\alpha}^s = \dot{\gamma}^s - d\dot{v}^s \alpha^s \tag{A.32}$$

where q, b, d are material parameters. An interaction matrix h^{rs} is necessary to account for interaction between dislocations and is responsible for latent hardening [Fivel and Forest, 2004a].

A.1.4 Lattice rotation

The previous continuum mechanical approach makes it possible to distinguish between the transformation of material and lattice directions. Material lines are made of material points that are subjected to the motion $\underline{\boldsymbol{u}}\,(\underline{\boldsymbol{X}}\,)$. The tangent to a material line at $\underline{\boldsymbol{X}}$ is a material direction $\underline{\boldsymbol{d}}$ in the reference configuration that transforms into the material direction $\underline{\boldsymbol{d}}'$ in the current configuration by means of the deformation gradient:

$$\underline{\boldsymbol{d}}'(\underline{\boldsymbol{X}}\,) = \underset{\sim}{\boldsymbol{F}}(\underline{\boldsymbol{X}}\,) \cdot \underline{\boldsymbol{d}}\,(\underline{\boldsymbol{X}}\,) \tag{A.33}$$

In contrast, lattice directions are not material insofar as they are not necessarily made of the same material points (atoms) in the initial and current configurations due to the passing of dislocations, but keep the same crystallographic meaning. According to the concept of isoclinic configuration, lattice directions are unchanged from the initial to the intermediate configuration of figure 4.1. Glide of dislocations through, and thus leaving, the material volume element do not distort nor rotate the lattice, although material lines are sheared. According

to the continuum theory of dislocations, statistically stored dislocations accumulating in the material volume element affect material hardening but do not change the element shape. Accordingly, an initial lattice direction $\underset{\sim}{\boldsymbol{d}}^{\sharp}$ is transformed into $\underset{\sim}{\boldsymbol{d}}^{\sharp\prime}$ by means of the elastic deformation:

$$\underset{\sim}{\boldsymbol{d}}^{\sharp\prime}(\underset{\sim}{\boldsymbol{X}}) = \underset{\approx}{\boldsymbol{E}}(\underset{\sim}{\boldsymbol{X}}).\underset{\sim}{\boldsymbol{d}}^{\sharp}(\underset{\sim}{\boldsymbol{X}}) \tag{A.34}$$

The kinematics of elastoplastic deformation recalled in section A.1.2 can be expanded in the case of small strains and small rotations, based on the polar decompositions of total, elastic and plastic deformations:

$$\underset{\approx}{\boldsymbol{E}} = \underset{\approx}{\boldsymbol{R}}^{e}.\underset{\approx}{\boldsymbol{U}}^{e} \simeq (\underset{\approx}{\mathbf{1}} + \underset{\approx}{\boldsymbol{\omega}}^{e}).(\underset{\approx}{\mathbf{1}} + \underset{\approx}{\boldsymbol{\varepsilon}}^{e}) \simeq \underset{\approx}{\mathbf{1}} + \underset{\approx}{\boldsymbol{\varepsilon}}^{e} + \underset{\approx}{\boldsymbol{\omega}}^{e} \tag{A.35}$$

$$\underset{\approx}{\boldsymbol{P}} = \underset{\approx}{\boldsymbol{R}}^{p}.\underset{\approx}{\boldsymbol{U}}^{p} \simeq (\underset{\approx}{\mathbf{1}} + \underset{\approx}{\boldsymbol{\omega}}^{p}).(\underset{\approx}{\mathbf{1}} + \underset{\approx}{\boldsymbol{\varepsilon}}^{p}) \simeq \underset{\approx}{\mathbf{1}} + \underset{\approx}{\boldsymbol{\varepsilon}}^{p} + \underset{\approx}{\boldsymbol{\omega}}^{p} \tag{A.36}$$

where $\underset{\approx}{\boldsymbol{R}}^{e}, \underset{\approx}{\boldsymbol{R}}^{p}$ and $\underset{\approx}{\boldsymbol{U}}^{e}, \underset{\approx}{\boldsymbol{U}}^{p}$ are rotations and symmetric stretch tensors, respectively. Accordingly, $\underset{\approx}{\boldsymbol{\varepsilon}}^{e}, \underset{\approx}{\boldsymbol{\omega}}^{e}$ (resp. $\underset{\approx}{\boldsymbol{\varepsilon}}^{p}, \underset{\approx}{\boldsymbol{\omega}}^{p}$) represent small elastic (resp. plastic) strain and rotation. The elastic rotation accounts for lattice rotation, as follows from the proposed kinematics of plastic slip. Similarly, the following holds for the total deformation:

$$\underset{\approx}{\boldsymbol{F}} = \underset{\approx}{\boldsymbol{R}}.\underset{\approx}{\boldsymbol{U}} = (\underset{\approx}{\mathbf{1}} + \underset{\approx}{\boldsymbol{\omega}}).(\underset{\approx}{\mathbf{1}} + \underset{\approx}{\boldsymbol{\varepsilon}}) \simeq \underset{\approx}{\mathbf{1}} + \underset{\approx}{\boldsymbol{\varepsilon}} + \underset{\approx}{\boldsymbol{\omega}} \tag{A.37}$$

so that

$$\underset{\approx}{\boldsymbol{\varepsilon}} = \underset{\approx}{\boldsymbol{\varepsilon}}^{e} + \underset{\approx}{\boldsymbol{\varepsilon}}^{p}, \quad \underset{\approx}{\boldsymbol{\omega}} = \underset{\approx}{\boldsymbol{\omega}}^{e} + \underset{\approx}{\boldsymbol{\omega}}^{p} \tag{A.38}$$

where all strain tensors are symmetric whereas all ω tensors are skew–symmetric.

In metals, elastic strain remains small whereas lattice rotations can become very large. That is why the kinematics of crystallographic slip is very often approximated as

$$\underset{\approx}{\boldsymbol{F}} \simeq \underset{\approx}{\boldsymbol{R}}^{e} \cdot \underset{\approx}{\boldsymbol{P}} \tag{A.39}$$

especially for the simulation of metal forming processes. Lattice rotation is then directly given by $\underset{\approx}{\boldsymbol{R}}^{e}$.

Let us consider also rotation rates by introducing the material spin tensor $\underset{\approx}{\boldsymbol{W}}$ which is the skew–symmetric part of the velocity gradient

$$\dot{\underset{\approx}{\boldsymbol{F}}} \cdot \underset{\approx}{\boldsymbol{F}}^{-1} = \underset{\approx}{\boldsymbol{D}} + \underset{\approx}{\boldsymbol{W}} = \dot{\underset{\approx}{\boldsymbol{E}}} \cdot \underset{\approx}{\boldsymbol{E}}^{-1} + \underset{\approx}{\boldsymbol{E}} \cdot \dot{\underset{\approx}{\boldsymbol{P}}} \cdot \underset{\approx}{\boldsymbol{P}}^{-1} \cdot \underset{\approx}{\boldsymbol{E}}^{-1} = \underset{\approx}{\boldsymbol{D}}^{e} + \underset{\approx}{\boldsymbol{W}}^{e} + \underset{\approx}{\boldsymbol{D}}^{p} + \underset{\approx}{\boldsymbol{W}}^{p} \tag{A.40}$$

where the elastic and plastic contributions have been split into their symmetric and skew–symmetric parts. The elastic spin tensor is therefore defined as

$$\underset{\approx}{\boldsymbol{W}}^{e} = \left(\dot{\underset{\approx}{\boldsymbol{E}}} \cdot \underset{\approx}{\boldsymbol{E}}^{-1}\right)^{skew} = \left(\dot{\underset{\approx}{\boldsymbol{R}}}^{e} \cdot \underset{\approx}{\boldsymbol{R}}^{e-1} + \underset{\approx}{\boldsymbol{R}}^{e} \cdot \dot{\underset{\approx}{\boldsymbol{U}}}^{e} \cdot \underset{\approx}{\boldsymbol{U}}^{e} \cdot \underset{\approx}{\boldsymbol{R}}^{e-1}\right)^{skew} \tag{A.41}$$

$$\simeq \dot{\underset{\approx}{\boldsymbol{R}}}^{e} \cdot \underset{\approx}{\boldsymbol{R}}^{e-1} = \dot{\underset{\approx}{\boldsymbol{R}}}^{e} \cdot \underset{\approx}{\boldsymbol{R}}^{eT} \tag{A.42}$$

where the exponent $skew$ denotes the skew–symmetric part of the tensor in brackets. The latter approximation is valid when elastic strain rates can be neglected compared to rotation rates, which is generally the case for metals at sufficiently high total strains. Note that for any rotation $\underset{\sim}{\boldsymbol{Q}}$, the rotation rate $\dot{\underset{\sim}{\boldsymbol{Q}}} \cdot \underset{\sim}{\boldsymbol{Q}}^{-1} = \dot{\underset{\sim}{\boldsymbol{Q}}} \cdot \underset{\sim}{\boldsymbol{Q}}^{T}$ is a skew–symmetric tensor due to the fact that a rotation is an orthogonal tensor[1]. The plastic spin rate is

$$\underset{\sim}{\boldsymbol{W}}^{p} = \left(\underset{\sim}{\boldsymbol{E}} \cdot \left(\sum_{s=1}^{N} \dot{\gamma}^{s} \underline{\boldsymbol{m}}^{s} \otimes \underline{\boldsymbol{n}}^{s} \right) \cdot \underset{\sim}{\boldsymbol{E}}^{-1} \right)^{skew} \tag{A.43}$$

$$\simeq \left(\underset{\sim}{\boldsymbol{R}}^{e} \cdot \left(\sum_{s=1}^{N} \dot{\gamma}^{s} \underline{\boldsymbol{m}}^{s} \otimes \underline{\boldsymbol{n}}^{s} \right) \cdot \underset{\sim}{\boldsymbol{R}}^{eT} \right)^{skew}$$

$$\simeq \underset{\sim}{\boldsymbol{R}}^{e} \cdot \left(\sum_{s=1}^{N} \dot{\gamma}^{s} \left(\underline{\boldsymbol{m}}^{s} \otimes \underline{\boldsymbol{n}}^{s} \right)^{skew} \right) \cdot \underset{\sim}{\boldsymbol{R}}^{eT} \tag{A.44}$$

In the case of small elastic strain and rotations, the expressions simplify and we obtain

$$\underset{\sim}{\boldsymbol{D}}^{p} \simeq \dot{\underset{\sim}{\boldsymbol{\varepsilon}}}^{p} = \sum_{s=1}^{N} \dot{\gamma}^{s} \left(\underline{\boldsymbol{m}}^{s} \otimes \underline{\boldsymbol{n}}^{s} \right)^{sym} \tag{A.45}$$

$$\underset{\sim}{\boldsymbol{W}}^{p} \simeq \dot{\underset{\sim}{\boldsymbol{\omega}}}^{p} = \sum_{s=1}^{N} \dot{\gamma}^{s} \left(\underline{\boldsymbol{m}}^{s} \otimes \underline{\boldsymbol{n}}^{s} \right)^{skew} \tag{A.46}$$

$$\underset{\sim}{\boldsymbol{D}}^{e} \simeq \dot{\underset{\sim}{\boldsymbol{\varepsilon}}}^{e} = \dot{\underset{\sim}{\boldsymbol{\varepsilon}}} - \dot{\underset{\sim}{\boldsymbol{\varepsilon}}}^{p}, \quad \dot{\underset{\sim}{\boldsymbol{W}}}^{e} \simeq \dot{\underset{\sim}{\boldsymbol{\omega}}}^{e} = \dot{\underset{\sim}{\boldsymbol{\omega}}} - \dot{\underset{\sim}{\boldsymbol{\omega}}}^{p} \tag{A.47}$$

A.2 The dislocation density tensor

A.2.1 Elements of tensor analysis

The Euclidean space is endowed with an arbitrary coordinate system characterizing the points $M(q^i)$. The basis vectors are defined as

$$\underline{\boldsymbol{e}}_{i} = \frac{\partial M}{\partial q^{i}} \tag{A.48}$$

The reciprocal basis $(\underline{\boldsymbol{e}}^{i})_{i=1,3}$ of $(\underline{\boldsymbol{e}}_{i})_{i=1,3}$ is the unique triad of vectors such that

$$\underline{\boldsymbol{e}}^{i} \cdot \underline{\boldsymbol{e}}_{j} = \delta^{i}_{j} \tag{A.49}$$

[1] meaning that $\underset{\sim}{\boldsymbol{Q}} \cdot \underset{\sim}{\boldsymbol{Q}}^{T} = \underset{\sim}{\boldsymbol{Q}}^{T} \cdot \underset{\sim}{\boldsymbol{Q}} = \underset{\sim}{\mathbf{1}}$

If a Cartesian orthonormal coordinate system is chosen, then both bases coincide.

The gradient operator for a tensor field $T(\underline{\boldsymbol{X}})$ of arbitrary rank is then defined as

$$\operatorname{grad} T = T \otimes \boldsymbol{\nabla} := \frac{\partial T}{\partial q^i} \otimes \underline{\boldsymbol{e}}^{\,i} \tag{A.50}$$

The gradient operation therefore increases the tensor rank by one.

The divergence operator for a tensor field $T(\underline{\boldsymbol{X}})$ of arbitrary rank is then defined as

$$\operatorname{div} T = T \cdot \boldsymbol{\nabla} := \frac{\partial T}{\partial q^i} \cdot \underline{\boldsymbol{e}}^{\,i} \tag{A.51}$$

The divergence operation therefore decreases the tensor rank by one.

The curl operator[2] for a tensor field $T(\underline{\boldsymbol{X}})$ of arbitrary rank is then defined as

$$\operatorname{curl} T = T \wedge \boldsymbol{\nabla} := \frac{\partial T}{\partial q^i} \wedge \underline{\boldsymbol{e}}^{\,i} \tag{A.52}$$

where the vector product is $\wedge$. The curl operation therefore leaves the tensor rank unchanged. The vector product on an oriented Euclidean space is

$$\underline{\boldsymbol{a}} \wedge \underline{\boldsymbol{b}} = \epsilon_{ijk} a_j b_k \, \underline{\boldsymbol{e}}_{\,i} = \underline{\underline{\boldsymbol{\epsilon}}} : (\underline{\boldsymbol{a}} \otimes \underline{\boldsymbol{b}}) \tag{A.53}$$

The component ϵ_{ijk} of the third rank permutation tensor is the signature of the permutation of $(1, 2, 3)$.

With respect to a Cartesian orthonormal basis, the previous formula simplify. We give the expressions for a second rank tensor $\underset{\sim}{\boldsymbol{T}}$

$$\operatorname{grad} \underset{\sim}{\boldsymbol{T}} = T_{ij,k} \, \underline{\boldsymbol{e}}_{\,i} \otimes \underline{\boldsymbol{e}}_{\,j} \otimes \underline{\boldsymbol{e}}_{\,k} \tag{A.54}$$

$$\operatorname{div} \underset{\sim}{\boldsymbol{T}} = T_{ij,j} \, \underline{\boldsymbol{e}}_{\,i} \tag{A.55}$$

We consider then successively the curl of a vector field and of a second rank vector field, in a Cartesian orthonormal coordinate frame

$$\operatorname{curl} \underline{\boldsymbol{u}} = \frac{\partial \underline{\boldsymbol{u}}}{\partial X_j} \wedge \underline{\boldsymbol{e}}_{\,j} = u_{i,j} \, \underline{\boldsymbol{e}}_{\,i} \wedge \underline{\boldsymbol{e}}_{\,j} = \epsilon_{kij} u_{i,j} \, \underline{\boldsymbol{e}}_{\,k} \tag{A.56}$$

$$\operatorname{curl} \underset{\sim}{\boldsymbol{A}} = \frac{\partial \underset{\sim}{\boldsymbol{A}}}{\partial x_k} \wedge \underline{\boldsymbol{e}}_{\,k} = A_{ij,k} \underline{\boldsymbol{e}}_{\,i} \otimes \underline{\boldsymbol{e}}_{\,j} \wedge \underline{\boldsymbol{e}}_{\,k} = \epsilon_{mjk} A_{ij,k} \, \underline{\boldsymbol{e}}_{\,i} \otimes \underline{\boldsymbol{e}}_{\,m} \tag{A.57}$$

We also recall the Stokes formula for a vector field for a surface $\mathcal{S}$ with unit normal vector $\underline{\boldsymbol{n}}$ and oriented closed border line $\mathcal{L}$:

$$\oint_{\mathcal{L}} \underline{\boldsymbol{u}} \cdot \underline{\boldsymbol{dl}} = -\int_{\mathcal{S}} (\operatorname{curl} \underline{\boldsymbol{u}}) \cdot \underline{\boldsymbol{n}} \, ds, \quad \oint_{\mathcal{L}} u_i dl_i = -\epsilon_{kij} \int_{\mathcal{S}} u_{i,j} n_k \, ds \tag{A.58}$$

[2] or rotational operator.

Applying the previous formula to $u_j = A_{ij}$ at fixed i leads to the Stokes formula for a tensor field of rank 2:

$$\oint_{\mathcal{L}} \underset{\sim}{\boldsymbol{T}} \cdot \underline{\boldsymbol{dl}} = -\int_{\mathcal{S}} (\operatorname{curl} \underset{\sim}{\boldsymbol{T}}) \cdot \underline{\boldsymbol{n}}\, ds, \quad \oint_{\mathcal{L}} A_{ij} dl_i = -\epsilon_{kij} \int_{\mathcal{S}} A_{ij,k} n_m\, ds \tag{A.59}$$

A.2.2 Dislocation density tensor

In continuum mechanics, the previous differential operators are used with respect to the initial coordinates $\underline{\boldsymbol{X}}$ or with respect to the current coordinates $\underline{\boldsymbol{x}}$ of the material points. In the latter case, the notation $\boldsymbol{\nabla}, \operatorname{grad}, \operatorname{div}$ and curl are used but in the former case we adopt $\boldsymbol{\nabla}_X, \operatorname{Grad}, \operatorname{Div}$ and Curl. For instance,

$$\underset{\sim}{\boldsymbol{F}} = \underset{\sim}{\mathbf{1}} + \operatorname{Grad} \underline{\boldsymbol{u}} \quad \Longrightarrow \quad \operatorname{Curl} \underset{\sim}{\boldsymbol{F}} = 0 \tag{A.60}$$

This result expresses the fact that the deformation gradient is a compatible field which derives from the displacement vector field. This is generally not the case for elastic and plastic deformation:

$$\operatorname{Curl} \underset{\sim}{\boldsymbol{E}} \neq 0, \quad \operatorname{Curl} \underset{\sim}{\boldsymbol{P}} \neq 0 \tag{A.61}$$

Elastic and plastic deformations are generally incompatible tensor fields, even though the product $\underset{\sim}{\boldsymbol{F}} = \underset{\sim}{\boldsymbol{E}} \cdot \underset{\sim}{\boldsymbol{P}}$ is compatible. It may happen incidentally that elastic deformation be compatible for instance when plastic or elastic deformation is homogeneous.

A consequence of the incompatibility of the elastic deformation is that, for an oriented surface $\mathcal{S} \subset \Omega$ of the body, with border $\mathcal{L}$, the vector $\underline{\boldsymbol{B}}$ belonging to the intermediate isoclinic configuration

$$\underline{\boldsymbol{B}} = \oint_{\mathcal{L}} \underset{\sim}{\boldsymbol{E}}^{-1} \cdot \underline{\boldsymbol{dl}} = -\int_{\mathcal{S}} (\operatorname{curl} \underset{\sim}{\boldsymbol{E}}^{-1}) \cdot \underline{\boldsymbol{n}}\, ds \tag{A.62}$$

does not vanish in general. It can be interpreted as the continuum Burgers vector for the circuit $\mathcal{L}$. It represents a generalization of the concept of Burgers vector for dislocations. This geometric definition was introduced by [Bilby et al., 1957, Teodosiu, 1970, Kröner and Teodosiu, 1972] within the context of the continuum theory of dislocations. The previous calculation leads to the definition of the dislocation density tensor

$$\underset{\sim}{\boldsymbol{\alpha}} := -\operatorname{curl} \underset{\sim}{\boldsymbol{E}}^{-1} = -\epsilon_{jkl} E^{-1}_{ik,l}\, \underline{\boldsymbol{e}}_i \otimes \underline{\boldsymbol{e}}_j \tag{A.63}$$

which is used to compute the resulting Burgers vector for dislocations crossing the surface $\mathcal{S}$:

$$\underline{\boldsymbol{B}} = \int_{\mathcal{S}} \underset{\sim}{\boldsymbol{\alpha}} \cdot \underline{\boldsymbol{n}}\, ds \tag{A.64}$$

The Burgers vector can also be computed by means of a closed circuit $\mathcal{L}_0 \subset \Omega_0$ convected from $\mathcal{L} \subset \Omega$:

$$\underline{\boldsymbol{B}} = \oint_{\mathcal{L}} \underset{\sim}{\boldsymbol{E}}^{-1} \cdot \underline{\boldsymbol{dx}} = \oint_{\mathcal{L}_0} \underset{\sim}{\boldsymbol{E}}^{-1} \cdot \underset{\sim}{\boldsymbol{F}} \cdot \underline{\boldsymbol{dX}} = \oint_{\mathcal{L}_0} \underset{\sim}{\boldsymbol{P}} \cdot \underline{\boldsymbol{dX}} \tag{A.65}$$

$$= \int_{\mathcal{S}_0} (\mathrm{Curl}\, \underset{\sim}{\boldsymbol{P}}) \cdot \underline{\boldsymbol{dS}} = \int_{\mathcal{S}} (\mathrm{Curl}\, \underset{\sim}{\boldsymbol{P}}) \cdot \underset{\sim}{\boldsymbol{F}}^T \cdot \frac{\boldsymbol{ds}}{J} \tag{A.66}$$

Nanson's formula[3] has been used. We obtain the alternative definition of the dislocation density tensor

$$\underset{\sim}{\boldsymbol{\alpha}} = \mathrm{curl}\, \underset{\sim}{\boldsymbol{E}}^{-1} = \frac{1}{J} (\mathrm{Curl}\, \underset{\sim}{\boldsymbol{P}}) \cdot \underset{\sim}{\boldsymbol{F}}^T \tag{A.67}$$

The present modern treatment of the dislocation density tensor was settled by [Cermelli and Gurtin, 2001a, Svendsen, 2002]. A statistical mechanics perspective of the dislocation density tensor can be found in [Kröner, 1969].

It can be noticed that the relation (A.67) implies

$$J(\mathrm{curl}\, \underset{\sim}{\boldsymbol{E}}^{-1}) \cdot \underset{\sim}{\boldsymbol{E}}^{-T} = (\mathrm{Curl}\, \underset{\sim}{\boldsymbol{P}}) \cdot \underset{\sim}{\boldsymbol{P}}^T \tag{A.68}$$

which is a consequence of (A.60), $\mathrm{curl}\, \underset{\sim}{\boldsymbol{F}} = \mathrm{curl}\, (\underset{\sim}{\boldsymbol{E}} \cdot \underset{\sim}{\boldsymbol{P}}) = 0$.

Within the small perturbation framework, we introduce the notations

$$\underset{\sim}{\boldsymbol{H}} = \mathrm{Grad}\, \underline{\boldsymbol{u}} = \underset{\sim}{\boldsymbol{H}}^e + \underset{\sim}{\boldsymbol{H}}^p, \quad \text{with} \quad \underset{\sim}{\boldsymbol{H}}^e = \underset{\sim}{\boldsymbol{\varepsilon}}^e + \underset{\sim}{\boldsymbol{\omega}}^e, \quad \underset{\sim}{\boldsymbol{H}}^p = \underset{\sim}{\boldsymbol{\varepsilon}}^p + \underset{\sim}{\boldsymbol{\omega}}^p \tag{A.69}$$

We have

$$\underset{\sim}{\boldsymbol{E}}^{-1} \simeq \underset{\sim}{\mathbf{1}} - \underset{\sim}{\boldsymbol{H}}^e \tag{A.70}$$

so that the dislocation density tensor can be computed as

$$\underset{\sim}{\boldsymbol{\alpha}} \simeq \mathrm{Curl}\, \underset{\sim}{\boldsymbol{H}}^e = -\mathrm{Curl}\, \underset{\sim}{\boldsymbol{H}}^p \tag{A.71}$$

since $\mathrm{Curl}\, \underset{\sim}{\boldsymbol{H}} = 0$ due to the compatibility of the deformation gradient.

A.2.3 Lattice curvature

Experimental techniques like EBSD provide the field of lattice orientation and, consequently, of lattice rotation $\underset{\sim}{\boldsymbol{R}}^e$ during deformation. Since

$$\underset{\sim}{\boldsymbol{\alpha}} = -\mathrm{curl}\, \underset{\sim}{\boldsymbol{E}}^{-1} = -\mathrm{curl}\, (\underset{\sim}{\boldsymbol{U}}^{e-1} \cdot \underset{\sim}{\boldsymbol{R}}^{eT}) \tag{A.72}$$

the hypothesis of small elastic strain implies

$$\underset{\sim}{\boldsymbol{\alpha}} \simeq -\mathrm{curl}\, \underset{\sim}{\boldsymbol{R}}^{eT} \tag{A.73}$$

[3] $\underline{\boldsymbol{ds}} = J \underset{\sim}{\boldsymbol{F}}^{-T} \cdot \underline{\boldsymbol{dS}}$

If, in addition, elastic rotations are small, we have

$$\underset{\sim}{\boldsymbol{\alpha}} \simeq -\mathrm{curl}\,(\underset{\sim}{\mathbf{1}} - \underset{\sim}{\boldsymbol{\omega}}^e) = \mathrm{curl}\,\underset{\sim}{\boldsymbol{\omega}}^e \tag{A.74}$$

The small rotation axial vector is defined as

$$\overset{\times}{\underline{\boldsymbol{\omega}}}{}^e = -\frac{1}{2}\underset{\approx}{\boldsymbol{\epsilon}} : \underset{\sim}{\boldsymbol{\omega}}^e, \quad \underset{\sim}{\boldsymbol{\omega}}^e = -\underset{\approx}{\boldsymbol{\epsilon}} \cdot \overset{\times}{\underline{\boldsymbol{\omega}}}{}^e \tag{A.75}$$

or, in matrix notations,

$$[\underset{\sim}{\boldsymbol{\omega}}^e] = \begin{bmatrix} 0 & \omega^e_{12} & -\omega^e_{31} \\ -\omega^e_{12} & 0 & \omega^e_{23} \\ \omega^e_{31} & -\omega^e_{23} & 0 \end{bmatrix} = \begin{bmatrix} 0 & -\overset{\times}{\omega}{}^e_3 & \overset{\times}{\omega}{}^e_2 \\ \overset{\times}{\omega}{}^e_3 & 0 & -\overset{\times}{\omega}{}^e_1 \\ -\overset{\times}{\omega}{}^e_2 & \overset{\times}{\omega}{}^e_1 & 0 \end{bmatrix} \tag{A.76}$$

The gradient of the lattice rotation field delivers the lattice curvature tensor. In the small deformation context, the gradient of the rotation tensor is represented by the gradient of the axial vector:

$$\underset{\sim}{\boldsymbol{\kappa}} := \overset{\times}{\underline{\boldsymbol{\omega}}}{}^e \tag{A.77}$$

One can establish a direct link between $\mathrm{curl}\,\underset{\sim}{\boldsymbol{\omega}}^e$ and the gradient of the axial vector associated with $\underset{\sim}{\boldsymbol{\omega}}$. For that purpose, the matrix form of $\mathrm{curl}\,\underset{\sim}{\boldsymbol{\omega}}^e$ is derived according to (A.57):

$$[\mathrm{curl}\,\underset{\sim}{\boldsymbol{\omega}}^e] = \begin{bmatrix} \omega^e_{12,3} + \omega^e_{31,2} & -\omega^e_{31,1} & -\omega^e_{12,1} \\ -\omega^e_{23,2} & \omega^e_{12,3} + \omega^e_{23,1} & -\omega^e_{12,2} \\ -\omega^e_{23,3} & -\omega^e_{31,3} & \omega^e_{23,1} + \omega^e_{31,2} \end{bmatrix} \tag{A.78}$$

or equivalently

$$[\mathrm{curl}\,\underset{\sim}{\boldsymbol{\omega}}^e] = \begin{bmatrix} -\overset{\times}{\omega}{}^e_{3,3} - \overset{\times}{\omega}{}^e_{2,2} & \overset{\times}{\omega}{}^e_{2,1} & \overset{\times}{\omega}{}_{3,1} \\ \overset{\times}{\omega}{}^e_{1,2} & -\overset{\times}{\omega}{}^e_{3,3} - \overset{\times}{\omega}{}^e_{1,1} & \overset{\times}{\omega}{}^e_{3,2} \\ \overset{\times}{\omega}{}^e_{1,3} & \overset{\times}{\omega}{}^e_{2,3} & -\overset{\times}{\omega}{}^e_{1,1} - \overset{\times}{\omega}{}^e_{2,2} \end{bmatrix} \tag{A.79}$$

from which it becomes apparent that

$$\underset{\sim}{\boldsymbol{\alpha}} = \underset{\sim}{\boldsymbol{\kappa}}^T - (\mathrm{trace}\,\underset{\sim}{\boldsymbol{\kappa}})\underset{\sim}{\mathbf{1}}, \quad \underset{\sim}{\boldsymbol{\kappa}} = \underset{\sim}{\boldsymbol{\alpha}}^T - \frac{1}{2}(\mathrm{trace}\,\underset{\sim}{\boldsymbol{\alpha}})\underset{\sim}{\mathbf{1}} \tag{A.80}$$

This is a remarkable relation linking, with the context of small elastic strains[4] and rotations, the dislocation density tensor to lattice curvature. It is known as Nye's formula [Nye, 1953].

[4] and in fact of small gradient of elastic strain.

A.3 Strain gradient plasticity: The "$curl H^p$" model

We consider now a strain gradient plasticity theory which includes the full curl of the plastic deformation tensor, $\underset{\sim}{\boldsymbol{H}}^p$, into constitutive modelling. This approach, therefrom to be referred to as the "$curl H^p$" model, was proposed by [Gurtin, 2002] and applied to a constrained layer and a composite problem in [Bittencourt et al., 2003, Cordero et al., 2010]. The balance and constitutive equations are introduced in the context of small perturbations. Then the model is applied to a crystal undergoing single slip. It will be shown that a specific form of the back stress arises from this application.

A.3.1 Balance equations

Following [Gurtin, 2002], we consider a continuum whose power density of internal forces takes the form:

$$p^{(i)} = \underset{\sim}{\boldsymbol{\sigma}} : \dot{\underset{\sim}{\boldsymbol{H}}} + \underset{\sim}{\boldsymbol{s}} : \dot{\underset{\sim}{\boldsymbol{H}}}^p + \underset{\sim}{\boldsymbol{M}} : \operatorname{curl} \dot{\underset{\sim}{\boldsymbol{H}}}^p. \tag{A.81}$$

For objectivity reasons, the stress tensor $\underset{\sim}{\boldsymbol{\sigma}}$ is symmetric whereas the micro–stress tensor $\underset{\sim}{\boldsymbol{s}}$ and the double–stress tensor $\underset{\sim}{\boldsymbol{M}}$ are generally asymmetric. The total power of internal forces in a domain V, with boundary ∂V, is

$$\begin{aligned}
\mathcal{P}^{(i)} &= \int_V \left(\underset{\sim}{\boldsymbol{\sigma}} : \dot{\underset{\sim}{\boldsymbol{H}}} + \underset{\sim}{\boldsymbol{s}} : \dot{\underset{\sim}{\boldsymbol{H}}}^p + \underset{\sim}{\boldsymbol{M}} : \operatorname{curl} \dot{\underset{\sim}{\boldsymbol{H}}}^p \right) dV, \\
&= \int_V \left(\left(\sigma_{ij}\dot{u}_i\right)_{,j} + \left(M_{ij}\epsilon_{jkl}\dot{H}^p_{ik} \right)_{,l} \right) dV \\
&+ \int_V \left(-\sigma_{ij,j}\dot{u}_i + s_{ij}\dot{H}^p_{ij} - \epsilon_{jkl}M_{ij,l}\dot{H}^p_{ik} \right) dV, \\
&= -\int_V \left(\sigma_{ij,j}\dot{u}_i - (\epsilon_{kjl}M_{ik,l} + s_{ij})\dot{H}^p_{ij} \right) dV \\
&+ \int_{\partial V} \left(\sigma_{ij}n_j\dot{u}_i + \epsilon_{jkl}M_{ij}n_l\dot{H}^p_{ik} \right) dS.
\end{aligned}$$

The power density of contact forces is taken as

$$p^{(c)} = \underline{\boldsymbol{t}} \,.\, \dot{\underline{\boldsymbol{u}}} + \underset{\sim}{\boldsymbol{m}} : \dot{\underset{\sim}{\boldsymbol{H}}}^p, \tag{A.82}$$

where $\underline{\boldsymbol{t}}\,, \underset{\sim}{\boldsymbol{m}}$ are, respectively, the surface simple and double tractions. Volume forces are not written for simplicity. The method of virtual power can be used to derive the field equations governing the continuum, based on the virtual motions $\dot{\underline{\boldsymbol{u}}}$ and $\dot{\underset{\sim}{\boldsymbol{H}}}^p$:

$$\operatorname{div} \underset{\sim}{\boldsymbol{\sigma}} = 0, \quad \sigma_{ij,j} = 0, \tag{A.83}$$

$$\operatorname{curl} \underset{\sim}{\boldsymbol{M}} + \underset{\sim}{\boldsymbol{s}} = 0, \quad \epsilon_{jkl} M_{ik,l} + s_{ij} = 0, \tag{A.84}$$

for all regular points of the domain V. Furthermore, the following boundary conditions on ∂V can be derived:

$$\underline{\boldsymbol{t}} = \underset{\sim}{\boldsymbol{\sigma}}.\underline{\boldsymbol{n}}, \quad t_i = \sigma_{ij} n_j, \tag{A.85}$$

$$\underset{\sim}{\boldsymbol{m}} = \underset{\sim}{\boldsymbol{M}}.\underset{\approx}{\boldsymbol{\epsilon}}.\underline{\boldsymbol{n}}, \quad m_{ij} = M_{ik} \epsilon_{kjl} n_l. \tag{A.86}$$

A.3.2 Energy and entropy principles, constitutive equations

Under isothermal conditions, the energy balance in its local form states that:

$$\rho \dot{e} = p^{(i)}, \tag{A.87}$$

where e is the internal energy density function and, ρ, the mass density. The entropy principle is formulated as

$$\rho(\dot{e} - \dot{\psi}) \geq 0 \tag{A.88}$$

where ψ is the Helmholtz free energy function. The free energy is taken as a function of the elastic strain, $\underset{\sim}{\boldsymbol{\varepsilon}}^e$, the dislocation density tensor, or $\operatorname{curl} \underset{\sim}{\boldsymbol{H}}^p$, and a generic internal hardening variable, q, viz. $\psi(\underset{\sim}{\boldsymbol{\varepsilon}}^e, \operatorname{curl} \underset{\sim}{\boldsymbol{H}}^p, q)$. As a result, the Clausius–Duhem inequality becomes

$$\left(\underset{\sim}{\boldsymbol{\sigma}} - \rho \frac{\partial \psi}{\partial \underset{\sim}{\boldsymbol{\varepsilon}}^e} \right) : \dot{\underset{\sim}{\boldsymbol{\varepsilon}}}^e + \left(\underset{\sim}{\boldsymbol{M}} - \rho \frac{\partial \psi}{\partial \operatorname{curl} \underset{\sim}{\boldsymbol{H}}^p} \right) : \operatorname{curl} \dot{\underset{\sim}{\boldsymbol{H}}}^p + (\underset{\sim}{\boldsymbol{\sigma}} + \underset{\sim}{\boldsymbol{s}}) : \dot{\underset{\sim}{\boldsymbol{H}}}^p - \rho \frac{\partial \psi}{\partial q} \dot{q} \geq 0. \tag{A.89}$$

Here, the constitutive assumption is made that the two first terms in the previous inequality are non dissipative and therefore should vanish. Then,

$$\underset{\sim}{\boldsymbol{\sigma}} = \rho \frac{\partial \psi}{\partial \underset{\sim}{\boldsymbol{\varepsilon}}^e}, \quad \underset{\sim}{\boldsymbol{M}} = \rho \frac{\partial \psi}{\partial \operatorname{curl} \underset{\sim}{\boldsymbol{H}}^p}. \tag{A.90}$$

It follows that the residual dissipation rate is

$$D = (\underset{\sim}{\boldsymbol{\sigma}} + \underset{\sim}{\boldsymbol{s}}) : \dot{\underset{\sim}{\boldsymbol{H}}}^p - R\dot{q} \geq 0, \tag{A.91}$$

where $R = \rho \partial \psi / \partial q$ is the thermodynamic force associated with the internal variable, q. The existence of a dissipation potential, namely $\Omega(\underset{\sim}{\boldsymbol{\sigma}} + \underset{\sim}{\boldsymbol{s}}, R)$, is postulated so that

$$\dot{\underset{\sim}{\boldsymbol{H}}}^p = \frac{\partial \Omega}{\partial (\underset{\sim}{\boldsymbol{\sigma}} + \underset{\sim}{\boldsymbol{s}})}, \quad \dot{q} = -\frac{\partial \Omega}{\partial R}. \tag{A.92}$$

A.3.3 Application of the "$curl H^p$" model to a single slip problem

For a crystal deforming under single slip conditions, the plastic deformation rate is given by:

$$\dot{\underset{\sim}{\boldsymbol{H}}}^p = \dot{\gamma}\underset{\sim}{\boldsymbol{P}} = \dot{\gamma}\underline{\boldsymbol{l}} \otimes \underline{\boldsymbol{n}}\,, \tag{A.93}$$

where $\underset{\sim}{\boldsymbol{P}} = \underline{\boldsymbol{l}} \otimes \underline{\boldsymbol{n}}$ is the orientation tensor, $\underline{\boldsymbol{l}}$ is the slip direction and $\underline{\boldsymbol{n}}$ the normal to the slip plane. The dissipation rate can then be expressed as,

$$(\tau + \underline{\boldsymbol{l}}\,.\underset{\sim}{\boldsymbol{s}}.\underline{\boldsymbol{n}}\,)\dot{\gamma} - R\dot{q} \geq 0, \tag{A.94}$$

where $\tau = \underline{\boldsymbol{l}}\,.\underset{\sim}{\boldsymbol{\sigma}}.\underline{\boldsymbol{n}}$ is the resolved shear stress. In the absence of a hardening variable, q, for simplicity, the following generalised Schmid law can be defined (for positive $\dot{\gamma}$):

$$|\tau - x| = \tau_c, \quad \text{with} \quad x = -\underline{\boldsymbol{l}}\,.\underset{\sim}{\boldsymbol{s}}.\underline{\boldsymbol{n}}\,, \tag{A.95}$$

meaning that plastic flow occurs when the effective resolved shear stress $|\tau - x|$ reaches the critical resolved shear stress τ_c. A kinematic hardening component, x, naturally arises in the formulation for which a more specific form is given next. The curl of the plastic deformation is then given by

$$\operatorname{curl} \underset{\sim}{\boldsymbol{H}}^p = \underline{\boldsymbol{l}} \otimes (\underline{\boldsymbol{n}} \times \boldsymbol{\nabla}\gamma). \tag{A.96}$$

For a two–dimensional case, one finds

$$[\operatorname{curl} \underset{\sim}{\boldsymbol{H}}^p] = \begin{bmatrix} 0 & 0 & \gamma_{,2}n_1n_2 - \gamma_{,1}n_2^2 \\ 0 & 0 & -\gamma_{,2}n_1^2 + \gamma_{,1}n_1n_2 \\ 0 & 0 & 0 \end{bmatrix}. \tag{A.97}$$

In the particular case when $\underline{\boldsymbol{l}} = \underline{\boldsymbol{e}}_1$, $\underline{\boldsymbol{n}} = \underline{\boldsymbol{e}}_2$, the only non–vanishing component of the dislocation density tensor is

$$(\operatorname{curl} \underset{\sim}{\boldsymbol{H}}^p)_{13} = -\gamma_{,1}. \tag{A.98}$$

Let us consider at this stage the simple quadratic potential:

$$\rho\psi(\underset{\sim}{\boldsymbol{\varepsilon}}^e, \operatorname{curl} \underset{\sim}{\boldsymbol{H}}^p) = \frac{1}{2}\underset{\sim}{\boldsymbol{\varepsilon}}^e : \underset{\approx}{\boldsymbol{C}} : \underset{\sim}{\boldsymbol{\varepsilon}}^e + \frac{1}{2}A\,(\operatorname{curl} \underset{\sim}{\boldsymbol{H}}^p) : (\operatorname{curl} \underset{\sim}{\boldsymbol{H}}^p)\,, \tag{A.99}$$

so that

$$\underset{\sim}{\boldsymbol{\sigma}} = \underset{\approx}{\boldsymbol{C}} : \underset{\sim}{\boldsymbol{\varepsilon}}^e, \quad \underset{\sim}{\boldsymbol{M}} = A \operatorname{curl} \underset{\sim}{\boldsymbol{H}}^p, \tag{A.100}$$

where $\underset{\approx}{\boldsymbol{C}}$ is the four–rank tensor of the elastic moduli, assumed isotropic hereafter, and A is a higher order modulus. According to the balance equation (A.84), it follows that

$$\underset{\sim}{\boldsymbol{s}} = -\operatorname{curl} \underset{\sim}{\boldsymbol{M}} = -\operatorname{curl}\operatorname{curl} \underset{\sim}{\boldsymbol{H}}^p. \tag{A.101}$$

For single slip, the double curl of plastic deformation is defined as

$$\operatorname{curl}\operatorname{curl}\underset{\sim}{\boldsymbol{H}}^p = \underline{\boldsymbol{l}} \otimes ((\underline{\boldsymbol{n}} \times \gamma_{,ij}\underline{\boldsymbol{e}}_i) \times \underline{\boldsymbol{e}}_j). \tag{A.102}$$

In the particular case of $\underline{\boldsymbol{l}} = \underline{\boldsymbol{e}}_1,\ \underline{\boldsymbol{n}} = \underline{\boldsymbol{e}}_2$, we obtain

$$\operatorname{curl}\operatorname{curl}\underset{\sim}{\boldsymbol{H}}^p = \gamma_{,12}\underline{\boldsymbol{e}}_1 \otimes \underline{\boldsymbol{e}}_1 - \gamma_{,11}\underline{\boldsymbol{e}}_1 \otimes \underline{\boldsymbol{e}}_2, \tag{A.103}$$

so that the back–stress takes the form

$$x = A(\operatorname{curl}\operatorname{curl}\underset{\sim}{\boldsymbol{H}}^p) : (\underline{\boldsymbol{l}} \otimes \underline{\boldsymbol{n}}) = -\gamma_{,11}. \tag{A.104}$$

A.4 Conclusions

The elastoviscoplasticiy theory of single crystals is the single well–established anisotropic nonlinear mechanical theory. Indeed, the multiplicative decomposition of the deformation gradient into elastic and plastic parts is only possible when a triad of directors can be unambiguously defined for the considered materials. Mandel showed that lattice directions in a single crystal determine privileged directors for the material. Such directors are more difficult to define for a composite material or for a polycrystal [Mandel, 1982]. The benefit is that the kinematic aspects of plastic deformation in single crystals is well–accepted today and that research can be focused on the development of relevant evolution equations for the internal variables like dislocation densities.

Discrete dislocation dynamics simulations are currently used as guidelines to develop advanced constitutive equations, as explained in the chapter by B. Devincre in part I. The transition from the single crystal to polycrystalline material volume elements can be done by means of analytical and computational homogenization methods, like simulations of the response of polycrystalline aggregates, see chapter by H. Proudhon in part III.

2D and 3D field measurement techniques have been used to validate the plasticity theory. For large metallic grains, the theory is essentially validated by the early contribution [Teodosiu et al., 1993] and subsequent comparisons between lattice rotation and total strain field measurements by means of EBSD and grids. More recent techniques give access to 3D data [Proudhon et al., 2010, Vaxelaire et al., 2010, Ludwig et al., 2009a].

Difficulties arise when tackling size effect problems in crystal plasticity. The introduction of the dislocation density tensor in modern crystal plasticity theory gives rise to the prediction of size effects that are in qualitative agreement with many experimental results. However, quantitative agreement is not met yet. The determination of scaling laws, like the Hall–Petch scaling $1/\sqrt{d}$ (with

d, the grain size) or Orowan's scaling $1/d$ for distances d between precipitates, are still not correctly retrieved by most strain gradient plasticity models because of the expensive nonlinear 3D computations required or because of the inadequate enhanced constitutive equations. These research issues are discussed in the contribution [Cordero et al., 2010] and in the references quoted therein.

Appendix B

Solving the trigonometric equation $A\cos(x) + B\sin(x) = C$

Here we consider the trigonometric equation:

$$A\cos(x) + B\sin(x) = C \tag{B.1}$$

We suppose the variable t such as $t = \tan(\frac{x}{2})$. We have therefore:

$$\cos(x) = \frac{1-x^2}{1+t^2} \text{ and } \sin(x) = \frac{2x}{1+t^2} \tag{B.2}$$

(B.1) become:

$$-(A+C)t^2 + 2Bt + (A-C) = 0 \tag{B.3}$$

and the determinant is :

$$\Delta = 4(A^2 + B^2 - C^2) \tag{B.4}$$

then:

$$t_1 = -\frac{B+\sqrt{\Delta}}{A+C} \text{ and } t_1 = -\frac{B-\sqrt{\Delta}}{A+C} \tag{B.5}$$

and finally:

$$x_1 = 2\arctan(-\frac{B+\sqrt{\Delta}}{A+C}) \text{ and } x_2 = 2\arctan(-\frac{B-\sqrt{\Delta}}{A+C}) \tag{B.6}$$

Appendix C

Band profile analysis

In this section, the position and the width of the bands are identified for the grain 4, at the final state of the experiment. FWHM and peak positions are given in pixel. Except for the in-situ analysis for the grain 10, all measurements are made with topographs taken during scan #23. The spatial resolution is 1 px = $0.7\,\mu\mathrm{m}$. The methodology used here is as follows:

- the topograph is rotated such as the set of bands of interest becomes horizontal;
- the positions of the bands are manually identified;
- a 30 pixels wide area is selected in the rotated image. The intensity is integrated over the horizontal direction in this area;
- the background around the band of interest is corrected by applying a linear correction;
- the profile of the intensity is interpolated by a Gaussian fit;

C.1 Grain 4

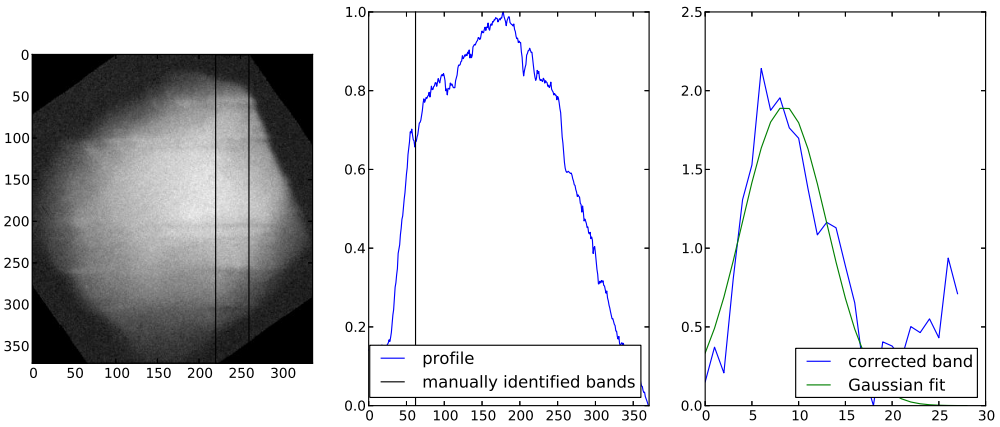

Figure C.1 – Grain 4, band #1, peak position = 62, FWHM = 10.71

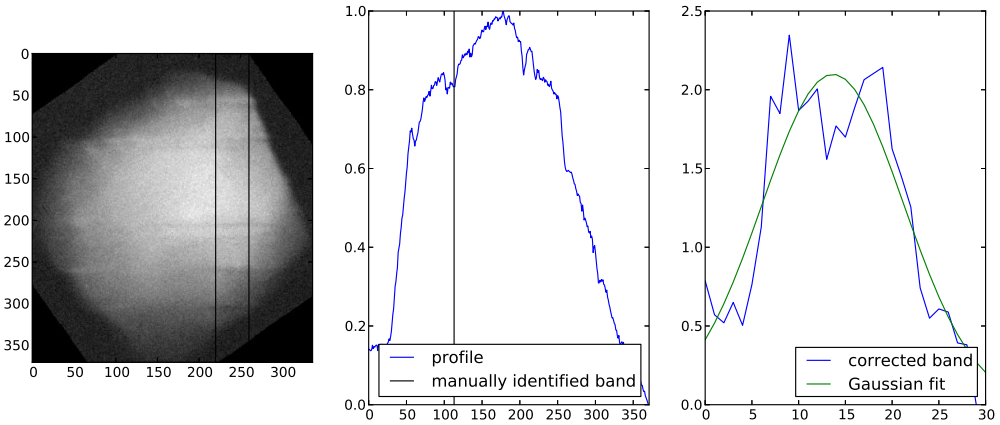

Figure C.2 – Grain 4, band #2, peak position = 113, FWHM = 17.83

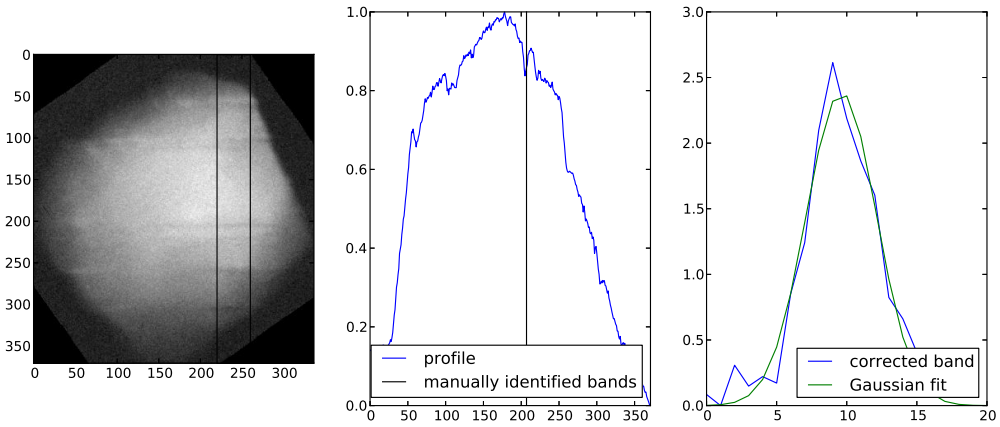

Figure C.3 – Grain 4, band #3, peak position = 207, FWHM = 5.92

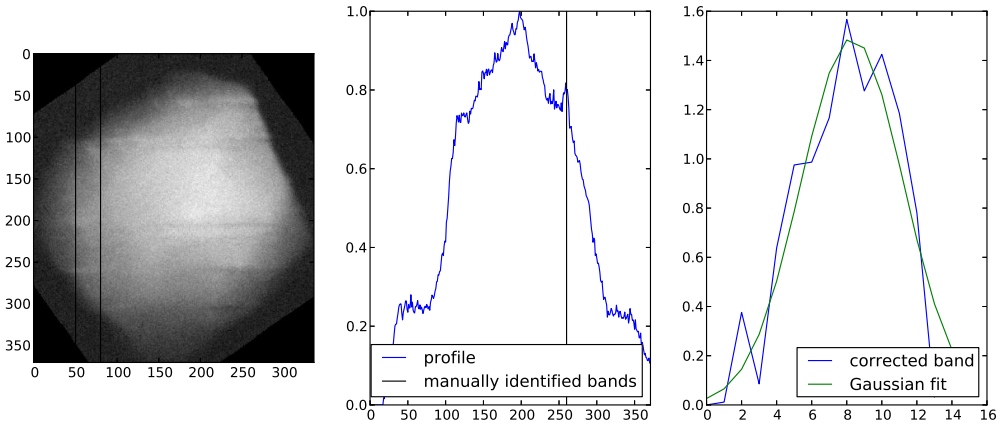

Figure C.4 – Grain 4, band #4, peak position = 260, FWHM = 6.88

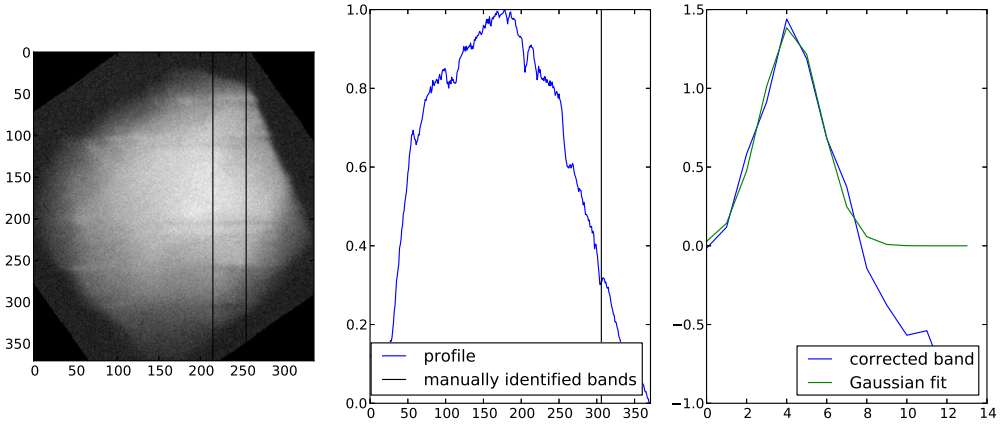

Figure C.5 – Grain 4, band #5, peak position = 306, FWHM = 3.53

C.2 Grain 10

C.2.1 In situ analysis for the primary slip system

Here the evolution of a band is analyzed in-situ, for five steps of the experiment, for the grain 10. The bands belong to the first activated slip system observed during the experiment.

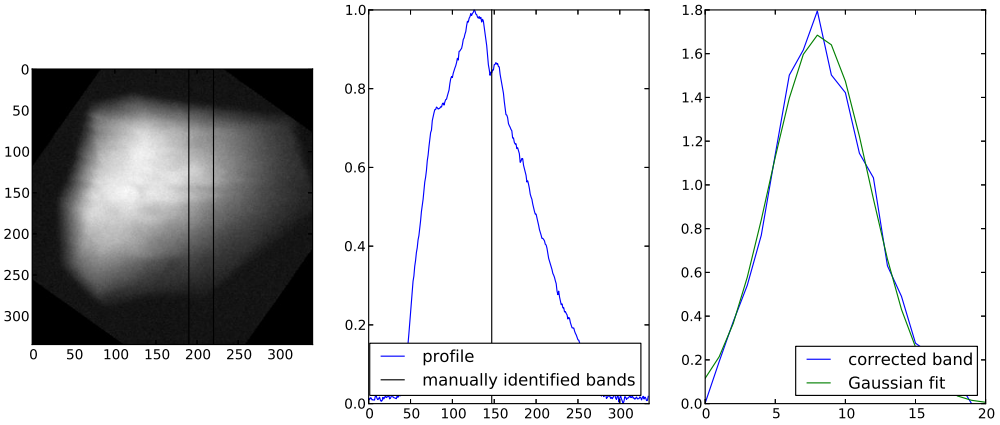

Figure C.6 – Grain 10, peak position = 147, FWHM = 8.31, scan #17

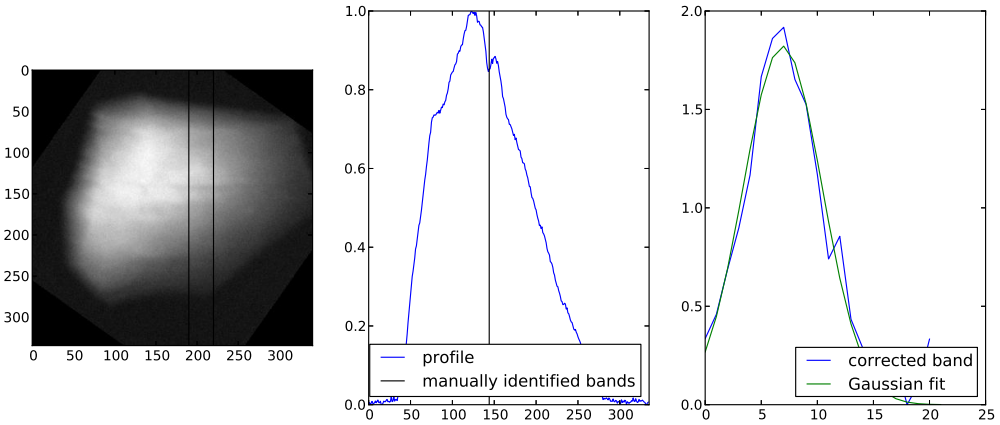

Figure C.7 – Grain 10, peak position = 144, FWHM = 8.30, scan #18

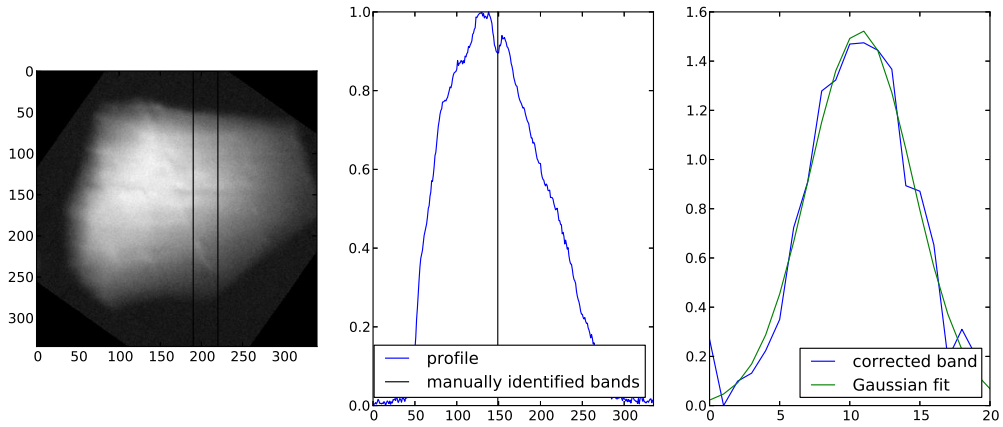

Figure C.8 – Grain 10, peak position = 149, FWHM = 8.72, scan #19

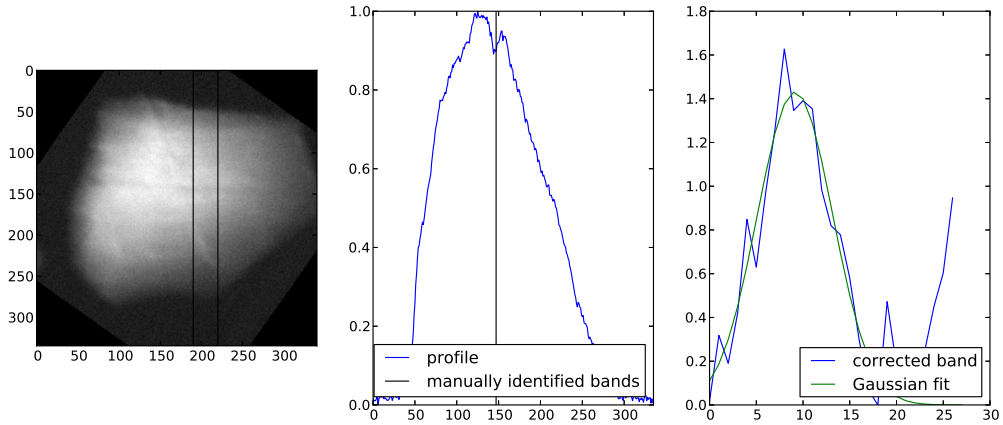

Figure C.9 – Grain 10, peak position = 147, FWHM = 9.51, scan #21

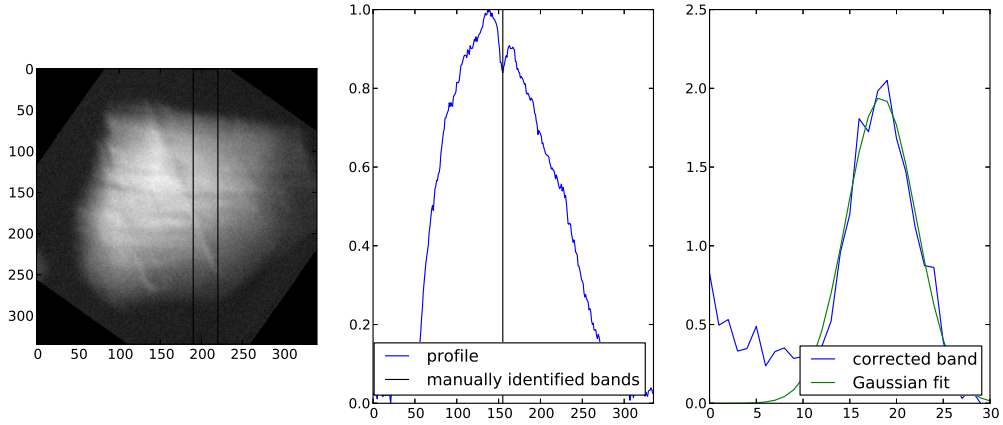

Figure C.10 – Grain 10, peak position = 155, FWHM = 10.34, scan #23

C.2.2 Secondary slip system

Here the position and the width of the two identifiable bands for the secondary slip system of the grain 10.

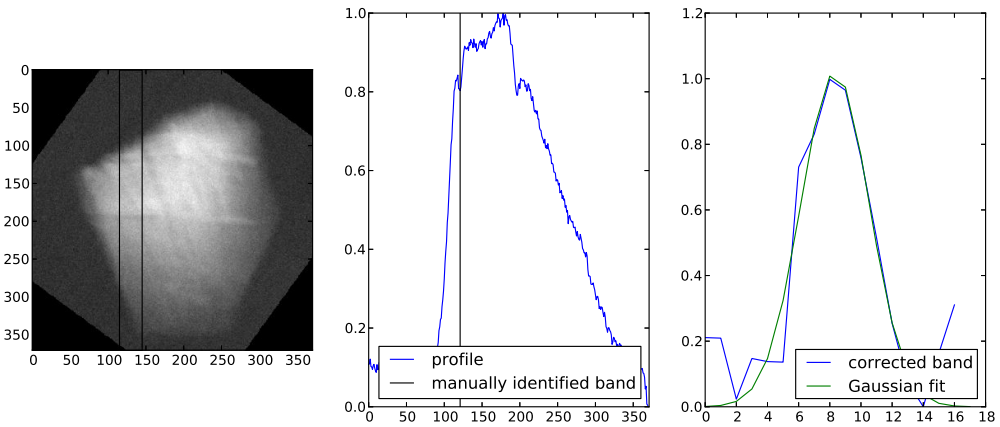

Figure C.11 – Grain 10, peak position = 121, FWHM = 5.81, band #1

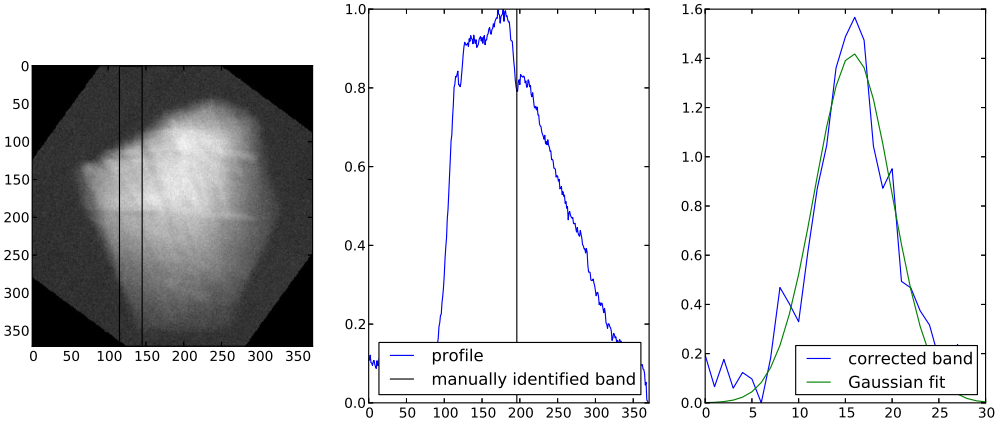

Figure C.12 – Grain 10, peak position = 196, FWHM = 9.69, band #2

C.3 Grain 18

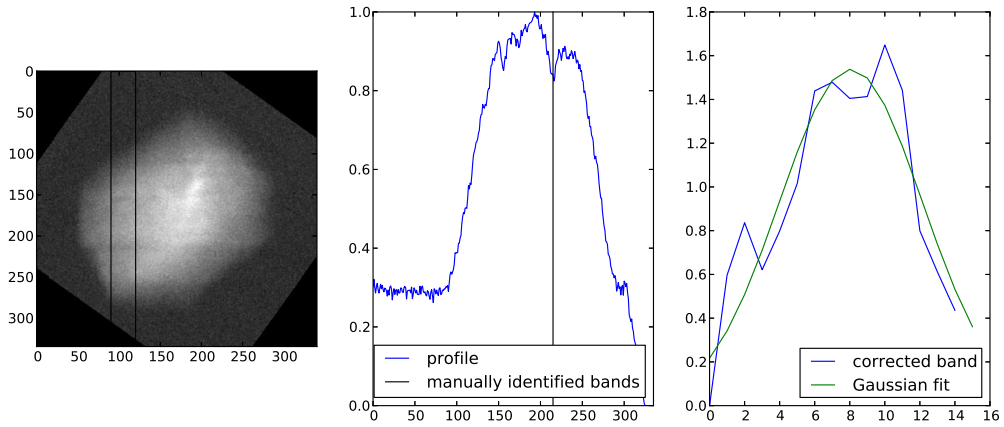

Figure C.13 – Grain 10, peak position = 215, FWHM = 9.59, band #1

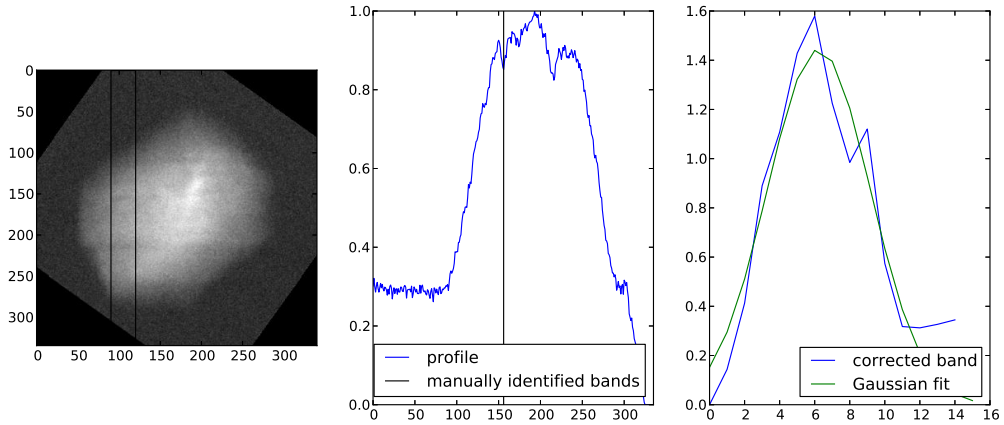

Figure C.14 – Grain 10, peak position = 156, FWHM = 6.9, band #2

Résumé

La compréhension des mécanismes de déformation dans les matériaux polycristallins est un problème important, qui conditionne notre capacité à concevoir et à produire des pièces de structure plus sures et avec un impact environnemental moindre. Cette compréhension est aujourd'hui limitée par notre capacité à observer à la fois la microstructure du matériau et ses mécanismes de déformation en trois dimensions (3D) aux petites échelles, et à informer les simulations mécaniques à partir des mécanismes physique de déformations du réseau cristallin. Des progrès considérables ont été faits dans les dernières décennies avec les observations de surfaces (i.e. technique EBSD associée a de la corrélation d'image) qui a permis de nombreuses études combinant des observations expérimentales à des simulations, à partir de la surface de la microstructure. Cependant, une comparaison précise sans connaitre la microstructure sous-jacente reste un défi. Dans ce travail, nous proposons une nouvelle méthodologie basée d'une part sur des mesures couplant la tomographie et la diffraction des rayons X, et d'autre part sur des simulations mécaniques de platicité cristalline. Cette approche permet une comparaison quantitative en volume entre les mécanismes de déformation, l'évolution de la courbure du réseau cristallin et les champs mécaniques simulés.
Pour ce faire, une machine de traction dédiée aux expériences 4D d'imagerie par diffraction sur grands instruments a été conçue, et utilisée pour déformer en tension un échantillon d'Aluminium Lithium. La cartographie 3D de la microstructure a été obtenue par tomographie par contraste de diffraction, et un agrégat de trois grains dans le volume de l'échantillon a été choisi comme région d'intérêt pour des observation 4D par topotomographie. L'apparition des premières bandes de glissement en volume et leur évolution au cours du chargement ont été observées le long de plans cristallographiques bien définis. Les trois grains ont montré une activité plastique le long de deux familles de plans différents, pas toujours en accord avec une analyse macroscopique du facteur de Schmid, ce qui est attribué à l'influence du voisinage sur l'activation des systèmes de glissement. Les changements d'amplitude et d'orientation de la courbure moyenne des grains ont été mesures avec un niveau de détail sans précédent, par une analyse tridimensionnelle des courbes de reflexions.
En parallèle, des simulations de la plasticité cristalline par éléments finis (CPFE) ont été menées utilisant la cartographie tridimensionnelle de la microstructure mesurée expérimentalement. Un chargement uniaxial de traction a été applique pour reproduire numériquement l'expérience, et comparer grain par grain l'activité plastique. L'activité des systèmes de glissement prédite par le modèle est conforme aux observations expérimentales d'une activité plastique le long de deux plans. Un cadre mathématique pour prédire l'angle de Bragg local en fonction des déformations et des rotations du réseau cristallin a été formulé. Un post-traitement des champs intragranulaires de déformation à partir des résultats des simulations CPFE a montré une excellente concordance avec les résultats expérimentaux. Ce résultat confirme que la topotomographie in-situ aux rayons X est un outil prometteur pour l'étude des premiers stades de la plasticité cristalline en volume.

Mots Clés

CPFEM, topotomographie, DCT, plasticité cristalline

Abstract

Understanding the intimate details of plastic deformation in polycrystalline materials is an important issue to improve material design and ultimately produce safer structural parts with less impact on the environment. This understanding is presently limited by our ability to observe both the microstructure of the material and the deformation processes in three dimensions (3D) at small length scales and inform mechanical simulations with physical deformation mechanisms of the crystal lattice. Considerable progress has been made in the last decade with surface observation (eg EBSD coupled to digital image correlation) which led to numerous studies combining experimental observations and simulations from the surface microstructure. However, an accurate comparison without knowing the underlying microstructure remain challenging. In this work, we propose a new methodology which allows a quantitative comparison between the observation of deformation mechanisms, the evolution of the grain lattice curvature and the simulated mechanical fields.
For that purpose, a mechanical stress rig dedicated for synchrotron 4D diffraction imaging experiments has been designed, and used to deform an Aluminium-Lithium specimen under tension. The 3D grain map has been obtained by diffraction contrast tomography analysis, and a cluster of three grains within the bulk has been selected to be the region of interest of the 4D observation by X-ray topotomography. The appearance and evolution of 3D crystalline defects as a function of the applied load has been observed to be located along well defined crystallographic planes. All three grains showed plastic activity on along two different set of planes, which is not always coherent with a macroscopic Schmid Factor analysis. The change of the amplitude and the orientation of the average grain curvature has been measured with an unprecedented level of detail by means of 3D rocking curve analysis.
In parallel, crystal plasticity finite element (CPFE) simulations have been carried using the 3D grain map measured experimentally. Tension loading was applied to reproduce the experiment numerically and compare the plastic activity on a grain by grain basis. The slip system activity predicted by the model matches in most cases the observed two slip system scenario. A mathematical framework to predict the local Bragg angle based on the stretch and rotation of the crystal lattice by the elastic strain tensor was derived. Post-processing the intragranular strains fields from the CPFE results allowed to simulate 3D rocking curves, showing excellent agreement with the experimental measurements. This result confirms that in situ X-ray topotomography is a promising tool to study the early stage of polycrystal plasticity within the bulk of millimetric material specimens.

Keywords

CPFEM, topotomography, DCT, crystal plasticity